

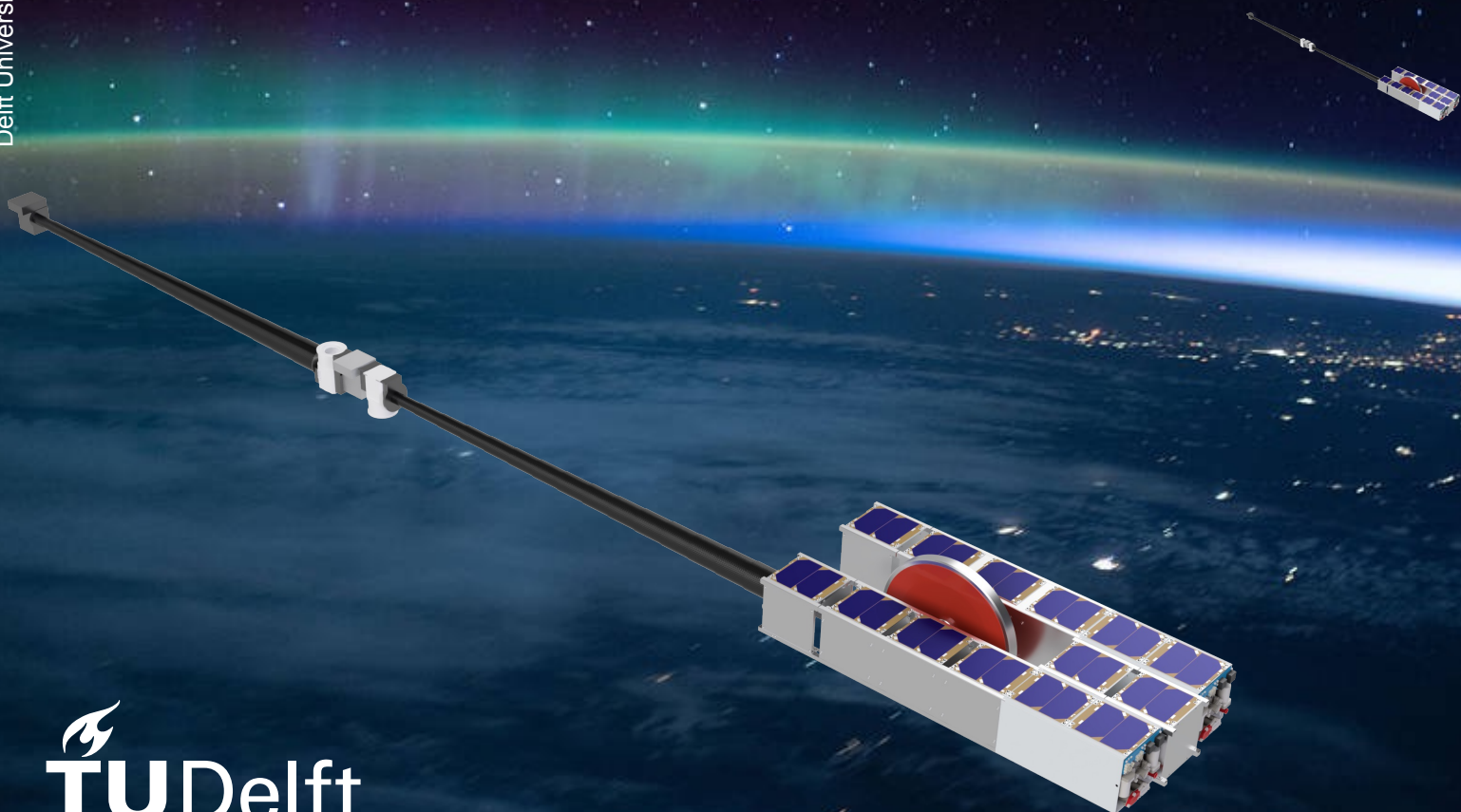
MAGEOS: Cubesat Mission for Measurements in Extreme VLEO

Final Technical Design Report

AE3200: Design Synthesis Exercise

Group 09 – Tuesday 21st June, 2022

Bas Andriessen	5067804	Tristan Hirs	5027578
Mattijs Berendsen	4687272	Bhavya Mahajan	5021553
Adrian Bradosche Pallarés	5016339	Tiago Teles	5047277
Jens Bremer	5019834	Justin Shioda	5050936
Koen den Dekker	4682149	Lucas van der Poll	5009235



Executive Summary

Functional Overview

In Chapter 2, different phases of the MAGEOS mission will be examined. For each phase, actions, also called functions, will be determined. To gain insight in the flow of functions for different mission phases, a functional flow diagram has been generated. Furthermore, a functional breakdown structure has been created. After the functional flow diagram and functional breakdown structure have been examined, the subsystems that will be used onboard the spacecrafts for the MAGEOS mission will be justified and discussed.

Design Approach

In Chapter 3, the approach to obtain the final design of the MAGEOS mission will be explained. An iteration diagram has been developed to ease the order of iterations. Tools for iterations, such as codes to determine the optimal boom length, drag, and lift coefficient, have been developed first. Making use of these tools, a final design has been obtained.

In attempt to limit the impact of the MAGEOS mission on climate change, the midterm report [1] featured a sustainability development strategy. In this final report, the total approximated emissions for the MAGEOS mission will be determined, as well as how the MAGEOS mission can contribute to monitoring climate change and potential dangers to Earth's ecosystems. In Table 3.3, all approximated emission the MAGEOS mission is expected to expel are presented.

Table 1: Total emission of the MAGEOS mission

Emission	Amount [kg]
Carbon dioxide (CO ₂)	10013.1
Water vapor	1910.6
Carbon soot	458.6
Nitrogen oxide (NO _x)	15.3
Aluminium oxide (Al ₂ O ₃)	34.9

Instrument Design

In Chapter 4, two measurement systems: a magnetometer and gravimeter, are presented. First, different ways of measuring the magnetic field are explained, including different technologies used throughout space missions and their accuracy. With this information a program was developed to simulate the magnetic fields near MAGEOS with different sources and sensors. An algorithm is developed to process magnetometer measurements and obtain a maximum error of 0.5 [nT]. After, the theory behind gravimeters is explored, with an accompanying simulation demonstrating the capabilities of MAGEOS. With this information a suitable suite of measurement devices are chosen and justified.

Orbit Design

In Chapter 5, the orbits of the MAGEOS spacecraft will be designed. The forecast location of the magnetic north and south pole is analysed, the effect of latitude on GNSS performance is determined, and the relative ground speed of different orbits determined. An analysis is performed to establish a representative launcher orbit, and the final orbit is selected such that it is Earth-repeating after 30 days, sun-synchronous and fulfills the customer's requirements.

Architecture Design

In Chapter 6, the final design for each subsystem is presented. The order in which the subsystems are described are as follows: First the spacecraft structure is discussed, after which an overview is given of the EPS system. This is followed by the propulsion, the thermal control, and the TTC system. After this the CDH system is described, and then the ADCS design is presented. At the end the final configuration is presented. Here the shape of the spacecraft and the location of each component are discussed, as well as the location of the center of mass and the spacecraft moment of inertia.

Final Design

In Chapter 8, an overview of the final design will be presented. The lay-out, from the inside and outside, as well as a mass and power breakdown are present. Furthermore, a sensitivity analysis will be presented. Within this analysis, slight deviations from the final design and their impact will be examined. Provisions are made for slight deviations will be given to the mass, power consumption, propellant, size, temperature, boom length, altitude and collected data.

Design Analysis

In Chapter 7, some characteristics for the final obtained design, as well as the method they have been explained was presented. In the aerodynamic characteristic estimation, the drag and lift coefficient will be determined making use of the Sentman equations. The final approximated drag and lift coefficient will be 2.6 [-] and a maximal lift coefficient of 0.2 [-]. The total drag that will be experienced during the nominal mission is 278 [μ N]. In the astrodynamics characteristic estimation, an analysis of the ΔV required for insertion into the operational orbit, the maneuvering sequence required for insertion into the operational orbit, and the ΔV required for orbital maintenance are determined.

A RAMS analysis, Reliability, Availability, Maintainability and Safety, has been performed as well on the MAGEOS mission. It was identified that the mission reliability is relatively low, approximately 42%. The availability to communicate with the ground stations is around the 6.1% per orbit, which is around the 325 [s] per orbit. Some safety critical systems, such as the propulsion unit and vehicle failures was examined as well.

Design Actualisation

In Chapter 9, the logistics, project design, development logic and cost breakdown are discussed. The MAGEOS mission can be divided up into 4 phases. First phase; Pre-Launch: All operations and facilities required onground before it is ready to launch. Then, how the spacecraft is built, mostly using commercial off-the-shelf components, the facilities required, such as: a cleanroom, thermal vacuum tests (ESA-ESTEC) and zero-g test (PH-LAB). Second phase; Orbit Insertion: CubeSat constellation is deployed and will manoeuvre to the intended orbit. After the initial checks of all systems a coasting phase begins, getting to correct orbit using several burns and taking approximately half a year. Third phase; Conduct Science: CubeSat constellation will start taking measurements and occasional maintenance. The spacecraft will collect data throughout its entire orbit, to map the magnetic and gravitational field. During normal operations, the drag is compensated for every 3.7 hours. Fourth phase; End-of-Life: CubeSat constellation will burn up into the Earth's atmosphere over a lowly populated area.

Post-DSE activities will cover the stages: Detailed definition, Qualification and Production, Utilisation, Disposal. All activities been planned in a Gantt chart. Since it is only launched in 2028, plenty of time for the development realisation of the mission. MAGEOS is required to get the regulatory licensing for radio transmission. Flight certification documentation is required to be allowed on the ride share mission, where proved it will not harm the launch vehicle or other spacecraft onboard. Engineering qualification model assembled for testing and support of the ground crew, as an in-orbit debugging tool.

Lastly the cost of the entire MAGEOS mission has been estimated at 4.7 million USD, with launch services being 2 million USD.

Risk Assessment

In Chapter 10, the risks associated with the MAGEOS mission will be examined. First, the risk will be identified and a likelihood as well as impact will be given to each risk. From this, a risk map will be made which will identify the risk rating. In total, 22 risks have been identified, from which 4 have no quantified likelihood. After mitigation and prevention strategies has been applied, 4 risks has a risk rating of moderate or higher. However, these will be accepted as general space mission risks. Launch risks for example, have a high impact and can't be mitigated more to reduce the impact.

Market Analysis

In Chapter 11, the possible customers for the MAGEOS mission will be examined. Furthermore, the direct as well as indirect competitors of the MAGEOS mission will be investigated and explained. In total, 4 direct competitors and 8 indirect competitors are mentioned as examples. Lastly, a SWOT analysis has been performed to identify the Strengths, Weaknesses, Opportunities and Threats of the MAGEOS mission. These should be exploited and accounted for when delivering MAGEOS to the market.

Requirements Compliance

In Chapter 12, it will be investigated if the final design adheres to the requirements making use of a requirements compliance matrix. Furthermore, a feasibility analysis will be performed.

Contents

		6.6 Command and Data Handling	72
		6.7 ADCS	76
		6.8 Final Configuration	84
	7	Design Analysis	87
	7.1	Aerodynamic Characteristics	87
	7.2	Astrodynamics Characteristics	92
	7.3	RAMS Analysis	104
	8	Final Design	108
	8.1	Final Design Overview	108
	8.2	Sensitivity Analysis	109
	9	Design Actualisation	112
	9.1	Operations Logistics	112
	9.2	Project Design & Development Logic	113
	9.3	Production Plan.	117
	9.4	Cost Breakdown	118
	9.5	Gantt Chart	121
	10	Risk Assessment	123
	10.1	Risk Identification	123
	10.2	Risk Analysis	127
	10.3	Risk Mitigation	128
	10.4	Reliability	130
	11	Market Review	132
	11.1	Market Customers	132
	11.2	Market Competitiveness	132
	12	Requirements compliance	135
	12.1	Requirements Compliance Matrix	135
	12.2	Power and battery storage	138
	12.3	Pointing accuracy	138
	12.4	Attitude stability	138
	13	Conclusion & Recommendations	139
		References	143
Nomenclature	vi		
1 Introduction	1		
2 Functional Overview	2		
2.1 Functional Flow Diagram	2		
2.2 Functional Breakdown Structure	2		
3 Design Approach	5		
3.1 Design Process	5		
3.2 Sustainable Development Strategy	7		
4 Instrument Design	10		
4.1 Magnetometer	10		
4.2 Magnetometer Simulation Tool.	13		
4.3 Gravimeter	21		
5 Orbit Design	37		
5.1 Magnetic Poles	38		
5.2 GNSS Performance	39		
5.3 Ground Speed	39		
5.4 Available Launchers	40		
5.5 Sun-synchronous Orbit.	41		
5.6 Earth Repeat Orbit	43		
5.7 Orbit Selection	44		
5.8 Constellation Selection.	46		
6 Architecture Design	47		
6.1 Structure & Mechanisms	47		
6.2 EPS	52		
6.3 Propulsion	56		
6.4 Thermal Control	63		
6.5 Telemetry, Tracking, and Command	67		

Nomenclature

Abbreviation	Definition
ADCS	Attitude Determination and Control System
ANN	Artificial neural network
A/C	Alternating Current
C.O.G.	Center of Gravity
CoA	Center of Area
CoM	Center of Mass
COTS	Commercial Off the Shelf
ECSS	European Cooperation for Space Standardization
GDOP	Geometric Dilution Of Precision
GNSS	Global Navigation Satellite System
GPS	Global Positioning System
LTAN	Local Time of the Ascending Node
MAGEOS	Magnetic and Gravitational Earth Observation Satellite
MCU	Micro Controller Unit
MMF	Magnetic Measurement Frame
MMOI	Mass Moment Of Inertia
NEC	North-East-Center
POD	Precise Orbit Determination
RAAN	Right Ascension of the Ascending Node
RTK	Real-Time Kinematics
S/C	SpaceCraft
SEE	Single Event Effect
SHAPE	Stable and Highly Accurate Pointing Earth-imager
SLR	Sattelite Laser Ranging
U	CubeSat unit (0.1 x 0.1 x 0.1 [m])
N	Noise
EWH	Equivalent Water Height
TTC	Telemetry, Tracking and Command
VLEO	Very Low Earth Orbit
EOL	End-Of-Life
RTK	Real Time Kinematics
REACH	Registration, Evaluation, Authorisation and Restriction of Chemicals

Symbols

Symbol	Definition	Unit
A	Cross-Sectional Area or Surface Area	[m ²]
a	Semi-major axis	m
B	Magnetic Field Strength	[T]
B_0	Mean value magnetic field at magnetic equator on Earth: $3.12 \cdot 10^{-5}$	[T]
c	Speed of Light	[m/s]

Symbol	Definition	Unit
E_b	Battery Energy Storage	[Wh]
e	Eccentricity	[-]
f_s	Sampling Frequency	[Hz]
G	Gravitational constant	[Nm ² /kg ²]
h	Orbital altitude	m
I_d	Inherent performance degradation	[-]
I	Current	[A]
i	Inclination	[°]
J_2	$1082 \cdot 10^{-6}$	[-]
L_d	Lifetime performance degradation	[-]
M_{earth}	Mass of Earth	[kg]
N	Noise	[W]
N_0	Noise Density	[W/Hz]
P	Power	[W]
r	Distance From Source	[m]
r	Radius	[m]
R_E	Earth Radius: $6.371 \cdot 10^6$	[m]
S	Incident solar flux	[W/m ²]
t	Time	[s]
T	Orbital period	[s]
T_D	Descent time for orbital decay	[s]
T_{ES}	Number of seconds in one year	[s]
V	Volume	[m ³]
\vec{B}	Magnetic Field Vector	[T]
\vec{I}	Spacecraft moment of inertia matrix	[kg m ²]
\vec{O}_2	Direction vector from spacecraft to earth	[m]
τ_g	Gravity gradient torque	[Nm]
μ_0	Permeability of Free Space	[N/A ²]
μ_E	Earth's standard gravitational parameter	[m ³ / s ²]
η	efficiency	[-]
ω	Argument of perigee	[°]
Ω	Longitude of Ascending node	[°]
θ	Colatitude	[°]
θ_S	Angle of incident solar flux	[°]

Chapter 1: Introduction

The costs of spacecraft missions are high. Costs of over US \$100 million are not rare, indicating the difficulty for the financing of space missions. In this report the MAGEOS mission will be described, which attempts to decrease the costly space missions tremendously, while at the same time obtaining the same or even higher accuracy for magnetic and gravitational field measurements. MAGEOS, an acronym for Magnetic And Gravitational Earth Observing Spacecraft, is a CubeSat which will fly at an altitude of 229.7 [km], in a Very Low Earth Orbit. The purpose of the MAGEOS mission is to demonstrate the feasibility of a newly developed attitude control system, as well as performing magnetic and gravitational field measurements at a very low altitude, where this mission will be used to test the accuracy that can be obtained with the current technology.

The mission objective of the MAGEOS mission is given as follows.

Measure the Earth's magnetic and gravitational fields in very low Earth orbit, providing cheap and high-quality science data to the scientific community.

To obtain this goal and adhere to all requirements, a cutting edge design has been developed, with state of the art technology and innovative algorithms for data processing making use of artificial intelligence.

The report is structured as follows. Firstly, a functional overview of the MAGEOS mission will be given in Chapter 2. Next, the design approach will be presented in Chapter 3. After this, the instrumentation design will be explained in Chapter 4. Then, the orbit design will be explained in Chapter 5. Next up, the architecture design will be explained in Chapter 6. After this, a design analysis will be presented in Chapter 7. Next, the final design will be presented in Chapter 8. After this, the design actualisation is presented in Chapter 9. Next, the risk assessment will be explained in Chapter 10.

Chapter 2: Functional Overview

During the MAGEOS mission, the spacecraft will go through several mission phases. During those phases, certain actions should be performed. This includes but is not limited to testing, starting and shutting-off systems, etc. In this chapter, the functional analysis of the spacecraft will be discussed. In Section 2.1, the functional flow diagram (FFD), will be presented and explained. In Section 2.2, the functional breakdown structure will be shown and an explanation about it will be given.

2.1. Functional Flow Diagram

To get a better understanding in the to be performed actions during the different phases of the MAGEOS mission, and the correct order of the to be performed actions, a functional flow diagram will be used. The functional flow diagram structures the different mission phases, as well as their performed actions, also called functions. The correct order of these functions are displayed making use of arrows, as well as logic. Logic is being used to control the flow, as certain functions such as tests can have a positive or negative outcome. In case the outcome is negative, the arrow with an *X* should be followed, while in case the test is positive, the arrow with an *V* should be followed.

The functional flow diagram as presented in Figure 2.1 (an updated version from the baseline report [2]), shows the mission phases of the MAGEOS mission in the correct order, as can be seen in the gray block. The launch phase as well as the Inject to Orbit phase will not be described in more detail, since they will be handled by the respective launcher and orbital transfer vehicle providers. The other mission phases are described to up to three levels of detail. An example of logic can be found in block 3.2. In that block, tests will be performed to make sure that all systems are started. In case this is not true, the system should go back to block 3.1 and try to start up the system again. In case the system is unable to startup all systems or the most important systems, the mission phase will switch to the End of mission phase, block 5.

2.2. Functional Breakdown Structure

The functional flow diagram described in Section 2.1, provides a clear overview of the mission phases, general functions, as well as their correct order. However, more detailed layers of each function are not presented. To obtain an even more in depth overview of the MAGEOS mission, a functional breakdown structure has been developed. This should create a more in depth overview for the design as well for the mission, such that it is clear which tasks at detailed level should be performed. For each mission phase, more detailed functions are shown. The main tasks in this diagram originate from the functional flow diagram, which can be seen in Figure 2.1. The functional breakdown structure of the MAGEOS mission is presented in Figure 2.2.

In Figure 2.2, it can be seen that the functions are layered by mission phase, and no longer in the order of execution, or the correct "flow". The functional breakdown structure is an updated version of the functional breakdown structure as presented in the baseline report [2]. It should again be noted that the launch and injection to orbit phase are not described into detail. The reason for this is that they will be performed by their respective operator. It can also be seen that the end of life phase has much less functions compared to the deployment and conduct mission phase.



Figure 2.1: Functional Flow Diagram of the MAGEOS mission [2].

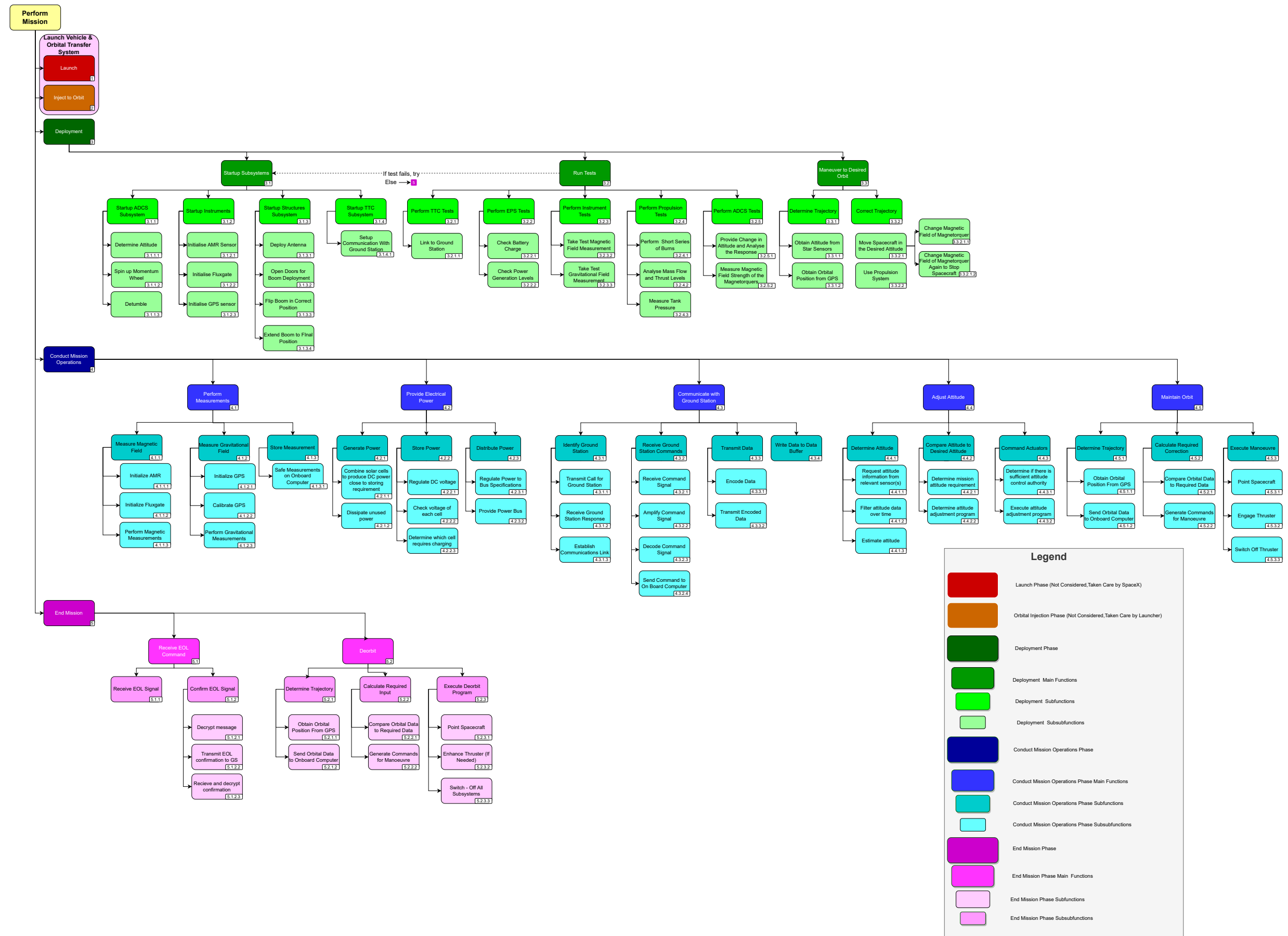


Figure 2.2: Functional Breakdown Structure of the MAGEOS mission [1].

Chapter 3: Design Approach

In this chapter, the design approach for spacecrafts for the MAGEOS mission will be explained, as well as the sustainability development strategy which will mainly be focused on total emission and possibilities to monitor climate control. The design process of the MAGEOS mission spacecraft missions will be given in Section 3.1. The sustainability development strategy will be presented in Section 3.2.

3.1. Design Process

In the mid term report, a trade-off has been performed between different concepts. From this trade-off, a final design concept was selected which would be used to obtain the final design configuration for the MAGEOS mission. The final concept from the mid term report will be briefly discussed below [1].

Concept 4

The Dual Magnetometer Modular concept is a dual vector magnetometer (fluxgate and AMR). The magnetometers will be mounted on a boom to decrease the influence of external noise sources. By making use of two magnetometers, the pair can be calibrated against spacecraft-induced noise sources. A GPS sensor and accelerometers will be used to perform gravitational field measurements. There will not be an Earth observational camera, due to volume, power and mass constraints. The propulsion unit will exist out of a water resistojet. For power generation, a lithium-ion battery with gallium-arsenide solar cells will be used. The spacecraft's structure will be created making use of a modular structure, for easy integration of different spacecrafts components and payloads. A telescopic mast will be used as a boom, for cost and mass reasons. An omnidirectional antenna will be used to make contact with the ground station. A spacecraft constellation of two spacecrafts will be used. A graphical overview of concept 4 can be seen in Figure 3.1.

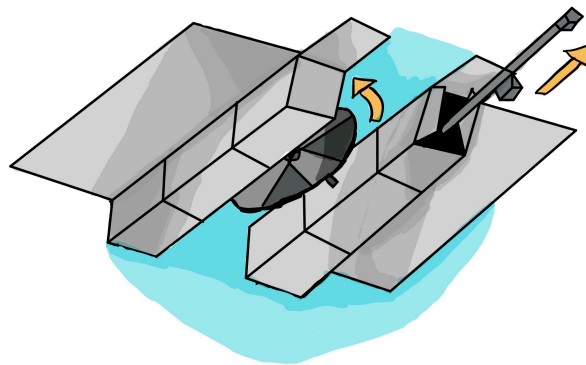


Figure 3.1: Concept 4 Design Sketch.

Concept 4 will be used as the baseline for the iteration process to obtain the final design. First, certain tools will be developed to predict important parameters and spacecraft characteristics. This includes a tool to find the aerodynamic coefficients of the spacecraft, a tool to find the mass moments of inertia, centroid and center of mass, a tool to estimate the correct boom length based on spacecraft interference, etc. In the meantime, the engineering budget from the customer will be used to determine acceptable limits for quantities such as power, mass and volume. After this, payload requirements will be used to find the optimal altitude for the mission. If a feasible option is found, the orbital inclination will be determined based on payload requirements, as well as a first estimation for the mission lifetime. Once this has been found, the engineering budget will be updated and the final orbit will be established. With these established, the tools to determine important spacecraft parameters have been finalised and

verified for use. Now, these can be used to find the geometry and geometrical characteristics of the spacecraft and the required power from the solar cells and battery size which should provide energy the spacecraft during an eclipse. From the geometry, the aerodynamic characteristics can be determined, as well as disturbance forces on the spacecraft. This leads to an updated mission lifetime. In case this does not meet the requirements, a Delta-V budget can now be estimated for orbital maintenance, collision avoidance and deorbit strategy. From the Delta-V budget, a thruster can be chosen as well as the total propellant mass needed for the mission. From the propellant mass, the tanks can be sized. Now, iteration will be performed to update the geometry with the new masses and positions of each subsystem. After the iterations have been performed, the final configuration will be obtained. In Figure 3.2, a graphical overview of the design and iteration process of the spacecrafts for the MAGEOS mission is presented.

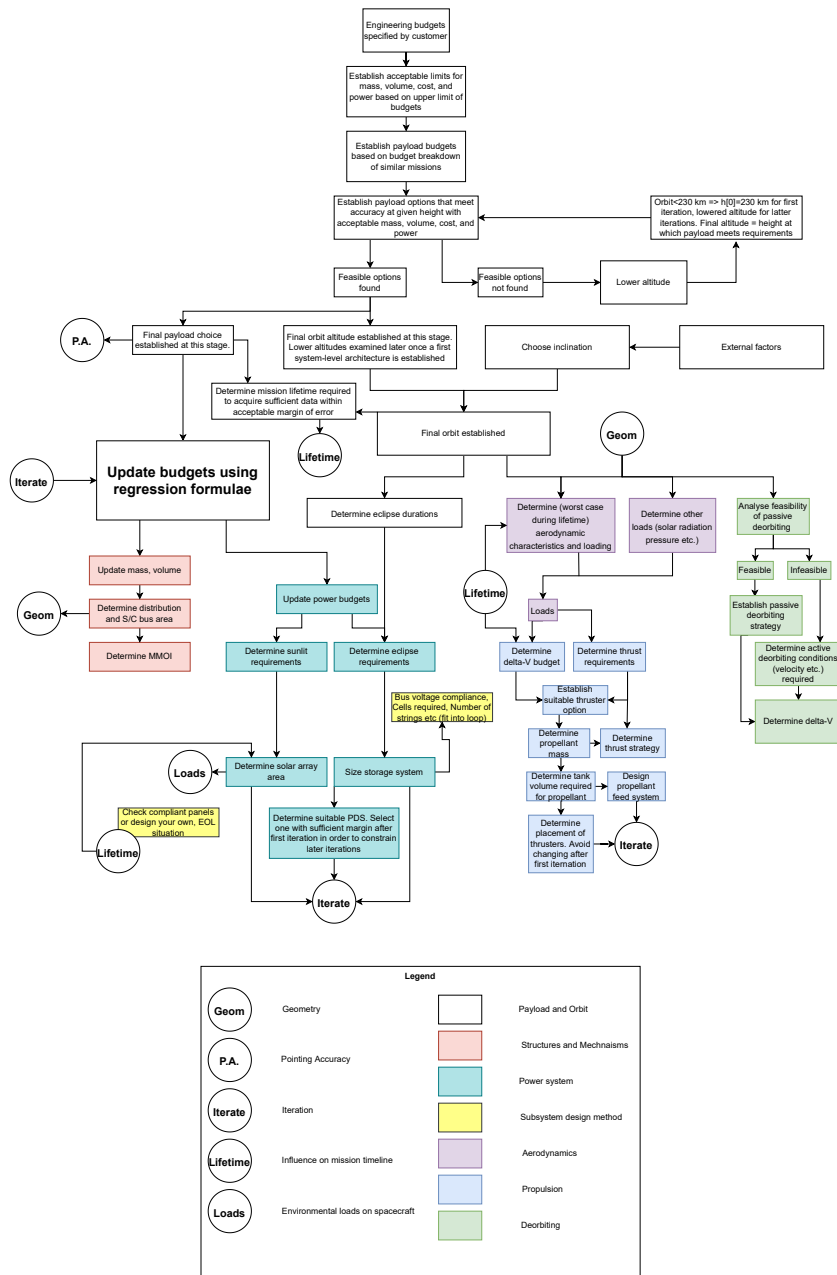


Figure 3.2: Design Process flow diagram for the MAGEOS mission.

3.2. Sustainable Development Strategy

Sustainability of the MAGEOS mission is a very important concept which the design team has monitored regularly during the design process. For this mission, only the environmental aspects will be considered. This includes organisational sustainability, such as bringing reusable water bottles, come to campus with public transport or by bike as much as possible, etc. During the design process, special care was taken to make the final design as sustainable as possible, taking into account the production phase, pre- and post launch phase. Furthermore, sustainability in space has also been taken into account, by considering and choosing an end of life strategy that will lead to the least amount of environmental damage and waste, as well as preventing space debris as much as possible. The MAGEOS mission can also be used to monitor the environmental change of the Earth and can thereby attribute to trace early signs of, for example, sea rise. All of these measures and considerations should lead to a final design which will have the least impact on the environment, as well as be able to monitor large scale environmental changes. Firstly, an approximation of the total emission for the MAGEOS mission will be presented. Next, the strategy behind all phases from the midterm report will be discussed as well as their results.

3.2.1. Emission During Production and Pre-Launch Phase

A satellite will have a large carbon footprint over its lifetime. Material, as well as personnel will develop a mission for a long time and therefore emit a lot of carbon dioxide. Table 3.1 shows a summary of the average emission of carbon dioxide for each part of a spacecraft, as well as personnel emission [3]. Making use of this, an estimate can be made on the average carbon footprint of the MAGEOS mission. Structure's mass includes machining and loss of materials. Another important consideration should be the transport from the production and test site to the launch site [4]. It is assumed that the development and testing of components will be done in Delft. The launch will happen from Vandenberg space launch complex in California, United states of America. Furthermore, it should be considered that off the shelf components should be transported to Delft from their storing facilities, which will also contribute to the carbon footprint of the mission.

Table 3.1: Emission of the MAGEOS mission launch vehicle

Type	Amount of CO ₂ Emitted	Total for Mission [kg]
Solar Cells	18.4 kg CO ₂ / kWh	0.9572
Electronics	100 kg CO ₂ / kg	993.06
Structure Mass	Aluminium 39 kg CO ₂ / kg	288.1
Battery	500 kg CO ₂ / kWh	25
Personal	420 kg CO ₂ / person per year	1615.4
Transport to launch site	16.1 kg CO ₂ / kg	594.4

3.2.2. Emission During Launch

In the midterm report [1], the Falcon 9 was selected to be the launcher of the MAGEOS mission, in accordance with requirement CON-SUS-4, which states that a reusable launcher should be used to limit the impact on the environment. It can be estimated that the first stage of a Falcon 9 has a carbon footprint of around 300 metric tons of carbon dioxide. Since there are plans to reuse the first stage 100 times [3], an approximate 3 metric tons of carbon dioxide will be emitted for each launch. The development of Falcon 9 has emitted around 350 [kg] of carbon dioxide for launch. By considering different launch possibilities, the ride share program, a program where a Falcon 9 rocket will launch multiple satellites into space will be used. This means that the total emission of the launch can also be divided between each spacecraft. During launch, assuming the first stage will be reused, a total of 425 metric tons of carbon dioxide (CO₂), 125 metric tons of water vapor, 30 metric tons of carbon soot and 1 metric ton of nitrogen oxide (NO_x) will be released [5]. Since a reusable Falcon 9 rocket has a payload to low Earth orbit capability of 15.5 metric tons [5], the total emission of the MAGEOS mission to space can be calculated. This is shown in Table 3.2. By reusing the first stage, the material waste as well as the emissions during the production of the first stage of the Falcon 9 will be reduced.

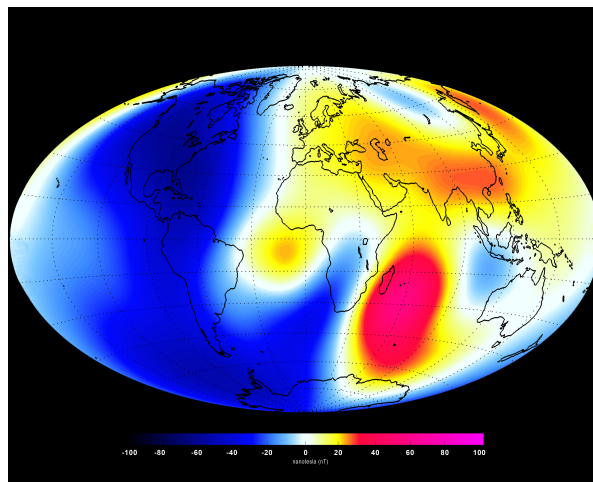
Table 3.2: Emission of the launch vehicle by launching the MAGEOS mission

Emission	Amount [kg]
Carbon dioxide (CO ₂)	6496.2
Water vapor	1910.6
Carbon soot	458.6
Nitrogen oxide (NO _x)	15.3

3.2.3. Sustainability Contributions of the Mission

The MAGEOS mission measures the magnetic and gravitational field vectors and magnitudes. These can be used to perform climate-related Earth observations, by measuring the changes in those fields. The gravitational field measurements can mostly contribute to this purpose, since it can be used to measure the ice mass loss, amount of terrestrial water storage, sea-level change and ocean dynamics [6]. The most interesting one is the terrestrial water storage. With these observations, it can be determined where freshwater is stored and where it will go to. GRACE data revealed a trend in moving freshwater from mid latitudes to higher and lower latitudes [6]. Our mission data could be used to see if this trend is still proceeding or has changed. This could help predicting water shortages in the future and mitigation plans can therefore be developed.

The magnetic field of the Earth, also called magnetosphere, is very important for all day life. It protects Earth's living creatures from the harsh environment from space. The magnetosphere shields us from charged particles released from the sun, particle radiation, solar plasma, as well as cosmic rays from deep space [7]. Although it has been shown that the magnetic field has been in its all time high in terms of strength, recent missions from ESA shows a decrease in magnetic field strengths at certain points on Earth, as can be seen in Figure 3.3. The blue areas show a decrease in magnetic field strength, while the red and yellow areas show an increase in magnetic field strength. If this trends continues, life on Earth could be in serious danger, because at some places radiation of space will be higher. The MAGEOS mission can be used to monitor this worrying trend and take mitigation strategies for life on Earth in time.

**Figure 3.3:** Change in magnetic field as observed by the SWARM mission from ESA in 2013 [7]

3.2.4. Emission During End-of-Life Strategy

To comply with the user requirement CON-SUS-01, which states that the spacecraft shall be disposed by total burning in the atmosphere, the spacecraft has been made from materials that are disposable by re-entry and a delta-V budget was budgeted to make sure that the spacecrafts velocity is large enough too make a total atmospheric burn up possible. Unfortunately, burning up a satellite in the atmosphere could harm the ozone layer [8]. Spacecrafts hitting the atmosphere are being outnumbered by the daily asteroids hitting Earths atmosphere daily. So why could spacecrafts possibly harm ozone layer? The

main reason for this is the composition of asteroids compared to spacecraft. Asteroids exist mainly out of oxygen, magnesium and silicon. During the re-entry of spacecrafts, a lot of aluminium oxide will be produced since the spacecrafts mainly consist out of aluminium [8]. Furthermore, other chemicals from the electronics as well as the solar panels will be released in the ozone layer. By burning up a lot of satellites, the chemical composition of the ozone layer could change compared to its natural state [8]. Aluminium oxide causes temporary "holes" in the ozone layer. This could harm life on Earth since the ozone layer protects us from harmful radiation. If the ozone layer holes are no longer temporary, an increase of skin cancer and eye problems, such as cataracts could be expected [8]. However, an interesting effect of burning up satellites in the atmosphere also arises. Aluminium oxide reflects light at certain wavelengths. If enough aluminium oxide is being expelled into the atmosphere, the albedo of the planet could change [8]. By increasing Earth's albedo, global warming could potentially be slowed down. However, side effects are unknown and could be even worse [8].

To conclude, burning up a satellite in the atmosphere could harm the ozone layer, but could also slow down global warming. Unfortunately, effects of the latter are unknown up to this point. The total emission of aluminium oxide during re-entry of the spacecraft will be around 34.9 [kg]. This number has been found by making use of the Equation 3.1, and performing a molar mass calculation assuming all used aluminium in the spacecraft has been used and has fully reacted with the oxygen in the atmosphere. Other chemicals of the spacecraft could possibly also react with the atmosphere and ozone layer, however it is hard to make predictions on those impacts and will therefore be neglected.



3.2.5. Total Emission of the Mission

To sum up, Table 3.3 is given to give a rough estimate of the emitted particles used and expelled during the MAGEOS mission. It should be noted that this is a rough first order estimate and that in reality numbers could be higher or lower.

Table 3.3: Total emission of the MAGEOS mission

Emission	Amount [kg]
Carbon dioxide (CO ₂)	10013.1
Water vapor	1910.6
Carbon soot	458.6
Nitrogen oxide (NO _x)	15.3
Aluminium oxide (Al ₂ O ₃)	34.9

3.2.6. Strategy

During the production and launch phase, the use of rare Earth materials has been avoided as much as possible. However, the electronics will contain some rare materials such as lithium for the batteries. The main structure will be made from aluminium. In accordance with CON-SUS-03, recycled aluminium will be used. To reduce the emissions during production, the test and manufacturing compartments are located close to each other. To decrease the total amount of emission during launch, requirements CON-SUS-04 was implemented in the design, which states that a reusable launcher should be used. The chosen launcher for the MAGEOS mission has been the Falcon 9, making use of a rideshare mission to further reduce the total emissions during launch. During the mission, the emission of the spacecraft will mainly be from the propulsion system. The propellant of the spacecrafts exists out of a non-toxic mix of nitrous oxide-propene. This is in accordance with the REACH regulations which will be explained more in Section 6.3. To take space sustainability into account, the spacecrafts will be burning up during re-entry, in accordance with CON-SUS-01. It will be made sure that the spacecrafts will be burned up over the ocean, to adhere CON-SUS-02, which states that the area in which the satellite is disposed of must be almost depopulated.

Chapter 4: Instrument Design

The instruments aboard MAGEOS are a magnetometer, a gravimeter, and an accelerometer. These instruments allow the collection of the required science data. As such, they are the driving components of the spacecraft design.

Sections 4.1 and 4.3 discuss the magnetometer and gravimeter designs respectively. They begin with a description of their requirements. Their mass, power and volume budgets are detailed. Next, the chosen technology is introduced and explained. The final instrument is then presented and discussed. Section 4.2 presents a simulation of the chosen magnetometer to verify its accuracy.

4.1. Magnetometer

The magnetometer onboard MAGEOS should be able to achieve the desired accuracy of 1 [nT] for the collection of high quality science data. In this section, all information pertaining to the selection of the magnetometer is presented. The full requirements are first given, design budgets are introduced and the instrument is selected. Once a selection is made, the instrument is simulated to ascertain if it is capable of recording sufficiently high quality data and to determine the required distance the instrument must be placed from the satellite body due to magnetic interference.

4.1.1. Magnetometer Requirements and Design Budgets

The main magnetometer requirement is the accuracy requirement of 1 [nT]. This means that the values the magnetometer records must be within 1 [nT] of the true value. There shall be two magnetometers, both fluxgate magnetometers, as determined in [1]. Since the scientific instruments are the purpose of the MAGEOS mission, the upper volume limit for the magnetometer is set to $1/3$ of the allowable volume of 16U; it is therefore 5U. There is a limited number of space-functioning fluxgate magnetometers which can be used to achieve the desired accuracy. Such instruments are typically designed for a specific satellite mission. One such example is the magnetometer setup onboard SWARM. SWARM utilises a custom-designed vector fluxgate magnetometer in conjunction with an absolute scalar magnetometer: both of these were designed specifically for the SWARM missions to fulfill the extremely high accuracy requirements of SWARM, which required better than 0.5 [nT] accuracy [9].

4.1.2. Fluxgate Magnetometer

As stated in Section 4.1.1, MAGEOS will utilise two identical fluxgate magnetometers. A fluxgate magnetometer was chosen for its *"long-proven performance and reliability in the space environment"* [10], as well as its ability to meet accuracy requirements. Fluxgate magnetometers for the purpose of collecting magnetic field data have a long history aboard satellites. Satellites as far back as the 1970's such as NASA's MagSat were already using the technology to provide the first models of Earth's magnetic field derived from space-collected data [11]. The same type of magnetometer has since been used on missions ranging from Orsted to SWARM [12].

Fluxgate magnetometers work on the principles of magnetic saturation and electromagnetic induction. A ferromagnetic material, such as iron, is saturated when an increase in applied magnetic field does not increase the magnetisation of the material. Therefore, once a material is saturated, the magnetic flux stops increasing. A fluxgate consists of such a ferromagnetic core wrapped by a pair of coils. When an AC current is applied to the driving coil, the core enters a cycle of magnetisation as shown below:

- Magnetised / Saturated
- Un-magnetised / Desaturated

- Inversely magnetised / Saturated
- Un-magnetised / Desaturated

This cycle can be visualised in the graph of Figure 4.1.

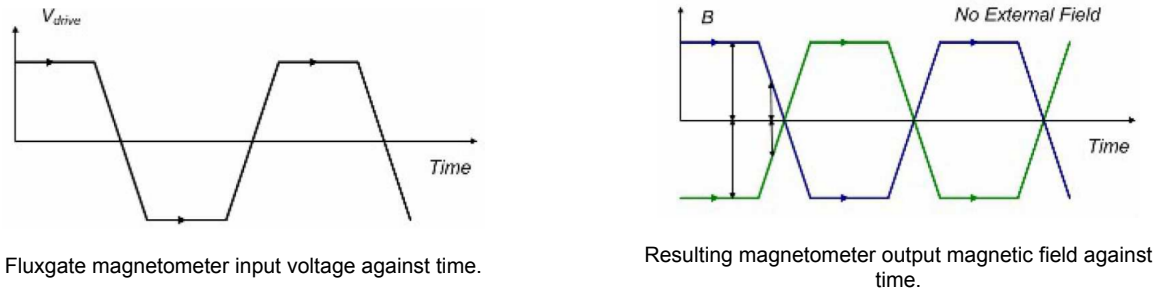


Figure 4.1: Fluxgate control signals [13].

Normally, the input voltage applied to the driving coil is matched by the induced output voltage in the output coil. However, the induced magnetic field of the core is affected by *any* external magnetic field, including the Earth's. When the core is aligned with the external field, it is more easily saturated, and when it is in opposition, it is less easily saturated. This effect can be seen in the alternating magnetic field and output voltage, which gives a measurement of the change in external magnetic field strength. Modern fluxgate magnetometers use the output coil to feedback a magnetic field which cancels out the sensed field. As a result, the sensed field strength is proportional to the current input into the output coil, known as the feedback current. *"This technique improves linearity of measurement, allows a much greater dynamic range ... and is used by the majority of modern devices"* [14]. If a fluxgate magnetometer is placed along each cartesian axis, the magnetic field vector can be measured as the summation of the magnetic field along each axis [1].

4.1.3. Criteria Affecting Magnetometer Accuracy

The accuracy of magnetometer measurements is not intrinsic to the instrument itself. The final accuracy of readings depends upon a multitude of factors, these primarily being:

- Resolution of the instrument
- Noise due to satellite magnetic interference
- Noise intrinsic to the instrument
- Sensitivity of the instrument

The final accuracy is a combination of all noise sources atop the underlying field value, measured to the nearest value the resolution of the instrument allows. The noise sources and instrument specifications are described below.

4.1.3.1. Resolution of the Instrument

Resolution is the smallest difference in magnetic field which the instrument can output. If the resolution is 1 [nT], only measurements in steps of 1 [nT] can be performed. The resolution of the instrument must be lower than the desired accuracy for the desired to be achievable. Resolution for magnetometers is given in terms of nanotesla for the instruments investigated for MAGEOS.

4.1.3.2. Noise due to Satellite Magnetic Interference

The main body of the spacecraft contributes significant noise to the magnetometer. Every electronic component produces its own magnetic field when a current is applied. Furthermore, the SHAPE plat-

form utilises magnetorquers which generate magnetic fields when active and a bias momentum wheel with magnetic bearings which produce a permanent magnetic field. Correction algorithms can be applied to reduce the effect of these disturbances, however the nature of ferromagnetic materials is such that the fields they produce are partially random, so perfect prediction of interference is functionally impossible. Hysteresis of ferromagnetism further contributes to the difficulties of perfectly modelling magnetic fields within the spacecraft.

To avoid this noise, the magnetometers are mounted upon a boom. This allows the magnetic interference from the spacecraft to be simplified. Since the strength of a magnetic field scales down proportionally to the inverse of the third power of distance. Furthermore, using two identical magnetometers, one placed at halfway and the other at the end of the boom, enables the use of the *"Dual Sensor Technique"* to filter noise from the spacecraft out of measurements [15]. The appropriate boom length is a function of spacecraft noise interference. A simulation is performed in Section 4.2 with the goal of determining how far the magnetometers must be placed from the spacecraft to achieve the sufficiently low noise for accuracy requirements to be met.

4.1.3.3. Noise Intrinsic to the Instrument

Instrument noise is characterised as any random variation in its output. This is usually provided as measurement in $[nT/\sqrt{Hz}]$, where $[Hz]$ represents the sampling frequency.

4.1.3.4. Sensitivity of the Instrument

Instrument sensitivity is the smallest change in the field which the instrument responds to. It is measured in $[nT/\sqrt{Hz}]$ and, similarly to resolution, must be lower than the desired accuracy. This value is a property of the chosen instrument.

4.1.4. Magnetometer Selection

Magnetometers for spacecraft use are extensively available, however the vast majority are for the purpose of attitude control. A magnetometer for attitude determination typically has resolution in excess of 5 [nT] [16]. There are a limited number of space-functioning fluxgate magnetometers which are designed for the purpose of collecting science data. Such instruments are typically designed for a specific satellite mission. One such example is the magnetometer setup onboard SWARM. SWARM utilises a custom-designed vector fluxgate magnetometer in conjunction with an absolute scalar magnetometer: both designed specifically for the SWARM missions to fulfill the extremely high accuracy requirements of sub 0.5 [nT] accuracy [9]. The instruments aboard SWARM are too large and power-consuming for MAGEOS' purposes. Combined, they occupy more than two units of space, and consume 5.5 [W] of power. Regardless, the specific design of an entire fluxgate magnetometer is beyond the scope of this project, therefore the instrument is selected from existing flight-tested designs.

The chosen magnetometer is the CASSIOPE fluxgate magnetometer known as MGF. This magnetometer has flown successfully on the CASSIOPE mission. Table 4.1 presents the specifications of this instrument.

Table 4.1: Specifications of the MGF [17].

Specification	Value
Resolution	0.0625 [nT]
Noise density	7 $[pT/\sqrt{Hz}]$
Power Consumption	2.6 [W]
Sensor Dimensions	70x50x60 [mm]
Electronics Dimensions	85x85x140 [mm]
Sensor Mass	0.58 [kg]
Electronics Mass	1.22 [kg]

The resolution is considerably better than the 1 [nT] limit, meaning that this instrument is sufficient to

achieve the desired accuracy. Noise is calculated from the presented noise density plot using Equation 4.1.

$$N = N_0 \cdot \sqrt{f_s} \quad (4.1)$$

Noise density is not constant for all sampling frequencies. As the sampling rate increases, the noise density decreases as shown in Figure 4.2.

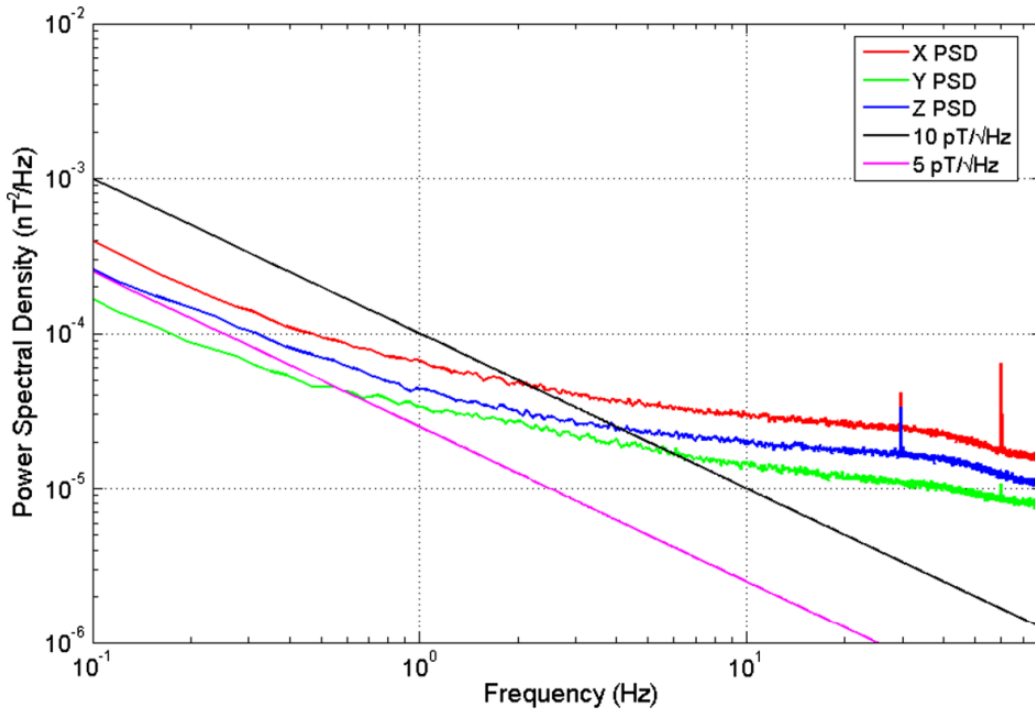


Figure 4.2: CASSIOPE fluxgate magnetometer power spectral density [17].

As an initial value, 10 [Hz] is decided as the sampling rate. Using Figure 4.2 and Equation 4.1, the noise from the instrument is estimated to be 14 [pT], sufficiently low to be of no significance to measurements.

A power consumption of 2.6 [W] is acceptable, as reference 6U CubeSats allocate approximately 20 [W] of power to the payload [18]. The sensors can be stored within CubeSat units prior to boom deployment. In the original design aboard CASSIOPE, the electronics are 130x110x70 [mm]. This has been reduced to the values in Table 4.1, maintaining the same volume but fitting within the CubeSat constraints. As only one dimension exceeds the constraints of a single CubeSat unit, the electronics can be housed within two CubeSat units.

As the magnetometer has been chosen, a simulation is done in Section 4.2 to properly estimate noise, validate that this magnetometer can satisfy requirements, and determine the required distance the magnetometers must be from the centre of the spacecraft, which is the required boom length.

4.2. Magnetometer Simulation Tool

This simulation tool is able to generate wire loops, dipoles, and magnetorquers in space and simulate the functioning of the magnetometer. Figure 4.3 provides an overview of the simulation process using a flow diagram. The simulation will first extract information from a list of inputs and create the respec-

tive magnetic sources and magnetometer. Then, together with the Earth's magnetic field (from data obtained from SWARM, scaled and rotated to fit the reference frame), and sources, it generates a total magnetic field vector at the positions of the magnetometers. The additional noise, originating from the magnetometer, is added to the signal to produce the magnetometer output. The cyan colored block in Figure 4.3, called machine learning, is a data-processing step which could be implemented to increase accuracy.

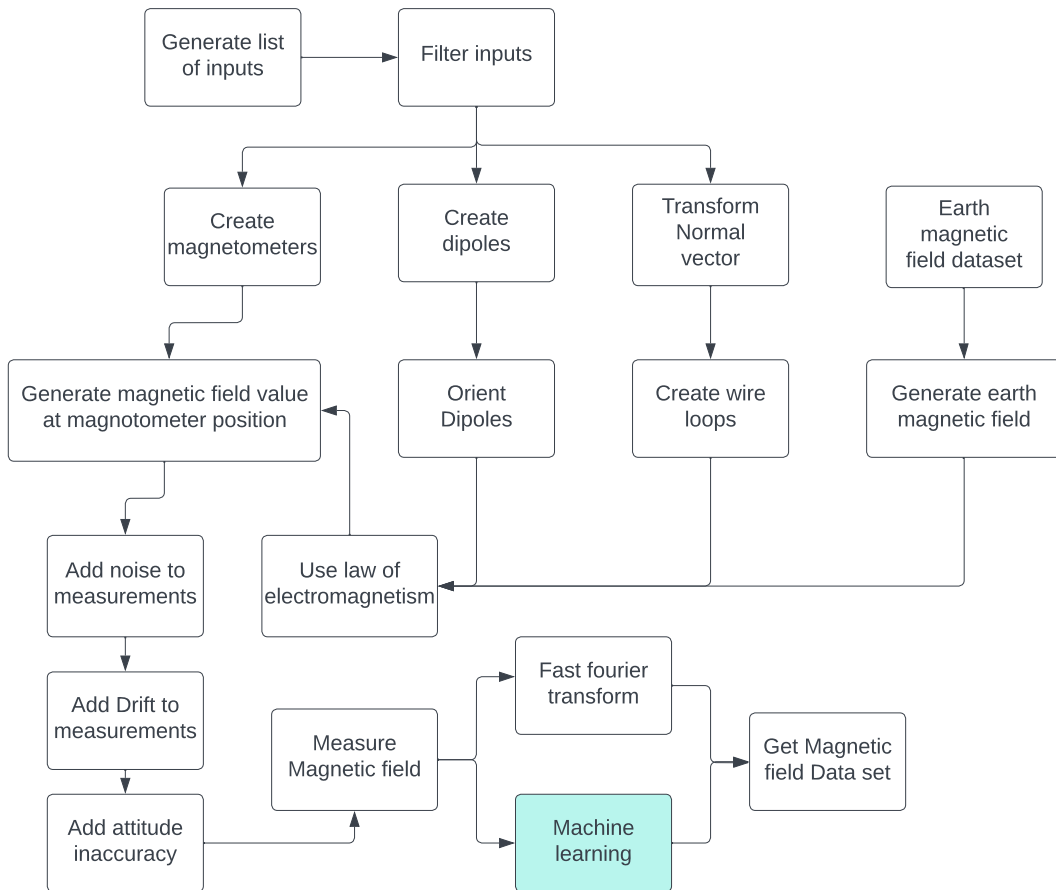


Figure 4.3: Flow diagram of the magnetometer simulation.

The magnetometer simulation tool is comprised of magnetic sources and sensors. The sources generate a magnetic field through some physical process (for example, a current carrying wire or a bar magnet). The magnetic sensors then sense the magnetic field strength at their position and apply some simulated measurement errors, based on the magnetometer's datasheet. The mathematical interpretation of this is shown in Equation 4.2, where \mathbf{B}_i is the magnetic field strength at a point \mathbf{r} at a time t caused by a magnetic source. $\mathbf{B}(\mathbf{r}, t)$ is the total magnetic field present at said point in space and time. In the next sections, the various sources and sensors implemented in the software are explained.

$$\mathbf{B}(\mathbf{r}, t) = \sum_i \mathbf{B}_i(\mathbf{r}, t) \quad (4.2)$$

The data is collected at 50 [Hz], along with radius of satellite in meters and the measured magnetic field in the NEC (North-East-Centre) frame. The data must be processed in two ways to be usable in the simulation. Firstly, the magnetic field vector is transformed from the NEC frame to the body-fixed magnetic measurement frame (MMF). Figure 4.5 shows how the coordinate systems are defined, and Equation 4.5 shows the mathematical definition of the transpose of the transformation matrix needed. Secondly, because the altitude of the SWARM satellites is not equal to MAGEOS, the transformed vector is scaled according to the inverse cube law, assuming the Earth's center is the source of the magnetic field.

$$\mathbb{T}_{NEC \leftarrow MMF} = \mathbb{T}_z(\theta) \cdot \mathbb{T}_y(\pi) \quad (4.5)$$

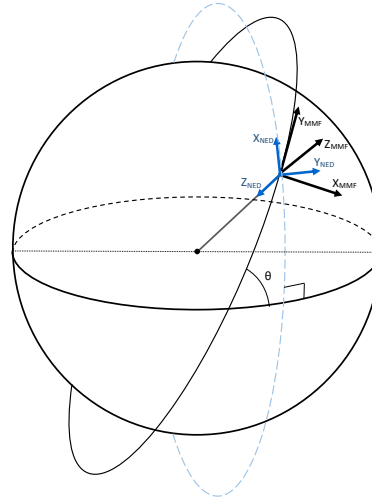


Figure 4.5: Reference Frame Definition, where θ is orbital inclination.

4.2.1.6. Dipole

The magnetic dipole is modelled using the equation for a magnetic dipole, shown in Equation 4.6. This can be used to model permanent magnets or the ferromagnetic core used in the magnetorquers. \mathbf{m} is the magnetic dipole moment vector, and \mathbf{r} is the vector from the center of the dipole to the reference point, with r being the magnitude of \mathbf{r} . μ_0 is as defined in the Jefimenko Wire description.

$$\mathbf{B}(\mathbf{r}) = \frac{\mu_0}{4\pi} \left[\frac{3\mathbf{r}(\mathbf{m} \cdot \mathbf{r})}{r^5} - \frac{\mathbf{m}}{r^3} \right] \quad (4.6)$$

4.2.2. Magnetic Sensors

4.2.2.1. Ideal Magnetometer

The ideal magnetometer has no manufacturing imperfections, no noise, and no internal errors. This sensor is present to compare its output to a more realistic magnetometer.

4.2.2.2. Magnetometer

The realistic magnetometer simulates noise, artificially reduces the resolution, introduces sampling rate limitations, as well as absolute error and drift errors. All these sources of error will reduce the effectiveness of the magnetometer by reducing its ability to faithfully determine the true magnetic field. This will be used to ensure that the selected magnetometer is accurate enough to determine the magnetic field contribution of Earth.

4.2.3. Simulation cases

The SHAPE platform was modelled as shown in Figure 4.6. The relevant simulation sources and sensors are shown. The coordinate system is defined by the red, green, and blue arrows, indicating

the x , y , and z axes, respectively. The magnetic dipole vectors are shown as orange vectors, with the base being the position of the dipole, and the arrowhead pointing in the direction of the magnetic moment. The two dipoles in the negative x axis are modelled after the on-board magnetorquers, which have a dipole in the non-spin axis of the momentum wheel. The magnitude of the dipole is $0.5 \text{ [Am}^2\text{]}$, according to the design requirements [20]. The momentum wheel itself is modelled at the origin, with its magnetic dipole collinear with the x axis. The solar panels are modelled as the black, closed loop lines. Finally, the two magnetometers are modelled on a boom, shown in the non-equally scaled Figure 4.7. The two simulation cases considered are a MAGEOS steady state condition and satellite exiting an eclipse (solar panel current increasing). Further elaboration is provided in the following sections.

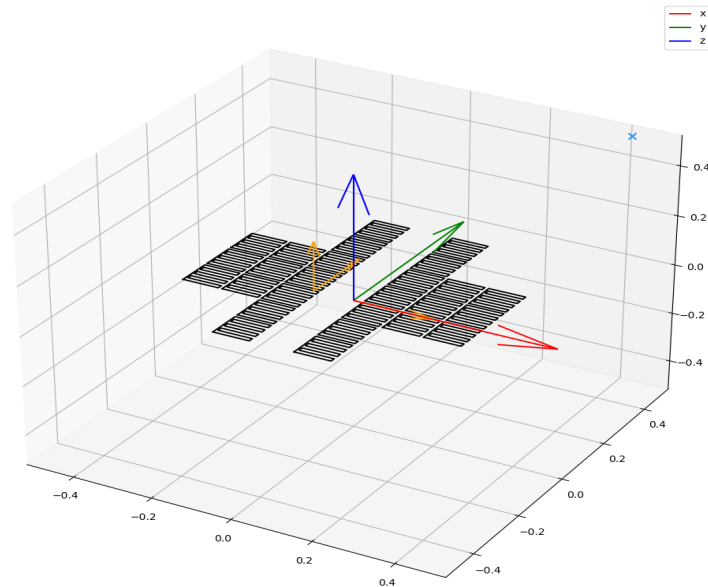


Figure 4.6: Magnetic Simulation Configuration. The magnetic moment of the magnetorquers and magnetic momentum wheel are shown in orange, the solar cell wiring in black. One magnetometer is shown as the blue cross, the second one is off-screen and not visible. The red arrow is the x-axis, green represents the y-axis and the blue arrow is the z-axis.

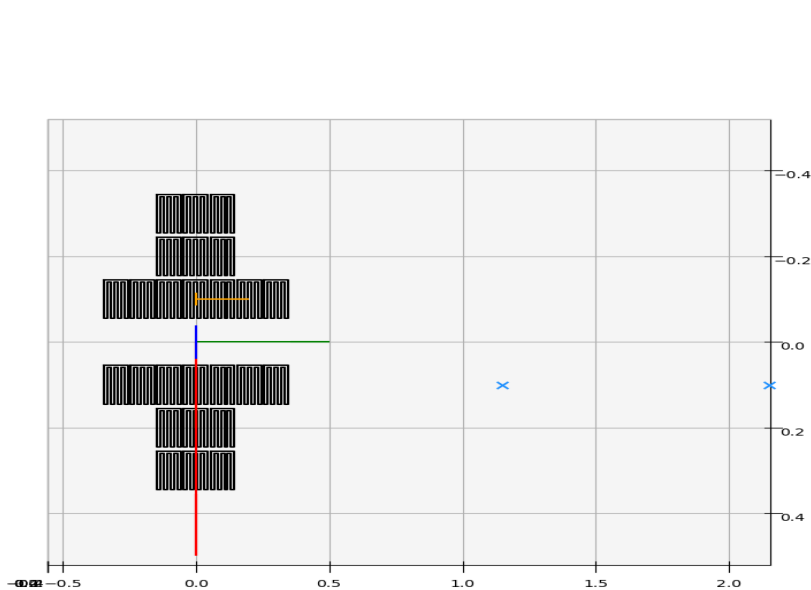


Figure 4.7: Magnetic Simulation Configuration Top-Down View. The second magnetometer is visible, colinear with the other magnetometer and the SHAPE body.

4.2.3.1. Steady state case

During the steady state case, the current of the solar panels is regarded as having a constant (zero) value with respect to time. This is done to see how the simulation performs without any changes in the magnetic field due to spacecraft components. For this case, the Biot-savart law (the Jefimenko steady state equation is used) is used to estimate the magnetic field generated by the solar panels, and the contribution of the dipoles to the measured magnetic field is quantified, with respect to the measured magnetic field of the Earth. The results are shown in Figure 4.8, where the contribution of the spacecraft is significant to the measured magnetic field. The only changes in the measured magnetic field are due to the magnetic field emanating from Earth.

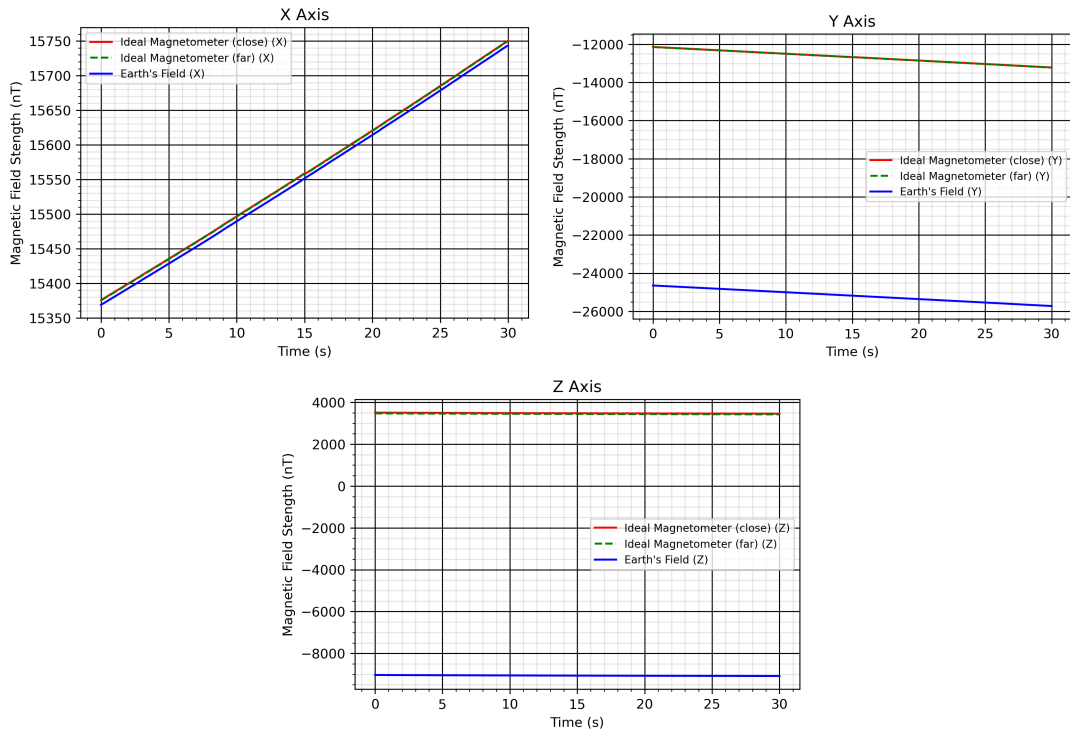


Figure 4.8: Steady state simulation of the spacecraft.

4.2.3.2. Entering eclipse case

The next case simulates the spacecraft's solar panels entering the eclipse, meaning that, suddenly, the current in the solar panels drops. The Jefimenko equations will be used to simulate the solar panels, and the magnetic dipoles present on the spacecraft will be removed. The input to the simulation is shown in Figure 4.9(a), where the current flowing through the the wires in the solar panels is zero for the first 5 [s]. As the spacecraft exits the eclipse, the current flowing through the solar panels is gradually increased to 4 [A] over 2 [s]. The effects of the change are shown in the other three images of Figure 4.9, with the Z-axis registering the largest relative difference. The transient effects are clearly present between 5 [s] and 7 [s] in the Z axis. Subtracting the true magnetic field from the measured magnetic field yields the spacecraft-originating noise, shown in Figure 4.10. The order of magnitude of noise is about 0.1 [nT], well below the required value.

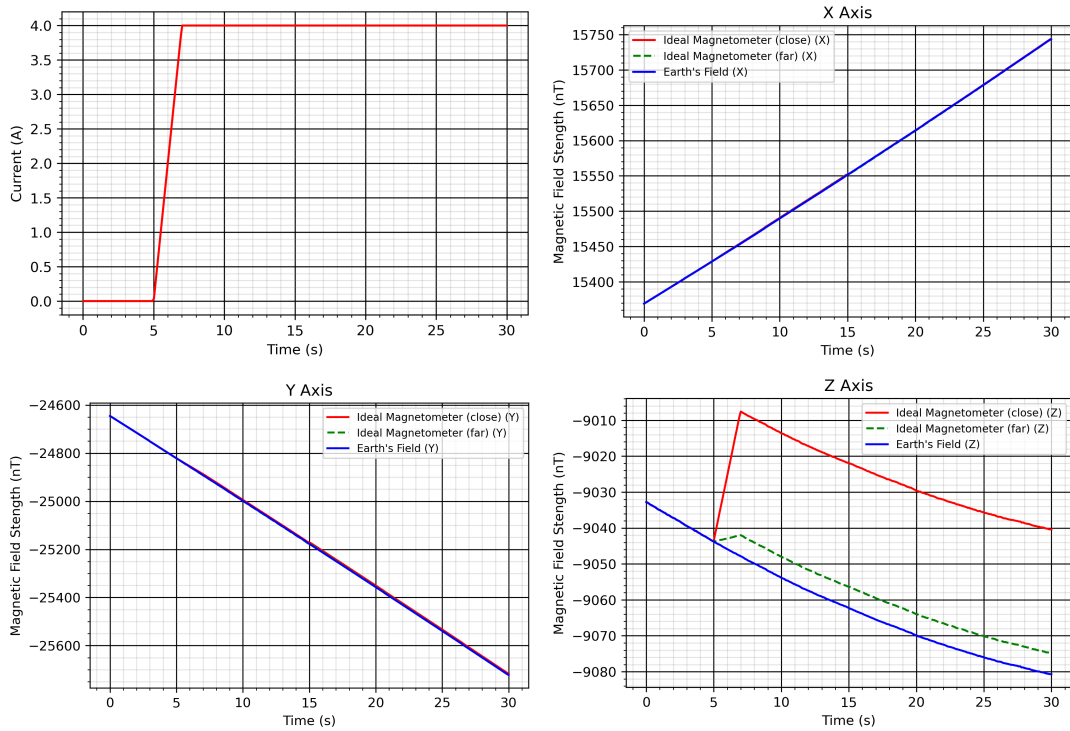


Figure 4.9: Simulation of current quickly flowing through the solar panels. No contribution from the dipoles.

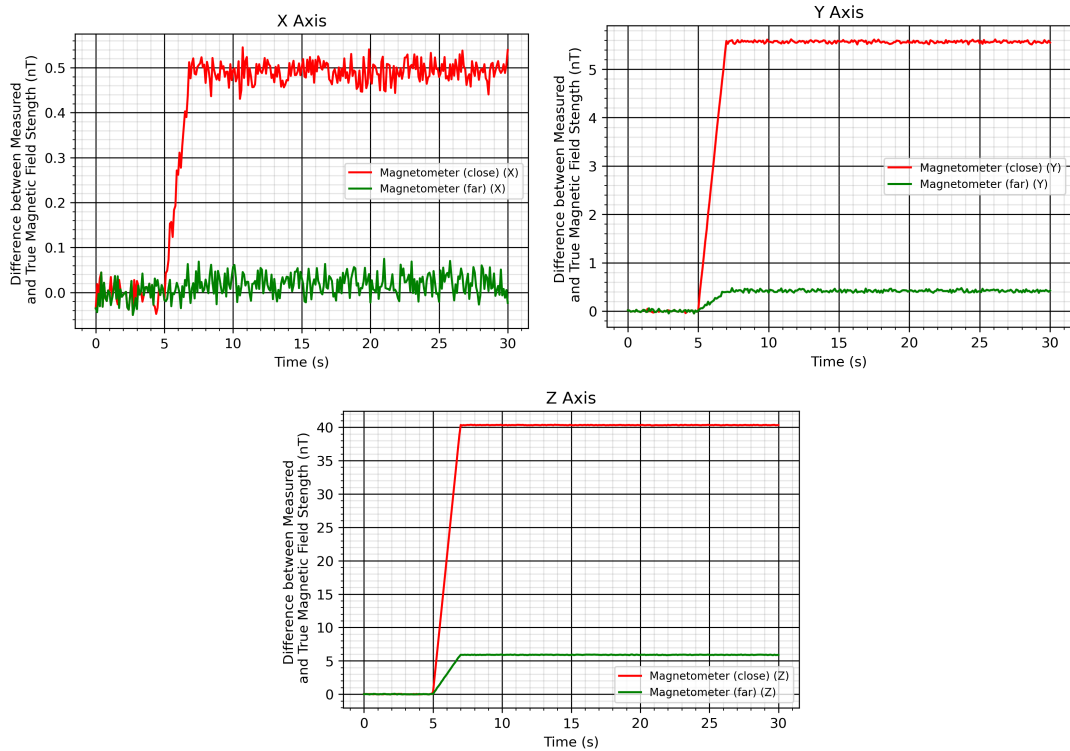


Figure 4.10: Simulation of current quickly flowing through the solar panels. No contribution from the dipoles. The vertical axis shows the difference between the measured and true magnetic field.

4.2.4. The Dual Sensor Technique

Using two sensors at different distances along the boom provides an improvement in accuracy. This is called the dual sensor technique. A spacecraft generates a magnetic field about it for which it is not feasible to generate an accurate magnetic map pre-launch [<https://doi.org/10.1029/JA076i016p03564>]. A magnetic map of the spacecraft allows to effectively determine which measurements are caused by the spacecraft and which ones are due to the external field. Without this, a single magnetometer cannot distinguish between the two: at best, some of the internal field could be filtered using knowledge of the magnetic maps of some components, but not every component's magnetic field is fully known and the interactions between components further complicate this.

The solution to this is the dual sensor technique. By mounting two sensors along the boom at different distances, the magnetic perturbations caused by spacecraft and external field can be accurately determined. The principle works due to the change in field strength with respect to a change in distance from the source. The field strength reduces by third power when distance increases. As a result, if one magnetometer is twice as far away from the spacecraft as the second, it experiences a field strength due to spacecraft-caused perturbations eight times weaker than that of the closer magnetometer. Contrastingly, ambient field perturbations result in the same change in recorded field strength for both magnetometers. Consequently, the field perturbations due to the spacecraft can be filtered out when they are distinguished from one another by this method.

To this end, the simulation tool was instructed to simulate magnetometers mounted at different boom lengths. MAGEOS was then simulated exiting an Earth eclipse for 30 [s], where the current in the solar panels suddenly rises. The measured magnetic field by both sensors is then processed using the algorithm suggested in [15], equations (13), (14) and (15), summarized in Equation 4.7, where α is the ratio of closest magnetometer $B_{obs}(r_1)$ to the magnetic source to the furthest magnetometer $B_{obs}(r_2)$. An optimal sensor distance α is found for each unique boom length. Figure 4.11 shows the result of the simulation and subsequent data processing, with the maximum absolute deviation from the true value plotted for different boom lengths. The accuracy of 1 [nT] is represented by the yellow horizontal line. Values below said line are acceptable, however some margin must be allowed for the non-simulated point knowledge errors.

$$B_{am} = [1 - \alpha]^{-1}(B_{obs}(r_2) - (B_{obs}(r_1))) \quad (4.7)$$

Additionally, the accuracy of a single magnetometer, placed at the end of the boom, is also plotted in red. As can be seen, a boom length in excess of 3 [m] would be needed to obtain the desired accuracy. This demonstrates the effectiveness of the dual sensor technique in improving the accuracy of the design.

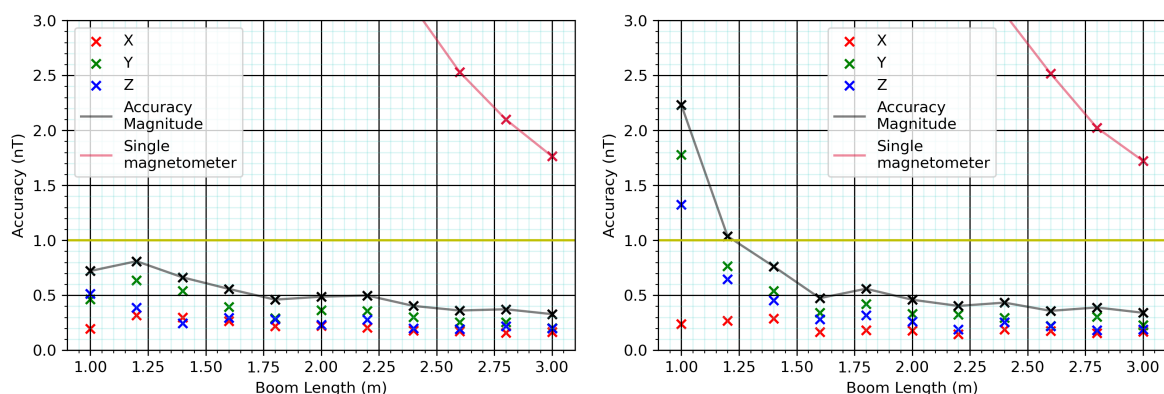


Figure 4.11: Magnetic field accuracy versus boom length simulation, based on SWARM data and magnetometer data sheet. A comparison between the dual magnetometer and single magnetometer is provided. (a) Shows performance in eclipse, (b) shows performance with 0.5 [A] flowing through each solar panel.

4.2.5. Results Discussion

In the simulation, the chosen magnetometer was placed on a boom in various conditions, such as exiting an eclipse or in a steady state. The simulations confirm that some provision need to be made. The effect of the current flowing through the cables is small, yet still enough to compromise the accuracy of the system. Ultimately a maximum deviation of 0.5 [nT] is seen between the further magnetometer and the true magnetic field. This can be seen in Figure 4.10 and more clearly in Figure 4.11, where the differences in the true magnetic field and the measured magnetic field are within the accuracy requirements.

One avenue which could be explored to expand on the functionality of the simulation is to simulate pointing knowledge errors. These could stem from the boom stiffness and ADCS platform on which the instrument is mounted on. This would allow for more accurate estimations of the magnetic field. Another way the magnetic data could be made more valuable is by representing it using spherical harmonics (discussed in more detail in Section 4.3), which would allow for distinguishing regions of larger magnetic activity, as well as different ways of representing changes.

The dual magnetometer configuration reduces the difference between the measured magnetic field and the true magnetic field. In the future, machine learning could be utilised to create a model able to filter even more spacecraft induced perturbations from the spacecraft by characterising the fields created by different spacecraft components and correlating them to changes in the measured magnetic field, further increasing accuracy. This solution especially would have to be rigorously proven to provide sufficiently accurate results.

4.2.5.1. Verification

The code was verified by testing each source and sensor at least once individually, then using simple combinations. For example, for the wires (Biot-Savart and Jefimenko), they were simulated in simple cases where analytical solutions exist, and compared against those. Further verification could be performed with more complex examples.

4.3. Gravimeter

MAGEOS will perform gravimetry according to TECH-INS-GRAV-1 [1], *"the gravimeter instrument shall take measurements with an accuracy better than 3 [cm] EWH"*. In previous works, notably [1] it was identified that for the desired level of accuracy, a method for distinguishing between the gravitational and non-gravitational (especially atmospheric drag and solar pressure) accelerations is needed. To this end, an accelerometer is used with a GNSS system to provide data regarding the acceleration due to gravity as well as accuracy 3D positioning, which can be processed into an EWH measurement.

The gravimeter section will provide a brief introduction into gravimetry, including the mathematical treatment. With this knowledge, it is possible to select a positioning/accelerometer configuration that matches the requirement. The final chosen positioning system will involve dual GNSS receivers, an accelerometer and a SLR retroreflector. The systems are chosen and sized in this section.

4.3.1. Theory

The theory behind gravimetry is presented in this section, first by introducing the idea of spherical harmonics, then justification is provided for normalising variables to prevent unbounded growth. With the information so far gravitational acceleration is related to the spherical harmonic representation of Earth's gravity field, allowing for the determination of a gravity field model. Finally, knowing the model, the unit of measurement can be changed from an acceleration to equivalent water height, relating the measured acceleration due to gravity to equivalent water height.

4.3.1.1. Spherical Harmonics in Gravimetry

The theory behind gravimetry lies in the spherical harmonic representation of Earth's magnetic field. The reader is referred to [21] for more information regarding the spherical harmonic model of Earth; a brief treatment is presented here. Mathematically, spherical harmonics are the solution to Laplace's

differential equation, shown in Equation 4.8, however in gravimetry the gravitational potential, $V(\phi, \lambda)$, is modelled as in Equation 4.9 [21], where $\mu = G \cdot M_e$, the standard gravitational parameter; a_e is the semi-major axis of Earth's reference ellipsoid; r , ϕ and λ are the satellite distance, latitude and longitude. $C_{\ell,m}$ and $S_{\ell,m}$ spherical harmonic coefficients of degree ℓ and order m ; and $P_{\ell,m}$ are the Associated Legendre Functions of degree ℓ and order m , (given in Equation 4.10) [21].

$$\frac{\partial^2 u}{\partial x^2} + \frac{\partial^2 u}{\partial y^2} + \frac{\partial^2 u}{\partial z^2} = 0 \quad (4.8)$$

$$V(r, \phi, \lambda) = V = \frac{\mu}{r} \sum_{\ell=0}^{\infty} \left(\frac{a_e}{r} \right)^{\ell} \sum_{m=0}^{\ell} P_{\ell,m}(\sin \phi) [C_{\ell,m} \cos m\lambda + S_{\ell,m} \sin m\lambda] \quad (4.9)$$

$$P_{\ell,m}(x) = \frac{(1-x^2)^{\frac{m}{2}}}{2^{\ell}} \sum_{k=0}^{\frac{\ell-m}{2}} (-1)^k \frac{(2\ell-2k)!}{k!(\ell-k)!(\ell-m-2k)!} \cdot x^{\ell-m-2k} \quad (4.10)$$

The spherical harmonics for $\ell = 1$ are shown in Figure 4.12, with positive shown in green and negative as red. In the images shown a different notation is used for m , where $M \in [-\ell, \ell]$ (the sine and cosine terms are combined in Equation 4.9). Intuitively, spherical harmonics can be understood as a set of orthonormal functions (when integrated over the surface of a sphere), where each function contributes independently of any other function to a solution. For modelling Earth's gravity, much higher values of ℓ tend to be used, with more the more accurate models normally truncated at $\ell \approx 100$ [22].

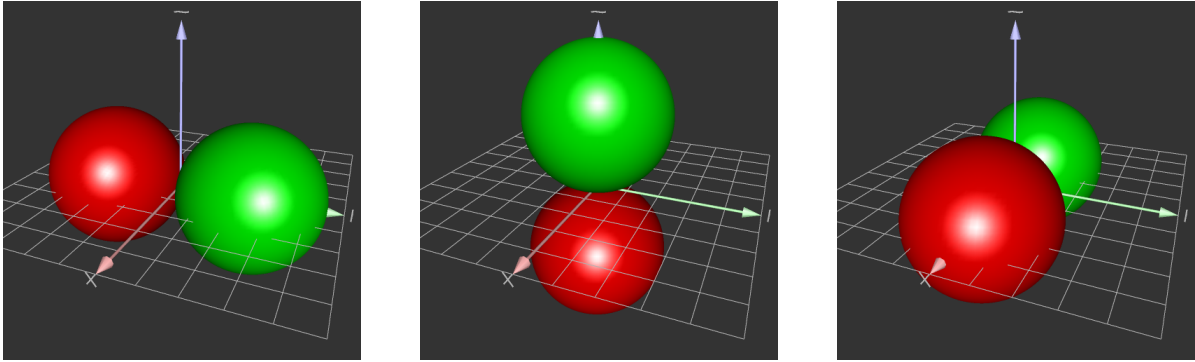


Figure 4.12: Spherical harmonics visualisation for $\ell = 1$. From left to right, $M = -1, 0, 1$. Green is positive and red is negative. From [23].

A gravitational model is fully defined by specifying μ , a_e , $C_{\ell,m}$ and $S_{\ell,m}$ up to the required degree ℓ and order m . The object of the on-board gravimeter will be to collect sufficient data to determine the coefficients.

4.3.1.2. Normalisation of Spherical Harmonic Coefficients

The coefficients $P_{\ell,m}$, $C_{\ell,m}$ and $S_{\ell,m}$ tend to extreme values as the degree of the spherical harmonic function increases [21]. Mathematically it can be explained by the Associated Legendre polynomials, which become very large for increasing degree, forcing $C_{\ell,m}$ and $S_{\ell,m}$ to very small numbers to counteract the effect. Hence, it is "numerically advantageous to normalize the Associated Legendre Functions and the coefficients" [21]. To this end, a scaling factor Λ is defined by Equation 4.11, with δ_{m0} being the Kronecker delta, defined by Equation 4.12.

$$\Lambda = \left[(2 - \delta_{m0})(2\ell + 1) \frac{(\ell - m)!}{(\ell + m)!} \right]^{\frac{1}{2}} \quad (4.11) \quad \delta_{xy} = \begin{cases} 1 & x = y, \\ 0 & \text{else} \end{cases} \quad (4.12)$$

The Associated Legendre polynomials and coefficients are then scaled according to Equation 4.13, Equation 4.14 and Equation 4.15. The variables in Equation 4.9 can be replaced with their normalized counterparts, shown in Equation 4.16.

$$\bar{P}_{\ell,m} = \Lambda \cdot P_{\ell,m} \quad (4.13) \quad \bar{C}_{\ell,m} = \frac{1}{\Lambda} \cdot C_{\ell,m} \quad (4.14) \quad \bar{S}_{\ell,m} = \frac{1}{\Lambda} \cdot S_{\ell,m} \quad (4.15)$$

$$V = \frac{\mu}{r} \sum_{\ell=0}^{\infty} \left(\frac{a_e}{r} \right)^{\ell} \sum_{m=0}^{\ell} \bar{P}_{\ell,m}(\sin \phi) [\bar{C}_{\ell,m} \cos m\lambda + \bar{S}_{\ell,m} \sin m\lambda] \quad (4.16)$$

4.3.1.3. Obtaining Gravitational Acceleration

The gradient of V in Equation 4.9 is equal to the gravitational acceleration acting of the orbiting body, which is a measurable value. Because the solution is given in spherical coordinates (latitude, longitude and a radial distance), it is natural to take the gradient in spherical coordinates, shown in Equation 4.17, where \underline{u}_- are the unit vectors in the r , ϕ and λ basis.

$$\vec{a} = \nabla V = \frac{\partial V}{\partial r} \vec{u}_r + \frac{1}{r} \frac{\partial V}{\partial \phi} \vec{u}_\phi + \frac{1}{r \cos \phi} \frac{\partial V}{\partial \lambda} \vec{u}_\lambda \quad (4.17)$$

The formulation in Equation 4.17 implies a transformation from the Gravimeter Measurement Frame (GMF) to the spherical frame (SPH). SPH is similar to NED in Section 4.2.1.5, except that crucially the radial component (parallel to down in NED) is pointing to the spacecraft from the geometric center of Earth rather than away.

To come to an inertial system to write equations of motion, the "Polar motion (the motion of the spin axis with respect to the Earth crust), Earth rotation (the largest effect) and precession and nutation (the motion of the spin axis with respect to the stars)" [21] are normally taken into account. For simple models this is not necessary.

In addition, external accelerational perturbations, caused by atmospheric drag, solar radiation or other sources need to be compensated for in the measurements. An accelerometer is typically used for this purpose, as it measures the total force experience by the spacecraft, assuming it behaves as a rigid body.

The gravitational acceleration is obtained using the combination of GNSS and accelerometer, solving the left hand side of Equation 4.17. Then, knowing the satellite's position (from the GPS measurement), a system of equations can be set up, and solved for using a least-squares method for the parameters that define the gravitational model.

$$\begin{aligned} \vec{a} = & \left\{ -\frac{\mu}{r^2} \sum_{\ell=0}^{\infty} (\ell + 1) \left(\frac{a_e}{r} \right)^{\ell} \sum_{m=0}^{\ell} \bar{P}_{\ell,m}(\sin \phi) [\bar{C}_{\ell,m} \cos m\lambda + \bar{S}_{\ell,m} \sin m\lambda] \right\} \vec{u}_r \\ & + \left\{ \frac{\mu}{r^2} \sum_{\ell=1}^{\infty} \left(\frac{a_e}{r} \right)^{\ell} \sum_{m=0}^{\ell} \frac{\partial \bar{P}_{\ell,m}(\sin \phi)}{\partial \phi} [\bar{C}_{\ell,m} \cos m\lambda + \bar{S}_{\ell,m} \sin m\lambda] \right\} \vec{u}_\phi \\ & + \left\{ \frac{\mu}{r^2} \sum_{\ell=1}^{\infty} \left(\frac{a_e}{r} \right)^{\ell} \sum_{m=1}^{\ell} m \frac{\bar{P}_{\ell,m}(\sin \phi)}{\cos \phi} [-\bar{C}_{\ell,m} \sin m\lambda + \bar{S}_{\ell,m} \cos m\lambda] \right\} \vec{u}_\lambda \end{aligned} \quad (4.18)$$

4.3.1.4. Accuracy of the model in Equivalent Water Height

To obtain the accuracy of the measured gravitational model in terms of EWH the method presented by John Wahr et al. is used [22]. A summary of the method is presented in this section. In [22] co-latitude, θ , was used in place of latitude, ϕ . The transformation between the two is $\theta = 90^\circ - \phi$, from which subsequent transformations can be derived, for example $\cos \theta = \sin \phi$ and $\sin \theta = \cos \phi$.

Wahr et al. begin by assuming a time-dependent geoid results in a change in the gravitational potential ΔV , which can be represented as changes in the spherical harmonic coefficients $\Delta \bar{C}_{\ell,m}$ and $\Delta \bar{S}_{\ell,m}$. Due to the superposition principle, this change in V can be added to the existing gravitational model, $V_{existing}$, to obtain the new gravitational potential, V_{new} , shown in Equation 4.19 [22]. All the variables in Equation 4.19 are as defined in previous sections.

$$V_{new} = V_{existing} + \Delta V = V_{existing} + \frac{\mu}{r} \sum_{\ell=0}^{\infty} \left(\frac{a_e}{r} \right)^\ell \sum_{m=0}^{\ell} \bar{P}_{\ell,m}(\sin \phi) [\Delta \bar{C}_{\ell,m} \cos m\lambda + \Delta \bar{S}_{\ell,m} \sin m\lambda] \quad (4.19)$$

The changes in the spherical harmonic coefficients caused by a time-dependent geoid are derived from [24] but taken from [22], shown in Equation 4.20 as the integral over the volume of a sphere. $\rho_{ave} \approx 5517$ [kg/m³] is the average density of the Earth, $\Delta\rho(r, \phi, \lambda)$ is the density redistribution causing the geoid change, and r is the radial distance of the geoid from the center of the Earth.

$$\begin{bmatrix} \Delta \bar{C}_{\ell,m} \\ \Delta \bar{S}_{\ell,m} \end{bmatrix} = \frac{-3}{4\pi\rho_{ave}(2\ell+1)} \int \Delta\rho(r, \phi, \lambda) \bar{P}_{\ell,m}(\sin \phi) \left(\frac{r}{a_e} \right)^{\ell+2} \begin{bmatrix} \cos m\lambda \\ \sin m\lambda \end{bmatrix} \cos \phi d\phi d\lambda dr \quad (4.20)$$

Defining $\Delta\sigma(\phi, \lambda)$ as the surface density (mass per unit area), the mathematical definition is shown in Equation 4.21 [22]. It is also assumed that $\Delta\rho$ exclusively changes near Earth's surface, i.e. $r \approx a_e$. With these assumptions in mind, the contribution of the geoid to the spherical harmonic coefficients can be quantised. Equation 4.22 is an integral over the surface of Earth that describes the direct gravitational attraction of the geoid on the observation instrument[22], called surface mass attraction. However, this increased surface mass "also loads and deforms the underlying solid Earth", which results in a further contribution to the gravitational potential, called solid Earth attraction, mathematically shown in Equation 4.23, which is identical to Equation 4.22 multiplied with k_ℓ , the load Love number of degree ℓ [22].

$$\Delta\sigma(\phi, \lambda) = \int_{\text{thin layer}} \Delta\rho(r, \phi, \lambda) dr \quad (4.21)$$

$$\begin{bmatrix} \Delta \bar{C}_{\ell,m} \\ \Delta \bar{S}_{\ell,m} \end{bmatrix}_{\text{surf mass}} = \frac{-3}{4\pi a \rho_{ave} (2\ell + 1)} \int \Delta\sigma(\phi, \lambda) \bar{P}_{\ell,m}(\sin \phi) \begin{bmatrix} \cos m\lambda \\ \sin m\lambda \end{bmatrix} \cos \phi d\phi d\lambda \quad (4.22)$$

$$\begin{bmatrix} \Delta \bar{C}_{\ell,m} \\ \Delta \bar{S}_{\ell,m} \end{bmatrix}_{\text{solid E}} = \frac{-3k_\ell}{4\pi a \rho_{ave} (2\ell + 1)} \int \Delta\sigma(\phi, \lambda) \bar{P}_{\ell,m}(\sin \phi) \begin{bmatrix} \cos m\lambda \\ \sin m\lambda \end{bmatrix} \cos \phi d\phi d\lambda \quad (4.23)$$

Equation 4.22 and Equation 4.23 can be summed to find the total change in the spherical harmonics, as shown in Equation 4.24. The equivalent water height can be computed by dividing the surface density $\Delta\sigma$ by the density of water $\rho_w = 1000$ [kg/m³] [22]. Equation 4.22, Equation 4.23 and Equation (11) in [22] can then be combined to solve for $\Delta \hat{C}_{\ell,m}$ and $\Delta \hat{S}_{\ell,m}$, the vector equation is shown in Equation 4.26.

$$\begin{bmatrix} \Delta \bar{C}_{\ell,m} \\ \Delta \bar{S}_{\ell,m} \end{bmatrix} = \begin{bmatrix} \Delta \bar{C}_{\ell,m} \\ \Delta \bar{S}_{\ell,m} \end{bmatrix}_{\text{surf mass}} + \begin{bmatrix} \Delta \bar{C}_{\ell,m} \\ \Delta \bar{S}_{\ell,m} \end{bmatrix}_{\text{solid E}} \quad (4.24)$$

$$\text{EWH}(\phi, \lambda) = \frac{\Delta \sigma(\phi, \lambda)}{\rho_w} = a_e \sum_{\ell=0}^{\infty} \sum_{m=0}^{\ell} \bar{P}_{\ell,m}(\sin \phi) [\Delta \hat{C}_{\ell,m} \cos m\lambda + \Delta \hat{S}_{\ell,m} \sin m\lambda] \quad (4.25)$$

$$\begin{bmatrix} \Delta \bar{C}_{\ell,m} \\ \Delta \bar{S}_{\ell,m} \end{bmatrix} = \frac{3\rho_w}{\rho_{ave}} \frac{1+k_\ell}{2\ell+1} \begin{bmatrix} \Delta \hat{C}_{\ell,m} \\ \Delta \hat{S}_{\ell,m} \end{bmatrix} \quad (4.26)$$

4.3.1.5. Spherical Harmonics Expansion

To obtain $C_{\ell,m}$ and $S_{\ell,m}$, a spherical harmonic expansion takes place up to a specified ℓ_{\max} and m_{\max} . In this work, this is performed using a least squares method outlined below. The aforementioned equations in Equation 4.18 can be set up in a system like that shown in Equation 4.27. For a system with zero error, it would be sufficient to find the inverse of A to solve for \vec{x} , the coefficients, knowing \vec{y} , the accelerations. Because the accelerations contain errors, however, a least squares approach is taken to estimate $C_{\ell,m}$ and $S_{\ell,m}$, shown in Equation 4.28.

$$A \cdot \vec{x} = \vec{y} \quad (4.27) \quad \hat{x} = (A^T A)^{-1} A^T \hat{y} \quad (4.28)$$

In the implementation, the spherical harmonic coefficients are stored in upper triangular matrices, similar to that shown in Equation 4.20. To convert between the upper triangular form and the vector form of \vec{x} , the indices of the relevant elements in the upper triangular matrix are obtained, and those elements are placed into a column vector. Next, both C and S coefficients with $\ell = 1$ are removed from the vector, as well as the S coefficients with $m = 0$, as these values reduce to zero in Equation 4.18.

$$C = \begin{bmatrix} C_{0,0} & C_{1,0} & C_{2,0} & \cdots & C_{\ell_{\max},0} \\ & C_{1,1} & C_{2,1} & \cdots & C_{\ell_{\max},1} \\ & & \ddots & \ddots & C_{\ell_{\max},2} \\ & & & \ddots & \vdots \\ & & & & C_{\ell_{\max},m_{\max}} \end{bmatrix} \quad (4.29)$$

The values of A , \vec{x} and \vec{y} are given in Equation 4.30, Equation 4.31 and Equation 4.32. The first third of rows correspond to n radial equations for the n number of points. The second third and last third contain the ϕ and λ components, respectively. The number columns in Equation 4.30 correspond to the number spherical harmonic coefficients being solved for. The elements in A are given by Equation 4.33, Equation 4.34 and Equation 4.35, which are deduced from Equation 4.18. The C & S superscript denotes that expression is both for cosine and sine components. For example, the term ${}^0 A_{\lambda_{2,3}}^C$ corresponds to the zeroth data point in the sample, the cosine coefficient in the longitudinal direction ($-\sin^3 \lambda$) with $\ell = 2$ and $m = 3$. It's full numerical value is ${}^0 A_{\lambda_{2,3}}^C = \frac{mu}{\sigma_r} \cdot 3 \cdot \frac{\bar{P}_{2,3}(\sin^0 \phi)}{\cos^0 \phi} \cdot -\sin^3 \lambda$.

$$A = \begin{bmatrix} {}^1A_{r_{0,0}}^C & \dots & {}^1A_{r_{\ell,m}}^C & \dots & {}^1A_{r_{\ell_{max},m_{max}}}^S \\ {}^2A_{r_{0,0}}^C & \dots & {}^2A_{r_{\ell,m}}^C & \dots & {}^2A_{r_{\ell_{max},m_{max}}}^S \\ \vdots & \vdots & \vdots & \vdots & \vdots \\ {}^nA_{r_{0,0}}^C & \dots & {}^nA_{r_{\ell,m}}^C & \dots & {}^nA_{r_{\ell_{max},m_{max}}}^S \\ {}^1A_{\phi_{0,0}}^C & \dots & {}^1A_{\phi_{\ell,m}}^C & \dots & {}^1A_{\phi_{\ell_{max},m_{max}}}^S \\ \vdots & \vdots & \vdots & \vdots & \vdots \\ {}^nA_{\phi_{0,0}}^C & \dots & {}^nA_{\phi_{\ell,m}}^C & \dots & {}^nA_{\phi_{\ell_{max},m_{max}}}^S \\ {}^1A_{\lambda_{0,0}}^C & \dots & {}^1A_{\lambda_{\ell,m}}^C & \dots & {}^1A_{\lambda_{\ell_{max},m_{max}}}^S \\ \vdots & \vdots & \vdots & \vdots & \vdots \\ {}^nA_{\lambda_{0,0}}^C & \dots & {}^nA_{\lambda_{\ell,m}}^C & \dots & {}^nA_{\lambda_{\ell_{max},m_{max}}}^S \end{bmatrix} \quad (4.30)$$

$$\vec{y} = \begin{bmatrix} {}^1a_r \\ {}^2a_r \\ \vdots \\ {}^na_r \\ {}^1a_\phi \\ \vdots \\ {}^na_\phi \\ {}^1a_\lambda \\ \vdots \\ {}^na_\lambda \end{bmatrix} \quad (4.31)$$

$$\vec{x} = \begin{bmatrix} C_{0,0} \\ C_{2,0} \\ \vdots \\ C_{\ell_{max},m_{max}} \\ S_{2,1} \\ \vdots \\ S_{\ell_{max},m_{max}} \end{bmatrix} \quad (4.32)$$

$${}^nA_{r_{\ell,m}}^{C\&S} = -\frac{\mu}{n_r^2}(\ell+1)\left(\frac{a_e}{n_r}\right)^\ell \bar{P}_{\ell,m}(\sin^n \phi) \left[\cos m^n \lambda + \sin m^n \lambda \right] \quad (4.33)$$

$${}^nA_{\phi_{\ell,m}}^{C\&S} = \frac{\mu}{n_r^2} \left(\frac{a_e}{n_r}\right)^\ell \frac{\partial \bar{P}_{\ell,m}(\sin^n \phi)}{\partial^n \phi} \left[\cos m^n \lambda + \sin m^n \lambda \right] \quad (4.34)$$

$${}^nA_{\lambda_{\ell,m}}^{C\&S} = \frac{\mu}{n_r^2} \left(\frac{a_e}{n_r}\right)^\ell m \frac{\bar{P}_{\ell,m}(\sin^n \phi)}{\cos^n \phi} \left[-\sin m^n \lambda + \cos m^n \lambda \right] \quad (4.35)$$

4.3.1.6. Simulation

With the gravimetry theory it is possible to simulate the system and obtain an equivalent water height as a function of latitude and longitude. Sampling uniformly on a sphere it is then possible to obtain a root mean squared error in terms of EWH, which can be compared to requirement TECH-INS-GRAV-1. The algorithms in [25] or [26] could be used to estimate the spherical harmonics, however for the purposes of this work a simple least squares method is used. The anticipated result is that the error will be larger as opposed to methods that use kalman filtering or use kinematic relations to improve the RMSE of measurements, as performed in [26]. However, due to being a preliminary report these improvements are left for future work.

?? shows the result of a simulation of points sampled uniformly on a sphere of radius $a_e + 300$ [km], where a_e is the volumetric radius of the Earth. The number of sample points equals the orbital period multiplied by the sampling frequency of the GNSS, equating to about 50000 points per orbit. To simulate a month, the root mean square error of the GPS positional error was scaled assuming independent samples. The method for estimating spherical harmonic coefficients is presented in Section 4.3.1.5.

With the estimated spherical harmonics it is possible to constructed an equivalent water height plot with the method presented in Section 4.3.1.4. Figure 4.14 shows the program flow of the gravimeter simulation program.

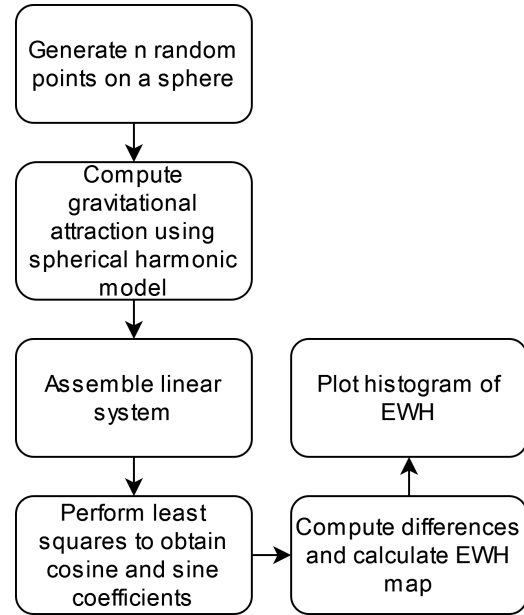


Figure 4.13: Gravimeter Simulation Block Diagram

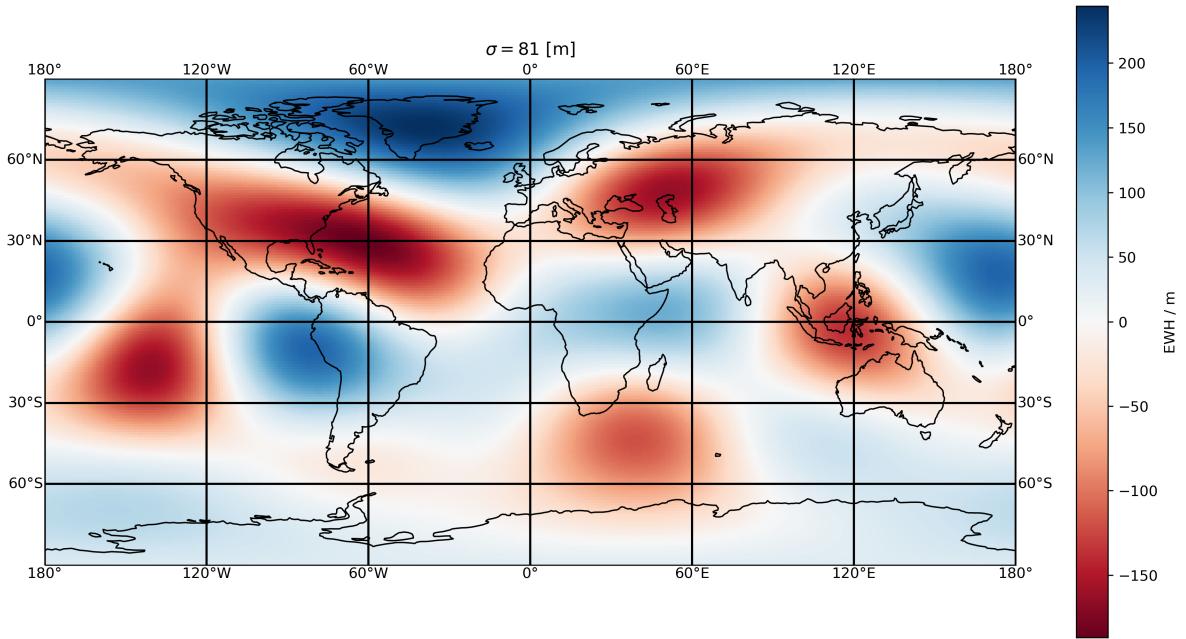


Figure 4.14: Equivalent Water Height for simulated data collected over the span of a month. The reconstruction was performed with $\ell_{\max} = 5$ and $m_{\max} = 5$. The standard deviation is $\sigma = 81$ [m].

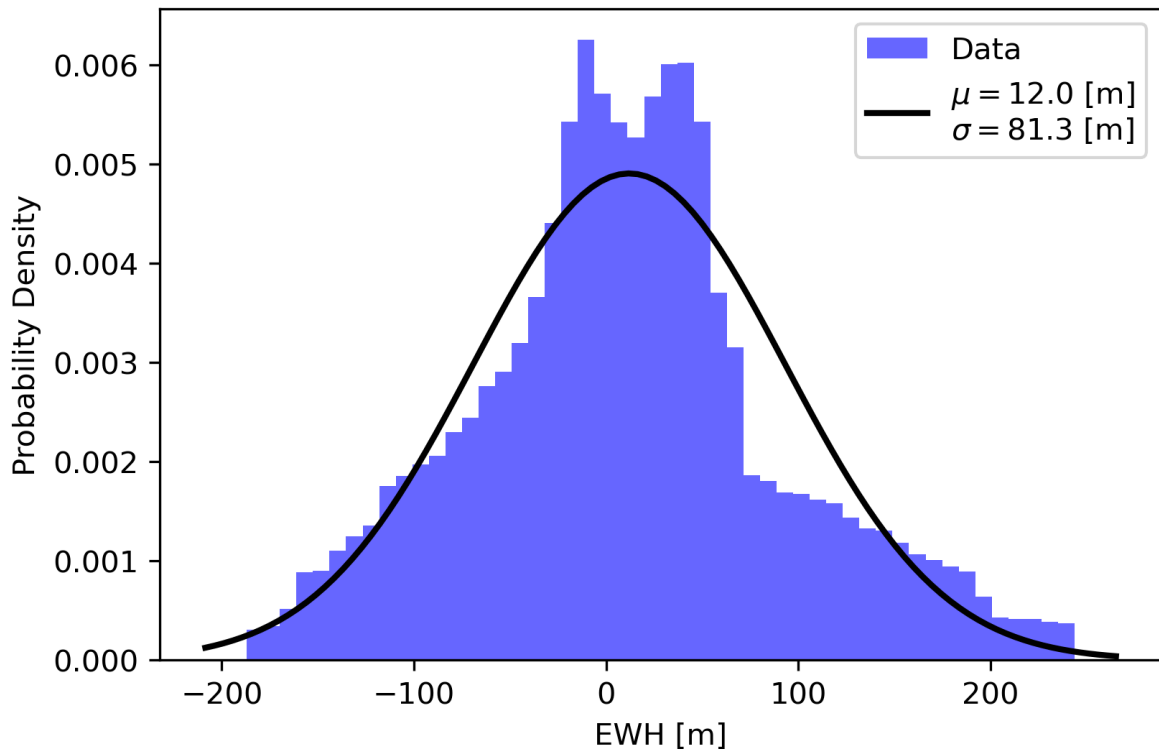


Figure 4.15: EWH histogram showing the distribution of error in terms of equivalent water height between the reconstructed spherical model of the Earth's gravitational field versus the JGM3 model.

A limitation to this approach is that as the points are randomly sampled, they are independent. Thus, the root mean squared error of measurements cannot be reduced by any means. If a satellite orbit were simulated, measurement points would be dependent, and hence kinematic or energy methods

could be combined to reduce the uncertainty in the positional error. The result of the uncertainties culminated in the error observed in Figure 4.14, and are plotted in the histogram in Figure 4.15. The most error can be observed near the North pole. The simulation shows that the satellite does not fulfill TECH-INS-GRAV-1, however some future work in the performance of the simulator could significantly increase the accuracy.

4.3.1.7. Verification

Verification was performed on the in-house built gravimetry simulation by testing edge cases and ensuring that the model could compute the spherical harmonics accurately with zero artificial error.

4.3.1.8. Future work

Future work should focus on implementing a simulation of a satellite orbit, which outputs position and accelerometer data (if it is to be simulated). A numerical scheme should be developed to compute the gravitational acceleration, which, using an algorithm such as that presented in [26], could be used to estimate the spherical harmonic coefficients. Crucially, the spherical harmonic coefficients should be calculated using the orthogonality properties of the associated legendre polynomials, Further, more verification should be performed to ensure the accuracy of the model.

4.3.2. GNSS Sensor

In Section 4.3.1, the theory behind gravitational measurements was explained. It was found that the required measurements are position and gravitational acceleration. Hence, the accuracy of the model is determined by how accurate these measurements are. The error can be described in many ways, including a power spectral density plot or root mean squared error. For the purposes of this work, the root mean square error will suffice.

In the selection of a position sensor, a GNSS sensor was chosen that had similar accuracy as the GPS sensor on SWARM. The latter mission performance is better than the requirement TECH-INS-GRAV-1. Choosing a GPS sensor with similar accuracy will hence help ensure that TECH-INS-GRAV-1 is met, if also an accelerometer is chosen with similar accuracy as SWARM.

Based on the simulation and the reasoning above, the chosen GPS for the MAGEOS mission is the GSD800 GNSS Receiver [27], which is a GNSS receiver suited to work with GPS, BeiDou and GLONASS signals [27]. While the simulation shows that the expect accuracy is about $\sigma = 81$ [m], better algorithms could be employed to reduce the error significantly. Using the reasoning that the sensor is similar in performance to SWARM, a similar accuracy should be expected.

The COTS antenna has to receive on the frequencies L1/E1 & L5/E5a [28]. The antenna chosen for our mission is the L1/L5 Active Ceramic Patch GNSS Antenna from Linx Technologies [29] shown in Figure 4.16. The volume of the antenna is $2.5 \times 2.5 \times 1.2$ [cm^3]. It contains a 10 [cm] long, 0.113 [cm] diameter coaxial cable MHF1/U.FL-type plug connector that has to be fitted in a 1 cube unit. The mass of the receiver is 0.0198 [kg] and it consumes 0.05 [W] of power. It is an omni-directional antenna, which is required for Earth satellites, due to their close proximity to Earth.



Figure 4.16: L1/L5 Active Ceramic Patch GNSS Antenna [29] supporting GPS providing omni-directional high gain with low noise



Figure 4.17: GSD800 GNSS Receiver [30]

For redundancy and better orbit determination, the same GNSS receiver and antenna pair are used twice in the spacecraft. This will decrease the root mean square of the position and also provide an additional positional measurement source.

An additional source from which the accuracy may be improved, is the use of real time kinematics. This is a technique for GNSS measurements that eliminate uncertainties in the phase of the received transmissions by comparing measurements. By comparing the phase received by a ground station, of which the location is known very well, to a different receiver, their relative position can be determined very accurately. As the ground station's position is known very well, the position with respect to the Earth of the second receiver can be determined very accurately as well, often down to 1 [cm] of uncertainty. The main downside to this technique is that it has a limited range, only working if these GNSS receivers are within 20 [km] of one another.[31] As the MAGEOS spacecraft will be orbiting far higher than 20 [km], RTK cannot be used directly. However, if the two MAGEOS spacecraft are close enough to one another, this technique can be applied between both of them. Although This will likely not improve the positional accuracy of one spacecraft with respect to the Earth, it will likely allow the relative position of both spacecraft to be determined quite well. Therefore, if the spacecraft constellation is designed such that the spacecraft are within 20 [km] of one another, the effect of this relative accuracy can be investigated.

4.3.3. Accelerometer

Although an accelerometer is necessary to eliminate the non-gravitational accelerations from the GNSS observations, it does not itself provide the desired final result. The accelerometer should therefore be accurate enough to remove undesired accelerations from the measurements, but the accelerometer being much more accurate than that will not significantly improve the final result. However, the accelerometer having a worse accuracy compared to the GNSS receiver does decrease the accuracy of the final measurements, so this must be avoided. In Figure 4.18, the accelerations the GOCE spacecraft experienced are shown, separated by direction and by source. This satellite orbited at 250 km, which is quite close to the altitude the MAGEOS mission will orbit at.

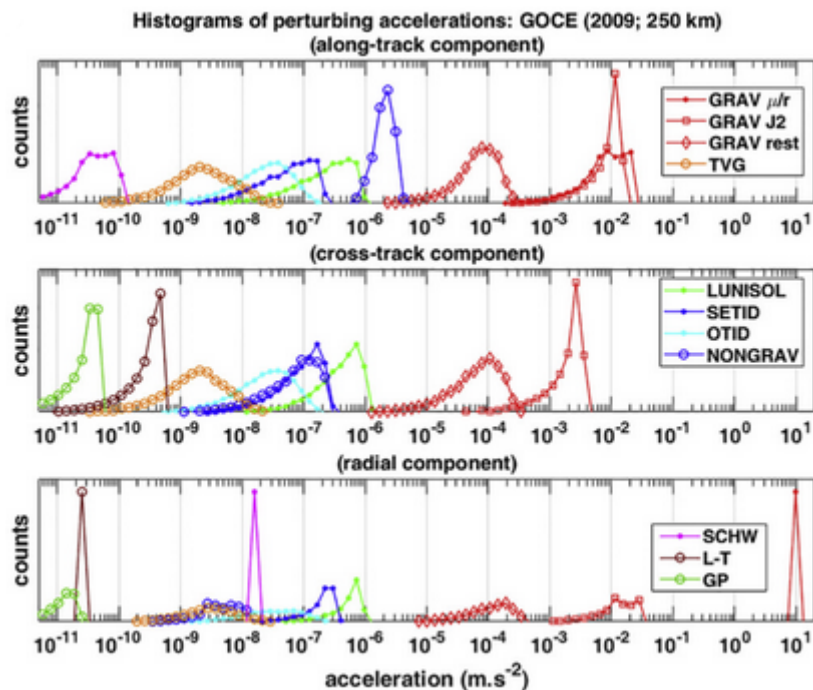


Figure 4.18: The acceleration perturbations per direction experienced by the GOCE satellite. The perturbations are separated into several components, in order from top to bottom: spherical Earth, J2-effect of Earth, perturbation due to additional changes in the gravity field of Earth, the time-varying gravity field, the accelerations from the Sun and Moon, accelerations from the tides of the Earth's crust, and the tides of the oceans, non-gravitational accelerations, and finally three relativistic effects.[32]

The purpose for which the accelerometer is included is to eliminate the non-gravitational accelerations. As can be seen in Figure 4.18, the non-gravitational accelerations differ in magnitude per component, ranging mostly between 10^{-5} and 10^{-6} [m/s^2] for the along-track component, 10^{-6} and 10^{-8} [m/s^2] for the cross-track component, and 10^{-8} and 10^{-9} [m/s^2] for the radial component. The accelerometer should therefore be selected such that it can remove these accelerations.



Figure 4.19: The ISA, three instruments aligned along different axes, mounted onto a baseplate.

The accelerometer that has been chosen is the Italian Spring Accelerometer (ISA), as shown in Figure 4.19. This accelerometer is currently on the Bepi-Colombo mission, launched in 2018, but will only arrive and be used in Mercury by late 2025, where it will measure the gravitational field amongst other objectives[33]. The estimated TRL is therefore 8, as it is not flight proven, but it is flight qualified. This accelerometer is, however, not suitable for a CubeSat mission due to its dimensions. An adapted model of this accelerometer is developed for the FISICA program. This version uses the same instrumentation, however, instead of having three accelerometers rigged onto a base plate, it is only one unmounted instrument along with its required circuitry. In ??, the characteristics of ISA, as well as its adapted version, are portrayed.

Mission	Mass [kg]	Volume [U]	Average power [W]	Measurement Accuracy [m/s^2]	# Measurement Dimensions	Intrinsic Noise [$m/s^2/\sqrt{Hz}$]
ISA	5.8	1.9 or 9.2	10.1	10^{-8}	3	10^{-9}
Downscaled ISA	0.2	0.17	0.075	10^{-8}	1	10^{-9}

Table 4.2: Accelerometer comparison ISA and its downscaled version

Unfortunately, although it can measure the accelerations in the along- and cross-track directions, this accelerometer does not have sufficient accuracy in the radial direction. Most of these non-gravitational accelerations are between 10^{-8} and 10^{-9} , as seen in Figure 4.18, which the chosen accelerometer cannot measure. This data was however for a satellite orbiting at 250 [km], whilst the MAGEOS spacecraft will orbit at 230 [km]. As the main non-gravitational acceleration is due to atmospheric drag, the non-gravitational accelerations will be higher at this lower orbit. Using Figure 4.20, it can be seen that the drag at 250 [km] is nearly half the value at 230 [km]. This means the perturbations will be more significant, but these will fall within the range of the accelerometer. The accelerometer will therefore be able to measure some of the radial perturbations, but not all. The downscaled ISA accelerometer is still selected as the accelerometer to be used, as it is still more accurate than other accelerometers of that size. Accelerometers that have higher accuracies do exist, but they are too large and heavy for this spacecraft.

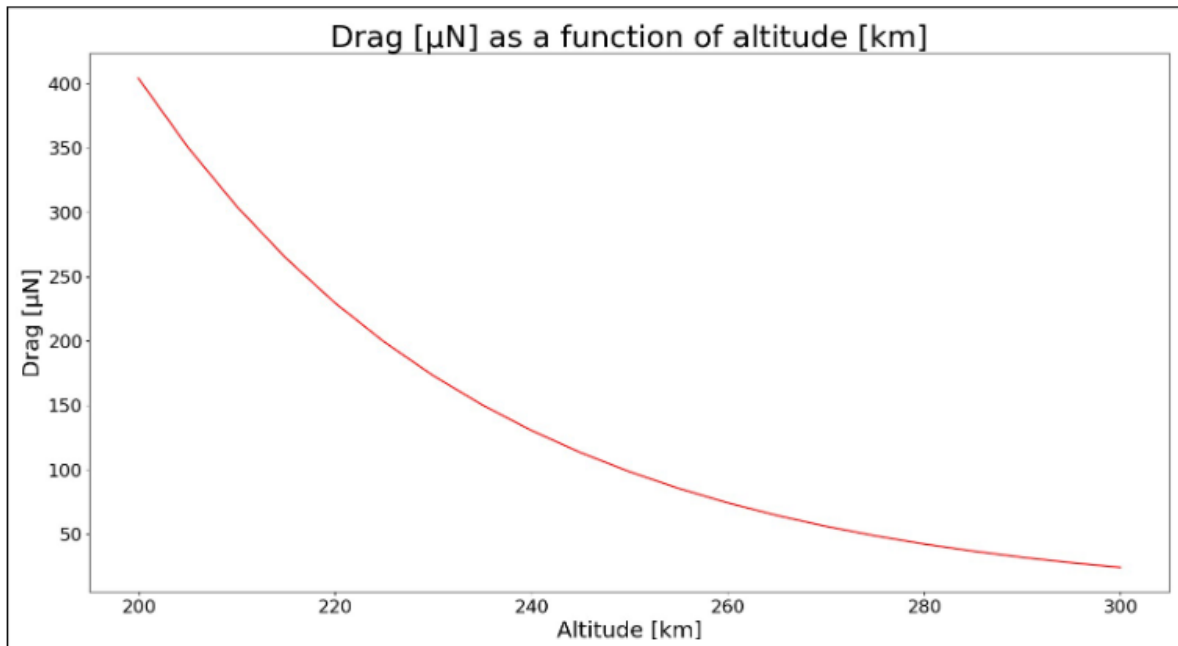


Figure 4.20: The atmospheric drag around the altitudes at which the MAGEOS spacecraft will orbit.

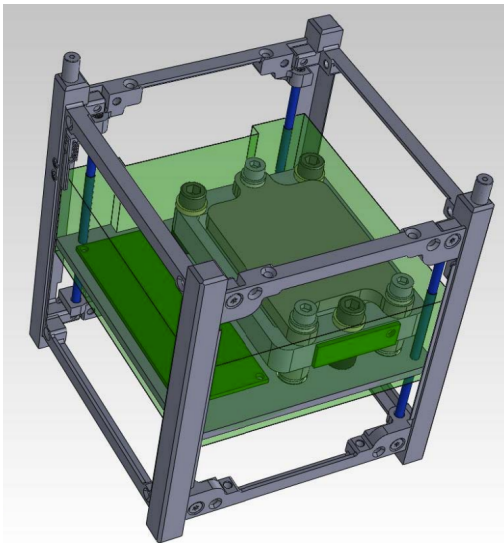


Figure 4.21: The adapted ISA, one instrument fit into a CubeSat unit.

To measure the acceleration in each axis, three of the adapted instruments are needed. One of such instruments fit into a cube can be seen in figure Figure 4.21. The base plate is the main difference between the original ISA and the adapted version, contributing to the discrepancy in mass and volume. The base plate is a stiff structure, which also provides thermal insulation and houses the front end electronics box. This is an important contribution in minimising the error budget of the instrument. The intrinsic noise is one contribution to the error of the instrument, but others include mechanical noise, calibration errors, thermal effects, response to in and out of band acceleration effects[34]. While the intrinsic noise is unchanged, the removal of the base plate increases the thermal effects and mechanical noise, meaning the error is higher after having removed the baseplate. However, the total error is reliant on the specific environment that the instrument is in. Due to the complexity of this comparison between the BelliColombo and MAGEOS, an accurate estimation is unfeasible to be made. Instead, a conservative estimation must be made, therefore the accuracy is expected to be lower by 20%.

The three accelerometers must be aligned in such a way that each accelerometer measures the acceleration in a different axis. Each accelerometer has a dimension of 80 X 60 X 25 [mm], and the electronic component needed for the assembly takes up 90 X 90 X 15 [mm]. All four of these components can be arranged in a fashion to take up 1 U. In this configuration, one accelerometer exceeds the dimensions of the cube by 5 [mm]. This is deemed to be acceptable, as 6.5 [mm] of space is kept available on the outside of the unit to accommodate wiring and electronics. Only a small volume in this extra space is used up, and so this should not pose a problem. In addition, space may be available in one of the adjacent units, which could accommodate the extra space needed for the accelerometers. Due to the way the accelerometers are arranged, a space of 85 X 65 X 65 [mm] is left vacant, which can be used

to accommodate other components.

4.3.4. SLR

Satellite laser ranging (SLR) is a system that can determine the range between a terrestrial laser and a retroreflective mirror on a spacecraft. Through analysis of the returning signal, the range, and even attitude, of the spacecraft can be calculated. The application of SLR within MAGEOS is to increase the accuracy of the GPS position estimation through calibration. While GPS has near global coverage, the most universal SLR system is that of the ILSR [35], which has ground stations spread unevenly around the world.

4.3.4.1. SLR Accuracy

SLR can provide distance measurements in the order of centimeters for spacecraft in LEO. This is done by rapidly emitting very short laser pulses in the order of 100 picoseconds, which results in pulses of roughly 3 [mm] in length [36]. There also exists SLR systems that fire shorter pulses at a higher rate. The time of flight of the pulses is measured, through which the distance can be determined. The speed of light through a vacuum is a known constant, however, through the atmosphere light travels a bit slower. The relative permittivity of air is slightly larger than 1 and independent of temperature [37, 38], this will cause a maximum error of 10^{-7} [s] on a single measurement. The error should be reduced since it will cause an error in the order of meters on the distance calculation. Therefore it needs to be accounted for in the calculation for the precise orbit determination.

Not only will the atmosphere cause the speed of light to be lower it also will refract the light. The error increases when the spacecraft is near the horizon. The spacecraft appears to be at a higher elevation than it actually is (Figure 4.22). This is due to the decreasing density of the atmosphere. Due to the refraction, the path taken by the light is also longer. This error can be up to ten meters at an elevation of 10° [39].

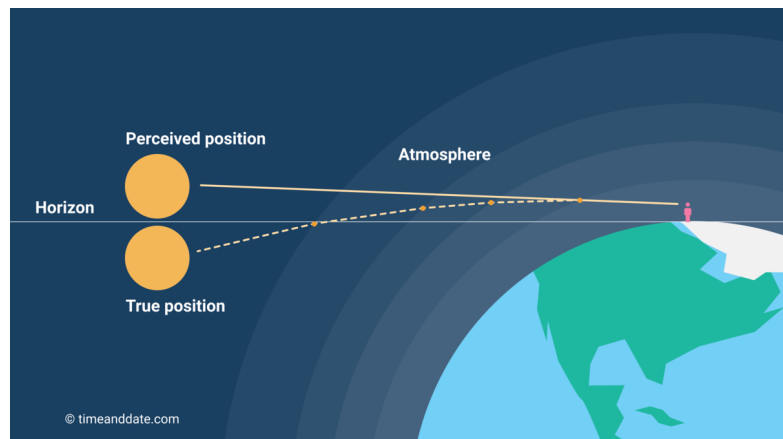


Figure 4.22: Refraction principle of the atmosphere [40]

Due to the low altitude of MAGEOS, it passes quickly over a ground station. Therefore the use of a low elevation angle is necessary to gather the required data for precise orbit determination. This can be achieved by implementing correcting models, the standard model used for SLR is the Marini-Murray model [41]. This model is accurate at elevations down to 10° . Later on Mendez and Pavlis developed a model which takes into account not only vertical but also horizontal gradients [42]. This makes it accurate all the way down to 3° of elevation.

Finally there are errors caused by atmospheric turbulence, this will cause disparities in the optical path length of the laser. When the turbulence is low/moderate, these errors remain small and negligible. However, for strong turbulence the errors can increase enough where they start to play a role in the final measurement. Luckily, strong turbulence does not occur frequently and by carefully monitoring the meteorological conditions, it can be avoided [43]. To conclude SLR can only provide accuracy in the order of centimeters if all of the above is taken into account, therefore the required computational power for the mission should include all these extensive calculations.

4.3.4.2. Retroreflector sizing

For the sizing of the retroreflector the link budget needs to be determined, next to that is the maximum angle of incidence of the retroreflector important. Since it needs to operate at at low elevation angles. The power received back on earth needs to be above a certain threshold in order for the detector to make a measurement, this is expressed in the effective cross section. the worst case scenario is at a low elevation angle, since the effective cross section is then at it smallest and the distance at its maximum. So this is what the reflector is designed for.

The SLR link budget equation is extensive and complicated, which has too many unknowns to use at the moment, since it takes into account all efficiencies, telescope area beam divergence, pointing error and jitter, atmospheric transmission [44, 45]. However, the relationship of the variables is important and with this it is possible to size the retroreflector down to use onboard MAGEOS. The number of photoelectrons (N_{pe}) recorded by the SLR detector scales with R^{-4} , where R is the slant range between the SLR ground station and the spacecraft, σ is the spacecraft optical cross-section as can be seen in Equation 4.36. This works in favor of MAGEOS since it orbits at a low altitude so therefore the retroreflector can decrease in size greatly. The optical cross-section of a corner cube σ_{cc} (Equation 4.37) is dependent on the reflectivity, ρ , the aperture of the corner cube, A_{cc} and the effective solid angle (a measure of field-of-view), Ω . This can be rewritten in terms of the cube diameter, D , and wavelength, λ . For the commonly used retroreflectors (38 [mm] diameter), the physical cross-section is 0.001 [m²], while the optical cross-section is 10 orders of magnitude larger, namely $5.3 \cdot 10^7$ [m²]. These two equations ensure us that the retroreflectors can be very small and do not constrain the mass and volume budgets significantly.

$$N_{pe} \propto \frac{\sigma}{R^4} \quad (4.36) \quad \sigma_{cc} = \rho A_{cc} \left(\frac{4\pi}{\Omega} \right) = \frac{\pi^3 \rho D^4}{4\lambda^2} \quad (4.37)$$

Next the maximum angle of incidence is taken into account, since it plays a significant role in the design of the retroreflector. Due to MAGEOS extremely low earth orbit, the angle of incidence is large at low angles of elevation. The 2 main design concepts are shown in Figure 4.23, firstly, a pyramidal design with 4 corner cube reflectors and secondly, an entire ring of 8 corner cube reflectors in a ring and one in the middle, the latter was is more suitable for low elevations, but also an increase in mass and costs.

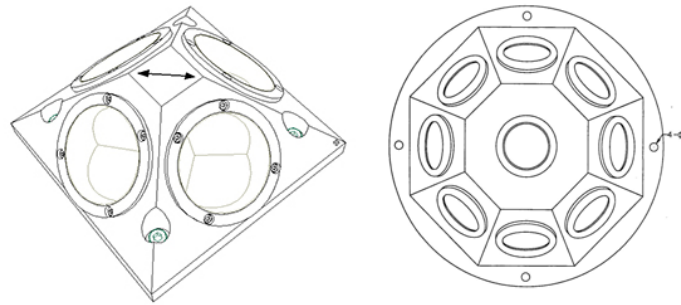


Figure 4.23: The 2 design concepts of the retroreflector, on the left a pyramidal design with 4 corner cube reflectors and on the right an entire ring of 8 corner cube reflectors in a ring and one in the middle. (Size not to scale)

In order to make a fair trade-off between the two concepts, a ground station visibility simulation is performed using GMAT [46]. The ground stations of the International Laser Ranging Service [47] were imported and 3 different angles of elevation were examined, namely, 15, 20 and 37 [deg]. First order calculations show that the pyramidal design can only function properly up to roughly 37 [deg] of elevation. Whilst the ring design is a bit more flexible and can go below 20 [deg] The contact time increases with a factor of 4 when going from a minimum elevation angle of 37 [deg] to 20 [deg]. If it is further reduced

to 15 [deg], a factor of 6 is achieved, however, this is hard to achieve and too little of an improvement over 20 [deg] to be worth pursuing. Furthermore, the longest time gap between two ground stations would be less than 4 hours for an elevation of 20 [deg], whilst for 37 [deg] it would be over 5 hours. This makes the ring design more favorable, since the contact time per ground station is already very short and this increase in contact time would greatly benefit the precise orbit determination. Combining all of the above, the ring design is chosen and will be tailored to the requirements of MAGEOS.

With an elevation angle of 20 [deg] selected, the maximum angle of incidence can be determined. This is shown in Figure 4.24, the darkened area corresponds to the operating window of the retroreflector. The intersection at an elevation of 20 [deg] corresponds to an maximum angle of incidence of 64 [deg]. This will be a driving requirement for the sizing of the retroreflector. Since a high incidence angle is required, fused silica retroreflectors are selected over their hollow counter part. Fused silica retroreflectors have significantly better performance at high angles of incidence, as can be seen in Figure 4.25. Furthermore, there are uncoated and backside-coated retroreflectors, with a reflectivity of 0.93 and 0.78 respectively. For the MAGEOS mission the uncoated retro reflector, with the lower reflectivity, is selected. The main reason being that it is not sensitive to polarization, which can reduce the effective cross section by a factor of 4. Therefore the lower efficiency massively outweighs the reduced effective cross section. Both technologies have a TRL of 9.

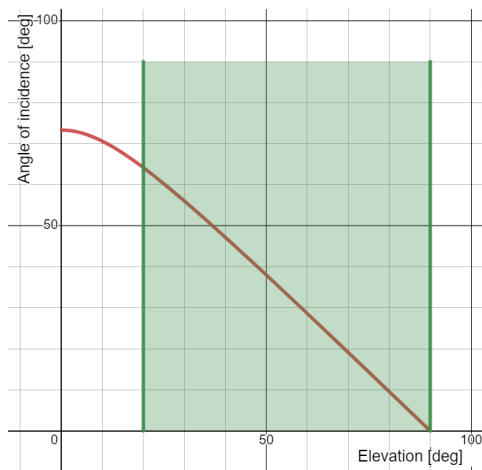


Figure 4.24: Angle of incidence vs elevation, the darkened area corresponds to the operating window of the retroreflector.

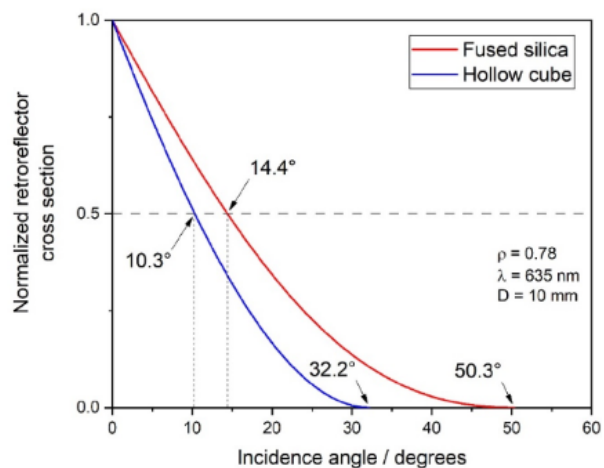


Figure 4.25: Normalized cross-section vs incidence angle for hollow and fused silica retroreflectors [48].

A retroreflector only returns the light back perfectly when it is stationary. If there is a relative velocity between the laser or the retroreflector a phenomenon named velocity aberration comes into play. This will cause the laser beam to be angularly deflected by an maximum amount of $\alpha_{max} = 2v/c$. The deflection increases with velocity which will impose a small problem for MAGEOS due to its high orbital speed. However, this effect can be mitigated by offsetting one of the cube's face angles by a small amount, in the order of arcseconds, this process is called 'spoiling'. This will cause the main lobe of the retroreflector to be slightly angled, compensating for the velocity aberration. A first order estimate can be made using Equation 4.38, if this inequality is satisfied, the signal is reduced by half (or even more) due to velocity aberration [49]. This is the case for MAGEOS, therefore 'spoiling' of the corner cube is required. Equation 4.39 [50] shows the relationship between velocity aberration and angle of incidence, this shows that the maximum velocity aberration happens at $\theta = 0$. The tangential velocity component is responsible for the aberration and therefore it drops off at lower angles of elevation. Fortunately, the angle of incidence is almost never equal to 0, since this requires very specific conditions e.g., the spacecraft perfectly overflying the SLR groundstation.

$$D_{cc} > D_{1/2} = \frac{0.8\lambda c}{\pi v} \quad (4.38) \quad \alpha = \theta - \arctan\left(\frac{c \sin \theta - 2v}{c \cos \theta}\right) \quad (4.39)$$

By looking at previous mission with retroreflectors onboard an estimate can be made for the sizing of the retroreflector. Astrocass CubeSat orbiting at 575 km altitude required 50,000 [m²] effective optical cross section with the use of 10 mm corner cube reflectors [51]. Shanghai Astronomical Observatory designed a mission with retroreflector for altitudes between 300 and 500 [km], they required a minimum effective reflection area of 1.05 [cm²] with the use of 13.6 mm corner cube reflectors [52]. These values will be used to estimate the required area at 230 [km] altitude, this results in a diameter in the range of 5.33 to 5.91 [mm] using Equation 4.36. This will be used in the calculation as the performance at worst conditions i.e. at the highest angle of incidence. The previously determined maximum angle of incidence: 64 [deg] and the selection of the ring design, make for a maximum angle of incidence 21.3 [deg]. At this angle of incidence the normalized effective cross section, σ_{cc} , is 0.3151 using Equation 4.40, 4.41 and 4.42 [48]. With the angle of incidence θ_{inc} and the refractive index, n , of fused silica being 1.457 [53].

$$\sigma_{cc}(\theta_{inc}) = \left[\frac{2}{\pi} \left(\arcsin(\mu) - \sqrt{2} \tan(\theta_{ref}) \right) \cos(\theta_{inc}) \right]^2 \quad (4.40)$$

$$\theta_{ref} = \arcsin\left(\frac{\sin(\theta_{inc})}{n}\right) \quad (4.41) \quad \mu = \sqrt{1 - (\tan(\theta_{ref}))^2} \quad (4.42)$$

This results in a diameter in the range of 7.12 to 7.89 [mm]. Off the shelf corner cube reflectors cost in the range of €129 - €218 [54–56], the cheaper ones come without a individual housing, therefore a cost estimate of €200 is used. With the ring design a total of 9 corner cubes are used, which makes it €1800. The 9 corner cubes also need a housing to orient them the correct way, this is estimated to increase the costs by 25% [52], which increases the total costs to €2250. However, the main costs of the SLR will be the operating costs of the groundstations. The International Laser Ranging Service does not publicly share the costs of their service and can only be known when signing a contract with them. Therefore the costs are estimated to be around US\$100,000, based on the AWS groundstations costs [57]. The mass estimation of the retroreflector array is roughly 20 to 70 [g] [52, 58], mainly dependant on the housing material selected.

In Figure 4.26 a ground station visibility summary is presented for the final design of the retro reflector. The contact times per groundstation are short, due to its low altitude and high velocity. However, due to the large number of groundstations available, the intervals between two groundstation are acceptable. There is also not a particular groundstation that under performs compared to the rest. Due to the cluster of groundstations in europe, and northern hemisphere in general, most data is accumulated over there. The SLR measurements in the northern hemisphere will have a better local orbit fit, resulting in a better accuracy over there.

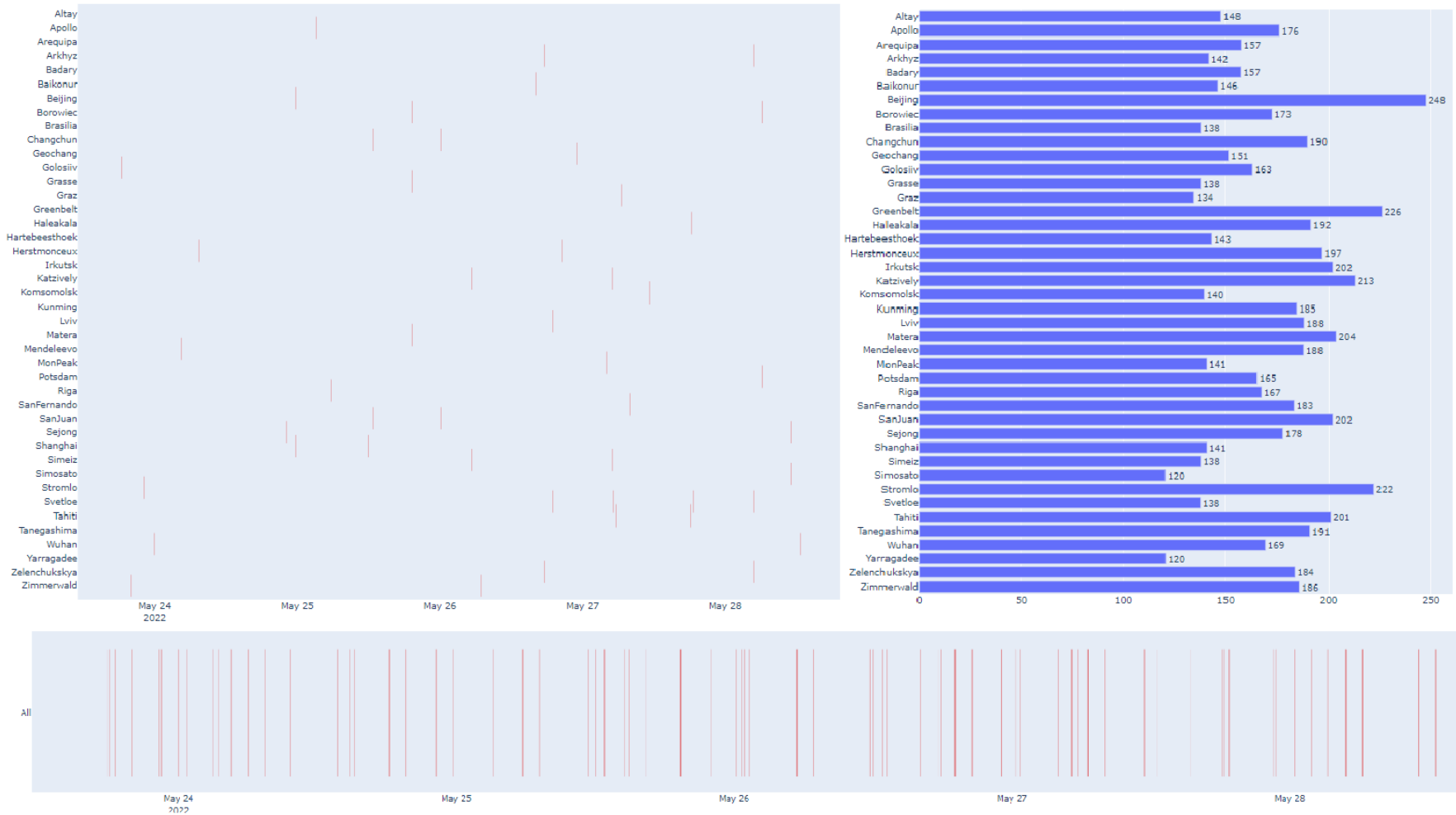


Figure 4.26: SLR ground stations visibility summary for an average arbitrary period of 5 days with a elevation of 20 [deg]. Top left shows the contact times per ground station. Top right shows the total contact duration per groundstation. Bottom figure shows the contact times of all groundstations combined.

Chapter 5: Orbit Design

An orbit can be defined by its six Keplerian elements. These six elements are the semi-major axis a , eccentricity e , argument of perigee ω , inclination i , longitude of the ascending node Ω (which can also be expressed as local time of the ascending node, when measured relative to the Earth), and true anomaly θ . In [1], an initial estimation of some of these elements was performed for a single spacecraft by evaluating their impact on ten critical trade-off criteria. It was found that an Earth repeat orbit with a repeat period of 30 [days], a semi-major axis of $a \in [200, 300]$ [km], and an inclination of $i \in [80, 100]$ [°] was optimal. A summary of the conclusions presented in [1] is shown in Table 5.1.

Table 5.1: Orbital parameters as determined in [1]

Parameter	Value
Semi-major axis	6571km - 6671km
Eccentricity	0
Argument of Perigee	Undefined for circular orbits
Inclination	80° - 100°
Longitude of the Ascending Node	No preference (Determined by launch parameters)

In this chapter, the conclusions reached in [1] will be further developed to finalise the design of the orbits for both MAGEOS spacecraft. A payload-centric approach is used to optimise the performance of the instruments while minimising the mission cost. The position of the magnetic poles is considered in Section 5.1, the impact of inclination on GNSS performance is considered in Section 5.2, and the effect on the ground speed is analysed in Section 5.3. Launcher availability, which is crucial to reduce the ΔV for the initial orbital correction, is analysed in Section 5.4, and the advantages of sun-synchronous and Earth repeat orbits are shown in Section 5.5 and Section 5.6 respectively.

5.1. Magnetic Poles

During the orbit design process, the location of the north and south magnetic poles have to be investigated since one of the main mission objectives of MAGEOS is to measure the magnetic field of Earth, which is the strongest at the magnetic poles. In 2020, the magnetic north pole was located at a latitude of $86.5^\circ N$ and the magnetic south pole at a latitude of $64.07^\circ S$ [59]. However, the poles are changing position over time, which can be seen in Figure 5.1 for the magnetic north pole. The inclination range of in Table 5.1 provides almost full Earth coverage, with the magnetic south pole well within the latitude boundaries, as can be seen in Figure 5.2. Consequently, the magnetic north pole location is the limiting factor for the inclination choice. Since the maximum latitude that can be imaged is equal to the inclination of the orbit, the inclination is required to be high enough to reach the magnetic north pole. Furthermore, the symmetry property of inclination for latitude (hence pole) coverage shall be addressed. An inclination of e.g. 85° vs 95° is equivalent in terms of latitude coverage, except for ground speed differences, as treated in Section 5.3. Moreover, due to the uncertainty in the exact location of the north pole during the mission lifetime, the inclination interval of $i \in [80, 100]^\circ$ can be further reduced to $i \in [82, 88] \cup [92, 98]^\circ$.

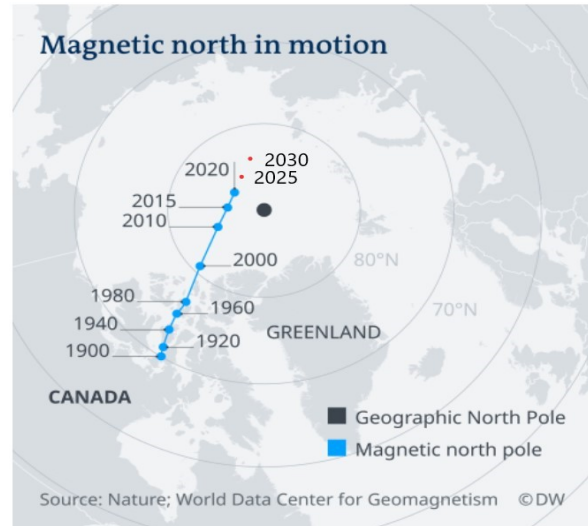


Figure 5.1: Historical magnetic north pole location in blue and an example of the forecasted shift in red. [60]

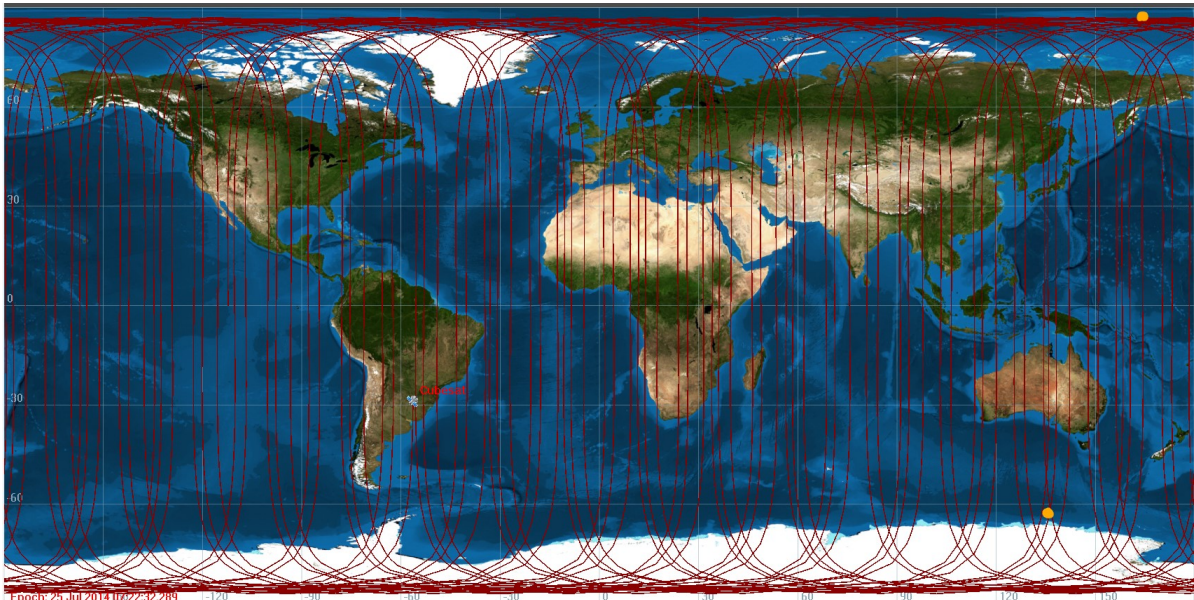


Figure 5.2: Example of ground track for an inclination of 87° with the magnetic poles shown in orange.

5.2. GNSS Performance

For a gravimetry mission, the total acceleration as obtained from GNSS, which includes GPS, is subtracted by the acceleration as measured by the accelerometer. It is therefore imperative that the quality of the GNSS receiver is as high as possible, as this will result in a higher gravimetry accuracy. There are several factors that reduce the GPS accuracy. For Earth orbiting S/C, in contrast to Earth receivers, most of these are either irrelevant or negligible, but the ionospheric delay remains as a significant factor [61]. By using a dual-frequency receiver, which is included in the chosen OrbFix GPS, this effect can be largely negated [61].

An important metric for GNSS performance is the geometric dilution of precision (GDOP) factor. Besides the error factors previously mentioned, the GNSS performance varies with latitude, as above a latitude of $\pm 55^\circ$, no GPS satellite is ever directly overhead. This effect can be observed in Figure 5.3, where the GDOP degrades starting at a latitude of 55° and deteriorating further at even higher latitudes. However, as can be seen in Figure 5.4, the time spent at latitudes higher than 55° is relatively short, 39% for a perfect polar orbit. During this period, the average increase in GDOP is $\leq 5.8\%$ compared to lower latitudes. Over an entire polar orbit the GDOP is then only about 2.3% higher, which is considered to be acceptable because the MAGEOS mission inherently needs a (near-) polar orbit to measure the magnetic north pole.

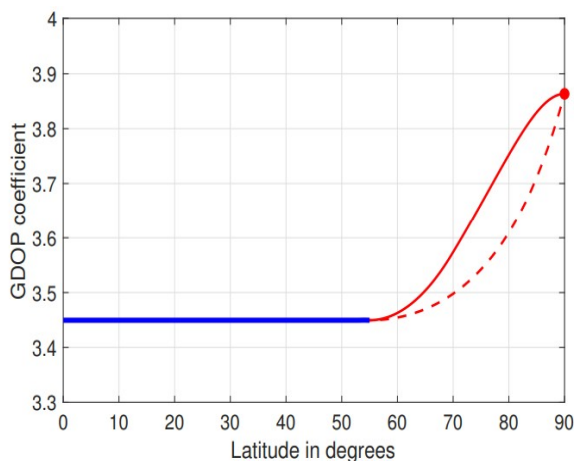


Figure 5.3: Example GDOP vs latitude from [62] showing degradation of GDOP (higher is worse) with increasing latitude

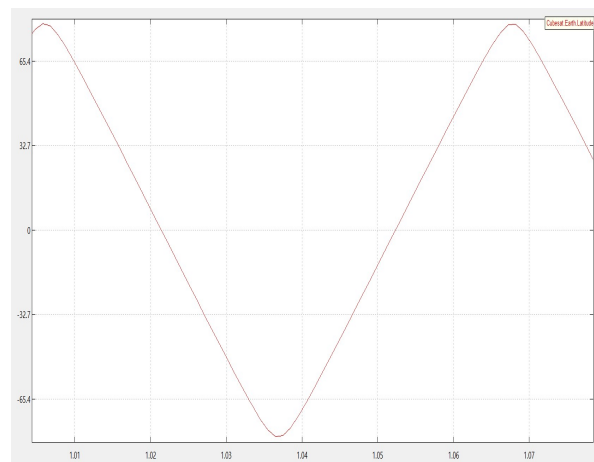


Figure 5.4: Example of a simulated orbit with $i = 80^\circ$ and $h = 250$ [km] showing latitude on y-axis and elapsed days on x-axis

Considering the above, the near-polar Earth observation mission will have a slightly worse GNSS performance near the poles. Therefore, the gravitational map near the poles shall be calibrated with other models which preferably also include models not based on the GPS measurement for gravimetry (i.e. GRACE).

5.3. Ground Speed

The ground speed of a spacecraft, which is measured relative to the Earth's surface, differs with the inclination of the orbit. It is desirable for the MAGEOS mission to collect measurements as closely in space as possible, so minimising ground speed is crucial. In Figure 5.5, the relative ground velocity for an orbit with $i = 80^\circ$ and an orbit with $i = 100^\circ$ is shown alongside the absolute velocity of the spacecraft. It can be concluded that the differences in ground velocity are negligible, in the order of 2%, and therefore it is not an important consideration in the orbit design process.

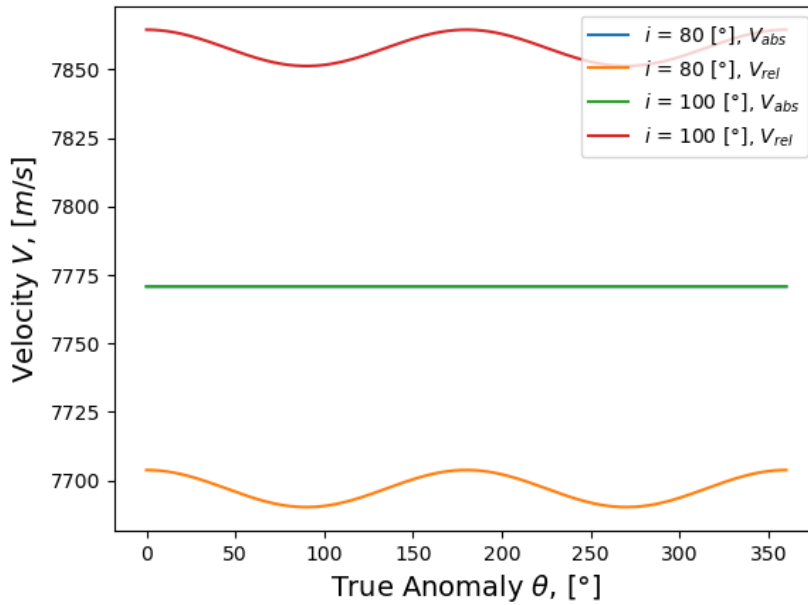


Figure 5.5: Relative velocity over an orbit with $i = 80^\circ$ and $i = 100^\circ$, both at $h = 230$ [km].

5.4. Available Launchers

To achieve the target cost of 5.0 [M\$], as set in requirement *CON-RES-1* [1], a rideshare mission must be used. This is due to the fact that the cost of an entire launcher is outside of the budget for the MAGEOS mission, so the cost is shared between many customers. A consequence of this is that the orbit MAGEOS is inserted into cannot be precisely specified to fit the desired orbit, and is chosen by the launch provider to maximise the satisfaction of the many customers on the launch.

The goal of MAGEOS is to launch in 2028 [1], so there is a limited number of rideshare missions available. As the ΔV requirements for maneuvering in orbit are costly, specifically for inclination changes, the final MAGEOS orbit must be selected such that it is close to the insertion orbit while still fulfilling the mission requirements.

In order to determine the most commonly used orbits, the satellite database compiled by the Union of Concerned Scientists was used [63]. This database contains the orbital parameters of thousands of satellites launched since 1974, and encompasses spacecraft in LEO, MEO, GEO, and highly elliptical orbits. Filtering needs to be performed to remove the spacecraft not in LEO, to exclude the spacecraft not in the considered ranges for a and i , and to ensure that only a single spacecraft per launch is considered. While the final orbits of the spacecraft in the database do not necessarily match-up with the orbits after orbital insertion by the launch provider, this was assumed to be the case in this analysis, as most maneuvers are prohibitively expensive for missions, particularly CubeSat missions.

The histograms for the altitude h and inclination i of the filtered data set are shown in Figure 5.6 and Figure 5.7 respectively. It can be deduced that the most common launch altitudes are $h \in [450, 850]$ [km], and that the most common launch inclinations are $i \in [97, 99]$ [°]. The initial launch parameters are therefore chosen to be $h = 600$ [km], and $i = 98^\circ$, as those values were found to be a good representation of the average orbit after orbital insertion. The longitude of the ascending node requirements are set and described in Section 5.5.

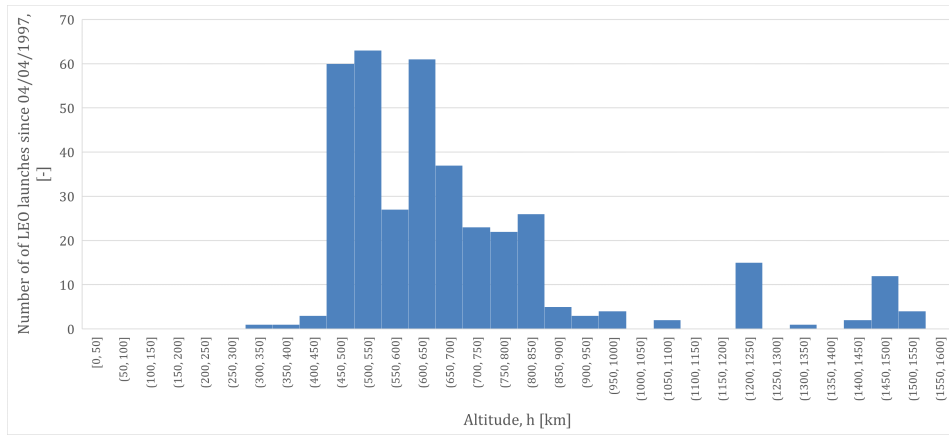


Figure 5.6: Histogram of LEO launch altitudes [63].

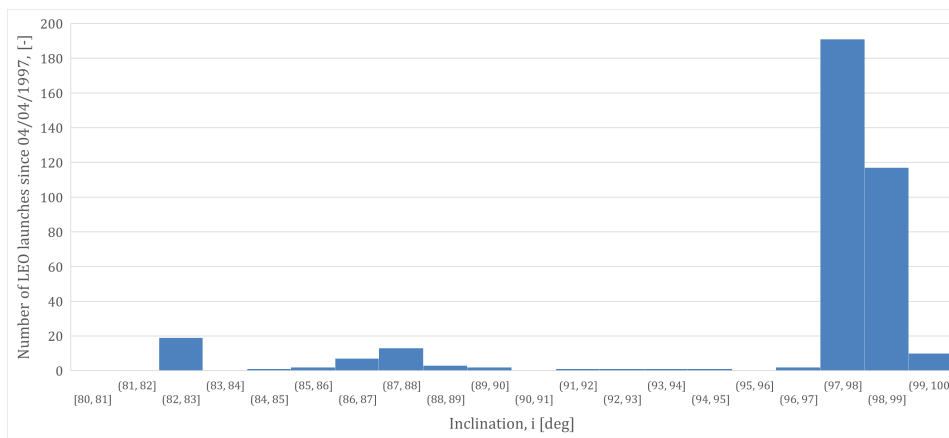


Figure 5.7: Histogram of LEO launch inclinations [63].

5.5. Sun-synchronous Orbit

The need for a Sun-synchronous orbit stems from the geometry of the spacecraft, i.e. only solar panels on one side of the S/C. To characterise the orientation of the spacecraft while in orbit, which is closely related to the geometry of the S/C, an axis system for the spacecraft must be defined.

Three principal axis for the spacecraft can be identified: Firstly, the *tangential axis* (in red) is defined as the axis parallel to the velocity vector. The *normal axis* (in blue) is defined as the axis perpendicular to the orbital plane, and the *radial axis* (in green) is defined as the axis that completes the orthogonal axis system. A diagram of the MAGEOS spacecraft alongside the axis system defined can be observed in Figure 5.8.

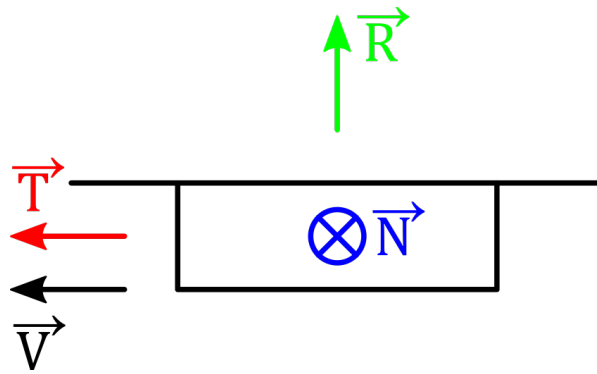


Figure 5.8: Axis system of MAGEOS mission.

To minimise the drag force experienced by the spacecraft, to ensure that the thrust force is aligned with the velocity vector, and to minimise other disturbances acting on the vehicle, the forward-aft axis of the spacecraft must be aligned with the *tangential axis*. Furthermore, to ensure that the direction of the angular momentum of the momentum wheel can remain constant throughout an entire orbit (therefore not requiring a constant torque acting on it to change its direction), the momentum wheel rotation axis must be aligned with the *normal axis*, which is perpendicular to the orbital plane and thus is only affected by the precession of the orbit, a much slower rotation. Consequently, the solar panels must always point in the *radial axis* direction of the orbit, the remaining orthogonal direction of the axis system.

By considering these constraints, it becomes apparent why a Sun-synchronous orbit is necessary. A Sun-synchronous orbit ensures that the orientation of the orbital plane relative to the Sun remains constant. By carefully selecting the LTAN to be either 12AM or 12PM, the total energy generated by the spacecraft over an entire orbit is maximised. If a LTAN of 6AM or 6PM would have been selected, the spacecraft would be constantly illuminated, however the orientation of the solar arrays would lead to no power generation, as their incidence angle would be 90 [°], as can be seen in Figure 7.7.

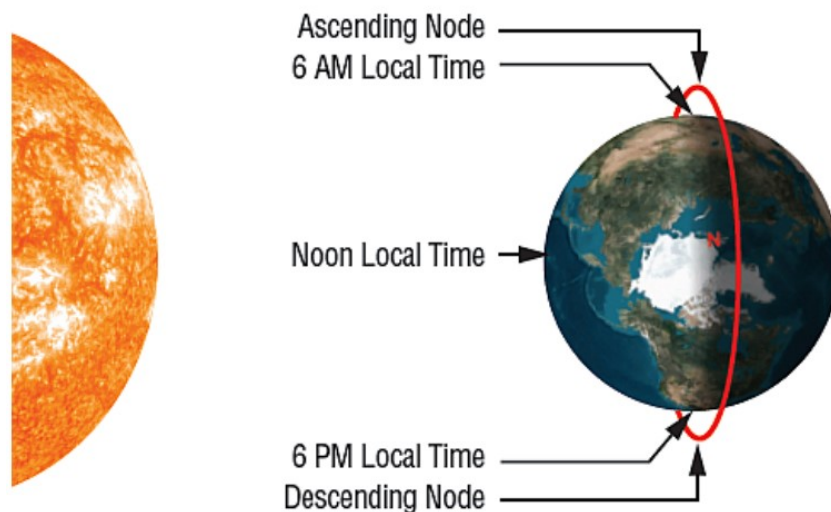


Figure 5.9: LTAN of 6AM, resulting in constant illumination, but no power generation for radially-pointed solar panels [64].

A Sun-synchronous orbit can be designed with Equation 5.1, which entails a relationship between the semi-major axis a , eccentricity e , and inclination i of the orbit. The precession of the orbital plane is caused by the J_2 effect, which is due to the oblateness of the Earth. A Sun-synchronous orbit requires

the inclination to be larger than 90° , i.e. a retrograde orbit.

$$\frac{d\Omega}{dt} = -3\pi J_2 \left(\frac{R_e}{a(1-e^2)} \right)^2 \cos(i) \frac{1}{2\pi} \sqrt{\frac{\mu}{a^3}} = \frac{2\pi}{T_{ES}} \quad (5.1)$$

5.6. Earth Repeat Orbit

To achieve requirement *TECH-ASTRO-ORBIT-1*, the MAGEOS spacecraft shall be able to take measurements at a latitude of 80° . This requirement ensures that most of the Earth's magnetic and gravitational fields can be measured. A balance between the spatial resolution and temporal resolution of data points must be achieved by taking the scientific goals of the mission into account, i.e. an Earth repeat orbit has to be designed. This balance can be numerically characterised by j , the number of orbits between ground track repeats, and k , the number of days between ground track repeats.

Two effects must be considered when designing an Earth-repeat orbit. Firstly, the rotation of the Earth must be considered. Due to the time the spacecraft takes to complete an orbit, its orbital period T , the Earth rotates by an angle ΔL_1 . Secondly, the effect of the Earth's precession must be considered. Due to the time the spacecraft takes to complete an orbit, the orbital plane will precess by an angle of ΔL_2 .

The equation that quantifies these effects, and thus allows for the design on an Earth-repeat orbit, is shown in Equation 5.2. This equation must be used in conjunction with Equation 5.1 to design the desired Sun-synchronous and Earth-repeat orbit.

$$j \cdot |\Delta L_1 + \Delta L_2| = k \cdot 2\pi \quad (5.2)$$

$$\Rightarrow j \cdot \left| -2\pi \frac{2\pi \sqrt{\frac{a^3}{\mu}}}{T_E} - \frac{3\pi J_2 R_e^2 \cos(i)}{a^2(1-e^2)^2} \right| = k \cdot 2\pi$$

In [1], it was determined that the number of days between ground track repeats shall be 30 [days]. Due to the newly added constraint of a Sun-synchronous orbit, a degree of freedom is removed from the system, and the solution space is no longer continuous: only specific combinations of a and i represent valid Sun-synchronous, Earth-repeat orbits. To increase the size of the solution space, $k = 29$ and $k = 31$ [days] were also considered, as their temporal resolution is almost identical to $k = 30$. Eighteen new valid repeat cycles were introduced as a result of this relaxation of k . The restrictions imposed by an Earth-repeat orbit with $k = 29$ [days] is shown in Figure 5.10, alongside the restrictions imposed by the Sun-synchronous orbit requirement.

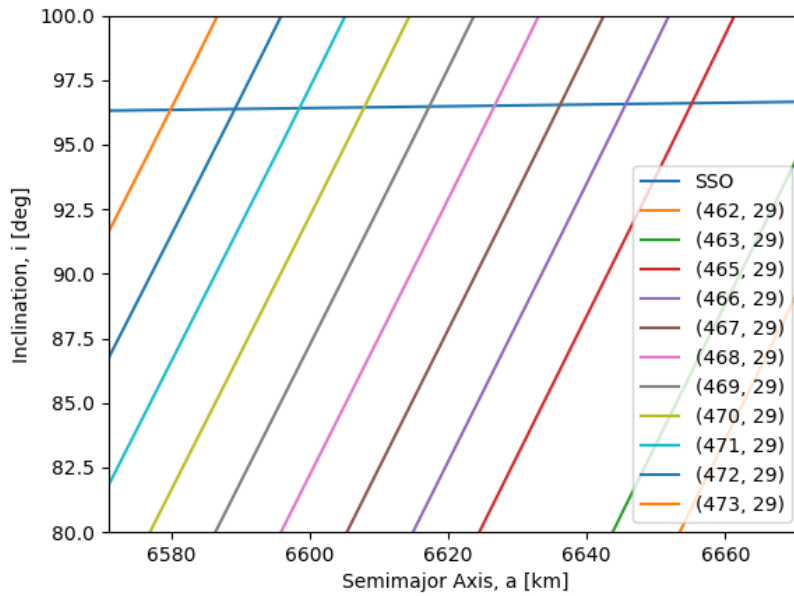


Figure 5.10: Inclination vs Semi-major axis plot. The intersection of the Sun-synchronous orbit with the Earth-repeat orbits represent valid solutions for $k = 29$ [days]. The $(j, k) = (464, 29)$ solution is excluded as it repeats prematurely (after 16 days)

Similarly to the process described in [1], combinations of j and k sharing common factors were excluded, ensuring that the ground track does not repeat prematurely. The intersections of the line labeled SSO, which enforces the Sun-synchronous orbit requirement, with the lines labeled (j, k) , which enforce the Earth-repeat requirement, represent valid combinations of a and i for the MAGEOS mission.

5.7. Orbit Selection

From the initial stakeholder requirements, an orbit below 230 [km] was required. Even though this requirement was later relaxed, the highest altitude below 230 [km] from the possible Sun-synchronous, Earth Repeat orbit options was chosen. This decision has been made based on the equations for the magnetic and gravitational field, Equation 5.3 and Equation 5.4. Specifically, the sensitivity of the two fields of interest with respect to altitude have been reported in Table 5.2. It can be seen that at an altitude of 290 [km], the field strength is only 2.7% and 4.0% lower for the gravitational field and magnetic field respectively compared to 200 [km]. Notably, this difference is relatively small. It is assumed that the local field strength can be used as a metric for the accuracy of the overall field. Concretely, in Table 5.2 the field strength at an altitude of 200 [km] is higher than at the other higher altitudes and consequently, it can safely be assumed that the accuracy of the overall field is better, since it is closer to the core of the field.

$$|B| = B_0 \cdot \left(\frac{R_E}{r}\right)^3 \cdot \sqrt{1 + 3\cos^2(\theta)} \quad (5.3)$$

$$|g| = \frac{GM_{earth}}{r^2} \quad (5.4)$$

Altitude [m]	Gravitational field strength [%]	Magnetic field strength [%]
200	100	100
230	99.1	98.6
260	98.2	97.3
290	97.3	96.0

Table 5.2: Decrease in field strength with altitude: field strength at 200 [km] altitude has been set to 100% in this idealized sensitivity test

Note that the field strength has merely been used for sensitivity purposes. However, in order to measure large gradients in e.g. gravitational field as caused by local mass deviations, shown in Figure 5.11, or in magnetic field as caused by solar wind, shown in Figure 5.12, there is a large advantage to go to a lower altitude. Although it is not trivial to give an estimate for the accuracy of the fields as a function of altitude, a lower altitude will increase the accuracy obtained monotonically.

When looking at Table 5.2 it seems like the benefits of going to an altitude lower than 230 [km] for the MAGEOS mission are relatively small (using field strength as a metric for overall field strength accuracy that can be obtained), while the drag increases exponentially [1]. Conversely, going to an altitude higher than 230 [km] has slightly lower field strengths, while the drag decreases exponentially. However, when incorporating the modelling errors caused by the idealized models used for the sensitivity analysis, it becomes apparent that MAGEOS will have significantly less error (higher accuracy) when orbiting at a lower altitude, which is larger than the error caused by just the difference in field strength at different altitude.

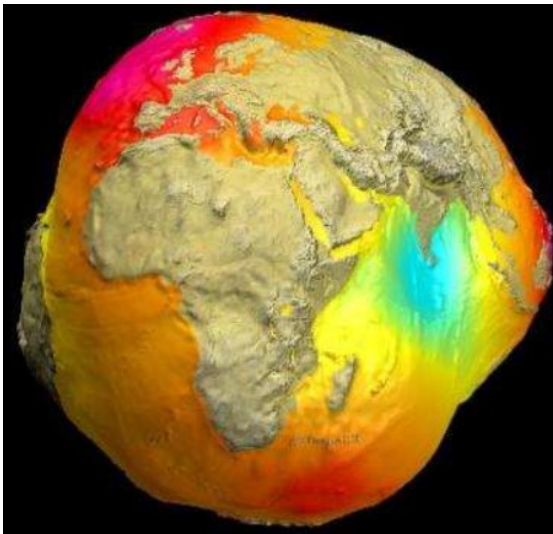


Figure 5.11: Gravity model from [65] showing large gradients in field strength on the surface. The perfect spherical model from Equation 5.4 has a gradient of 0 everywhere on the surface, introducing large modelling errors resulting in decreased accuracy.

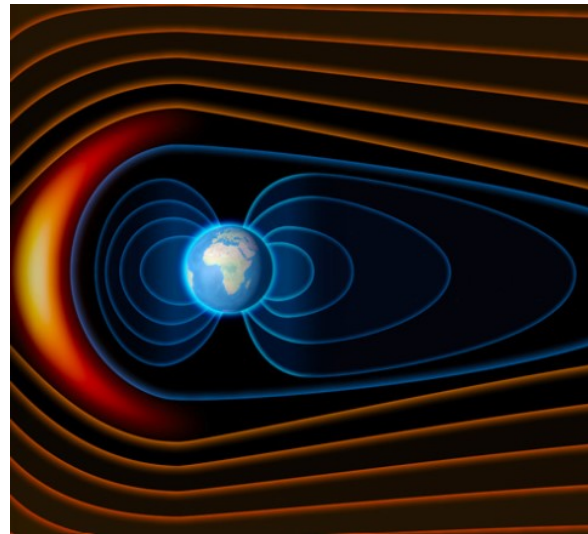


Figure 5.12: Solar wind (from the left) compresses the magnetic field' shape on Earth's Sun-facing side and stretches it into a long tail on the night-facing side [66]. The perfect dipole model from Equation 5.3 does not incorporate this, introducing large modelling errors resulting in decreased accuracy.

Considering the uncertainty in the relation between altitude and accuracy of the fields that can be obtained, an orbital altitude close to the initial stakeholder requirement of <230 [km] has been chosen. From the Concurrent Engineering approach within the team, it was known that the other subsystems could be designed to maintain that orbital altitude. The possible Sun-synchronous, Earth repeat orbit options below 230 [km] are shown in Table 5.3.

Table 5.3: Sun-synchronous, Earth Repeat Orbits with $h \leq 230$ [km]

Repeat Cycle (j,k)	h [km]	i [°]
(471, 29)	227.5	96.40
(472, 29)	218.2	96.38
(473, 29)	208.9	96.34
(487, 30)	229.7	96.42
(504, 31)	223.0	96.39
(505, 31)	214.3	96.37

The highest altitude, but below 230 [km] from the options is the fourth option in the table, i.e. the orbit with a repeat cycle of (487, 30), 229.7 [km] altitude and 96.42° inclination. The orbital altitude of 229.7 [km] is achieved at an orbital velocity of 7.77 [km/s] and an orbital period of 5336.985 [s]. Note that out of the options remaining, the inclination is nearly identical while the orbital altitude differs by only tens of kilometers. This increases the confidence that the orbits remaining below 230 [km] are all comparable and that a (sub-) optimal orbit has been chosen compliant to be Sun-synchronous earth repeating.

5.8. Constellation Selection

In [1] it was decided that MAGEOS will consist of 2 CubeSats in an in-line constellation Figure 5.13, in the same orbital plane at approximately the same ground track. The latter will allow to compare datapoints of the 2 Cubesats at close proximity, providing calibration yielding more accurate data for the measured fields. The parameter to tune for the constellation selection is the separation between the two CubeSats. Since the 2 CubeSats need to compare datapoints in the spatial domain at close proximity, the spacing is determined by the frequencies of the instruments in combination with the orbital velocity. Specifically, the CubeSats need to be separated such that when the second S/C passes the orbital position of the first S/C it has performed an integer number of measurements. The frequency of the main instruments of the MAGEOS mission is shown in Table 5.4. It can be seen that the frequency of the magnetometer is larger than the GPS. Therefore, the GPS frequency is the limiting factor for determining the separation. Furthermore, the frequency of the magnetometer is exactly an integer number larger than the GPS, meaning that the gravitational and magnetic data samples align after each period of the GPS.

Table 5.4: Measurement frequency of the instruments on MAGEOS

Instrument	Measurement frequency [Hz]
GPS [67]	10
Magnetometer	160

Moreover, exploring the option of using the RTK technique for improved position accuracy, the 2 CubeSats have to be separated at a distance of at most 20 [km] [31]. For collision avoidance and exhaust plume interference of the front S/C on the second S/C, it is preferred to have the separation as large as possible. Hence, the largest separation below 20 [km] was chosen. The largest integer number of GPS samples that can be fitted inside 20 [km] is 25, resulting in a separation of 19.425 [km] between the 2 CubeSats corresponding to a time difference of 2.5 [s] Figure 5.14.

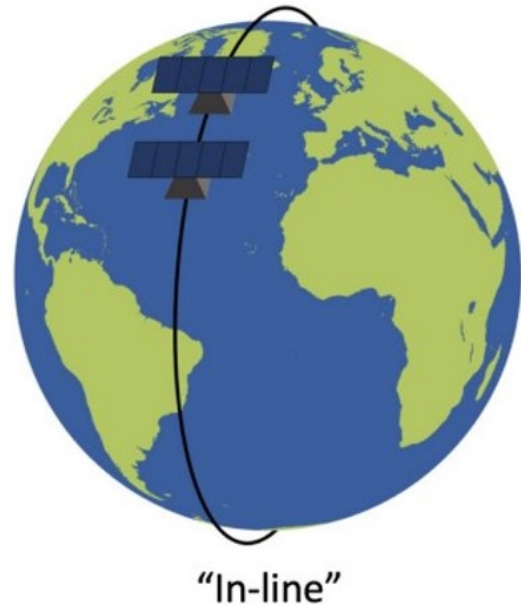


Figure 5.13: In-line constellation [68] used for MAGEOS

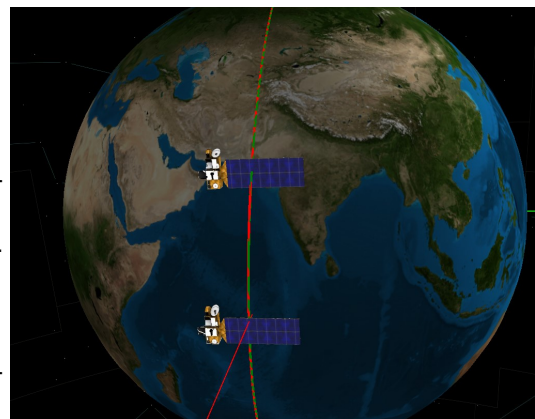


Figure 5.14: Two CubeSats of MAGEOS spaced at 19.425 [km] corresponding to 2.5 [s]

Chapter 6: Architecture Design

6.1. Structure & Mechanisms

The structure must support and protect subsystems on the spacecraft. It must withstand loads during launch and in orbit, and provide sufficient mounts for all spacecraft components. Additionally, it may shield components of the spacecraft from radiation, and provide some passive thermal control. The structure must be compatible with the mechanisms on the spacecraft, including both the magnetometer boom and solar panel deployment systems. The requirements that the structure must adhere to are listed in Table 6.1.

Table 6.1: The Structural requirements of MAGEOS [1]

Identifier K=Key, D=Driving, R=Removed	Requirement	V&V Method
TECH-STRUC-1	The spacecraft structural integrity shall not be compromised by radical particles	Analysis
TECH-STRUC-3	No components in the spacecraft structure shall cold weld during the entire mission	Analysis
TECH-STRUC-4	The spacecraft structure shall provide mountability for all spacecraft systems	Inspection

During the midterm [1], the concept chosen for the structure was a modular structure, because its main benefits are its low mass and high adaptability. For the design process, the modular units from Endurosat were used as a basis for any further configuration and calculation. Figure 6.1 and Figure 6.2 showcases the 1U and 3U version.

Each unit type has its own advantages and disadvantages. The 1 U has the dimensions of 100 x 100 x 113.5 [mm]. The extra space on top and on the bottom is to provide any electrical wiring. Furthermore, the extrusions are used to connect with other units if required. The components within the unit can be mounted using four slots in each corner as can be seen in Figure 6.1. All sides of the unit are open. Components like solar panels or other units can be mounted on these sides to provide shielding and functionality instead of having plates.

The biggest disadvantage of the 1U type is that if a component is larger than 1U, it can not fit inside the allocated space for 1U, even if the two units are assembled next to each other. This is the main advantage of the 3U modular unit. As can be seen in Figure 6.2, the barriers which are present in the stacked 1U are not present. This creates opportunities for larger components. The two different type of structures thus offer different capabilities. The dimensions of the 3U is 100 x 100 x 340.5 [mm].

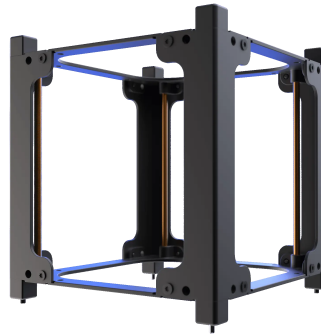


Figure 6.1: Endurosat's 1U modular structure



Figure 6.2: Endurosat's 3U modular structure

6.1.1. Boom Structure

MAGEOS requires a 2 meter boom for the magnetic field measurements as detailed in Section 4.2. This boom utilises a telescopic design of concentric rings. The material chosen was a carbon fibre laminate, chosen for its low density of $1900 \frac{kg}{m^3}$ and excellent structural properties. The boom system including mounted instruments must be stored in 4 units to allow sufficient space for the remaining components. Halfway along the boom is a structure consisting of two star sensors and a magnetometer and at the end of the boom is the second magnetometer. The boom consists of two telescopic sections to accommodate this. The instruments on the boom require a total of 25 [cm] when stored. The two boom segments must therefore have a stowed length of at most 6.1 [cm], leaving 2.8 [cm] for structure.

The full structural design of a carbon fibre boom was beyond the scope of this mission, therefore the MAGEOS boom has been based upon an existing design. The reference design for this boom is the Oxford Space Systems 'AstroTube' carbon fibre telescopic boom [69]. This design utilises carbon fibre segments of 0.3 [mm] thickness. The MAGEOS boom uses 0.5 [mm] thickness segments to improve stiffness and is therefore slightly overdesigned. The boom consists of two sections of telescopic boom. Each section of boom must be 89 [cm] to achieve the desired final length. The number of segments per boom used is 15. Given these values, the initial and final boom radii can be defined. The final segment radius is constraining, as it must be large enough that there is sufficient internal space for electronics, and sufficiently large to remain stiff and stable. Wires used aboard spacecraft typically have diameters not in excess of 5 [mm] [70]. The final segment internal radius was chosen to be 10.5 [mm] to allow the accommodation of multiple wires and to keep sufficiently high moment of inertia such that stiffness remains high. A technical drawing of the finalised telescopic boom section can be seen in Figure 6.3. The total mass of each boom segment was then calculated to be 75.24 [g] using the volumes of each segment and the aforementioned density of the carbon fibre laminate used.

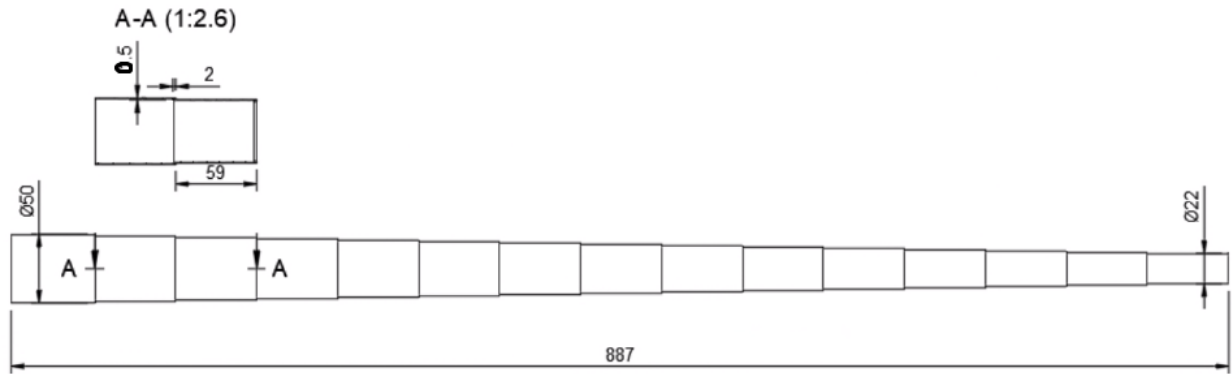


Figure 6.3: Boom technical drawing.

Two of these boom segments are used for the total boom. The total mass due to structure is therefore 150.5 [g]. The first is mounted at the root on the spacecraft and at the tip to the combined star sensors and magnetometer block. The second is mounted to these instruments and ends with the second magnetometer at the tip. The final assembled boom is presented collapsed and extended in Figure 6.4 and Figure 6.5 respectively.



Figure 6.4: Final assembled boom collapsed.



Figure 6.5: Final assembled boom extended.

The MAGEOS boom has to be extended from MAGEOS itself. Due to its stowed size, it can not simply be extended from a rigid base as the boom would not extend far enough from the centre of the spacecraft. The solution that has been used is an innovative deployment mechanism. The boom is housed in four units. The lower panels of these units can rotate open, functioning as a door. Although this weakens the structure, the time that the doors are opened is short, since the doors will be closed after the boom is fully extended. Consequently, the loads during the extension phase are not of concern, compared to the steady-state loads present during the stowed phase. The boom is mounted to a plate which is able to rotate 180°, allowing the boom to extend directly from the edge of the spacecraft. In Figure 6.6 the mechanism can be seen. A low power low torque motor is used to rotate the boom connected to the plate. The torque and therefore power requirements are minimal as deployment occurs in space, a slow rotation rate is desired for reliability and deployment time is not an issue. A 3 × 3 [mm] Texas Instruments motor driver will be used [71].



Figure 6.6: Boom deployment mechanism, stowed and deployed

Once the boom has rotated through 180° , the base plate locks in place. Finally, the telescopic segments are extended until maximum length, at which point the magnetometers are sufficiently far from the spacecraft body for measurements to be taken. The fully deployed boom can be seen in Figure 6.7.

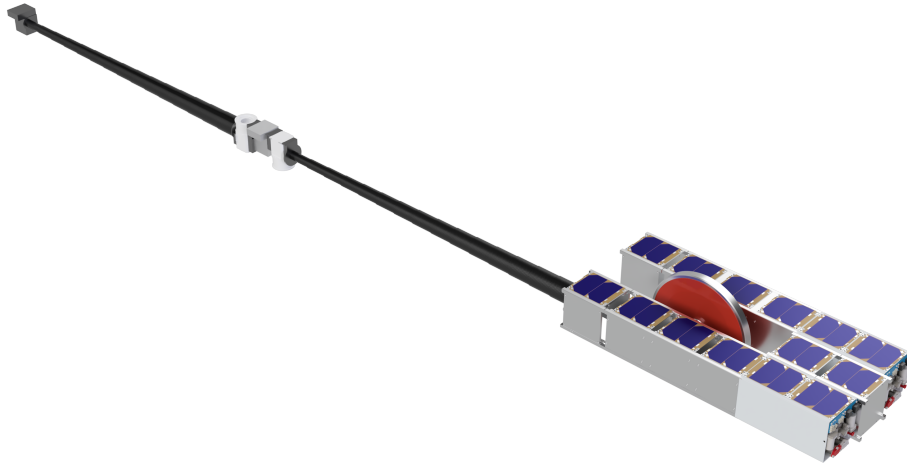


Figure 6.7: Fully extended boom.

Full structural analysis of the boom design is beyond the scope of this report, however a vibration analysis has been performed to observe how the boom responds to disturbance forces. Some assumptions were made regarding the boom. For simplicity, the boom was modelled as two rigid beams. The first fixed on one side of the spacecraft, the second fixed to the free end of the first. The mass of booms are assumed to be 0.0 [kg], two masses are placed representing the mounted instruments. Mass number one is placed at the end of boom one and weighs 1.0 [kg] (M1), the second is placed at the end of boom two and weighs 0.6 [kg] (M2). The setup described is shown in Figure 6.8.

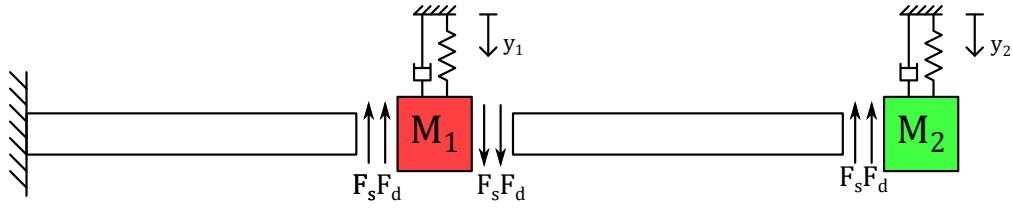


Figure 6.8: Boom Reference system

The equations of motion for M_1 and M_2 are shown in Equation 6.1 and Equation 6.2 respectively. Each beam has a stiffness k and a damping coefficient c . A disturbance force F_{ext} is applied on each mass.

$$m_1 \cdot \ddot{y}_1 = -k_1 \cdot y_1 - c_1 \cdot \dot{y}_1 + k_2 \cdot (y_2 - y_1) + c_2 \cdot (\dot{y}_2 - \dot{y}_1) + F_{ext,1} \quad (6.1)$$

$$m_2 \cdot \ddot{y}_2 = -k_2 \cdot (y_2 - y_1) - c_2 \cdot (\dot{y}_2 - \dot{y}_1) + F_{ext,2} \quad (6.2)$$

The stiffness k of each beam is determined using Equation 6.3, where E is the Young's modulus of carbon fiber, I is the moment of inertia of the average section of the beam, and L the length of the beam. The damping coefficient c of each beam is determined using Equation 6.4, where the damping ratio ζ is assumed to be 0.002 [-].

$$k = \frac{3EI}{L^3} \quad (6.3)$$

$$c = \zeta \cdot c_{crit} \Rightarrow c = \zeta \cdot 2\sqrt{km} \quad (6.4)$$

Equation 6.1 and Equation 6.2 can be represented in state-space form shown as shown in Equation 6.5 and Equation 6.6.

$$\dot{\vec{x}} = A\vec{x} + B\vec{u} \quad (6.5)$$

$$\vec{y} = C\vec{x} + D\vec{u} \quad (6.6)$$

\vec{x} is the state vector, and is shown in Equation 6.7, \vec{u} is the input vector, and is shown in Equation 6.8, and \vec{y} is the output vector, and is shown in Equation 6.9.

$$\vec{x} = \begin{bmatrix} y_1 \\ \dot{y}_1 \\ y_2 \\ \dot{y}_2 \end{bmatrix} \quad (6.7)$$

$$\vec{u} = \begin{bmatrix} F_{ext,1} \\ F_{ext,2} \end{bmatrix} \quad (6.8)$$

$$\vec{y} = \begin{bmatrix} y_1 \\ y_2 \end{bmatrix} \quad (6.9)$$

Matrix A is show in Equation 6.10, Matrix B in Equation 6.11, Matrix C in Equation 6.12, and Matrix D in Equation 6.13.

$$A = \begin{bmatrix} 0 & 1 & 0 & 0 \\ -(k_1 + k_2)/m_1 & -(c_1 + c_2)/m_1 & k_2/m_1 & c_2/m_1 \\ 0 & 0 & 0 & 1 \\ k_2/m_2 & c_2/m_2 & -k_2/m_2 & -c_2/m_2 \end{bmatrix} \quad (6.10)$$

$$B = \begin{bmatrix} 0 & 0 \\ 1/m_1 & 0 \\ 0 & 0 \\ 0 & 1/m_2 \end{bmatrix} \quad (6.11)$$

$$C = \begin{bmatrix} 1 & 0 & 0 & 0 \\ 0 & 0 & 1 & 0 \end{bmatrix} \quad (6.12)$$

$$D = \begin{bmatrix} 0 & 0 \\ 0 & 0 \end{bmatrix} \quad (6.13)$$

The state-space system can be numerically solved to determined the properties of the modeled system. The state is propagated using Equation 6.5, and the output obtained using Equation 6.6.

6.1.1.1. Boom Analysis Results

The results from the boom analysis are shown in Figure 6.9 and Figure 6.11 for a one-second time window. The same results are shown in Figure 6.10 and Figure 6.12 for a sixty-second time window. As can be seen, the angular velocity of the beam never exceeds a value of 0.01 [deg/s], and the displacement never exceeds a value of 0.015 [mm]. These results prove that the beam is sufficient for the required mission.

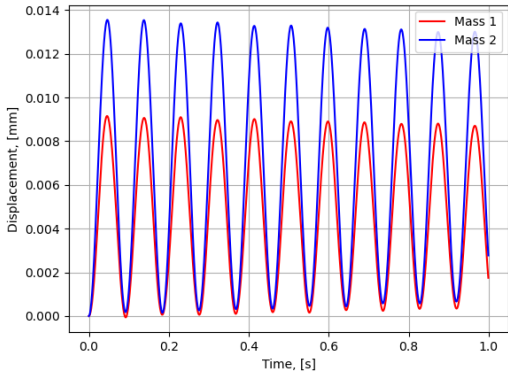


Figure 6.9: Displacement of boom over one second.

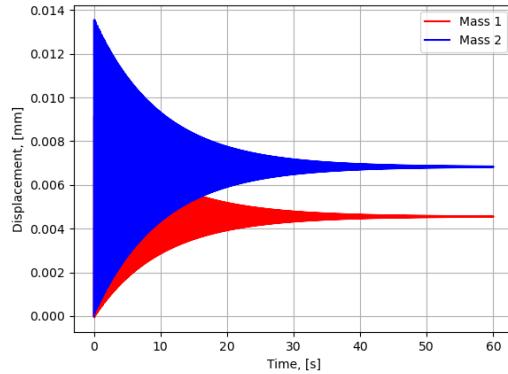


Figure 6.10: Displacement of boom over sixty seconds.

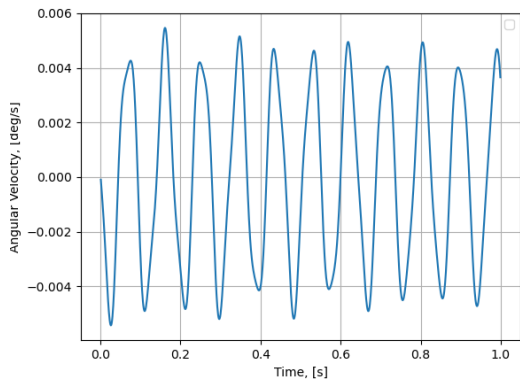


Figure 6.11: Angular velocity of boom over one second.

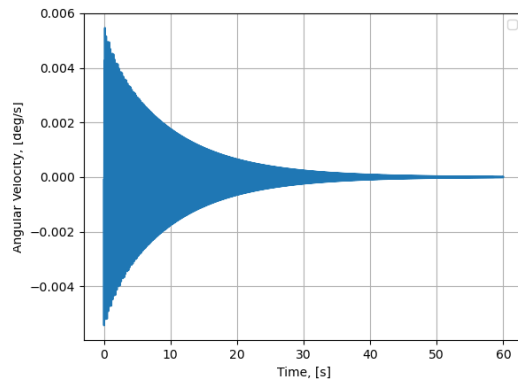


Figure 6.12: Angular velocity of boom over sixty seconds.

6.2. EPS

Nearly all components aboard the spacecraft require electrical power to function. This is facilitated by the electrical power system (EPS). The EPS is in charge of the generation, storage and distribution of the electrical power within the spacecraft. In the midterm report [1], the configuration of the EPS was selected. The power is to be generated by a solar array of single junction Ga-As cells and it is to be stored in Li-ion batteries. Single junction cells are very rarely used for cubesat applications, and so as a result very few off-the-shelf components exist for this type of cells. Therefore triple-junction cells were also considered to be an option for the solar array. The values of all EPS requirements were also determined, based on initial estimates. These can be seen in Table 6.2.

Table 6.2: The EPS requirements of MAGEOS [1].

Identifier K=Key, D=Driving, R=Removed	Requirement	V&V Method
TECH-EPS-GEN-1	The electrical power system shall provide 32W of power during daytime at EOL.	Analysis
TECH-EPS-GEN-2	The electrical power system shall provide 32W of power during eclipse at EOL.	Analysis
TECH-EPS-STR-1	The electrical storage system shall have an available capacity of 36Wh at EOL.	Analysis
TECH-EPS-STR-2	The electrical storage system shall be able to withstand at least 11900 charge/discharge cycles with less than 20% degradation.	Demonstration
TECH-EPS-STR-3	The batteries shall not be charged above 90% or depleted below 20% during operations.	Analysis
TECH-EPS-DIS-1	The power management system shall protect the spacecraft systems against electrical anomalies.	Demonstration
TECH-EPS-DIS-2	The electrical path efficiency shall be no less than 90%.	Test

Of these requirements none are key or driving requirements, so no extra attention has to be put into any one part of this subsystem. Using these requirements, the initial iterations were performed.

6.2.1. Solar Array

To determine the final size of the EPS system, the final power needed for each subsystem to operate is needed. These can be found in Table 6.3.

Table 6.3: The power requirements of each subsystem.

Spacecraft Subsystem	Power Requirement (W)
Magnetometer	2.60
Gravimeter	4.55
ADCS	1.41
TCS	0.00
CDH	0.40
TTC	6.00
Propulsion	42.00

Of these power requirements, all except the propulsion and the TTC must be provided continuously throughout the orbit, in both sunlight and eclipse. The propulsion subsystem of the spacecraft must only be supplied with power when the thruster is fired, which occurs for 1.05 [s] every 2.5 orbits, as can be seen in Section 6.3. The TTC system is only in use when the spacecraft can communicate with a ground station, which happens on average during 6.1% of an orbit, as presented in Section 7.2. The power during eclipse, as well as the power for the propulsion and TTC system will be supplied from the Li-ion secondary batteries, which are charged by the solar array during daylight. The solar array also will provide power to the rest of the subsystems throughout the orbit. To provide a clear overview of the power needs of each subsystem, an electrical block diagram was created, which can be seen in Figure 6.13.

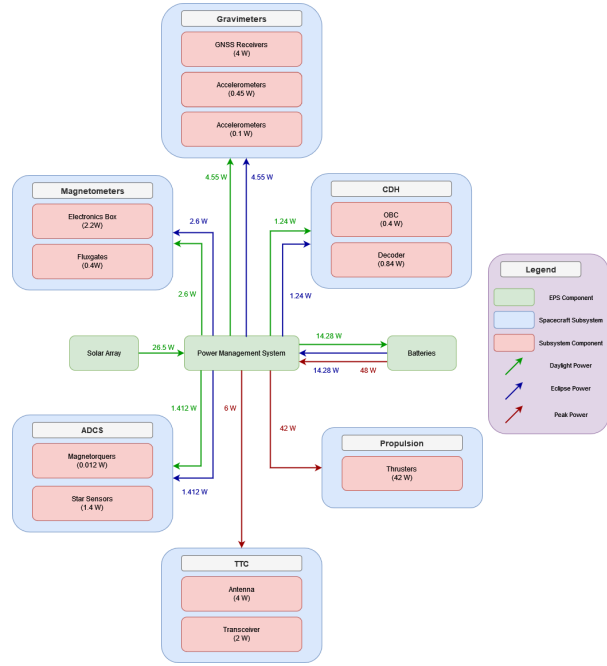


Figure 6.13: The EPS block diagram for a MAGEOS spacecraft.

As the solar array is fixed to the body of the spacecraft, it can not rotate to face the incident solar flux most optimally. Once the solar array is in sight of the sun, it starts generating power proportional to the cosine of the incidence angle. All power needed to supply the subsystems and charge the batteries must therefore be generated throughout exactly half an orbital period. The amount of energy and power the solar array must generate can then be calculated using Equation 6.14 Equation 6.15. In this equation the subscripts SA , d , e , TTC and p refer to the solar array, daytime, eclipse time, TTC system and propulsion system respectively.

$$E_{SA} = \frac{P_d}{\eta_d} \cdot t_d + \frac{P_e}{\eta_e} \cdot t_e + \frac{P_{TTC}}{\eta_{TTC}} \cdot t_{TTC} + \frac{P_p}{\eta_p} \cdot t_p \quad (6.14)$$

$$P_{SA} = \frac{E_{SA}}{t_d} = \frac{P_d}{\eta_d} \cdot \frac{t_d}{t_d} + \frac{P_e}{\eta_e} \cdot \frac{t_e}{t_d} + \frac{P_{TTC}}{\eta_{TTC}} \cdot \frac{t_{TTC}}{t_d} + \frac{P_p}{\eta_p} \cdot \frac{t_p}{t_d} \quad (6.15)$$

A safety factor of 20% is placed on all the power requirements of the subsystems, to accommodate for any unexpected additional power needs, or unexpected solar power loss. In Figure 6.13, it can be seen that the power drawn from the batteries passes through the power circuit twice, once when it is generated and once when it is drained from the battery. This means that the electrical path efficiency during eclipse must be better than 0.81, which is the square of the efficiency of the electrical path requirement of 0.9 [W]. As the power supplied to the TTC and propulsion system is also drawn from the batteries, the electrical path efficiency for these is also 0.81. These lowest efficiency values were therefore used. The required solar array power was determined to be 26.5 [W], which can be used to calculate what the solar array area should be [72]. This can be calculated using Equation 6.16.

$$A = \frac{P_{SA}}{S \cdot \eta \cdot I_d \cdot L_d \cdot \cos(\theta_s)} \quad (6.16)$$

The average value used for the angle θ is 50.46 [deg]. This can be derived from Section 5.5. During half of the orbit, power can be generated during daytime with an incidence angle varying with the cosine. The average cosine of the incidence angle is 0.6366, corresponding to the incidence angle just mentioned.

Using Equation 6.16, the required area of the solar array was found to be 0.134 [m²]. The solar cells that are used are 1U CubeSat solar panels developed by ISISpace, which can be seen in Figure 6.14. These cells are triple-junction Ga-As cells, with an efficiency of 30%. Using the calculated solar array area, 14 of these 1U panels are needed. Each 1U panel can supply 2.3 [W] of power, so 14 units are capable of producing the required average of 26.5 [W] of power needed by the spacecraft. Each 1U solar panel has a mass of 50 [g], resulting in a total solar panel mass of 0.7 [kg]. With the solar array sized, the size of the battery still needs to be determined, which is done in Section 6.2.2.

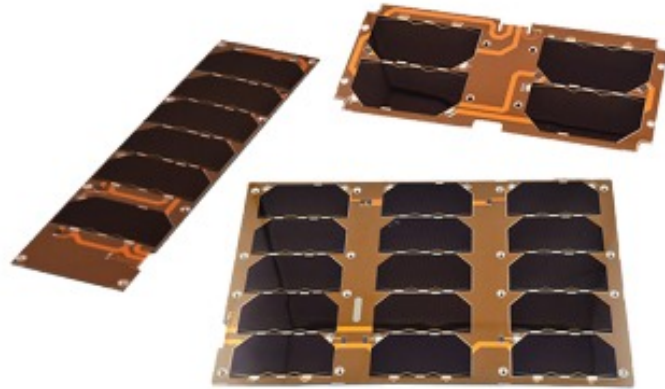


Figure 6.14: Several configurations of 1U solar panels by ISISpace. A single panel is a unit containing 2 cells [73].

6.2.2. Batteries

The battery needs to be able to store all the energy necessary to provide power to all subsystems during the time when the solar array can not , which includes the energy needed to operate the thruster and the TTC system during the time in which they should be active in an orbit. The total energy the battery should be able to store can be found using Equation 6.17.

$$E_b = \left(\frac{P_e \cdot t_e}{\eta_e} + \frac{P_{TTC} \cdot t_{TTC}}{\eta_{TTC}} + \frac{P_p \cdot t_p}{\eta_p} \right) \quad (6.17)$$

This leads to a total stored energy of 10.7 [Wh]. Throughout the mission lifetime, the battery will undergo almost 12000 cycles, during which it must not lose more than 20% of it's capacity, according to TECH-EPS-STR-2. It has been shown that reducing the depth of discharge of a battery significantly extends the cycle life [74]. Therefore, to ensure the on-board battery remains having sufficient capacity throughout the life of the mission, the battery has been oversized. By doubling the battery capacity, the loss over time can be accounted for. The battery should therefore be able to store 21.5 [Wh] of energy. The battery that will be used can be seen in Figure 6.15. It has a capacity of 25 [Wh], has a mass of 125 [g] and dimensions of 95 x 89 X 7 [mm].

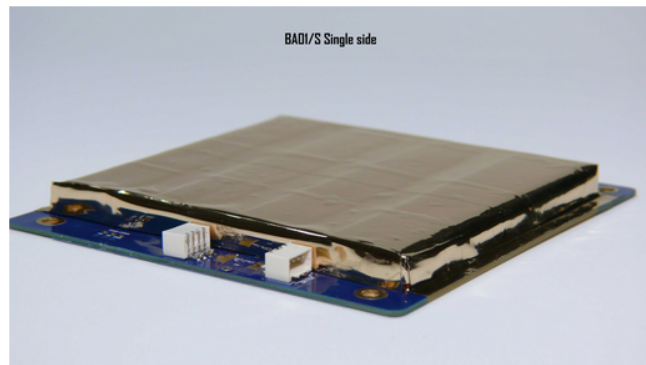


Figure 6.15: The 25 [Wh] battery from EXA, which will be used in MAGEOS' spacecraft [75].

6.2.3. Power Management System

The final component that must be included in the EPS subsystem is an electrical power management system. This component manages the incoming and outgoing power from the EPS system and converts it to the desired current and voltage for each subsystem it has to supply to. The PMS is part of the electrical path, which has a requirement of less than 90% loss. The component selected for this purpose can be seen in Figure 6.16. It consumes only 20 [mA] of current at 3.7 [V], which results in a power usage of 0.074 [W]. This is only 0.28% of the average power generated throughout an orbit, which is deemed acceptable. The component weighs 193 [g] and dimensions of 95.7 x 90.2 x 21.2 [mm]. It also contains a smaller battery with a power capacity of 10.2 [Wh], which will function as a backup battery for incidental peak power demands.



Figure 6.16: The electrical power management system from Endurosat, which will be used in MAGEOS' spacecraft [76].

6.2.4. EPS code verification

All calculations made for the EPS system were performed using a Python program. This program was verified using unit tests for each function, and then system tests for the entire program. The unit tests consist of tests using simple values, extreme values and zeroes, to observe the behaviour of the function to these sets of numbers. The system test was performed by entering numbers for which the outcome is already known, to see if the program outputs the same value. As the program passed these tests, the code has been verified to function properly and so the values obtained from it can be accepted.

6.3. Propulsion

As mentioned previously, the MAGEOS mission orbits the Earth at an altitude of 229.7 [km], in the VLEO region. While this region significantly enhances both payload performance and operational capabilities, it also has a major drawback: the presence of high atmospheric drag caused by the relatively dense atmosphere, especially at altitudes less than 250 [km] [77]. This atmospheric drag has an extremely detrimental effect on mission lifetime lest a suitable propulsion system is present onboard to compensate for it. These effects can be seen in Figure 6.17, wherein the orbit radius for a MAGEOS-like S/C rapidly decreases to an orbit radius of 6477 [km] i.e. an altitude of 106 [km] within 10 days, meaning that the S/C rapidly de-orbits within 2 weeks. Thus, in order to ensure that the MAGEOS mission can fulfill its objectives and does not de-orbit before the mission EOL, a propulsion system has been chosen according to the revised requirements shown in Table 6.4. Following this, an orbit control strategy has been determined in accordance with the propulsion system's characteristics, as shown in Section 6.3.3.

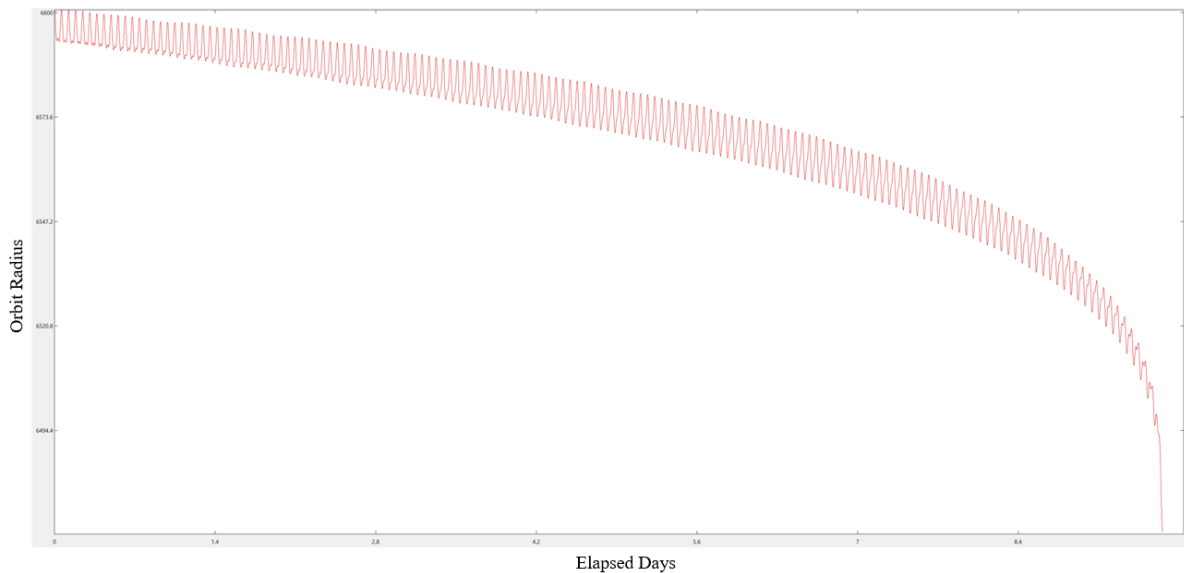


Figure 6.17: Orbit radius v/s Elapsed days in orbit

Table 6.4: The propulsion system requirements for MAGEOS [1]

Identifier K=Key, R=Removed	Requirement	V & V Method
TECH-PROP-1 (R)	The propulsion system shall have a specific impulse greater than TBD seconds	Test
TECH-PROP-2 (R)	The propulsion system shall have a ΔV budget of TBD m/s	Analysis
TECH-PROP-3 (R)	The propulsion system shall deliver an acceleration smaller than TBD m/s ²	Analysis
TECH-PROP-4 (R)	The propulsion system shall be capable of restarting TBD times	Demonstration
TECH-PROP-5	The thruster exhaust plumes shall not obstruct the path of the S/C	Analysis
TECH-PROP-6 (R)	The propulsion system shall have a throttle range of TBD% to 100% of nominal thrust	Test
TECH-PROP-7 (R)	The propellant shall not degrade within the mission duration	Analysis
TECH-PROP-8 (R)	The propulsion system shall have a minimum pulse duration of less than TBD s	Demonstration
TECH-PROP-9 (D)	The propulsion system shall deliver a minimum total impulse of 2687 [N · s]	Test
TECH-PROP-10 (D)	The propulsion system, including propellant, shall not occupy more than 6U of volume	Inspection
TECH-PROP-11 (D)	The propulsion system shall deliver a minimum thrust of 100 [mN]	Test
TECH-PROP-12	The thrust delivered by each thruster shall not be more than 1000 [mN] during operation	Demonstration
TECH-PROP-13	The propulsion system shall have an equal number of thrusters placed symmetrically about the S/C's yaw axis	Inspection
TECH-PROP-14	The thrust delivered by each thruster shall be throttleable within $\pm 10\%$ of the nominal thrust	Test

TECH-PROP-15 (D)	The propulsion system shall have a minimum life-time of one year	Demonstration
TECH-PROP-16	The propulsion shall consume a maximum of 1400 [J] of electrical energy during burns	Test
TECH-PROP-17 (K)	The propellants used by the propulsion system shall be compliant with REACH [78] regulations	Inspection

These requirements have been chosen using the following rationales:

- TECH-PROP-5: The thrusters must have a plume that dissipates swiftly and does not have an aperture angle that causes unwanted perturbations in the data measured by the instruments onboard.
- TECH-PROP-9: The propulsion system, in accordance with the orbit maintenance requirements mentioned in Section 6.3.3, needs to deliver a minimum total impulse of 2687 [N · s] irrespective of the thrust level.
- TECH-PROP-10: This requirement was derived on the basis of the preliminary S/C volume budget.
- TECH-PROP-11: The propulsion system must have a thrust level sufficient to enable quasi-impulsive maneuvers. Thus, a minimum level of 100 [mN] was chosen on the basis of the LUMIO mission's propulsion system [79]. This S/C is similarly sized to MAGEOS, with a comparable volume and mass.
- TECH-PROP-12: The thrust level of each thruster must be limited in order to minimise unbalancing torques. Thus, a maximum level of 1000 [mN] per thruster was chosen on the basis of the LUMIO mission's propulsion system [79].
- TECH-PROP-13: This requirement has been generated in order to constrict imbalances due to factors such as thruster misalignment.
- TECH-PROP-14: This requirement has been chosen to allow for compensation of disturbance torques caused due to factors such as thruster misalignment.
- TECH-PROP-15: This requirement has been derived from the required mission lifetime.
- TECH-PROP-16: This requirement has been derived from limitations on the EPS.
- TECH-PROP-17: The customer states that the MAGEOS mission must be sustainable and utilise non-toxic substances. Thus, the propellant will be chosen such that it is compliant with REACH [78] regulations, a key framework regulating the use of chemical substances.

6.3.1. Revised Trade-off

During the midterm design phase, water resistojets were nominated to be the COTS propulsion system of choice, owing to their higher thrust-to-power ratios, lower costs, relatively lower power consumption and sustainability. However, upon carrying out a feasibility analysis of COTS water resistojets, such as the ones developed by Pale Blue [80] and Bradford Space [81], they were deemed to be infeasible due to their nevertheless insufficient thrust-to-power ratios and low specific impulses. These attributes led to higher burn times and the consumption of unacceptable levels of electrical energy, along with the requirement of large volumes of fuel in addition to the ones inherently present within the propulsion system. Thus, a trade-off was again carried out in order to compare various options and analyse their feasibility and compliance to the revised requirements, as shown in Table 6.5.

Table 6.5: Trade-off table for the propulsion subsystem

Criteria Option	Thrust	Specific pulse	Im-	Mass	Volume	Power	Cost
Mono-propellant	Several available options	Lower		Higher	Acceptable	Acceptable	Acceptable
Bi-propellant	Acceptable number of options	Acceptable		Acceptable	Higher	Acceptable	Acceptable
Cold Gas	Adaptable to any level	Extremely low		High for required thrust	High for required thrust	Lowest	Lowest
Resistojet	Lesser options	Extremely low		High for required thrust	High for required thrust	Higher power	Acceptable
Ion	Non-existent options	High		Low	Low	Extremely high	Acceptable
Electrospray	Non-existent options	Extremely high		Low	Low	High	Acceptable
Field-Emission Electric Propulsion	Non-existent options	Extremely high		Low	Low	High	Acceptable
Hall-Effect	Acceptable number of options	High		Acceptable	Acceptable	Extremely high	Acceptable
Pulsed-Plasma	Non-existent options	Acceptable		Low	Acceptable	High	Acceptable

	Excellent, exceeds requirements		Correctable deficiencies
	Good, meets requirements		Unacceptable

Following the trade-off, electric propulsion systems were entirely ruled out owing to their insufficient thrust-to-power ratios, which were again found to cause exorbitant burn times and consume unacceptable levels of electrical energy, in spite of having outstanding specific impulses, availability of high-density propellants such as solid iodine and potential for air-breathing systems. Cold gas systems were also rejected, primarily due to their extremely low specific impulses, which would lead to unacceptable propellant masses and volumes. Subsequently, monopropellant systems were rejected as well due to having lower specific impulses as compared to bi-propellant systems, in spite of a wider array of compliant COTS options being available. Thus, bi-propellant systems were finally nominated to be the candidate of choice and were further investigated to find a suitable COTS option, with priority given to solutions by European manufacturers due to ease of sourcing and lack of ITAR restrictions.

6.3.2. Propulsion System Selection

Upon carrying out a thorough survey of COTS bi-propellant systems for CubeSats, three options were chosen for detailed analysis. The first proposed option is the PM200 propulsion module by AAC Clyde Space [82]. This system utilises nitrous oxide as an oxidant and propene as the fuel, delivering a nominal thrust of 0.5 [N] with a specific impulse of >285 [s]. The system is available in a 1U configuration with a wet mass of 1.41 [kg] and is meant for use onboard 3U-12U CubeSats, offering a total impulse of >850 [N · s]. However, the system is capable of incorporating additional propellant within the system if required, owing to the use of additive manufacturing. The system can be seen in Figure 6.18.



Figure 6.18: The PM-200 propulsion module by AAC Clyde Space [82]

The second option is the Peregrine propulsion system by Benchmark Space Systems [83]. This system utilises a high test hydrogen peroxide (HTP) and non-toxic hypergolic miscible fuel (NHMF) combination, providing thrust levels between 0.1-22 [N], depending on the thruster quantity along with a specific impulse between 270-300 [s]. The system is meant for CubeSats >6 U, with the COTS volume-wet mass configurations of 2U, 2.5 [kg], 3.5U, 4 [kg], and 7.8U, 7.5 [kg] available. The 2U, 3.5U and 7.8U configurations offer a total impulse of 1750 [N · s], 3500 [N · s], and 10000 [N · s], respectively. However, this propulsion system can be customised as well, up to a total impulse of 200 [kN · s]. The 3.5U system is shown in Figure 6.19.



Figure 6.19: The Peregrine 3.5U configuration by Benchmark Space Systems [83]

The third and last option is the Dawn Aerospace Cubedrive [84] propulsion module. Much like the PM200, this propulsion module utilises a nitrous oxide-propene mix as propellant and is capable of providing thrust between 0.39-1.37 [N] with a constant specific impulse of 285 [s]. Moreover, the thruster is capable of dual-mode operation, either as a cold-gas system, with either the fuel or the oxidiser being used, or a bipropellant system. The systems are meant for CubeSats ranging from 3U-24U+ and are available in COTS volume-wet mass configurations of 0.8U, 1.17 [kg], 1U, 1.41 [kg], 1.5U, 1.85 [kg] and 2U, 2.4 [kg], with each configuration housing one thruster only. The 0.8U, 1U, 1.5U, and 2U configurations offer a total impulse of >425 [N · s], >850 [N · s], >1500 [N · s] and >2200 [N · s], respectively. Dawn Aerospace offers extensive customisation capabilities as well. The 2U system is shown in Figure 6.20.



Figure 6.20: The 2U Cubedrive module by Dawn Aerospace [84]

In order to make a final choice regarding the propulsion system employed onboard MAGEOS, the feasibility and performance of the selected candidates were analysed in the context of the propulsion subsystem requirements. Based on these factors, the 2U version of the Dawn Aerospace Cubedrive module was selected. The PM200 system was eliminated due to lower thrust levels compared to the other systems and the lack of COTS high total impulse options, with the COTS option being meant for a 12U CubeSat at most. The Peregrine system was eliminated as well, owing to its lower total impulse-to-system volume ratios, lower total impulse-to-system mass ratios, lower specific impulse, non-compliance with REACH [78] and increased mission risks due to the use of hypergolic propellant. Moreover, Benchmark Space Systems is a US-based company, which means that the product may be ITAR regulated and relatively expensive to procure. Thus, the Cubedrive system emerged as the victor, offering an excellent thrust range, a constant specific impulse of 285 [s] and a very high impulse density system. The system is also REACH compliant and easy to procure due to Dawn Aerospace's establishment in Delft, The Netherlands. Two modules of 2U each have been chosen for use onboard MAGEOS as this was the lowest volume configuration that was deemed feasible upon analysis of possible orbit control strategies. The lower volume Cubedrive systems, while feasible in theory, would barely provide a satisfactory ΔV while requiring much more frequent burns, which would lower the overall lifetime of the propulsion system. The two 2U modules provide a small surplus of ΔV , meaning that there is scope for extension of mission lifetime as well, as will be shown in Section 6.3.3.

6.3.3. Orbit Control Strategy

Upon selection of the two 2U Cubedrive propulsion modules, a corresponding orbit control strategy was determined in order to not exceed the modules' combined total available ΔV of 279.82 [m/s], calculated using Equation 6.18, while maintaining the orbit altitude within acceptable limits. The orbit control strategy was designed with the motive that modifications to the COTS solution would be avoided as much as possible. The first step in determining the strategy was to decide the kind of manoeuvre used for reverting the orbit to its original altitude of 229.7 [km]. It was decided to use a Hohmann transfer for this purpose, owing to its relatively low ΔV requirements and the quasi-impulsive capability offered by the propulsion system. Following this, various limiting altitudes were analysed in order to determine the maximum allowable decay before the propulsion system activates and orbit correction burns are carried out. The rationale behind the analysis is two-fold:

- The limit-case altitude must be within 0.02% of the nominal altitude of 229.7 [km] in order to limit

deviations in the orbit's precession over one year to <0.1 [°] and maintain a Sun-Synchronous orbit.

- The orbit control ΔV required for a mission lifetime of one year must be $<72.46\%$ of the total available ΔV for orbital maintenance in order to leave a sufficient margin for constellation maintenance, EOL manoeuvres and contingency.

$$\Delta V = I_{sp} \cdot g_0 \cdot \ln\left(1 + \frac{M_p}{M_d}\right) \quad (6.18)$$

The orbit control ΔV is quantified by two factors: the ΔV required for the Hohmann transfer, and the ΔV required to compensate for the drag incurred during the transfer. The Hohmann transfer ΔV further comprises the ΔV for the perigee manoeuvre and the ΔV for the apogee manoeuvre, calculated using Equation 7.22 and Equation 7.23, respectively. The transfer time for the Hohmann transfer was calculated using Equation 7.25. The ΔV required for drag compensation during the transfer manoeuvre was calculated using Equation 6.19, assuming a constant drag equal to the worst-case drag at the limit-case altitude and the lowest possible mass i.e. the S/C's dry-mass in order to obtain a conservative estimate which accounts for the stochastic nature of atmospheric drag and an upper limit of time equal to the transfer time. The burn durations have been neglected in this calculation due to the quasi-impulsive nature of the burns. The propulsion system shall provide the ΔV for transfer drag compensation during the perigee burn itself along with the perigee manoeuvre ΔV , and executes the apogee manoeuvre as normal once the target altitude is reached. Finally, the total ΔV per orbit correction manoeuvre was calculated using Equation 6.20.

$$\Delta V_D = \int_0^{T_{transfer}} \frac{D}{M_d} dt \quad (6.19)$$

$$\Delta V_{OC} = \Delta V_D + \Delta V_1 + \Delta V_2 \quad (6.20)$$

Subsequently, the burn time for both the perigee burn and the apogee burn were determined using Equation 6.21, with a total delivered thrust of 1 [N] in accordance with the aforementioned quasi-impulsive manoeuvre requirement. Each propulsion module delivers a thrust of 0.5 [N]; however, due to the minimum impulse-bit requirement of 0.059 [N · s], the burn times must be >0.118 [s]. The total manoeuvre time was then calculated using Equation 6.22, following which the number of manoeuvres per year was calculated using Equation 6.23. Lastly, the total orbit control ΔV per year was calculated using Equation 6.24.

$$t_b = \left(1 - e^{-\frac{\Delta V}{g_0 \cdot I_{sp}}}\right) \cdot g_0 \cdot M_d \cdot \frac{I_{sp}}{T} \quad (6.21)$$

$$T_M = T_{transfer} + t_p + t_a \quad (6.22)$$

$$n = \frac{365}{T_{Descent} + \frac{T_M}{60 \cdot 60 \cdot 24}} \quad (6.23)$$

$$\Delta V_{drag} = \Delta V_{OC} \cdot n \quad (6.24)$$

Through the use of the aforementioned formulae, the variation in the total orbit control ΔV per year with the limiting altitude was analysed. Based on the aforementioned altitude-selection constraints

and the rapid increase in total ΔV with altitude, a cut-off altitude of 229.6675 [km] was selected. The time to decay to this altitude from 229.7 [km] is 2.97 [h], leading to a total of 2358 orbit corrections being carried out during the mission lifetime of one year, with each manoeuvre lasting 44.49 [min]. The thrusters activate 4716 times per year, with a perigee burn time of 0.879 [s] and an apogee burn time of 0.146 [s]. The total orbit correction ΔV thus required is 159.07 [m/s], which is sufficiently under the previous margin of 72.46% and leaves room for extension of the mission lifetime.

6.4. Thermal Control

The thermal control system manages the temperature of the spacecraft's subsystems. The components which have a temperature requirement will need a form of thermal control to satisfy this requirement. requirement on the thermal control system can be found in Table 6.7.

Table 6.7: The Thermal control system requirements of MAGEOS [1]

Identifier K=Key, R=Removed	Requirement	V & V Method
TECH-THERM-1	The temperature of the subsystem shall stay within the survivable temperature range for each subsystem	Analysis
TECH-THERM-2	The temperature of the subsystems shall stay within operational temperature range for each subsystem for more than 95 percent per orbit	Analysis

As mentioned earlier, each subsystem has its own temperature range requirement. An assessment is made for each subsystem and its temperature range. These temperature ranges for each subsystem are put in Table 6.8. Next to that is also the amount of heat the subsystem dissipates and which material it is made of.

Table 6.8: Subsystem requirements and information for thermal control

Subsystems	Dissipated Heat [W]	Material	Surface Treatment	Survivability Limits	Operational Limits
Cubesat Structure	0	Aluminium AL6061	MLI	-200/200°	-200/200°
Solar Panels	1	Gallium Arsenide	black	-200/200°	-150/150°
Electrical Power System	1	Epoxy Glass Laminate	Green	-180/180°	-25/45°
Command & Data Handling	0.2	Epoxy Glass Laminate	Green	-180/180°	-25/45°
Telemetry and Telecommunication	0.1	Epoxy Glass Laminate	Green	-180/180°	-25/45°
On board computer (OBC)	0.05	Epoxy Glass Laminate	Green	-180/180°	-25/45°
Propulsion System	0.5	Aluminium AL6061	Polished Aluminium	-200/200°	-30/60°

As seen in Table 6.8 the survivability temperature range is at from -180/180°C to -200/200°C. The operational temperature limits are from -150/150°C to -200/200°C for the solar panels, propulsion system and chassis. The operational limits for the other subsystems like batteries and electronics are stricter with a limit of -25°C to 40°C.

Further some properties of the materials and coatings used are presented in Table 6.9.

Table 6.9: Material and optical coating properties

Material / Coatings	Density [kg / m ³]	Capacity [J / kg K]	Absorptivity	Emmissivity
Aluminium AL6061	2700	896	0	0
Gallium Arsenide	5317.6	333	0	0
Epoxy Glass Laminate	1850	1210	0	0
MLI	≈ 0	≈ 0	0.01	0.1
Polished Aluminium	≈ 0	≈ 0	0.08	0.24
Black	≈ 0	≈ 0	0.85	0.95
Green	≈ 0	≈ 0	0.88	0.66

In the thermal analysis, the density and capacity of the optical coatings are regarded as negligible. As the materials themselves are not exposed due to the optical coatings is the absorptivity and emmissivity of the materials zero.

Thermal Model

The thermal model consist of an assembly of panels. The panels are configured to represent the MAGEOS spacecraft as realistically as possible. Figure 6.21 gives an exploded overview of the panel arrangement. Each panel is configured to have to surface properties which can differ from one another. The body of the spacecraft is made from Aluminium 6061 structure and has a thin foil of MLI. The dual surface panels will also have optical properties on both sides. Table 6.10 gives an list of all the panels used in the thermal model. The dimensions of the panels together with the orientation and transformation are also given. Table 6.11 gives an idea of the materials used for each surface and its optical coating. The deployed boom is the only assembly with different type of materials and optical coating. The boom is made of carbon composite on both sides and have also the same optical coatings.

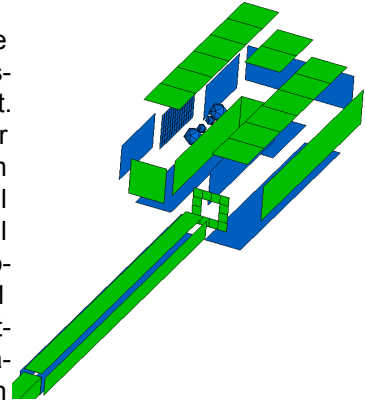


Figure 6.21: Exploded view of the MAGEOS thermal model

Table 6.10: Thermal model panels with the orientation and transformations

Component Name	Dimensions			Rotations			Translations			Node [xxxx]
	X [m]	Y [m]	Z [m]	X [deg]	Y [deg]	Z [deg]	X [m]	Y [m]	Z [m]	
Boom										
Boom_0_NX	0.97	0.05	0	90	0	0	0.735	0.075	0	503x
Boom_0_NZ	0.97	0.05	0	180	0	0	0.735	0.1	-0.025	501x
Boom_0_PX	0.97	0.05	0	-90	0	0	0.735	0.125	0	504x
Boom_0_PZ	0.97	0.05	0	0	0	0	0.735	0.1	0.025	502x
Boom_1_NX	0.97	0.05	0	90	0	0	1.705	0.075	0	507x
Boom_1_NZ	0.97	0.05	0	180	0	0	1.705	0.1	-0.025	508x
Boom_1_PX	0.97	0.05	0	-90	0	0	1.705	1.25	0	506x
Boom_1_PZ	0.97	0.05	0	0	0	0	1.705	0.1	0.025	505x
Panel_0Z_PX_Boom_0	0.1	0.025	0	0	90	0	0.25	0.1375	0	209x
Panel_0Z_PX_Boom_1	0.1	0.025	0	0	90	0	0.25	0.0625	0	209x
Panel_0Z_PX_Boom_2	0.025	0.025	0	0	90	0	0.25	0.1	0.0375	209x
Panel_0Z_PX_Boom_3	0.025	0.025	0	0	90	0	0.25	0.1	-0.0375	209x
Spacecraft_Panels										
Panel_0Z_0NY	0.4	0.1	0	-90	0	0	0.05	-0.05	0	206x
Panel_0Z_0PY	0.4	0.1	0	90	0	0	0.05	0.05	0	208x
Panel_0Z_0X	0.1	0.1	0	0	90	0	-0.015	0	0	207x
Panel_0Z_NX	0.1	0.3	0	0	-90	0	-0.35	0	0	203x
Panel_0Z_NY	0.2	0.1	0	90	0	0	-0.25	-0.15	0	202x
Panel_0Z_NY_PX	0.2	0.1	0	90	0	0	0.15	-0.15	0	600x
Panel_0Z_PX	0.1	0.1	0	0	90	0	0.25	-0.1	0	201x
Panel_0Z_PY	0.6	0.1	0	-90	0	0	-0.05	0.15	0	204x
Panel_NZ_NX	0.2	0.1	0	180	0	0	-0.25	0	-0.05	103x
Panel_NZ_NY	0.6	0.1	0	180	0	0	-0.05	-0.1	-0.05	102x
Panel_NZ_PY	0.6	0.1	0	180	0	0	-0.05	0.1	-0.05	101x
Panel_PZ_NX	0.2	0.1	0	0	0	0	-0.25	0	0.05	304x
Panel_PZ_NY	0.6	0.1	0	0	0	0	-0.05	-0.1	0.05	302x
Panel_PZ_PY	0.6	0.1	0	0	0	0	-0.05	0.1	0.05	301x
Radiator	0.2	0.1	0	90	0	0	-0.05	-0.15	0	600x
Thermal Nodes										
CDH	-	-	-	-	-	-	0.025	-0.1	0	9020
EPS	-	-	-	-	-	-	-0.075	-0.1	0	9030
Electronics	-	-	-	-	-	-	0.075	-0.1	0	9001
TTC	-	-	-	-	-	-	-0.025	-0.1	0	9010

Table 6.11: Thermal panel's material an optical coating choices

Component Name	Surface 1			Node	Surface 2			Node
	Material	Thickness	Optical Coating		Material	Thickness	Optical Coating	
Boom								
Boom_0_NX	CC	5.00E-04	Polished Al	5031	CC	5.00E-04	CC	5032
Boom_0_NZ	CC	5.00E-04	CC	5011	CC	5.00E-04	CC	5012
Boom_0_PX	CC	5.00E-04	CC	5041	CC	5.00E-04	CC	5042
Boom_0_PZ	CC	5.00E-04	CC	5021	CC	5.00E-04	CC	5072
Boom_1_NX	CC	5.00E-04	CC	5071	CC	5.00E-04	CC	5082
Boom_1_NZ	CC	5.00E-04	CC	5081	CC	5.00E-04	CC	5072
Boom_1_PX	CC	5.00E-04	CC	5061	CC	5.00E-04	CC	5062
Boom_1_PZ	CC	5.00E-04	CC	5051	CC	5.00E-04	CC	5052
Panel_0Z_PX_Boom_0	Foil	1.00E-06	MLI	2091	AI 6061	1.00E-03	MLI	2092
Panel_0Z_PX_Boom_1	Foil	1.00E-06	MLI	2093	AI 6061	1.00E-03	MLI	2092
Panel_0Z_PX_Boom_2	Foil	1.00E-06	MLI	2095	AI 6061	1.00E-03	MLI	2092
Panel_0Z_PX_Boom_3	Foil	1.00E-06	MLI	2097	AI 6061	1.00E-03	MLI	2092
Spacecraft_Panels								
Panel_0Z_0NY	Foil	1.00E-06	MLI	2061	AI 6061	1.00E-03	MLI	2062
Panel_0Z_0PY	Foil	1.00E-06	MLI	2081	AI 6061	1.00E-03	MLI	2082
Panel_0Z_0X	Foil	1.00E-06	MLI	2071	AI 6061	1.00E-03	MLI	2072
Panel_0Z_NX	Foil	1.00E-06	MLI	2031	AI 6061	1.00E-03	MLI	2032
Panel_0Z_NY	Foil	1.00E-06	MLI	2021	AI 6061	1.00E-03	MLI	2022
Panel_0Z_NY_PX	Foil	1.00E-06	MLI	6001	AI 6061	1.00E-03	MLI	6002
Panel_0Z_PX	Foil	1.00E-06	MLI	2011	AI 6061	1.00E-03	MLI	2012
Panel_0Z_PY	Foil	1.00E-06	MLI	2041	AI 6061	1.00E-03	MLI	2042
Panel_NZ_NX	Foil	1.00E-06	MLI	1031	AI 6061	1.00E-03	MLI	1032
Panel_NZ_NY	Foil	1.00E-06	MLI	1021	AI 6061	1.00E-03	MLI	1022
Panel_NZ_PY	Foil	1.00E-06	MLI	1011	AI 6061	1.00E-03	MLI	1012
Panel_PZ_NX	Foil	1.00E-06	SolarCells	3041	AI 6061	1.00E-03	Polished Al	3042
Panel_PZ_NY	Foil	1.00E-06	SolarCells	3021	AI 6061	1.00E-03	Polished Al	3022
Panel_PZ_PY	Foil	1.00E-06	SolarCells	3011	AI 6061	1.00E-03	Polished Al	3012
Radiator	AI 6061	1.00E-03	Polished Al	6003	AI 6061	1.00E-03	Polished Al	6002

Transient Solution

The computations of the thermal model using the polar radiative case is put into two graphs. One of the graphs, Figure 6.22, lays out the temperature of all the internal components which are presented in the requirements table. Figure 6.23 presents the temperature ranges for the external parts of the spacecraft. From the figure, maximum and minimum temperature for all internal subsystems fall within the thermal requirement range. The electronics, TTC, EPS and CDH systems have stable temperatures during its orbit. The propulsion systems vary more during orbit, which is expected as the propulsion system is exposed to the environment.

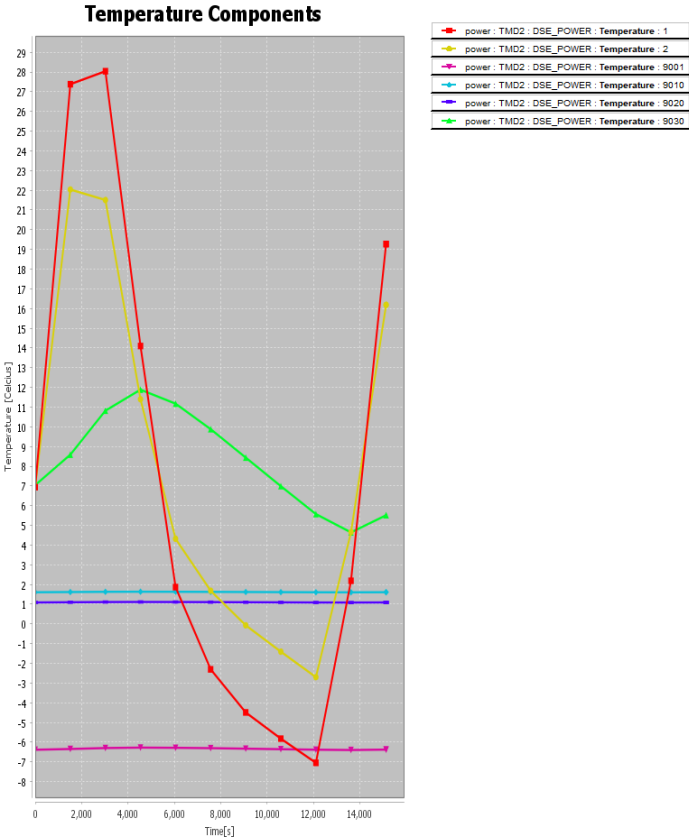


Figure 6.22: MAGEOS temperature graph of internal thermal nodes

Looking at the external parts of the spacecraft, its observed that the boom has a stable temperature of around 20 degrees Celcius. The solar panels do vary a lot during orbit due to the material and optical coating used for the solar panels. But the temperature range fall within the operation temperature range. Laststly, the purple graph is the spacecraft underside, which also falls within the thermal requirement range.

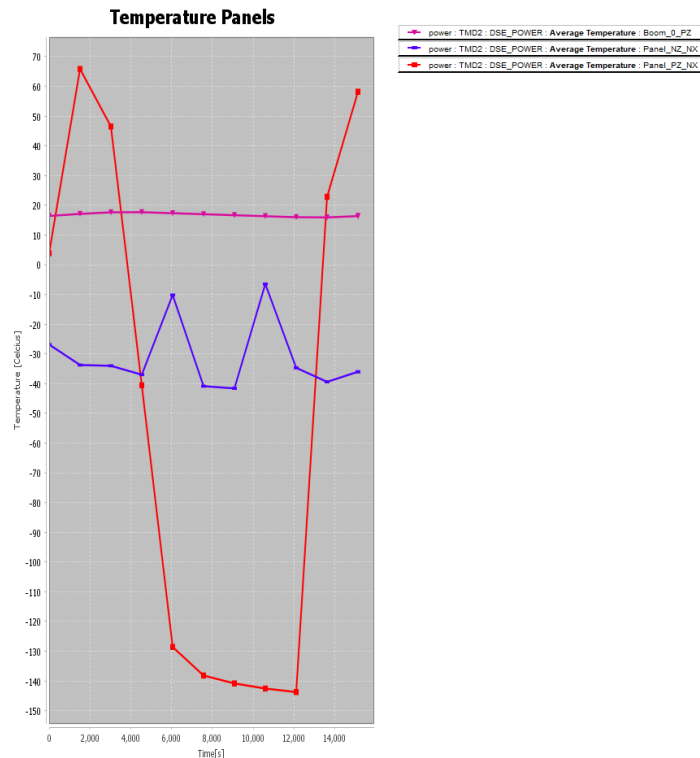


Figure 6.23: MAGEOS temperature graphs of external panels

To conclude the thermal simulation design, all subsystems comply with the thermal requirement. Using the thermal modelling tool has confirmed that with the use of MLI as an insulation foil and a passive radiator are sufficient for maintaining the spacecraft temperature range within the required range.

6.5. Telemetry, Tracking, and Command

The telemetry, tracking, and, command system provides the connection between the ground and the spacecraft. It allows the spacecraft to send down its payload and housekeeping telemetry data, as well as allow the ground station to track the spacecraft's position, and send commands to the spacecraft. If the system critically fails, the mission is over, as any data that the spacecraft generates will never reach the ground. Sizing the TT&C system primarily involves calculating the link budget to see what power is necessary to send the data from the antenna on the spacecraft to the ground and vice versa. Next, the data must be encoded and transmitted for the downlink, as well as received and decoded for the uplink, performed by appropriate hardware.

6.5.1. Link Budget

Constructing the link budget can be done by making a summation of the gain that the signal experiences as it goes from the transmitter to the receiver. Then, the signal to noise ratio can be calculated to see if the signal can reliably be reconstructed.

The link budget will be designed so that an appropriate signal to noise ratio for the downlink and uplink will be obtained. All contributions to the link budget will be represented in decibel. By doing so, all gains and losses can be added or subtracted for each contribution, which include: transmitter power P_T , transmitter antenna gain G_{TA} , loss factor of the transmitter L_T , transmission path loss L_{TP} , antenna pointing loss L_{PL} , free space loss L_{FS} , receiving antenna gain G_{RA} , loss factor of the receiver L_R , the bitrate of the signal, B_R and the white noise spectral density N_0 . The signal to noise ratio calculation can be seen in Equation 6.25.

$$\frac{Eb}{N_0} = P_T + G_{TA} - L_T - L_{TP} - L_{PL} - L_{FS} + G_{RA} - L_R - R - T_s \quad (6.25)$$

In order to present all gains and losses in decibel, they must be converted as follows:

$$G [dB] = 10 \cdot \log_{10} G \quad (6.26)$$

The transmitter power, P_T , can be adjusted depending on what antenna is used, and can be represented in decibel making use of Equation 6.26.

The loss factor of the transmitter and receiver are estimated to be 0.8 and 0.7 respectively, and can be represented in decibel making use of Equation 6.26.

The receiver and transmitter gain G_{RA} and G_{TA} can be calculated for an antenna using the diameter of the receiver D_r , the signal wavelength λ , and radiation efficiency n :

$$G_r = \frac{\pi^2 D_r^2}{\lambda^2} \cdot n \quad (6.27)$$

The transmission path loss, L_{TP} , is the loss due to the signal traveling from the transmitter to the transmitter antenna, and the receiver antenna to the receiver. Since no value is known for this, it will be estimated to be -0.3 [dB].

The antenna pointing loss, L_{PL} , is related to the angle away from the antenna boresight, θ , and the 3 [dB], or half power, beam width θ_{3dB} , as follows:

$$PL [dB] = 12 \left(\frac{\theta}{\theta_{3dB}} \right)^2 \quad (6.28)$$

Next, the free space path loss, L_{FS} can be calculated. This loss is due to the spreading of the signal in space, increasing the area of the signal, but decreasing the power flux density. The total free space path loss, FSPL, in decibel is related to the distance propagated d , and the wavelength λ :

$$FSPL [dB] = 10 \cdot \log_{10} \left(\frac{4\pi d}{\lambda} \right)^2 \quad (6.29)$$

The maximum value for d is related to the orbital altitude h and the radius of the earth R as follows:

$$d = \sqrt{(R+h)^2 - R^2} \quad (6.30)$$

The turn around ratio for S band communication is 240/221 for downlink/uplink [85]. This means that the downlink will have a higher frequency than the uplink.

The bit rate of the signal also has an effect on the signal to noise ratio. Encoding is possible in order to reduce the signal to noise ratio, as each bit has redundancy, however this does increase the amount of bits that must be sent. Since the signal to noise ratio is not critical, as well as the fact that the bit rate actually is constraining, no encoding will be used. The signal bit rate B_R throughout the mission, in terms of the data rate to be sent down D , the encoding ratio R , and the fraction of time in sight of a ground station C_T is:

$$B_R = \frac{DR}{C_T} \quad (6.31)$$

The white noise spectral density, N_0 can be calculated using the Boltzmann's constant k , as well as the system noise temperature T_s , as follows:

$$N_0 = kT_s \quad (6.32)$$

The system noise temperature has many variables, from noise temperature of specific components, to the weather. An estimation can be made for clear weather, relying only on the frequency of the signal, using Table 6.12.

Table 6.12: Relationship between system noise temperature and the frequency of the signal, divided into uplink and downlink [86].

	Frequency [GHz]				
	Downlink			Uplink	
	0.2	2-12	20	0.2-20	40
System Noise [K]	221	135	424	614	763

In order to fully assess the link budget, receivers, transmitters, and antennas must be chosen. However, due to the limitations of a CubeSat in terms of volume and availability of COTS components, the link budget will be used to verify the feasibility of the components, instead of driving their choice.

Furthermore, the ground station plays an important role in the link budget. In Section 7.3.2, the choice is made to use the amazon web service for ground stations, meaning values for the transmitter, receiver and antenna on the ground are set. This service will be used in the link budget analysis going forward.

6.5.2. Transceiver choice

As chosen in the midterm report [1], a transceiver will be used on MAGEOS, being a volume and mass efficient choice for the TT&C system. A COT option was found for the transceiver, being the S-Band Transceiver I, from Endurosat [87]. This transceiver fits well on a CubeSat, works in the S-band, and makes use of a RS485 connection. The characteristics of the transceiver are as follows:

Table 6.13: Characteristics of the Endurosat S-Band Transceiver I, used in MAGEOS.

Characteristic	Value	Unit
Frequency Range (Tx)	2200 to 2290	[MHz]
Frequency Range (Rx)	2025 to 2110	[MHz]
Configurable Data Rate	0.1 to 125	[kbps]
Mass	200	[g]

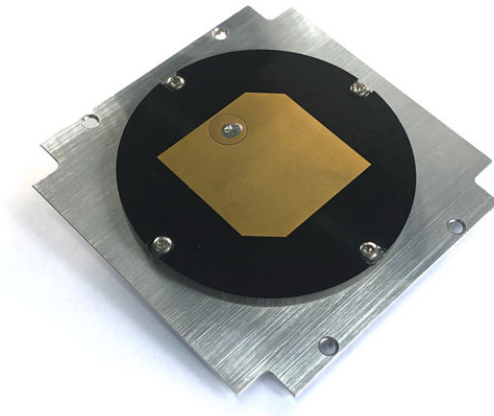


Figure 6.24: S-band Patch Antenna from ISISPACE [88].

6.5.3. Antenna choice

For the antenna, the COT S-band Patch Antenna from ISISPACE [88] was found, which can be seen in Figure 6.24. This antenna is compatible with the Endurosat transceiver, and also fit in a CubeSat. The characteristics of the antenna are as follows:

Table 6.14: Characteristics of the ISISPACE S-Band Patch Antenna, used in MAGEOS.

Characteristic	Value	Unit
Maximum gain	6.5	[dBi]
Half power beam width	100	[deg]
Mass	50	[g]
Frequency Range	2200-2290	[MHz]
Bandwidth	100	[MHz]
Diameter	80	[mm]

6.5.4. Encoder and Decoder Choice

Encoding and decoding the signal is an essential step in sending data from the satellite to the ground station and vice versa. There are dedicated encoders and decoders available, instruments that only perform these two, or even just one, task. However, there is also software available that can encode and decode the messages. This reduces mass, volume and power needs, under the assumption that the on board computer is able to run the software. The software MixW [89] will be used, as long as the on-board computer is able to run this software.



Figure 6.25: The logo of the MixW software, used for encoding and decoding signals.

6.5.5. Link Budget Values

With options available for the transceiver and antenna, their feasibility is verified by implementing them into the link budget. The link budget will also make use of the orbit, as described in Chapter 5, and the bit rate, as described in Section 6.6. The values of all the gains and losses in the link budget, as described in Equation 6.25, as well as the inputs to find these gains and losses are listed below in Table 6.15:

Table 6.15: Values of variables describing the uplink and downlink link budget.

Characteristic	Downlink	Uplink	Unit
Transmitter power, P_T	2	2	[W]
	3.01	3.01	[dB]
Transmitter antenna gain, G_{TA}	6.5	-	[dBi]
	4.1	39.5	[dB]
Transmitter loss factor, L_T	0.8	0.8	[-]
	0.97	0.9	[dB]
Transmission path loss, L_{TP}	0.3	0.3	[dB]
Half power angle transmitter	50.0	1.86	[deg]
Half power angle receiver	1.86	50.0	[deg]
Pointing offset transmitter	70	0.19	[deg]
Pointing offset receiver	0.19	70	[dB]
Antenna pointing loss L_{PL}	23.64	23.64	[dB]
Receiver loss factor, L_T	0.7	0.7	[-]
	1.55	1.55	[dB]
Data rate	5.40	0.60	[kb/s]
Fraction of time in sight of ground station	0.061	0.061	[-]
Encoding ratio	1	1	[-]
Signal bitrate	108.00	11.98	[kb/s]
System noise temperature T_s	200	614	[k]
White noise spectral density, N_0	23.01	27.88	[dB]
Signal to noise ratio	11.47	16.81	[dB]
Margin	11.47	16.81	[dB]

As can be seen in Table 6.15, the margin of the signal to noise ratio is 11.47 [dB] for the downlink, and 16.81 [dB] for the uplink. At least a three [dB] gain is recommended, meaning it exceeds requirements and the signal will be able to be reliably decoded.

The bandwidth required to accommodate the bit rate can be estimated using the Shannon-Hartley theorem, which can be seen in Equation 6.33, where C is the channel capacity, B is channel bandwidth, and $\frac{S}{N}$ is the signal to noise ratio (in magnitude, not decibel).

$$C = B \cdot \log_2 \left(1 + \frac{S}{N} \right) \quad (6.33)$$

Converting the signal to noise ratio to a unit less number, and using the bit rates of the uplink and downlink, the bandwidth for each can be found. The results are shown in Table 6.16

Table 6.16: Final values for the link budget.

Characteristic	Downlink	Uplink	Unit
Channel capacity	108000	11980	[bit/s]
Signal to noise ratio	11.47	16.81	[dB]
Bandwidth required	29.98	2.26	[kHz]

The theoretical resultant required bandwidth is therefore 29.98 [kHz] for the uplink, and 2.26 [kHz] for the downlink. In reality, slightly more is necessary, as the Shannon-Hartley bandwidth can never be approached by a real systems. Still, these bandwidths are easily supported by the transceiver and antenna, as seen in Table 6.13 and Table 6.14, being able to support bandwidths in the magnitude of [MHz].

6.6. Command and Data Handling

Command and Data Handling (C&DH) can perform an array of functions, serving as the 'brain and nervous system of the spacecraft' [90]. These functions include: handling of sensory information, from the payload, as well as housekeeping data; authorize, generate, and perform commands; track time; and act as a memory. If designed for, the C&DH system can perform all of these functions. However a more powerful C&DH system comes at the cost of mass, volume, and power. Processes and calculations such as GPS calculations and attitude determination are performed on computers found within those subsystems, although the data outputted by their sensors are handled and stored by C&DH. The requirements for the C&DH system for the MAGEOS mission are given in Table 6.17.

Identifier K=Key, D=Driving, R=Removed	Requirement	V&V Method
TECH-OBC-1	The on-board computer shall be able to store TBD bytes of data	Demonstration
TECH-OBC-2	The on-board computer shall be able to perform the nominal mission operations autonomously	Demonstration
TECH-OBC-3	The on board computer shall have a command data rate of at least TBD bits/s	Demonstration
TECH-OBC-4	The on-board computer shall have soft error correction	Analysis

Table 6.17: The C&DH requirements of MAGEOS [1].

In order to size the C&DH subsystem, first the data rate of the spacecraft must be estimated. This can be broken down into telemetry data rate, divided into payload and housekeeping data rates, as well as the command data rate.

6.6.1. Data Rate

Data rate is the amount of data, in bits, that must be transferred between two devices per unit of time.

6.6.1.1. Payload Data Rate

The payload data rate for MAGEOS is the number of bits collected per unit of time by the two GPS, six accelerometer, two magnetometers, and a star sensor. These are presented in Table 6.18. The accelerometers and magnetometers have built in thermometers, and these data rate are included in the data rate of the entire instrument.

Table 6.18: Values for the data rate of different payload instruments [17, 91].

Instrument	Frequency [Hz]	Bits per Sample	Duty Cycle [%]	Bitrate [kb/s]	Amount
GNSS Receiver	10	168	100	1.68	2
Accelerometer	10	200	100	2.0	6
Magnetometer	160	-	100	15.6	2
Star Sensor	-	-	100	625.0	2

The total payload data rate is 46.56 [kb/s] without the star sensor, and 1296.56 [kb/s] including the star sensor.

6.6.1.2. Housekeeping Data Rate

The housekeeping data rate for MAGEOS is the number of bits collected by sensors related to the well-being of the on board equipment. This mostly includes data like equipment temperature, currents, voltages, and some other measurements such as the tank pressure [90]. Such measurements can be taken by power and mass sensors. In order to estimate the housekeeping data rate, a compiled list of all equipment to be monitored must be constructed. These measurements, outlined in Table 6.19, will all be performed with the same sampling frequency since this nullifies the bits required for indicating time of measurement. This frequency will be equal to 0.5 [Hz], as that is assumed to provide an appropriate temporal resolution.

Table 6.19: List of telemetry data to be collected for on-board equipment, with the amount of sensors

Instrument	Voltage	Current	Temperature	Additional measurements
Accelerometer	6	6	-	-
GNSS Receiver	1	1	1	-
GNSS antenna	1	1	1	-
S-Band Patch Antenna	1	1	1	-
Transceiver	1	1	1	-
Magnetometer	2	2	-	-
Bus Power	1	1	-	-
Propellant tanks	-	-	1	Pressure, volume, flow rate
Solar arrays	4	4	4	-
Thrusters	1	1	1	-
Total	10	18	18	3

The total amount of housekeeping sensors is thus 49. Knowing how many sensors there are, the bit per sample for the sensor must be determined. I²C provides an appropriate number of channels and sufficient data rate for these sensors. I²C is a bi-directional half-duplex communication channel, meaning commands can be issued to the sensors using it. An identifier is necessary in order to know which sensor is producing a certain measurement. Since there are 49 sensors, and $2^6 = 64$, 6 bits is sufficient to create a unique identifier for each. The number of bits per sample must also be determined. Since a higher number of bits increases the amount of discrete values that any measurement can be stored as, the sensitivity of the sensors, as well as the desired range of the measurements, should be determined. The operational temperature range of equipment, in combination with the accuracy of the chosen thermometer, can effectively be used to get an appropriate number of bits. The range that can be represented should be a bit larger than the operational temperature range, as then it is known when components are too hot or cold, and the amount of bits should be in relative size to the uncertainty of the measurement to not increase the uncertainty.

An appropriate thermometer to be used on MAGEOS is the ISL71590SEH, "Radiation Hardened, 2-Terminal Temperature Transducer" [92]. This thermometer has an accuracy of 1 [K], and an operational range of -55 to 150 [° C]. The operational ranges of the instruments found on MAGEOS can be found in Table 6.8. The largest thermal operational range is for the structure, with a range of 400 [K], yet most critical systems will vary only by 70 [K] at temperatures of -25 to 45 [° C]. This makes the

sensors viable for the sensitive systems, although it cannot measure the entire operational limits for the systems that experience the largest temperature differences. The minimum amount of bits in order to cover the operational range of 70 [K] at the accuracy of the thermometer is seven, giving 128 discrete levels. This is an appropriate value which also allows for some measurement outside the operational limits for the critical systems. The systems with a higher operational limit will have an increased difference between discrete measurements, so that the seven bits will cover the full -55 to 150 [$^{\circ}$ C] range. The bits to store the value of each temperature is thus seven. An additional bit is added in order to request a value. Since commands use the same I²C channel, it can be included in the bit per sample for the calculations. These 8 bits, plus the 6 bits for the identifier for a total of fourteen, will be used for the thermometers, as well as all the other sensors. With a total of 49 sensors, a sampling frequency of 0.5 [Hz], and a bit per sample of 14, the housekeeping data rate is equal to 0.371 [kb/s].

6.6.1.3. Command Data Rate

The command data rate includes all instructions, originating from the ground station or the on-board computer, that are sent to subsystems in the spacecraft to carry out a certain function. This function can be to perform some action action, or change mode of operation. Ground station commands can be estimated to be sent every 24 hours. These periodic commands can be in the form of real-time commands or stored sequence commands, depending on whether the command must be performed upon receiving it or be stored with a time tag for later issue. Commands are also sent from the on-board computer, stored on the on-board computer, and performed when certain conditions (time, telemetry data) are met [90]. Commands are in the form of text, which can be represented in ASCII, meaning the bit per command can be estimated if the amount of characters of an average command is known. Each character within ASCII can be represented with 8 bits (256 different characters), and an estimation of 40 characters per command is used, achievable with the usage of short form techniques [93]. This means each command uses 320 bits.

The amount of commands to be sent per unit of time is difficult to calculate. There are sensors which require a bit in order to be requested to provide a measurement. This bit rate has already been included in housekeeping data rate. More complex instruments require more complex commands, for example the thrusters and transceiver. However, these instruments can be instructed to enter certain operational modes, meaning it is not necessary for devices to receive new commands with an interval in the order of milliseconds or seconds. Instead, a certain amount of commands per orbit can be used. It is assumed that each device needs 500 commands per orbit. These instruments are represented in Figure 6.27, and are as followed: magnetometers (2x), accelerometers (6x), GPS receivers (2x), GPS antenna, star sensors (2x), thrusters (2x), momentum wheel bearings, magnetorquers(3x), power management system, transceiver, communications antenna. There are therefore 20 instruments on board with which the OBC interfaces with. This results in a command data rate of 3.2 [Mb] per orbit. An orbital period of 5336.985 [s] results in a data rate of 0.5996 [kb/s].

6.6.2. On-Board Computer and Data Acquisition Unit Sizing

The OBC and data acquisition must work in unity in order to receive the data from the payload and sensors around the spacecraft. Different channels must be used to accommodate the different data inputs. Therefore it is necessary to identify which channels are necessary, and from there, the OBC and data acquisition unit can be chosen. As alluded to, the I²C channels will be used for the housekeeping data sensors. Additionally, the propulsion, ADCS and EPS systems, as well as all payload instruments, with the exception of the star sensors, can make use of the I²C. This is because I²C can provide 100 [kb/s] in standard mode, with up to 400 [kb/s] in fast mode. The total bit rate of command, housekeeping, and payload, not including the star sensors is 47.68 [kb/s]. This means I²C is sufficient, even without the fast mode. The star sensors have an output of 625 [kb/s] and have a RS485 interface. Additionally, the transceiver has a RS-485 or CAN interface. For these instruments the I²C isn't compatible, and thus won't be used for the star sensor.

The ISIS On-Board Computer is an OBC designed for implementation within CubeSats, with flight heritage since 2014, depicted in figure Figure 6.26 [94]. It has a clock speed of 400 [MHz], with connections



Figure 6.26: The On-board computer from ISISPACE, which will be used in the spacecraft [94]

available for I²C, 2 UART connections (RS232 + RS232/RS485/RS422), ADC, JTAG and USB. I²C will allow for the ISIS On-Board Computer to handle the housekeeping and payload data. The I²C channel provides up to 128 unique identifiers, more than the amount needed for MAGEOS, as it has only 49 sensors and 17 other instruments (star sensors and transceiver not included). The clock speed of the ISIS On-Board Computer is enough to allow the I²C to operate all I²C channels. Additionally, one of the UART connections works for RS-485, allowing the transceiver or a star sensor to be connected. The other UART connection is, however, RS232. This means neither a star sensor or the transceiver can be attached. With the usage of a bi-directional RS485 - RS232 converter, either instrument could use the RS232 channel. An example of such a converter is the SerialComm RS232 to RS485 bi-directional converter [95], which will be used in MAGEOS. Still, there would be 1 channel too little. Therefore from ISISPACE, an ISIS EM Daughter Board can be included on the OBC. This board adds additional RS-232 interfaces, which can be compatible with the transceiver or star sensor using another converter. The transceiver will be connect using the RS485 interface on the OBC, one star sensor will connect using the RS232 interface on the OBC and a converter, and the second star sensor will connect using a RS232 interface on the daughter board.

With the described configuration, the OBC will allow all instruments to interface with the OBC. The ISIS on board computer also provides high reliability due to years of flight heritage, and also beneficially circumvents the need for a data acquisition unit due to the many interfaces. For this reason, it will be used for the MAGEOS mission.

6.6.3. Data Storage

The data storage on the spacecraft must be able to store all software for the operation of the spacecraft, commands that are yet to be issued, and data that is not yet sent to a ground station. Of these contributions to the data storage, the largest by multiple orders of magnitude is the payload and housekeeping data. As per TECH-OBC-1, the spacecraft must be able to store TBD bytes of data. This amount is dependent on the maximum amount of data the spacecraft could ever accumulate before being able to send it to the ground station. The most critical case for this would be if the ground station network is inoperative for some amount of time. The case for which will be designed for is that the spacecraft is not able to send any data down for 24 hours. While the total data rate is 1297.5 [kb/s] (1296.56 [kb/s] for payload data, 0.343 [kb/s] for housekeeping data, and 0.599 [kb/s] for command data), the star sensor data will be processed on board and not be sent to the ground station. Additionally, data of the magnetometers and accelerometers will be processed to require less data. They can be turned into three-dimensional vector measurements, similar to that of the GNSS receiver, requiring only 168 bits per sample, with a frequency of 10 [Hz]. This totals the bit rate of the payload that must be stored to 5.4 [kb/s]. With a day length of 86400 [s], the data storage must be able to hold at least $0.466 \cdot 10^6$ [kb], or 0.05825 [GB].

This amount of data fits on the two 2 [GB] SD cards that the ISIS OBC comes with normally, no additional

request is necessary. Using this integrated SD card slot reduces complexity, as the OBC handles the connections between the input channels and the data storage. With two SD cards, soft error correction is possible and will be performed, in accordance with TECH-OBC-4.

6.6.4. Data Handling Block Diagram

The C&DH system architecture as a whole is summarized in the data handling block diagram, as can be seen in Figure 6.27. This diagram shows: the on board computer with its interfaces; the data storage; command and data lines; the payload and housekeeping data rates; and the command data rates. Most arrows show two way communication. This is because the OBC interfaces with the instruments through I²C, or with versions of UART for the star sensors. For the blocks within the groups housekeeping data and payload data (except for the GPS antenna), as well as the transceiver, data is sent to the OBC. This data is stored in the data storage unit, except for the star sensor data. This is stored in the internal storage of the OBC for a short period of time, until it can be processed. All blocks where a command data rate is specified show how much data the OBC send to these instruments.

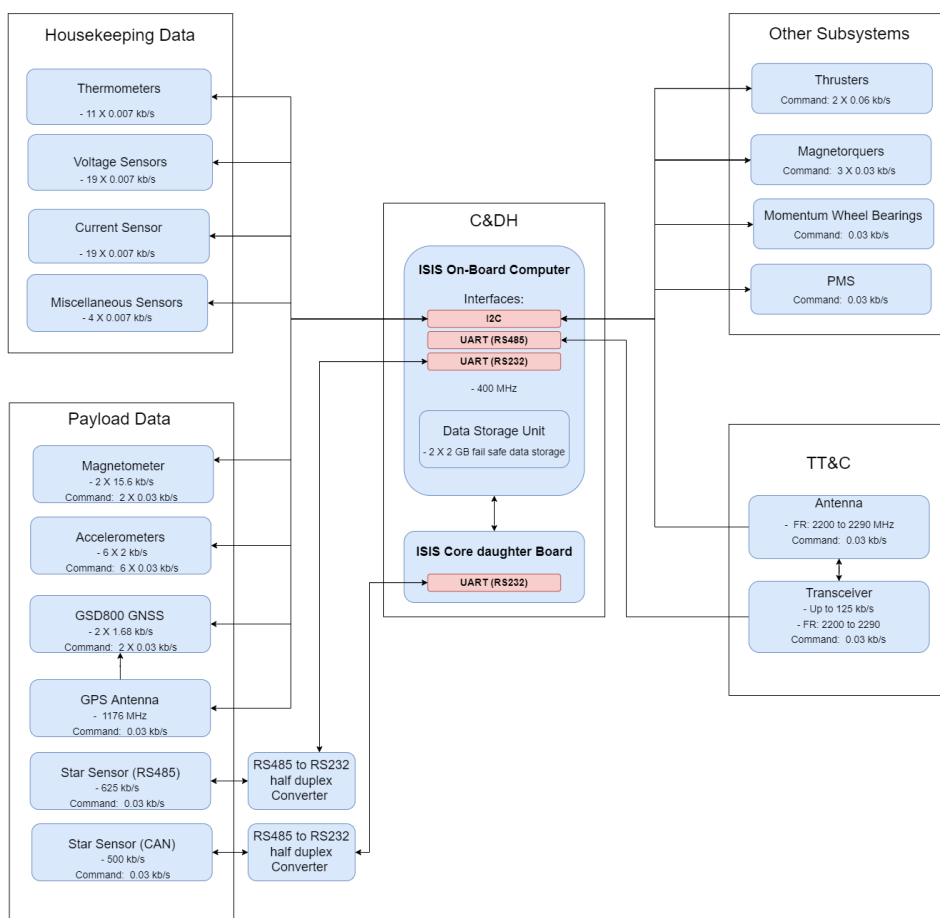


Figure 6.27: The handling block diagram showing the C&DH system architecture of MAGEOS.

6.7. ADCS

The ADCS system is a crucial subsystem which influences the accuracy of the measurements during flight. The attitude determination has the greatest influence as this subsystem will gather data about the orientation of the spacecraft from which the attitude error is deduced. The attitude control subsystem will ensure the stability of the spacecraft platform. These systems are resized such that the requirements are met.

Table 6.20: The ADCS requirements of MAGEOS [1]

Identifier K=Key, D=Driving, R=Removed	Requirement	V & V Method
TECH-ADCS-1 (K)	The ADCS system shall be derived from the SHAPE ADCS platform	Inspection
TECH-ADCS-2	The center of mass of the spacecraft shall be within TBD 70mm of the spacecraft Geometric centre	Test/ Model
TECH-ADCS-DET-1	The spacecraft shall be able to determine it's attitude with an accuracy greater than 1°	Analysis
TECH-ADCS-CTRL-1 (R)	The ADCS system shall provide a stable platform for the magnetometer measurements	N/A
TECH-ADCS-CTRL-2 (R)	The ADCS system shall provide a stable platform for the gravimeter measurements	N/A
TECH-ADCS-CTRL-3 (R)	The ADCS system shall provide a stable platform for Earth observation	N/A
TECH-ADCS-CTRL-4 (R)	The ADCS system shall continuously counteract the disturbance torques on the spacecraft	N/A
TECH-ADCS-CTRL-5	The ADCS system shall provide a pointing accuracy of greater than 1°	Analysis
TECH-ADCS-CTRL-6	The ADCS system shall provide an attitude stability greater than 0.1°/s	Analysis

6.7.1. Mass Moment of Inertia Analysis

A major part of the stability and controllability of the spacecraft is the Mass Moment of Inertia (MMOI). It is of importance that the MMOI is as small as possible and that the Center of Mass (CoM) is as close as possible to the Geometric center (CG). This section will cover the analysis process and end results of the (final) design. Further is the verification and validation process of the analysis and design elaborated.

6.7.1.1. MMOI Analysis process

The MMOI analysis requires two data sheets to determine the MMOI and CoM of the spacecraft. A data sheet with a list of components and their properties such as dimensions, position, mass and which unit this component belongs to. The other data sheet contains the spacecraft configuration, meaning the amount of units used and placed with respect of each other. It also contains the information about the deployed solar panel configuration. Figure 6.28 gives an overview of the analysis process. As seen in the figure is the information from the spacecraft configuration extracted. Together with the component data sheet, components are filtered out per unit such that the program is able to calculate the CoM and MMOI properly. The Center of Mass for each unit is calculated. Further, using the positions of the units and solar panels, the center of area is calculated. Then using all the processed information, the CoM and MMOI of the whole spacecraft is calculated. A deeper look will be given to the position and MMOI calculation. These will be discussed to further elaborate the analysis process.

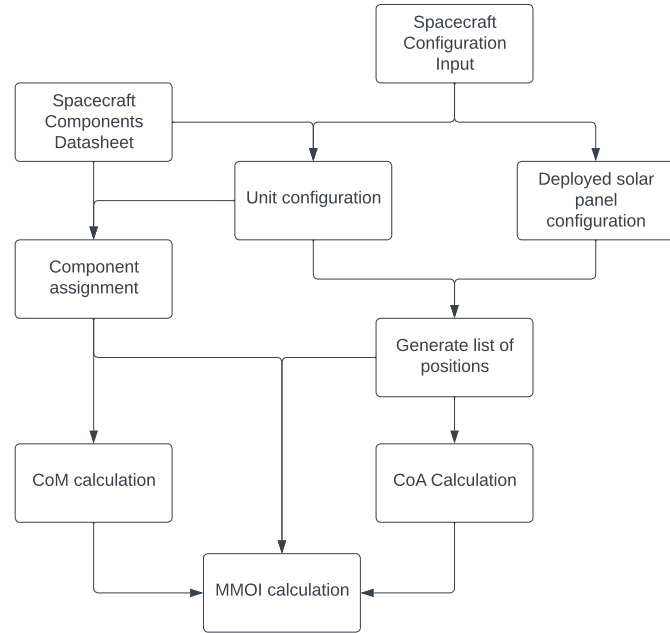


Figure 6.28: Flow chart of the MMOI analysis process.

Firstly, the calculation process of the position for each solar panel and unit. This process locates the different components to a reference point. Then the geometric center is located by taking the average position of the occupied area. This is done with Equation 6.35.

$$\vec{p}_{GC} = \frac{\sum \mathbf{A} \cdot \vec{p}}{\sum \mathbf{A}} ; \quad \mathbf{A} = \begin{bmatrix} A_x & 0 & 0 \\ 0 & A_y & 0 \\ 0 & 0 & A_z \end{bmatrix}, \quad \vec{p} = \begin{bmatrix} p_x \\ p_y \\ p_z \end{bmatrix} \quad (6.34)$$

$$\vec{p}_{CoM} = \frac{\sum m \cdot \vec{p}}{\sum m} \quad (6.35)$$

Where p is the position vector of each unit/solar panel and the area matrix A as defined in Equation 6.35. Further are the position of the components related to the geometric center of the unit, which is exactly in the centre of the unit structure. Using that information the center of mass of a unit can be determined together with its MMOI around the CoM. The MMOI of a component is determined by simplifying the component into a cuboid shape. The equation to calculate the MMOI of a cuboid is given as follows. Here the l_x , l_y and l_z are the dimensions as presented in Figure 6.29. The subscript is the indication of the length along that axis direction.

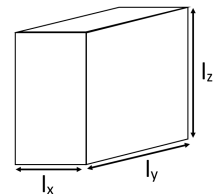


Figure 6.29: Dimensions of a cuboid.

$$\begin{bmatrix} I_{xx} \\ I_{yy} \\ I_{zz} \end{bmatrix} = \frac{1}{12} m \cdot \begin{bmatrix} l_y^2 + l_z^2 \\ l_x^2 + l_z^2 \\ l_x^2 + l_y^2 \end{bmatrix} \quad (6.36) \quad \begin{bmatrix} I_{xx} \\ I_{yy} \\ I_{zz} \end{bmatrix}_{\text{CoM}} = \begin{bmatrix} I_{xx} \\ I_{yy} \\ I_{zz} \end{bmatrix} + m \cdot \begin{bmatrix} (p_y - p_{y\text{CoM}})^2 + (p_z - p_{z\text{CoM}})^2 \\ (p_x - p_{x\text{CoM}})^2 + (p_z - p_{z\text{CoM}})^2 \\ (p_x - p_{x\text{CoM}})^2 + (p_y - p_{y\text{CoM}})^2 \end{bmatrix} \quad (6.37)$$

After the calculation of the components in an unit, Steiner's theorem is applied to obtain the MMOI around its CoM or CoA. Steiner's equation can be seen in Equation 6.37. This equation is to get the MMOI around the CoM. To get the MMOI around the CoA, the p_{CoM} is replaced with p_{GC} .

Verification procedure of Simulation Tool

The verification of the simulation tool was done by taking a reference geometry with dummy components. The center of mass for each of the individual units was calculated together with the MMOI around each axis. After manually checking if the position for each units are correct with respect to the CoA, is the CoM checked together with the mass moment of inertia. During these system tests, frequent unit tests are conducted to check for any wrongly converted SI units, lost data or wrongly formatted data.

6.7.2. Momentum Wheel

The bias momentum wheel provides passive stability. Momentum wheels use the gyroscopic effect to reduce the rotation induced by disturbance torques. The momentum wheel provides no control itself, it simply reduces the effect of disturbances. Therefore, the momentum wheel works in conjunction with the magnetorquers; the wheel reduces the disturbances, thereby increasing pointing accuracy, and the magnetorquers correct for the reduced disturbance. The momentum wheel is sized after the structure, mass and geometry have been determined as its requirements are entirely dependent on these criteria. Furthermore, the orbital period used for calculations is 5337 [s]. The momentum wheel design is from the original SHAPE platform [96] but must be scaled for MAGEOS. The coordinate system used for the design of the momentum wheel is presented in Figure 6.30.

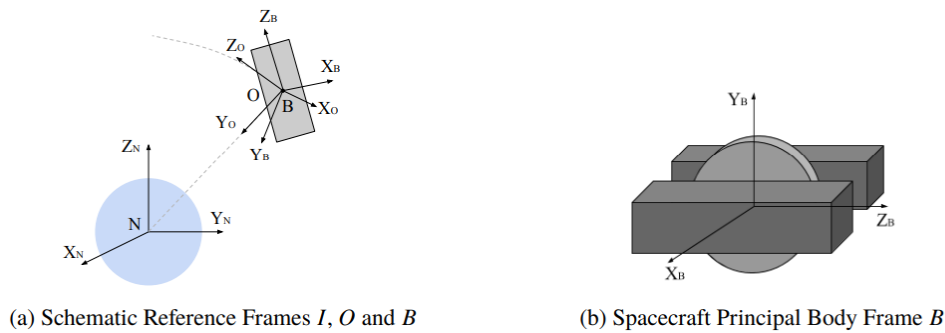


Figure 6.30: Momentum wheel reference frame from SHAPE platform [96].

Figure 6.31 details how the gyroscopic effect reduces the impact of disturbance torque.

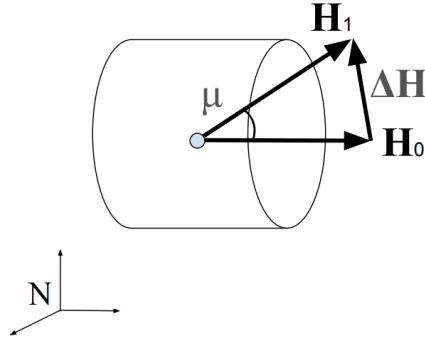


Figure 6.31: Momentum wheel response to disturbance [96].

The angle μ is dependent upon the magnitude of the disturbance angular momentum ΔH . Following this disturbance, the wheel settles with a new angular momentum vector H_1 . μ is effectively the resulting drift from the desired spacecraft attitude due to a disturbance torque. Typically, the maximum allowable μ is given per orbit; for SHAPE it is 1 [Deg] as per requirement TECH-ADCS-CTRL-5. This means that, per orbit, the spacecraft pointing angle is allowed to shift 1 [Deg] due to these disturbance pointing torques. The magnetorquers can then correct for this change.

$$\mu = \frac{\tau t_n}{\|H\|} \quad (6.38)$$

The angle μ due to a given disturbance can be reduced by increasing the angular momentum of the wheel as seen in Equation 6.38. The sizing of the momentum wheel is therefore dependent on the magnitude of the disturbance torques and their effect duration per orbit; the change in angular momentum due to these disturbance torques in a single orbit. It is necessary, therefore, to quantify these disturbance torques.

There are four main sources of torque disturbance for a spacecraft [96]. These are:

- Gravity gradient disturbance
- Aerodynamic disturbance
- Magnetic field disturbance
- Eddy-current disturbance

All but the aerodynamic torque can be neglected. This is done because, due to VLEO, the aerodynamic disturbance torque will be two orders of magnitude greater than the others. Typical gravity gradient torques are in the order of 10^{-7} [Nm], magnetic field torques are in the order of 10^{-7} [Nm] and eddy current torques are in the order of 10^{-8} [Nm]. For VLEO, aerodynamic torques are in the order of 10^{-5} [Nm] [96]; therefore at least a factor 100 greater than the others. Furthermore, non-aerodynamic torques are cyclic meaning that during a full orbit their disturbances to the pointing angle will roughly 'even out'.

Aerodynamic torque must be approximated before sizing can be done.

6.7.2.1. Aerodynamic Disturbance Torque

As the spacecraft orbits the Earth it experiences a drag force due to the limited atmosphere in LEO. This drag force acts at the centre of pressure of the spacecraft. The centre of pressure does not necessarily coincide with the centre of mass; the distance between these points results in a torque.

For the design of the momentum wheel, the maximum expected aerodynamic torque is used as an

approximation. This occurs when the centre of mass is furthest from the centre of pressure. This maximum distance is assumed to be 7 [cm]. This value is considered an overestimation of the worst-case as the spacecraft is designed such that the centre of mass coincides exactly with the centre of pressure and for minimum c.g. shift. The equations for this maximum disturbance are given by Equation 6.39 and Equation 6.40.

$$F_a = -0.5\rho C_D v^2 \vec{v} S \quad (6.39)$$

S is the incident surface area, v the velocity magnitude and \vec{v} its unit vector.

$$\tau_a = \vec{I}_{cp} \times \vec{F}_a \quad (6.40)$$

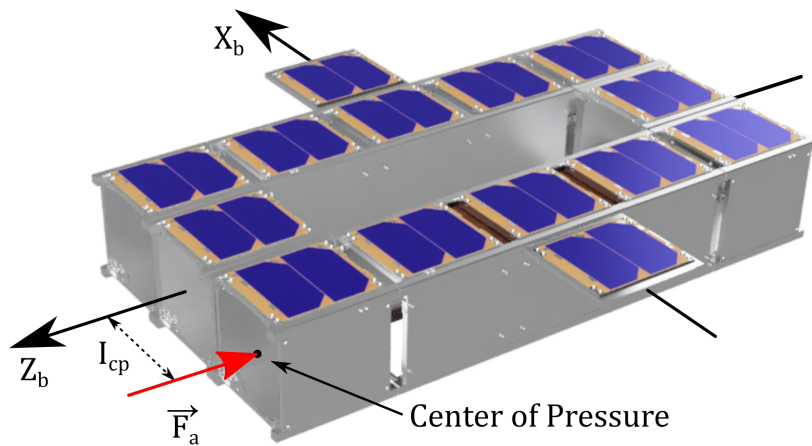


Figure 6.32: Aerodynamic disturbance torque (with example CubeSat as reference).

Figure 6.32 provides a simple illustration of how a torque is generated by this distance. \vec{I}_{cp} is the vector between the centre of pressure and centre of mass. This vector is taken to be the maximum; 7 [cm] distance along the x axis. The aerodynamic variables are given in Section 7.1. The resulting maximum aerodynamic torque is determined to be $2.1 \cdot 10^{-5}$ [Nm]. This corresponds to an angular momentum requirement of 6.423 [Nms] to keep μ below 1 [Deg] per orbit. The aerodynamic disturbance is by far the largest factor; this is the driving requirement for the momentum wheel design.

6.7.2.2. Sizing

With a defined angular momentum requirement the wheel can be sized. Beginning with the formula for angular momentum of a hollow cylinder Equation 6.41.

$$H = I_{xx}\omega \quad (6.41)$$

The angular velocity ω is chosen to be 8000 [rpm]; the given momentum wheel design of SHAPE must run above 5000 [rpm] for the magnetic bearings to function. This can be used to derive the required moment of inertia of the momentum wheel from Equation 6.41. The required mass moment of inertia about the spin axis is therefore 7.66694×10^{-3} [kg/m²]. This mass moment of inertia is a function of the cylinders inner and outer radius, thickness and material density as per Equation 6.42. The mass of a hollow cylinder is given by Equation 6.43.

$$I_{xx} = 0.5m(r_o^2 + r_i^2) \quad (6.42)$$

$$m = \rho\pi t(r_o^2 - r_i^2) \quad (6.43)$$

Substituting Equation 6.43 in to Equation 6.42 and defining $\zeta = \frac{r_i}{r_o}$ results in Equation 6.44.

$$I_{xx} = 0.5\rho\pi tr_o^4(1 - \zeta^4) \quad (6.44)$$

Finally, this is rearranged to get the outer radius of the momentum wheel r_o as a function of the material density ρ , the ratio of outer to inner radius ζ and the wheel thickness t as in Equation 6.45.

$$r_o = \left(\frac{2I_{xx}}{\rho\pi(1 - \zeta^4)t} \right)^{\frac{1}{4}} \quad (6.45)$$

ζ and t are defined as 0.8 and 8 [cm] respectively. A limit of 12 [cm] is set upon the outer radius of the wheel to constrain the momentum wheel to the 3 units of space available in the centre of the spacecraft configuration seen in Figure 6.36. The material is chosen to be aluminium 6061 as this is the material of the original SHAPE momentum wheel [96]. This has a density of 2700 [kg/m³]. The resulting wheel has a mass of 0.88 [kg].

6.7.2.3. Final design

The final momentum wheel can be seen in Figure 6.33.



Figure 6.33: Final momentum wheel design.

6.7.3. Magnetorquer

The magnetorquer will provide stability about the other two axis the momentum wheel cannot. The magnetorquer is designed by van Hengel, and the relevant design parameters are provided by [97]. Figure 6.34 shows a sensitivity analysis, where the current is varied of an optimised design, and the changes in mass, volume, produced magnetic dipole moment and power are noted. The sensitivity analysis is performed with different core options, elaborated on in [97]. In the work 4-79 Mo-Permalloy was identified as the best core material overall, with "14.2 [mm] in length and 12.9 [mm] in diameter, and will have a mass of 18.1 [g]" [97].

Crucially, the power is in the order of [mW], vastly below the power requirements of other subsystems. Hence, it is negligible in this analysis. Additionally, it can be observed that for increasing current the magnetic dipole moment increases, meaning that more power (within reason) can be supplied to the magnetometer and a linear increase in magnetic dipole moment is expected.

The analysis performed in [97] shows that the volume of one magnetometer is $(\pi * 14.2[\text{mm}]/2)^2 * 12.9[\text{mm}] = 6.4 [\text{ml}]$ and its mass is 18.1 [g], to produce a magnetic dipole moment of 0.5 [Am²]. The input power can be varied outside of the range used in [97] to produce a larger magnetic dipole moment if needed to provide more control authority.

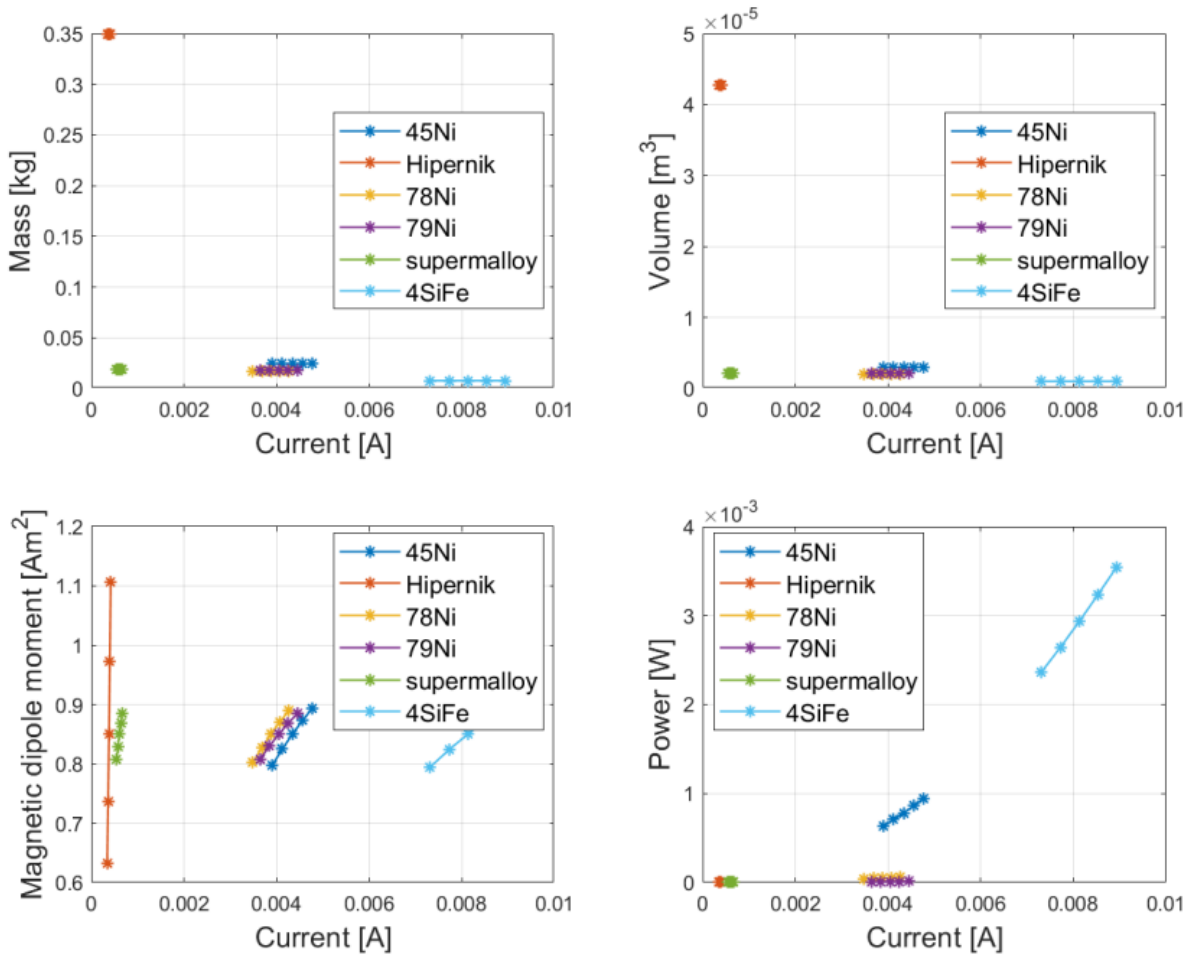


Figure 6.34: Sensitivity Analysis of Magnetorquer with varying supplied current [97].

6.7.4. Star Sensor

When performing a measurement, the magnetometer instrument determines the magnetic field vector in its own reference frame, frame B . In order to express this vector in the reference frame of the Earth, frame E , a transformation T_{EB} must be applied. The required transformation is shown in Equation 6.46

$$\vec{B}|_E = T_{EB} \cdot \vec{B}|_B \quad (6.46)$$

Constructing the T matrix requires that the orientation of the S/C be accurately known relative to the Earth, therefore a star-tracker will determine the S/C's orientation relative to outer space. The star

sensors from [98], and shown in Figure 6.35, are used, as they are able to determine the attitude of the S/C in relation to outer space to within 5 [arcsec] at 3σ . The RMS error is therefore $\epsilon_{\alpha} = 5/3 = 1.66$ [arcsec].

The maximum intensity of the magnetic field experienced by MAGEOS can be determined using Equation 5.3. At $h = 229.7$ [km], the maximum intensity, achieved at the poles, is 56102 [nT]. Using Equation 6.47, the RMS error due to lack of sufficient attitude determination knowledge is shown. For MAGEOS, the magnetic field error can be determined to be 0.45 [nT].

$$\epsilon_{RMS,B} = \epsilon_{RMS,\alpha} \cdot |B| \quad (6.47)$$



Figure 6.35: KairoSpace Star Tracker.

6.8. Final Configuration

In order to determine the size the ADCS subsystem components should have, the position of the center of gravity, as well as the moments of inertia must be known. For this, the configuration of the spacecraft should be determined. The final outer structure can be seen in Figure 6.36.



Figure 6.36: A MAGEOS spacecraft from above



Figure 6.37: A MAGEOS spacecraft from the below

To determine the center of gravity and the moment of inertia, the location of each component in the

spacecraft must be known as well. This layout can be seen in Figure 6.38.

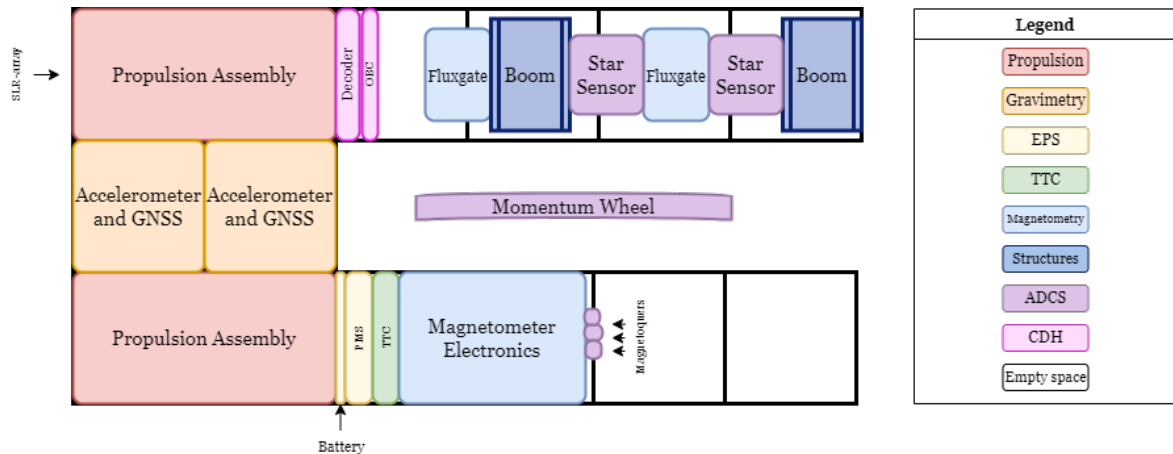


Figure 6.38: The internal component layout of a MAGEOS spacecraft. The spacecraft velocity vector is to the right in this image

The propulsion system of the spacecraft must be all the way at the back, to ensure the exhaust plumes from the thrusters do not interfere with any other subsystem. This is the left side in Figure 6.38. The 2U propulsion assemblies are set at the left and right side at the back of the spacecraft. As the momentum wheel will be occupying the center of gravity, an accelerometer cannot be placed there. An off-center accelerometer will measure accelerations due to rotation in addition to actual accelerations. This problem can be alleviated by including two accelerometer units, so their accelerations can be compared to cancel out rotational effects. The accelerometer units are placed in between the propulsion assemblies, and they are arranged such that the individual accelerometers for each axis are not in line with the corresponding accelerometers in the other cube, so the effects of rotations on the measured accelerations can be effectively removed. The gaps present within the accelerometer units are adjacent to one another, forming a larger hollow space inside of them. This space is sufficient large to accommodate the GNSS receivers and their antennas side by side.

The left side of the spacecraft is mostly dedicated to the magnetometer boom, as both collapsed boom elements, the star sensors, and the fluxgate magnetometers are stored in these units. At the start of the mission, this entire boom will be rotated out until it is arrayed in the velocity direction, after which it will be extended to hold the magnetometers at the desired distance from the spacecraft. The left side of the spacecraft also contains the CDH subsystem, which was placed here for balance reasons. The center of the spacecraft does not contain any cubesat units, instead four units worth of space are left open to accommodate the momentum wheel, the center of which should coincide with the center of mass of the entire spacecraft. The right side of the spacecraft is dedicated to the remainder of the spacecraft components. In order from the back of the spacecraft to the front, the right side contains the EPS subsystem, the TTC subsystem, the electronics box for the magnetometer, and finally the three magnetorquers. This leaves nearly two entire cubesat units at the front right empty. This arrangement of components was chosen because the deployed boom shifts the center of mass forward very significantly, and so the remaining components were shifted to the back of the spacecraft as much as possible. Therefore, although more components could be incorporated into these empty units, this would only worsen the forward shift of the center of mass, and so it was deemed to be preferable to leave this space empty.

14 solar array units are needed to provide power to the spacecraft. Each of these units has dimensions

of 10 x 10 [cm]. conveniently, the MAGEOS spacecraft also has 14 cubesat units. The configuration of the solar panels can therefore be quite simple: every cubesat unit will be covered by a solar array unit. This simplifies the design, as all the cubes are mostly uniform on the outside, and so deployed solar panels are present.

The configuration of a MAGEOS spacecraft results in the center of geometry being positioned at 27.1 [cm] from the back face of the spacecraft. Due to the symmetry of the other axes, the center of geometry is located halfway the width and height of the spacecraft, 15 [cm] from the side and 5 [cm] from the bottom. With the configuration of components aboard the spacecraft, at the start of life the center of mass is 109 [mm] forward of the center of geometry, 0.13 [mm] to the left, and 1.76 [mm] above it. This means that the momentum wheel must be attached to the third row of units from the front, where it is placed 31 [mm] in front of the center of those units of the spacecraft. This way its centroid coincides with the center of gravity of the spacecraft. The moment of inertia about each axis are as follows: $I_{xx} = 5.53 \cdot 10^6$ [kg mm²], $I_{yy} = 1.71 \cdot 10^5$ [kg mm²] and $I_{zz} = 5.66 \cdot 10^6$ [kg mm²].

As propellant is consumed to maintain the orbital altitude, the position of the center of mass also shifts. The furthest position the center of mass can deviate, occurs when all the propellant is consumed. At this point, the center of mass moves to 26.8 [mm] ahead of the momentum wheel, degrading the stability of the spacecraft. This is accepted as an inevitable event which will be taken into account whilst using the data acquired later in the mission lifetime, as any attempt to mitigate the shift during the mission would be far too complex and prone to failure.

Chapter 7: Design Analysis

7.1. Aerodynamic Characteristics

In this section, the drag and lift coefficient for the MAGEOS spacecraft, C_d and C_l , will be determined. In Section 7.1.1, the used method and assumptions made will be explained. Since this method uses a new developed Python code, this code will be verified and validated in Section 7.1.2. The results for the lift and drag coefficient determination will be presented in Section 7.1.3.

7.1.1. Method and Assumptions for the Aerodynamic Parameter Estimation

The determination of the lift and especially the drag coefficient is important for the design of a space mission in a very low Earth orbit. The main reason for this, is that for this region of altitudes, the air is much denser compared to the more higher located altitudes [99]. A direct consequence of this is that the drag force in this region will also be higher, and will therefore decrease the mission life of a spacecraft [99]. The drag force of a spacecraft can be found making use of Equation 7.1.

$$D = \frac{1}{2} \rho V^2 A_{ref} C_d \quad (7.1)$$

In Equation 7.1, C_d represents the drag coefficient, which is a parameter depending on an objects geometry [100]. For geometries in a continuous flow, computational fluid dynamics can be used to determine the drag coefficient parameter. However, when a geometry is located outside the continuous flow, this tool can no longer be used. This is due to the fact that particles are no longer behaving as a fluid, but as independent particles [101]. These particles interact with the spacecraft wall. There are two types of interactions: incident particle flux, where particles will collide with the geometry wall and will thereby lose all their kinetic energy and re-emitted particle flux, where parts of the particles will not fully emit their kinetic energy with the spacecraft wall but will "bounce" to the spacecraft wall and will thereby retain parts of their initial kinetic energy [101]. To determine the lift and drag coefficients, use is being made of the Sentman equations for free molecular flow for a flat plate [102], shown in Equation 7.2 and Equation 7.3, making use of rewritten equations [101].

$$C_{l_{i,j}} A_{ref_i} = \left[l_i Q_j Z_{i,j} + \frac{l_i}{2} \frac{v_{re}}{v_{inc}} (\gamma_i \sqrt{\pi} Z_{i,j} + P_{i,j}) \right] A_i \quad (7.2)$$

$$C_{d_{i,j}} A_{ref_i} = \left[\frac{P_{i,j}}{\sqrt{\pi}} + \gamma_i Q_j Z_{i,j} + \frac{\gamma_i}{2} \frac{v_{re}}{v_{inc}} (\gamma_i \sqrt{\pi} Z_{i,j} + P_{i,j}) \right] A_i \quad (7.3)$$

Where G_j , $P_{i,j}$, Q_j and $Z_{i,j}$ are given by Equation 7.4, 7.5, 7.6 and 7.7 respectively.

$$G_j = \frac{1}{2S_j^2} \quad (7.4)$$

$$P_{i,j} = \frac{1}{S_j} e^{-\gamma_i^2 S_j^2} \quad (7.5)$$

$$Q_j = 1 + G_j \quad (7.6)$$

$$Z_{i,j} = 1 + erf(\gamma_i S_j) \quad (7.7)$$

In Equation 7.7, the error function, shortened $erf(x)$, is used. The definition of the error function is presented in Equation 7.8.

$$erf(x) = \frac{2}{\sqrt{\pi}} \int_0^x e^{-y^2} dy \quad (7.8)$$

To determine the speed ratio S_j , which can be seen in Equation 7.9, which is an important parameter to determine the incident particle flux, use being made of Equation 7.10 which determines a particle most probable thermal velocity [101]. In this equation, the total temperature in the orbit should be used. This will be obtained from the NRLMSISE-00 model [103].

$$S_j = \frac{v_r}{c_{mpj}} \quad (7.9)$$

$$c_{mpj} = \sqrt{2 \frac{k}{m_j} T} \quad (7.10)$$

The subscript j represents the particle type present. In the simulation, all the particles from the NRLMSISE-00 model will be used and summed over. This summation will be done according to Equation 7.11. Where C_{a_i} is either the drag coefficient or the lift coefficient. The particles considered are helium, dioxygen, dinitrogen, oxygen, argon, hydrogen and nitrogen [103]. To obtain the density of each particle, Equation 7.12 is being used.

$$C_{a_i} = \sum_j \frac{\rho_j}{\rho} C_{a,j,i} \quad (7.11)$$

$$\rho = n \frac{M}{N_a} \quad (7.12)$$

To determine the velocity of the re-emitted particles, use is being made of Equation 7.13. In this equation, the energy accommodation coefficient α is being used. This coefficient determines the amount of kinetic energy the incident particles will have after they have been re-emitted by the spacecrafts wall [101]. The energy accommodation coefficient differs for different altitudes. Furthermore, this is dependent on the number density of the particles as well as the temperature [101]. To obtain the correct energy accommodation coefficient for the correct altitude, use is being made of Equation 7.14.

$$\frac{v_{re}}{v_{inc}} = \sqrt{\frac{1}{2} \left[1 + \alpha \left(\frac{4RT_w}{v_{inc}^2} - 1 \right) \right]} \quad (7.13)$$

$$\alpha = \frac{5 \cdot 10^{-17} n_o T}{1 + 5 \cdot 10^{-17} n_o T} \quad (7.14)$$

The above presented method is valid for a flat plate, under a certain angle with the incoming flow. A definition of this angle is presented in Figure 7.1. The angle θ is being used in Equation 7.15 and Equation 7.16 to obtain γ_i and l_i .

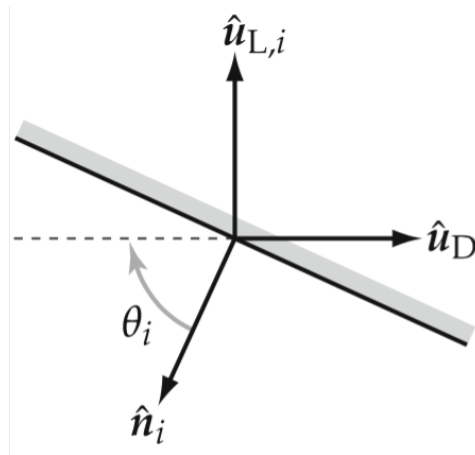


Figure 7.1: Definition of angle θ_i for a flat plate [101]

$$\gamma_i = \cos \theta_i \quad (7.15)$$

$$l_i = \sin \theta_i \quad (7.16)$$

To specify a certain geometry, the geometry is divided in panels. For each panel, the lift and drag coefficient will be calculated, where after it will be summed up scaled to a certain reference area. For this simulation, the shaded area of each individual plate will be used as reference area, so the area

which will be seen by the incoming particles [104]. This can be seen in Figure 7.2. The subscript i in all the aforementioned equations are specifying each individual plate. To obtain the total lift and drag coefficient for a specified geometry, Equation 7.17 is being used. Where A_{ref} is the summed contribution of all individual reference areas.

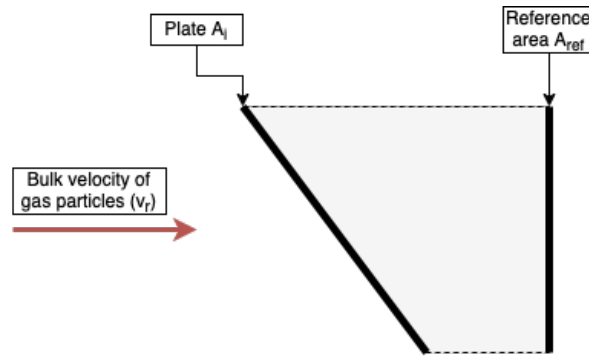


Figure 7.2: Reference area as seen by the incoming particles

$$C_a = \sum_i \frac{C_{a_i} A_{ref_i}}{A_{ref}} \quad (7.17)$$

A Python code has been developed to perform the calculations for a the specified spacecraft geometry. A flow diagram of the code is given in Figure 7.4. From the flow diagram, it could be seen that the inputs for the code are the geometry of the spacecraft, as well as the orbital altitude. The spacecraft geometry should be provided in terms of areas of each individual plate in $[m^2]$. It should be noted that the spacecrafts geometry is simplified as only containing the frontal panels, as well as the top panels. The reason for this simplification is that the bulk velocity vector is orthogonal over an entire orbit, and that there is no sideslip. Due to this simplification, it is assumed that the particles will not interact with the surfaces on the side and back of the geometry. The flow could interact with the front and back of the panel due to the difference in pitch velocity. An example of a geometry simplification for a cube can be seen in Figure 7.3.

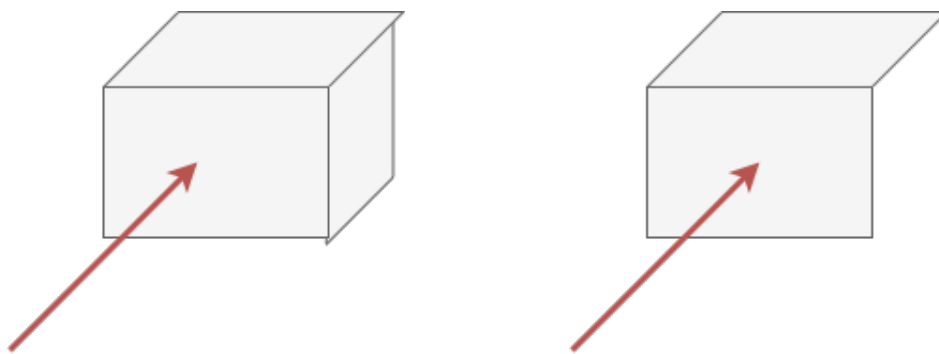


Figure 7.3: Simplification of geometry of a cube. On the left, a normal cube having six sides. On the right the simplified geometry only containing out of 2 sides of the cube. The red arrows represents the incoming particles direction

Another input of the code is the spacecrafts orbital altitude, given in $[km]$. From the inputs, the orbital velocity will be calculated making use of Equation 7.18, assuming a circular orbit. Furthermore, from the NLRMSISE-00 model, the density, temperature and number density of each longitude and

latitude will be obtained. From the temperature and number density of atomic oxygen, the energy accommodation coefficient can be obtained making use of Equation 7.14. Making use of the Sentman equations, provided the spacecrafts geometry, the bulk velocity as well as the density, temperature and number density of each particle, iterating over angles ranging from 0-90 [deg] of pitch angle of the spacecraft, latitudes, longitudes, plates of the spacecraft geometry and all particles in the atmosphere, the drag and lift coefficient can be obtained. The maximum drag and lift coefficients for each pitch angle will be stored. With this data, a final result can be obtained, as will be further explained in Section 7.1.3.

$$V = \sqrt{\frac{\mu}{a}} \quad (7.18)$$

The developed python code can be accessed in the groups GitHub [105]. The code has been developed to ease the iteration process for orbit determination, as well as the required delta-V estimation for drag compensation and final mission time life. Furthermore, it has been used for the determination of the amount of propellant needed for the mission.

For the development of this code, certain assumptions have been made, as well as choices. The most important choice of is the choice of Sentman's model for molecular flow and the accompanying equations. Although other analytical models exists to predict the lift and drag coefficient for a spacecraft, such as Cook's and Schaaf and Chamber's model [104], Sentman's model was chosen due to the simplicity of the model, as well as the widely available literature. The simplicity of the model was an important parameter due to the limited time available to develop the code. The downside of this model is that it is less accurate, compared to other models. However, Sentman's model is overestimating the lift and drag coefficients. Therefore, it will also overestimates drag which could potentially lead to higher mission time life since the real experienced drag will possibly be lower. Another downside of Sentman's model is that it oversimplifies the random motion of particles by making use of the energy accommodation coefficient [101]. To have a more accurate prediction of the random motion of particles, the use should be made of Direct Monte Carlo Simulation, shortened DSMC. The decision was made to use the simplified method due to the complexity of implementing the DSMC method in Sentman's model as well as the time constrain.

The last assumption that causes discrepancies is the assumption to simplify the geometries to be existing out of panels, not taking into account the sides that are not being opposed to particles. In reality, there will be sideslip, such that those panels will be opposed to particles. Furthermore, due to panels, the geometry of the spacecraft is being oversimplified and more detailed areas such as antennas will not correctly be account for in the simulation.

For the final analysis of the spacecraft geometry, it is recommended to make use of the ADBsat software [106]. This software package makes use of different models and DSMC to obtain the lift and drag coefficients of a geometry. Although in this software use made of a panel method as well, a more specified mesh can be generated by uploading a CAD file of a geometry. The reason why this approach has not been used in this report is the time consuming CAD file development, as well as the processing time of each individual run of the program.

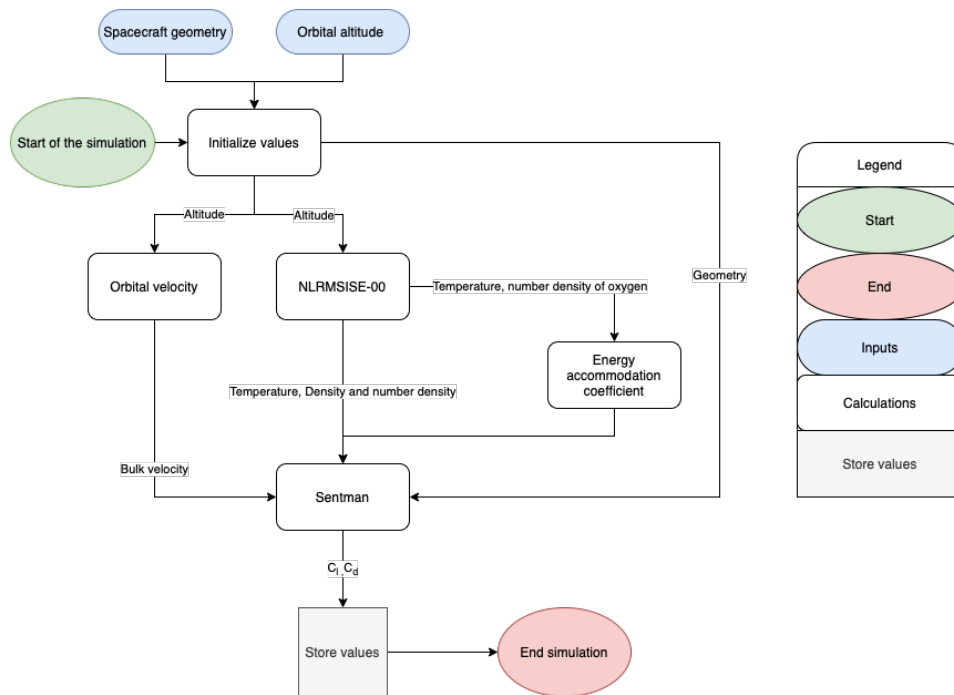


Figure 7.4: Flow diagram of the developed code to obtain the drag and lift coefficient

7.1.2. Verification and Validation for the Aerodynamic Parameter Estimation

Verification and validation of a developed code is very important. For the aerodynamic parameter estimation Python code [105], it is very hard to perform validation on the code. It is unknown at this point if the code predicts the lift and drag coefficient correctly because there are no measurement points available at this time.

For the verification process, another in house model will be used. These codes will be compared on their given lift and drag coefficient. Since two different models has been used for these codes, slight deviations in shape of the graphs can occur. It has been found that the shapes of the curve are very similar compared to each other. Another verification method that has been used is walk-through-testing. Each line of code has been examined closely on mistakes in formulas, constants and inputs. No major mistakes or deviations has been found during this process, and the slight deviations that were found, being making use of the wrong constants, has been corrected. Furthermore, degenerate testing, checking whether an input change in a function will generate the expected output change, as well as extreme value testing, the codes reaction to unpredicted inputs, has been performed. The code behaved as expected on these two test. Lastly, input check testing has been performed to make sure that the correct orbit altitude and spacecraft geometry has been used in the code. It was concluded that the input was correct for the final configuration of the spacecraft and orbital altitude.

With these tests performed, the code has been verified and validated. However, it should be noted that better codes exists and it is not recommended to use this code to predict the lift and drag coefficient very precisely for a given spacecraft geometry.

7.1.3. Results for the Aerodynamic Parameter Estimation

Making use of the final orbital altitude of 229.7 [km] and a geometry input as can be seen in Figure 7.6, the final lift and drag coefficient polar can be generated. It can be seen in Figure 7.5.

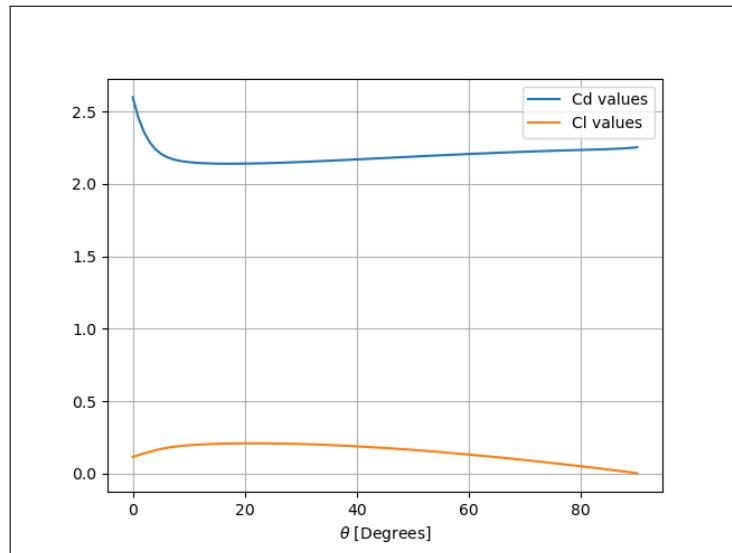


Figure 7.5: Maximum drag and lift polar of the MAGEOS spacecraft at an altitude of 229.7 [km]

From this figure, it can be seen that the maximum drag coefficient is 2.6 and a maximal lift coefficient of 0.2. This are the maximum lift and drag coefficient of the spacecraft orbit, circling around the entire Earth. The maximum drag the spacecraft will experience is predicted to be $278 [\mu\text{N}]$. It should be noted that the final drag coefficient of the drag polar is lower compared to the initial value. The reason for this is unknown, and therefore, all angles after the $45 [\text{deg}]$ will be disregarded. The angle θ is the angle between the particles direction and the front of the spacecraft, as can be seen in Figure 7.3.

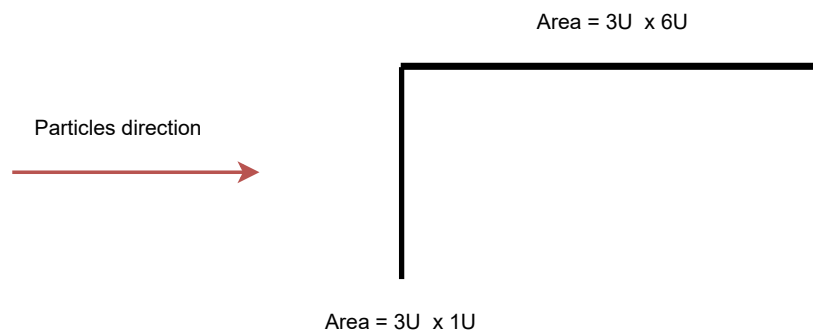


Figure 7.6: Simplified geometry of the final MAGEOS spacecraft sideview

7.2. Astrodynamics Characteristics

The astrodynamics characteristics starts with the discussion of the Keplerian elements of the insertion orbit and the operational orbit. Moreover, the ΔV required for the manoeuvre from insertion orbit to operational orbit is calculated considering several strategies. Besides, the constituents of the ΔV for orbital maintenance are treated. These 2 ΔV manoeuvres summed yield the required ΔV for MAGEOS.

7.2.1. ΔV for Orbit Insertion

manoeuvres need to be performed to reach the *operational orbit* of the MAGEOS spacecraft, ideally requiring a minimal amount of ΔV . The *insertion orbit*, defined as the orbit of the spacecraft immediately after separating from the launcher, needs to be corrected via a series of thruster burns to reach the *operational orbit*, the orbit designed in Section 5.7, in which the spacecraft will perform its mission. To manoeuvre from the *insertion orbit* to the *operational orbit*, a *coasting orbit* may be required.

Three parameters need to be corrected to reach the operational orbit. The semi-major axis a , which needs to be reduced from 6971 [km] to 6601 [km], the inclination i , which needs to be reduced from 98 [deg] to 96.4 [deg] and the longitude of the ascending node, which needs to be corrected by up to 30 [deg]. The semi-major axis and inclination of the insertion orbit were obtained in Section 5.7 following a statistical approach, where the orbits of thousands of other spacecraft were analysed. Due to the limitations of the dataset used, such an approach was unfeasible for the LTAN estimation, so an interval was assumed. The assumption that the insertion LTAN deviates by less than two hours from the operational LTAN was made. If a uniform distribution of insertion LTAN over the range of [0, 360] [deg] is assumed, this limits the available launches to 1 in 3.

An overview of the orbital elements of the insertion and operational orbit is shown in Table 7.1.

Table 7.1: Overview of Keplerian elements for the insertion and operational orbit.

Parameter	Insertion Orbit	Operational Orbit
a [km]	6971	6601
e [-]	0	0
i [deg]	98	96.42
$LTAN$ [hrs]	10PM-02AM or 10AM-02PM	12AM or 12PM
ω [°]	Undefined	Undefined

In Figure 7.7, a top-view of the Earth can be observed. On the left side of the figure, the operational orbit with a LTAN of 12AM is shown alongside the range of orbits deviating from it by less than two hours. On the right side of the figure, the same can be observed for a LTAN of 12PM. The total acceptable launch window range of 8 hours indeed corresponds to 1 of 3 available launches. Launching MAGEOS from a launch pad close to the equator within this timewindow will ensure that the insertion orbit is within the set acceptable range. MAGEOS can also be launched from a launch pad not close to the equator, as long as the calculated trajectory of the chosen launcher has an LTAN within the set allowable range.

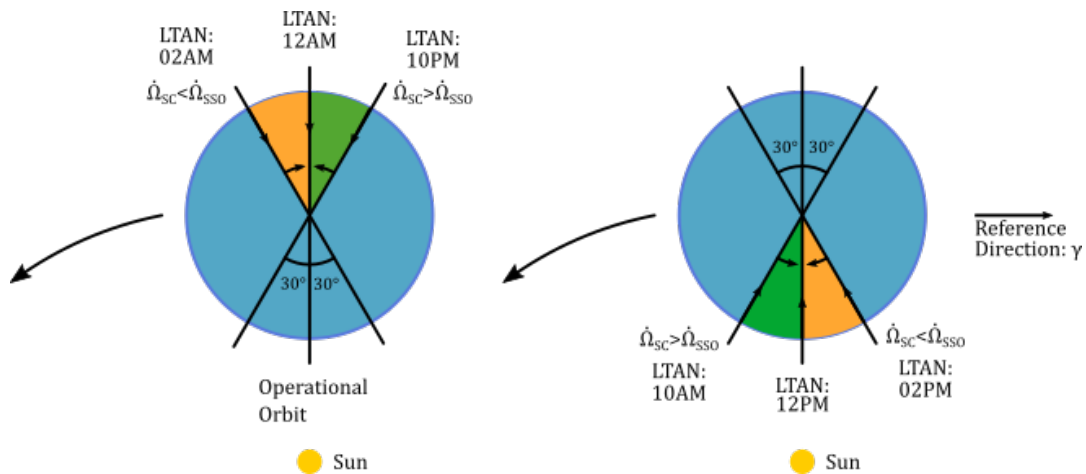


Figure 7.7: Range of acceptable launch windows to achieve an LTAN of 12AM or 12PM in the operational orbit. Orange coasting orbit has lower precession rate than operational orbit and green has higher precession rate.

Three possible strategies were identified to reach the operational orbit. In the first, a manoeuvre is performed to correct each individual Keplerian parameter, such that three distinct thruster burns are performed. In the second strategy, the inclination is corrected simultaneously with the RAAN and the

semi-major axis is corrected afterwards using a Hohmann transfer. In the third, the RAAN is passively corrected due to a difference in precession rate, and the inclination and semi-major axis are corrected using separate manoeuvres. The choice for the allowed insertion window in Table 7.1 was decided from an initial analysis as this allowed for a reasonable time to coast passively to the LTAN of the operational orbit, while the range is not too limiting.

7.2.1.1. Separate Ω and i manoeuvres

The separate Ω and i manoeuvres can be best performed at high altitude, which for MAGEOS is the insertion orbit. The required ΔV to change from the launch orbital plane (altitude of 600 [km]) at $i = 98$ [deg] to the inclination of MAGEOS at $i = 96.42$ [deg] is $\Delta V_{inclination} = 0.2085$ [km/s], independent of whether the inclination manoeuvre is performed before/after the Ω manoeuvre.

$$\Delta V_{inclination} = \sqrt{2V^2(1 - \cos\Delta i)} \quad (7.19)$$

The required ΔV for a pure Ω change can be calculated with Equation 7.20 and Equation 7.21, using the convention for the angles shown in Figure 7.8. Note that the figure shown can also be used for a pure inclination change calculation, just shown to be $\Delta V_{inclination} = 0.2085$ [km/s], or a combination of Ω and i change which will be shown in Section 7.2.1.2.

$$\theta = \arccos(\sin^2(i)(\cos(\Omega_2 - \Omega_1) - 1) + 1) \quad (7.20)$$

$$\Delta V = 2V \sin\left(\frac{\theta}{2}\right) \quad (7.21)$$

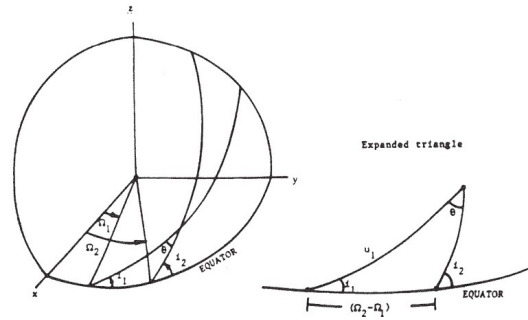


Figure 7.8: Convention of angles for orbital planes [combined_manoeuvre]

The ΔV to change the semi-major axis, is the same for all three strategies established in Section 7.2.1. The required ΔV for this Hohmann transfer can be calculated with Equation 7.22 Equation 7.23 Equation 7.24.

$$\Delta V_1 = |V_a - V_{c_{initial}}| = \left| \sqrt{\mu \left(\frac{2}{r_a} - \frac{1}{a_T} \right)} - \sqrt{\frac{\mu}{a_{initial}}} \right| = 0.10387 \text{ [km/s]} \quad (7.22)$$

$$\Delta V_2 = |V_{c_{final}} - V_p| = \left| \sqrt{\frac{\mu}{a_{final}}} - \sqrt{\mu \left(\frac{2}{r_p} - \frac{1}{a_T} \right)} \right| = 0.10530 \text{ [km/s]} \quad (7.23)$$

$$\Delta V_{Hohmann} = \Delta V_1 + \Delta V_2 = 0.20917 \text{ [km/s]} \quad (7.24)$$

The Hohmann transfer time can be calculated with Equation 7.25, assuming an impulsive manoeuvre due to the high thrust used for this manoeuvre, as will be treated in Section 7.2.1.5.

$$T_{transfer} = \frac{1}{2} \cdot 2\pi \sqrt{\frac{a_{transfer}^3}{\mu}} = \frac{1}{2} \cdot 2\pi \sqrt{\frac{(\frac{1}{2}(2R_E + r_{operational} + r_{initial}))^3}{\mu}} = 2781.6 \text{ [s]} \quad (7.25)$$

The change in Ω can be performed before or after the inclination change. In Table 7.2, the total ΔV required for the out-of-plane manoeuvres are shown for the two possible order of manoeuvres, together with the ΔV for the in-plane Hohmann manoeuvre. Notably, the difference in ΔV for all manoeuvres is relatively small. Hence, for this strategy, there is no strong preference for first performing an i or Ω change.

Table 7.2: ΔV required for a change in Ω of $\frac{\pi}{6}$ [rad], inclination change of 1.58° and Hohmann transfer

Order manoeuvres	ΔV for Δi [km/s]	ΔV for $\Delta \Omega$ [km/s]	ΔV for Δa [km/s]	$\Delta V_{insertion}$ [km/s]
First Δi , then $\Delta \Omega$	0.2085	3.8897	0.2092	4.3074
First $\Delta \Omega$, then Δi	0.2085	3.8761	0.2092	4.2938

7.2.1.2. Combined Ω and i manoeuvre

Another option considered is to combine the inclination change and longitude of ascending node change into a single manoeuvre. In general, combining manoeuvres allows for a smaller required ΔV , as $|\Delta \vec{V}_1 + \Delta \vec{V}_2| \leq |\Delta \vec{V}_1| + |\Delta \vec{V}_2|$, however not all manoeuvres can be combined, as the pre- and post-manoevrue orbits must share a common position, where the impulsive manoeuvre is performed. A diagram of the combined manoeuvre, including all relevant angles, is shown in Figure 7.9.

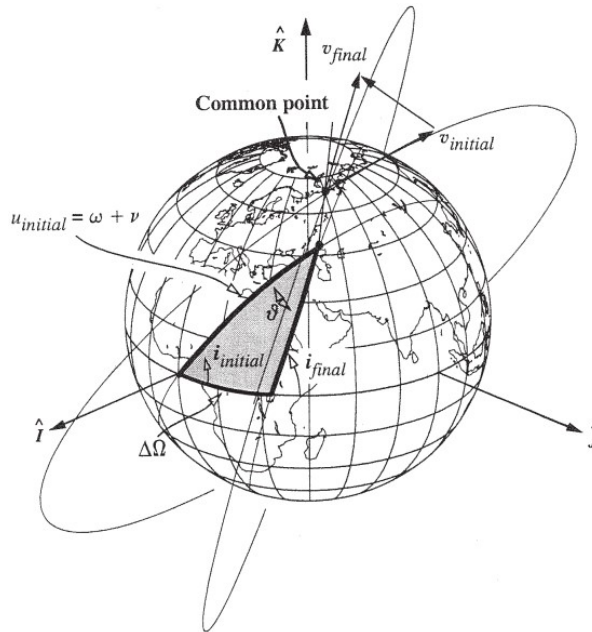


Figure 7.9: The combined manoeuvre must be performed at a common point of both orbits [combined_manoevrue].

For a circular orbit, the velocity of the spacecraft is given by $V = \sqrt{\mu/a}$, which is independent of i or Ω , so the combined manoeuvre only affects the direction of the velocity vector of the spacecraft. The angle θ between the pre- and post-manoevrue velocity vector is given by Equation 7.26.

$$\theta = \arccos(\cos(\Omega_2 - \Omega_1) \cdot \sin(i_1) \sin(i_2) + \cos(i_1) \cos(i_2)) \quad (7.26)$$

$$\theta = \arccos(\cos(30^\circ) \cdot \sin(98^\circ) \sin(96.42^\circ) + \cos(98^\circ) \cos(96.42^\circ)) = 29.798 \text{ [deg]}$$

Using Equation 7.21, the ΔV required for the combined Δi and $\Delta \Omega$ correction manoeuvre is calculated to be 3.8885 [km/s]. In Table 7.3, the ΔV required for the combined manoeuvre is shown, together with the ΔV for the in-plane Hohmann manoeuvre, resulting in the total ΔV for insertion for this strategy. The latter is about 4.7% lower than for the options in Table 7.2.

Table 7.3: ΔV required for combined manoeuvre, followed by Hohmann transfer

ΔV for combined manoeuvre [km/s]	ΔV for Δa [km/s]	ΔV for insertion manoeuvres [km/s]
3.8885	0.2092	4.0977

7.2.1.3. Passive Ω manoeuvre

The final strategy considered is to let the RAAN/LTAN of the MAGEOS spacecraft approach the RAAN/LTAN of the operational orbit without performing an expensive manoeuvre. Different orbits precess at different rates, since the parameters in Equation 5.1 are different for different orbits, so by orbiting for a specified period of time in a coasting orbit, the RAAN/LTAN of the S/C orbit will approach the RAAN/LTAN of the operational orbit. Once the RAAN/LTAN of the operational orbit is achieved, a manoeuvre must be performed to transit from the coasting orbit to the operational orbit, which has the correct precession rate. Thereby, the RAAN/LTAN of the operational orbit will be achieved and it will keep precessing at the Sun-Synchronous rate of the operational orbit to keep the LTAN constant.

Starting from the insertion orbit, the MAGEOS spacecraft performs a manoeuvre: either an inclination change Δi or a semi-major axis change Δa , in order to have the maximum difference in precession rate, as shown in Figure 7.7, thus minimising coasting time. At time $t = 0$ [s], the RAAN of the coasting orbit is defined as $\Omega_{coasting,t=0}$. The evolution of $\Omega_{coasting}$ due to precession is given by Equation 7.27.

$$\Omega_{coasting}(t) = \Omega_{coasting,t=0} + \dot{\Omega}_{S/C} \cdot t \quad (7.27)$$

Similarly, the RAAN of the operational orbit, which is defined as the RAAN whose LTAN is either 12AM or 12PM, can be determined relative to its value at $t = 0$ [s]. Since the operational orbit is Sun-Synchronous, it precesses at a fixed, Sun-Synchronous rate, equal to about $1.9924 \cdot 10^{-7}$ [rad/s]. The evolution of $\Omega_{operational}$ due to precession is given by Equation 7.28.

$$\Omega_{operational}(t) = \Omega_{operational,t=0} + \dot{\Omega}_{SSO} \cdot t \quad (7.28)$$

When $\Omega_{coasting} = \Omega_{operational}$, the RAAN of both orbits will have converged. When such a condition is achieved, the MAGEOS spacecraft will manoeuvre to the operational orbit.

$$\Omega_{coasting}(t) = \Omega_{operational}(t) \quad (7.29)$$

$$\Rightarrow (\Omega_{operational,t=0} - \Omega_{coasting,t=0}) + (\dot{\Omega}_{SSO} - \dot{\Omega}_{S/C}) \cdot t = 0$$

$$\Rightarrow \pm \frac{\pi}{6} + \left(\frac{2\pi}{T_{ES}} - \dot{\Omega}_{S/C} \right) \cdot t_{max} = 0$$

$$\Rightarrow t_{max} = \frac{\mp \frac{\pi}{6}}{\frac{2\pi}{T_{ES}} + 3\pi J_2 \left(\frac{R_E}{a(1-e^2)}\right)^2 \cos(i) \frac{1}{2\pi} \sqrt{\frac{\mu}{a^3}}}$$

In Figure 7.10, Equation 7.29 is plotted for a circular orbit. Periods larger than one year are immediately rejected, and plotted in gray. The insertion orbit is plotted in blue, and the operational orbit in red. Two possible coasting orbits are considered, and are shown in Table 7.4 and in Figure 7.7.

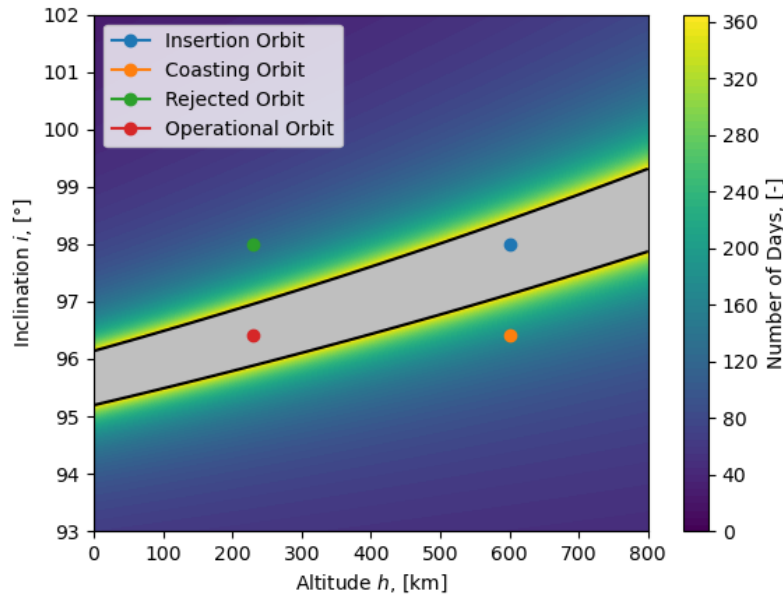


Figure 7.10: Number of days required to get from $\Omega_{insertion}$ to $\Omega_{operational}$ for different coasting orbits.

Table 7.4: Two feasible options for the coasting orbit showing coasting time required and precession rate compared to operational SSO

Sequence	First manoeuvre	Second manoeuvre	Coasting Time [days]	Precession Rate
Orange (Chosen)	Inclination	Semi-major axis	175	$\dot{\Omega}_{S/C} < \dot{\Omega}_{SSO}$
Green (Rejected)	Semi-major axis	Inclination	125	$\dot{\Omega}_{S/C} > \dot{\Omega}_{SSO}$

The first option, indicated by orange, requires an inclination change to be performed to reach the coasting orbit, where the spacecraft will coast for 175 [days]. Subsequently, a Hohmann transfer must be performed to reach the operational orbit. As the precession rate of the coasting orbit is lower than the precession rate of the operational orbit, its starting LTAN must be larger than the operational LTAN, and therefore is restricted to the range $LTAN \in [12AM, 02AM] \cup [12PM, 02PM]$.

The second option, indicated by green, requires a Hohmann transfer to be performed to reach the coasting orbit, where the spacecraft will coast for 125 [days]. Subsequently, an inclination change must be performed to reach the operational orbit. As the precession rate of the coasting orbit is higher than the precession rate of the operational orbit, its starting LTAN must be smaller than the operational LTAN, and therefore is restricted to the range $LTAN \in [10AM, 12PM] \cup [10PM, 12AM]$.

Both options require no additional ΔV for a $\Delta\Omega$. However, in contrast to Section 7.2.1.1 and Section 7.2.1.2, a significant orbit insertion wait period is required. The orange option is preferred as the

MAGEOS spacecraft does not experience significant drag at its initial altitude of 600 [km], and therefore does not require considerable drag compensation throughout the 175 day period. Additionally, the inclination change manoeuvre requires less ΔV if performed at the higher altitude.

The total ΔV required using this approach is $\Delta V_i = 208.5$ [m/s] for the inclination correction, and $\Delta V_a = 209.2$ [m/s] for the semi-major axis correction, resulting in a required ΔV of 417.7 [m/s].

7.2.1.4. Total ΔV for orbit insertion

The total ΔV for orbit insertion consists of inclination correction, RAAN correction and Hohmann transfer. Summing up these values for the chosen option, which consists of changing inclination followed by a passive Ω manoeuvre and active Hohmann transfer, the $\Delta V_{insertion}$ can be calculated and is shown in Table 7.5.

Table 7.5: Required ΔV for orbit insertion

$\Delta V_{inclination}$ [km/s]	ΔV_{RAAN} [km/s]	$\Delta V_{Hohmann}$ [km/s]	$\Delta V_{insertion}$ [km/s]
0.2085	0	0.2092	0.4177

7.2.1.5. Propulsion options for orbit insertion

The ΔV for orbit insertion can be provided through two different methods. The first option is to utilise the propulsion system onboard the MAGEOS S/C. A major disadvantage of this method is that it requires additional propellant to be stored on the S/C, thus requiring more mass and volume, or reducing the mission lifetime in case the propellant mass is kept constant. However, a key advantage is that the cost increase is relatively low, since the fuel tanks and required instrumentation components can be effortlessly upscaled by Dawn Aerospace. The other option for orbit insertion is to use an orbital transfer vehicle which is able to suffice the ΔV for orbit insertion and is ejected after once the same has been provided. The main advantage of this method is that no additional propellant mass and volume is required onboard the S/C itself, while also allowing for extension of the mission lifetime through the use of leftover propellant. However, the main disadvantage is that it is relatively costly compared to just using the onboard propulsion system, even when accounting for up-scaling of the propulsion system.



Figure 7.11: Orbiter Transfer Vehicle configuration [107]

Upon carrying out a trade-off on the basis of the aforementioned factors, an orbit transfer vehicle was deemed to be the superior option due to volume being a more constraining factor for the MAGEOS

mission as compared to the mission cost, which allowed for more leeway. Subsequently, the Orbiter orbit transfer vehicle from Launcher Space [107] was selected and further investigated. Orbiter is a satellite transfer vehicle that can transport one or more S/C into space at a competitive price. The satellite transfer vehicle configuration and the platform configuration are shown in Figure 7.11 and ??, respectively. Orbiter is compatible with every major rideshare capable launch vehicle as can be seen in Figure 7.12. This is in agreement with the launch phase of MAGEOS since it is proposed to launch aboard a rideshare capable launch vehicle. Moreover, Orbiter integrates with every CubeSat and small satellite separation system.

Furthermore, Orbiter can perform any combination of manoeuvres to modify the orbit, precisely and accurately placing satellites into the desired orbit. The high-thrust chemical propulsion system ensures that manoeuvres are accomplished quickly in order to limit the time for orbital insertion, providing a total ΔV of 500 [m/s]. With the required ΔV for orbital insertion, this leaves about 80 [m/s] for unforeseen manoeuvres and possibly part of the orbital maintenance phase as treated in Section 7.2.2. The orbiter mass is 200 [kg] and the payload capacity of 400 [kg] is more than enough to host the 2 S/C of the MAGEOS mission. With an average available payload power of 150 [W], MAGEOS subsystems can amply powered as well.

Orbiter can be bought in two forms which differ in price. The first form is a dedicated transfer vehicle, the cost of which is US\$400 thousand for the transfer vehicle configuration plus the launch vehicle cost. Based on the launch vehicle choice and final mass, the launch vehicle cost is >US\$1 million.

The second form in which Orbiter can be bought is a shared transfer vehicle. This option is rejected since in this case the ΔV provided by Orbiter is shared among the different parties of the launch. Orbiter proves to be a viable option only if the full 500 [m/s] ΔV capability can be used by MAGEOS. Else, the Orbiter would be used only for part of the orbit insertion and the onboard propulsion system would have to be activated during orbit insertion, thus requiring extra propellant.

Consequently, the first form i.e. the dedicated transfer vehicle is chosen and the launch vehicle cost can be determined. The launcher that has been chosen is the Falcon 9 from SpaceX [108], shown in Figure 7.13. This launcher is competitively priced, has high reliability, and is reusable, which is one of the factors contributing to MAGEOS' sustainability objectives.



Figure 7.12: Orbiter is compatible with the launch vehicles shown [107]

!

This launcher is compatible with Orbiter as can be seen in Figure 7.12. Besides, this launcher has frequent launches to a SSO in a circular orbit at 500-600 km can therefore be assumed to be available for launches in 2028. The altitude corresponds to the altitude used for the orbit design in Section 5.4, and was used in the calculation for the ΔV for orbit insertion in Section 7.2.1. The cost of using the Falcon 9 for rideshare can be calculated with [108]. For MAGEOS, the first keyword that has been specified on this page is SSO for the desired orbit. The payload for MAGEOS comprises the Orbiter with a mass of 200 [kg] and the mass of the 2 CubeSats of MAGEOS, which was set to 50 [kg] at the time of launcher selection. Consequently, input payload mass was set to 250 [kg]. Furthermore, to mount the Orbiter to the cylinder of Falcon 9, a port is required, which can be seen in Figure 7.14. The 'available ports' keyword has been set to 24 [inch]. The 2 CubeSats of MAGEOS easily fit within the envelopes shown and the configuration will look similar to Figure 7.15.

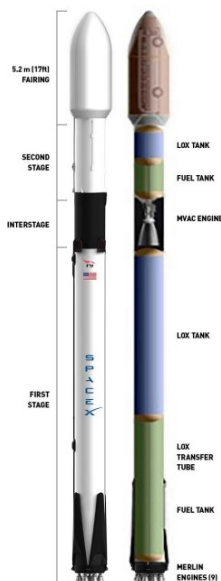


Figure 7.13: Falcon 9 [108]

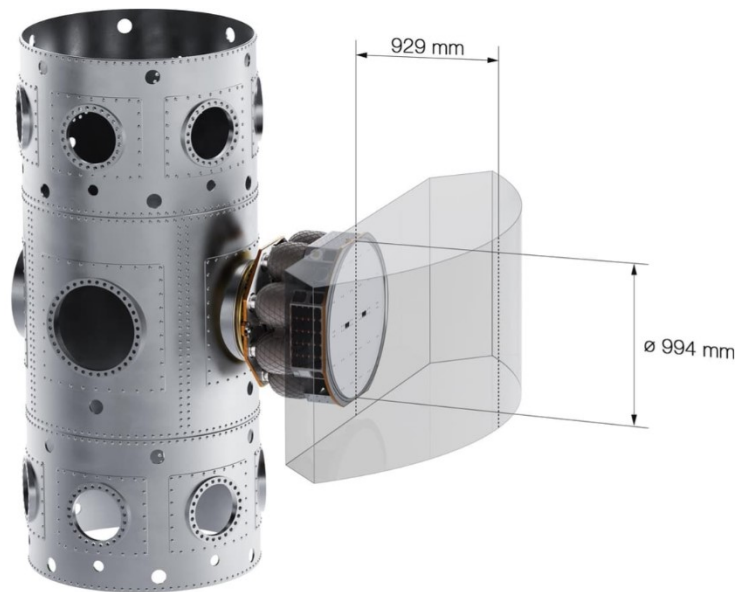


Figure 7.14: Orbiter mounted to cylinder of Falcon 9 by means of a 24" (0.6096 [m]) port showing the envelopes for the 2 configurations [107] shown in Figure 7.11 ??



Figure 7.15: Separation of Orbiter with 2 S/C attached in the Orbiter platform configuration [107]

Moreover, on the page for add-ons, a separation system for the payload can be chosen. Since the Orbiter and MAGEOS' CubeSats together form the payload for Falcon 9, the 24 [inch] separation system has to be chosen to separate the Orbiter with MAGEOS from the Falcon 9. Separation of the MAGEOS CubeSats from Orbiter is done actively by Orbiter.

The estimated price for the launch vehicle cost is US\$2.13 million. Hence, the total cost to use Orbiter on a Falcon 9 is US\$2.53 million.

7.2.2. ΔV for Orbital Maintenance

The mission ΔV budget comprises three segments: the ΔV for drag compensation, the ΔV for constellation maintenance, and the ΔV for de-orbiting. The driving factor in the overall ΔV budget is the ΔV for drag compensation, owing to MAGEOS' low orbit. The ΔV s have been calculated as shown below.

- **ΔV for drag compensation:**

The ΔV for drag was determined in conjunction with the propulsion system, as shown in Section 6.3.3. The reason for calculating the ΔV after the selection of the propulsion system was that the ΔV was heavily dependent on the orbit control strategy chosen. Moreover, the orbit control strategy was to be chosen such that the resulting ΔV is compliant with the COTS propulsion system's ΔV capability and does not require additional propellant onboard the S/C, in order to curb the volume occupied by the propulsion system. Consequently, a ΔV_{drag} of 159.07 [m/s] was determined for drag compensation, including orbit raising.

- **ΔV for constellation maintenance:**

The ΔV for constellation was taken to be 10% of the ΔV for drag compensation. The ΔV for constellation maintenance is used to correct the orbit of both MAGEOS S/C to maintain formation and is significantly less than the ΔV for drag compensation. Thus, the aforementioned value of 10% has been considered to be a reasonable and conservative estimate, resulting in a $\Delta V_{constellation}$ of 15.91 [m/s].

- **ΔV for de-orbiting:**

According to requirement CON-SUS-1 [2], the S/C shall be disposed of by total burning, resulting in no space debris and no collision on the ground. According to the Canadian Space Agency [8], the CubeSat platform is typically capable of fully burning up in the atmosphere upon re-entry. Using a database such as [109], it can be found for instance that in 2021 all CubeSats that de-orbited burned up in the atmosphere [110]. However, the MAGEOS mission contains denser elements, such as magnetorquers, which are more likely to survive the reentry process [111]. The strategy that will be employed to also burn up these elements is the 'Design for Demise' concept from ESA. This strategy contains multiple measures that can be taken to increase the chance of a full burn-up. One of them is to break-up at a relatively high altitude Figure 7.16, which shall expose MAGEOS to a longer burn-time, increasing the confidence that MAGEOS fully burns up. Moreover, smaller S/C such as MAGEOS break-up earlier than larger satellites. The confidence that the magnetorquers burn-up is therefore still high. Alongside this, dismissable elements such as meltaible joints holding the satellite panels can be incorporated in the design of MAGEOS to expedite the break-up altitude and consequently increase the burn-time and confidence in complete burn-up of MAGEOS. Consequently, only a marginal 5% of the ΔV_{drag} is incorporated into the design of MAGEOS in order to account for stochastic processes during de-orbiting and the re-entry, resulting in a $\Delta V_{de-orbiting}$ of 7.95 [m/s].

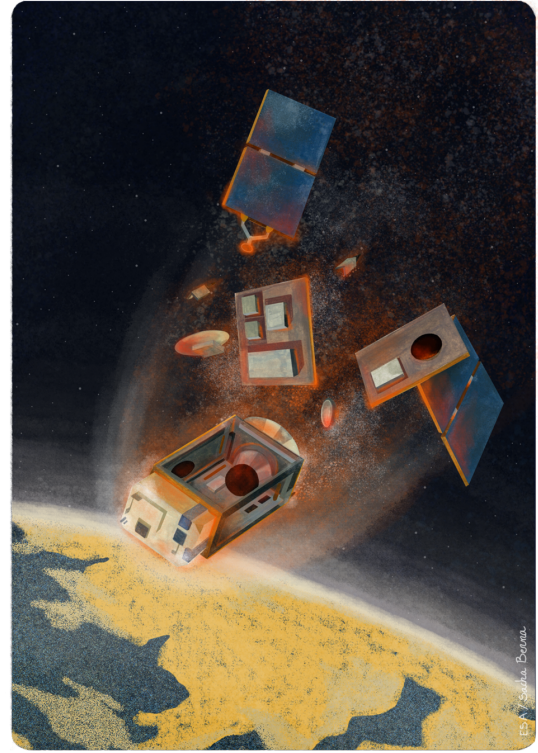


Figure 7.16: Break-up of a CubeSat, followed by complete burn-up [111]

Lastly, the total ΔV budget for orbit maintenance was calculated by adding all of the aforementioned ΔV s and then taking a 20% margin in addition to that. The relatively high margin has been chosen since the MAGEOS mission is at an early design stage and still possesses significant uncertainty. This results in the total $\Delta V_{total\,maintenance}$ of 219.52 [m/s], as shown in Table 7.6. This ΔV undershoots the total propulsion system ΔV capability by 60 [m/s], meaning that there is a scope for mission lifetime extension.

Table 7.6: Required ΔV for orbit maintenance

ΔV_{drag} [km/s]	$\Delta V_{constellation}$ [km/s]	$\Delta V_{de-orbiting}$ [km/s]	$\Delta V_{total\,maintenance}$ [km/s]
0.15907	0.015907	0.0079535	0.21952

7.2.3. Total mission ΔV

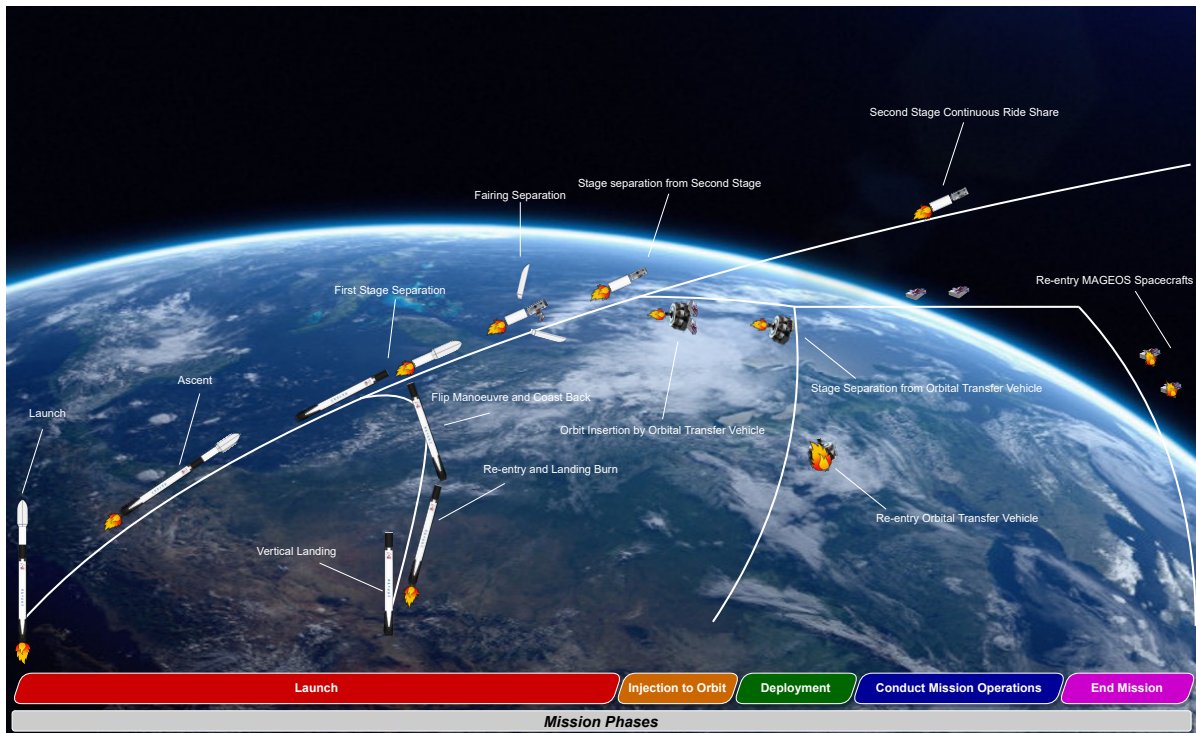
The total mission ΔV is the sum of the ΔV for orbit insertion and the ΔV for orbital maintenance and is reported in Table 7.7. The final column, $\Delta V_{tot,margin}$, includes a margin of 20% on top of the value, ΔV_{tot} , which is the sum of $\Delta V_{insertion}$ and $\Delta V_{maintenance}$. The margin is used, accounting for the uncertainties in the calculated ΔV values and factors that require a negligible ΔV or require more time to quantify what ΔV would be required, i.e. atmospheric winds. This will ensure with high confidence that enough ΔV is onboard of MAGEOS. Any propellant that is still left after the mission lifetime can be used to extend the mission.

Table 7.7: Total ΔV required for entire mission

$\Delta V_{insertion}$ [km/s]	$\Delta V_{maintenance}$ [km/s]	ΔV_{tot} [km/s]	$\Delta V_{tot_{margin}}$ [km/s]
0.4177	0.2195	0.6372	0.7647

7.2.4. Flight Profile Diagram

The trajectory of MAGEOS can be best summarized in a Flight Profile Diagram, which is shown in Figure 7.17. It shows the different milestone activities performed during the mission phases.

**Figure 7.17:** Flight Profile Diagram of the MAGEOS mission

It should be noted that the length of the mission phases do not correspond to the actual time a mission phase takes. In Table 7.8, a more detailed timing for each phase will be given, including important events. It is assumed that the Orbital Transfer Vehicle is ejected after orbital insertion. However, in case there is ΔV left to be delivered by the Orbital Transfer Vehicle, the Orbital Transfer Vehicle can be ejected during orbital maintenance until all ΔV has been delivered. The Avionics onboard of the Orbital Transfer Vehicle can be programmed accordingly. Moreover, the engine startup time for the Orbital Transfer Vehicle was assumed to be 10 [s].

Table 7.8: Duration events during the MAGEOS mission

Mission Elapsed Time	Event
T -3 [s]	Engine Start Sequence [112]
T +0 [s]	Liftoff [112]
T +67 [s]	Maximum Dynamic Pressure [112]
T +145 [s]	Main Engine Cut-off [112]
T +148 [s]	First Stage Separation [112]
T +156 [s]	Second Engine Startup [112]
T +195 [s]	Fairing Deployment [112]
T +514 [s]	Second Engine Cut-off [112]
T +600 [s]	Stage Separation from Second Stage [112]
T +605 [s]	Startup Spacecraft
T +605 [s]	Orbital Transfer Vehicle Engine Startup
T +615 [s]	Start Inclination Change
T +615 [s]	Orbital Transfer Vehicle Engine Shut-off
T +615 [s]	Start Coasting orbit
T +175 [days], +615 [s]	Orbital Transfer Vehicle Engine Startup
T +175 [days], +625 [s]	Start Hohmann transfer
T +175 [days], +3407 [s]	Operational orbit achieved
T +175 [days], +3407 [s]	Separation of Spacecraft 1 from Orbital Transfer Vehicle
T +175 [day], +3409.5 [s]	Separation of Spacecraft 2 from Orbital Transfer Vehicle
T +175 [days], +3409.5 [s]	Start mission
T +1 [years], +175 [days], +3409.5 [s]	Mission lifetime reached
T +1 [years], +175 [days], +3409.5 [s]	Passive Re-entry of S/C
T +1 [years], +185 [days], +3409.5 [s]	End of mission

7.3. RAMS Analysis

To define the systems reliability, availability, maintainability and safety characteristics, a RAMS analysis will be performed. First, the systems reliability will be discussed, approximating the systems total reliability bases on statistics for the chosen design configuration, as well as the redundancy philosophy for the MAGEOS mission. Next, the availability of the system will be discussed. This includes the ground contact time and amount of measurements that could be performed. The maintainability of the spacecraft will briefly be discussed, however since the MAGEOS mission exist out of a two spacecraft configuration, maintainability will be difficult. Lastly, the safety critical functions will be addressed.

7.3.1. Reliability

The systems total reliability is mainly depending on the subsystems reliability, as well as payload reliability and launcher reliability. In Table 7.9, the reliability of all the used subsystems as well as the launcher is given. Since the attitude control systems makes use of systems which have a low TRL level and has never been used before, the reliability number is unknown. Therefore, it will be assumed that the reliability of this system will be the same as for the current system. The data given in Table 7.9 is defined for subsystems after 2 years lifetime. This will be used as worst case data, since at the beginning of life, the failure of a subsystems is very unlikely [113].

Table 7.9: Reliability of MAGEOS (Sub)Systems

(Sub)System	Reliability [113–116]
ADCS	94%
CDHS	91%
COMMS	92%
STS & DepS and P/L	94%
EPS	79%
Prop	≈ 100%
TCS	96%
TT&C	76%
Launcher	98.8%

Making use of the Table 7.9 and the formula to find the total reliability described in Equation 7.30, the total reliability of the MAGEOS mission is estimated in Equation 7.31.

$$R_{total} = \prod R_i \quad (7.30)$$

$$R_{MAGEOS} = R_{ADCS} \cdot R_{CDHS} \cdot R_{COMMS} \cdot R_{STS} \cdot R_{EPS} \cdot R_{Prop} \cdot R_{TCS} \cdot R_{TT\&C} \cdot R_{Launcher} \quad (7.31)$$

This will result in a total reliability of the MAGEOS mission of 42%.

Certain components have redundancy in the MAGEOS mission to make sure that a failure of those components does not lead to a mission failure. The redundancy of the components are given below.

- 2 x GPS for gravitational measurement for each spacecraft (1 redundant)
- 2 x Magnetometer for each spacecraft (1 redundant)
- 20% redundancy battery storage
- 20% redundancy of solar panels

7.3.2. Ground station availability

The MAGEOS mission will fly in a constellation of 2 S/C, for 1 year at an altitude of 229.72 [km] and an inclination of 96.42 [deg]. The S/C will perform measurements which will be transferred to 10 ground stations from Amazone [57] shown in Figure 7.18 after the measurements have been performed. Furthermore, S/C commands will be transferred to the S/C by the ground stations as well. Assuming a minimum required elevation angle for sufficient signal quality of 7 [deg], which is the default of the software GMAT used, the total contact time per orbit is about 6.1% for the operational orbit of MAGEOS. Equivalently, this results in a total contact time per orbit of about 5.43 [min]. The time windows during which the different ground stations can have contact with the S/C are shown in Figure 7.19 for January 2028.

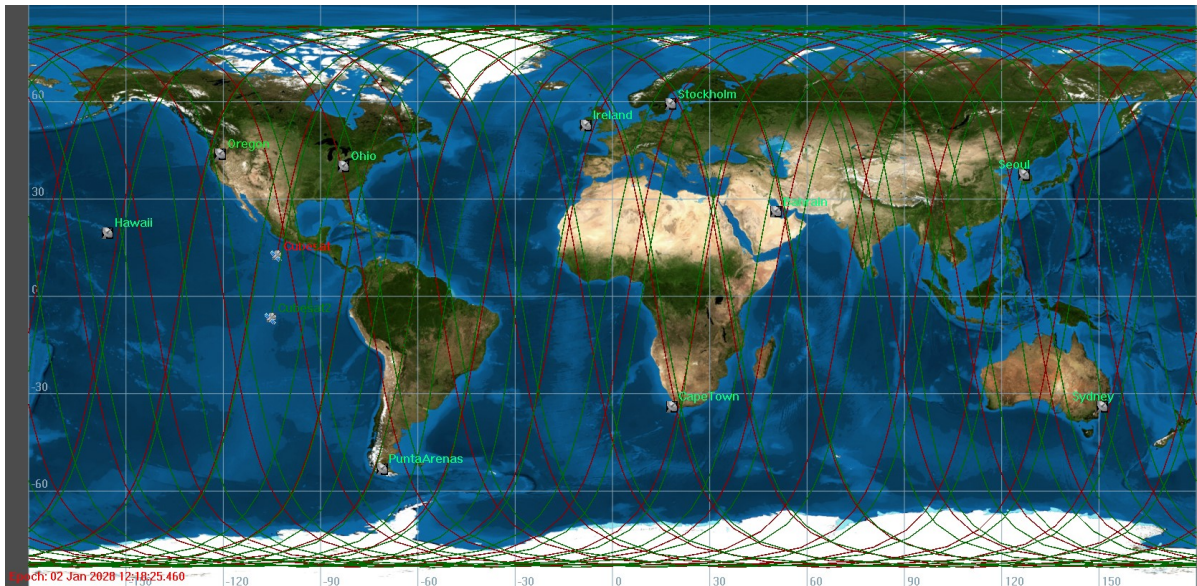


Figure 7.18: Amazon Web Services simulated in GMAT showing the 2 CubeSats of MAGEOS

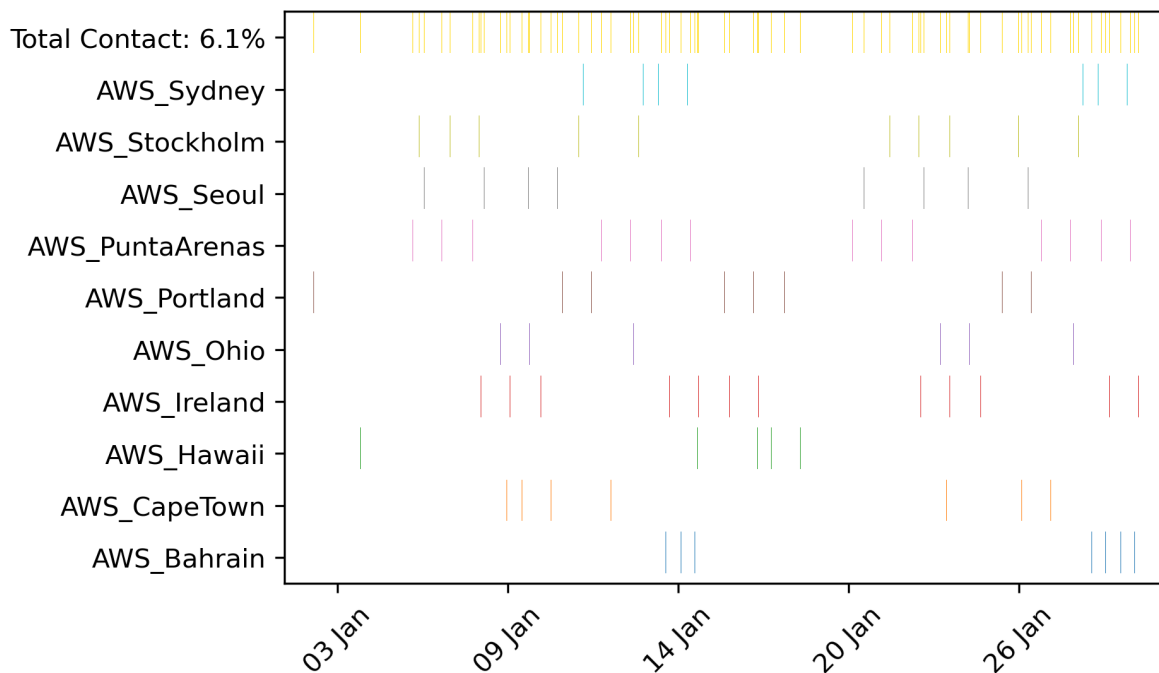


Figure 7.19: Ground stations visible to make contact with MAGEOS in January 2028, simulated under operational orbit conditions

On the page of Amazon [57], 4 pricing options are available. These include narrowband vs wideband and reserved vs on-demand. Narrowband is here defined as any pass where the instantaneous bandwidth is less than 54 [MHz] and wideband is greater than or equal to 54 [MHz]. As it is known in advance when MAGEOS will be launched and that it will be operating for at least a year, a reserved contract can be signed.

In Table 6.16, it can be seen that the bandwidth for both uplink and downlink is smaller than 54 [MHz] and the sum as well. Consequently, narrowband reserved was chosen, at a price of US\$3 per minute.

The total price for using ground stations can be calculated by multiplying the price rate in minutes with the total number of minutes in a year that the S/C are visible by the ground stations. In one year, the S/C are visible for about 32083 [min]. The estimated price for ground station usage is thus US\$96251. This is an upper bound, because it assumes that all data is sent down during a time window equal to the time the ground stations are in view. However, if the data is sent to the ground stations by MAGEOS in a time shorter than the time that the ground stations are in view, the actual antenna time usage is shorter and consequently the costs since Amazon only charges per actual antenna time. The upper bound cost was used as a cost estimate for the ground station usage and no additional margin was incorporated.

Finally, the ground station availability for SLR, as was treated in Section 4.3.4.2, is 1.5%. Note that these are different ground stations than the ones used for TTC.

7.3.3. Maintainability

Since the MAGEOS mission is a space mission, the maintainability is nearly impossible. The systems and subsystems of the spacecrafts can not be physically maintained. However, software can be updated on the spacecraft if failures or bugs in the spacecrafts software do occur. Furthermore, daily commands will be given to the spacecraft to make sure that the spacecraft is always stand-by for unforeseen events or measurements.

7.3.4. Safety

The MAGEOS mission has some safety critical systems that should be addressed. They are listed below.

- Propulsion fire and explosion
- Boom deployment in the wrong direction or inside the spacecraft
- Detachment of the momentum wheel
- Orbital Transfer Vehicle failure
- Deployment failure

The above mentioned safety critical system could potentially lead to the end of the MAGEOS mission.

Chapter 8: Final Design

8.1. Final Design Overview

8.1.1. Mission duration

The mission duration of MAGEOS is designed for 1 [years]. This is more than 80% longer than the design of SHAPE [117] on which MAGEOS is based and considered long enough to map the gravitational and magnetic field.

8.1.2. Mass and power breakdown

The mass and power breakdown is reported per spacecraft of MAGEOS in Table 8.1 and Table 8.2 respectively.

Subsystem	Component	Mass [kg]
ADCS	2 Star Sensors	0.3940
ADCS	Momentum Wheel	0.9000
ADCS	3 Magnetorquers	0.0543
Propulsion	2 Propulsion Assemblies	3.2000
EPS	Batteries	0.1150
EPS	14 Solar panels	0.7000
EPS	Power Management System	0.1930
Structures	14 Unit Structures	3.6936
Structures	2 Booms	0.1500
TCS	MLI	0.0150
TCS	Passive Radiators	0.2460
TT&C	Antenna	0.0500
TT&C	Transceiver	0.200
C&DH	On board computers	0.1000
C&DH	Converter	0.0240
Payload (Gravimeter)	2 GPS (GSD800)	0.1100
Payload (Gravimeter)	2 Antennae	0.0400
Payload (Gravimeter)	2 Accelerometer Units	1.2000
Payload (Gravimeter)	SLR Retroreflector array	0.0700
Payload (Magnetometer)	Electronics box	1.4000
Payload (Magnetometer)	2 Fluxgates	1.2000
Dry mass without harness		14.0550
Dry mass with harness		15.1829
Wet mass without margin		16.7830
Wet mass with 10% margin		18.4600

Table 8.1: Mass breakdown of 1 S/C of MAGEOS

Subsystem	Component	Power [W]
ADCS	2 Star Sensors	1.40000
ADCS	Momentum Wheel	0.00000
ADCS	3 Magnetorquers	0.03600
Propulsion	2 Propulsion Assemblies	0.00243 (Avg. power)
EPS	Batteries	0.00000
EPS	14 Solar panels	0.00000
EPS	Power Management System	0.07400
Structures	14 Unit Structures	0.00000
Structures	2 Booms	0.00000
TCS	MLI	0.00000
TCS	Passive Radiators	0.00000
TT&C	Antenna	0.22400 (Avg. power)
TT&C	Transceiver	0.12200 (Avg. power)
C&DH	On board computers	0.40000
C&DH	Converter	0.00000
Payload (Gravimeter)	2 GPS (GSD800)	4.00000
Payload (Gravimeter)	2 Antennae	0.10000
Payload (Gravimeter)	2 Accelerometer Units	0.45000
Payload (Gravimeter)	SLR Retroreflector array	0.00000
Payload (Magnetometer)	Electronics box	3.20000
Payload (Magnetometer)	2 Fluxgates	0.00000
Total power without margin		15.66000
Total power with 10% margin		17.23000

Table 8.2: Power breakdown of 1 S/C of MAGEOS

8.2. Sensitivity Analysis

To investigate the sensitivity of a design by changing parameters in certain systems, a sensitivity analysis will be performed on the final design of the MAGEOS mission. This will be performed by investigating the final design compliance in case parameters of subsystems have changed. This will be done by showing worst case values and the consequence of this change.

8.2.1. Mass

In case the masses of components change, the center of gravity will change as well. This results in a off set in predicted center of gravity and could lead to an in stable ADCS system, since the momentum wheel should be in the center of gravity. This means that slight deviations of the masses of each component could lead to ADCS problems. The off set of the center of gravity will be the largest for deviations in the components that are located further away from the center of gravity compared to the components that are located closer to the center of gravity. Besides position, the magnitude of the deviation is also an important parameter. This could lead to a decrease in spacecrafts stability and obtainable accuracy, meaning that not all requirements can be met.

Another important aspect of an unknown center of gravity is the uncertainty in gravitational field measurements. The gravitational field will be measured making use of accelerometers and GPS sensors. To process the data, the center of gravity should be precisely known. In case the center of gravity is unknown, the data can no longer be processed meaning that the requirement to determine the gravitational field can no longer be met.

Furthermore, in case the spacecrafts are heavier than predicted beforehand, the launch becomes more expensive. The total mission cost could than go over the budget of 5 million euros, meaning that the design does not meet all the requirements anymore.

8.2.2. Power consumption

All subsystems needs power to be able to operate. In case the EPS system could not provide enough power or other subsystems consumes more power than initially indicated, the mission could not be performed properly. However, a 20% margin was added to the power budget, so slight deviations in power consumption can not lead to a mission failure. Next to this, some subsystems could be powered down to safe power.

8.2.3. Propellant

In case less propellant is brought on the spacecraft than anticipated beforehand, the mission lifetime would be reduced. Furthermore, emergency manoeuvres such as collision avoidance can not be performed or could decrease the lifetime even more, since the propellant that will be used for this manoeuvres can not be used for orbital maintenance. Constellation maintenance could also be a potential problem for gravitational measurements. Some margin for propellant has been brought onboard for this manoeuvres. Meaning that it could still meet the requirements

8.2.4. Size

In case the size of the spacecraft is larger than expected, the spacecraft might not fit in the launcher. This means that the mission can not be performed. Each spacecraft of the MAGEOS mission has the following dimensions: 80 x 30 x 12 [cm]. To fit in the designated payload area, the spacecraft should have a maximum dimension of 99.4 x 99.4 x 92.9 [cm]. This means that a large deviation in spacecraft dimensions could be given to still be able to fit in the designated payload area. Meaning the spacecraft will still be able to meet the requirements.

In case the spacecraft dimensions differ, the drag coefficient will also differ. This could lead to an increase in drag meaning that more propellant should be needed for orbital maintenance. This leads to a decrease in lifetime, meaning that the requirement for mission lifetime will not be met.

8.2.5. Temperature

The thermal control system of the spacecraft protects the payload and subsystems of the spacecraft from the sudden a large temperature changes in space. The maximum temperature the thermal control system is developed for is 173 [k] and 437 [k]. The thermal control system makes sure that all components work in their ideal operating temperature. In case the outside temperature is higher or lower compared to the maximum and minimal temperature the thermal control system is designed for, the components could no longer be held in their ideal operating temperature. This could lead to the failure of those components. Luckily, the components often have a broad range of operating temperatures and therefore a slight deviation in maximum and minimum outside temperature could still mean that the requirements can be met.

8.2.6. Boom length

The spacecrafts for the MAGEOS mission contain a 2 meter long boom. The reason for this length is the influence of the magnetic field the electronics of the spacecrafts, such as the magnetic biased momentum wheel and solar panels, can have on the magnetic field measurements. Furthermore, two different magnetic field measurement devices are brought onboard the spacecraft that should have a certain off set distance from each other. In case the boom length is not 2 meter but shorter, or the distance between the two magnetic field measurement devices is too short, the required accuracy can no longer be met. Increasing the boom length or distance does not directly lead in a decrease of accuracy. To conclude, a decrease in boom length could mean that the accuracy requirement for the magnetic field measurement can no longer be met.

8.2.7. Altitude

The altitude of the MAGEOS mission is set at 229.7 [km]. Since a circular orbit is chosen, this is also the maximum altitude. For this altitude, drag and link budget calculations have been performed. From these, components have been selected. In case the orbit is deviating, parts of the mission can no longer be met. In case the altitude is higher, the drag will decrease, leading to an increase in mission lifetime.

However, the link budget might not be closed anymore. This results in an inability of communication between the spacecraft and the ground stations, leading to a mission failure. In case the altitude is lower, the drag will be higher. This leads to a decrease in lifetime, meaning that the requirement for mission lifetime can no longer be met.

8.2.8. Data Collected

The MAGEOS mission collects a lot of data by performing magnetic and gravitational field measurements. Furthermore, sensor data from subsystems such as temperature, current and voltage will be collected to determine the overall condition of the spacecraft. All of this data will be digital and should be stored in the spacecraft's computer, where after it will be transferred to a ground station. In case the data rate of all these sensors and measurement devices is higher than expected, more data should be stored in the spacecraft and later on be transferred to a ground station. However, if the amount of data is too large, the contact time with the ground station is too short, leading to not fully downloaded data of the spacecrafts. This means that less data can be stored later on at the spacecraft's onboard computer and that not all collected data is immediately available. For measurement data could this not be a problem. However, for sensor data, this could be a problem. Since the most recent data could not be transferred. In case a problem could be detected from this data that should be solved directly by uploading a command, this could potentially be uploaded too late resulting in a possibility of the loss of a spacecraft, resulting in a mission failure.

Chapter 9: Design Actualisation

9.1. Operations Logistics

The operations and logistics for the MAGEOS are described in this section, it is an update and extension of the operation plan described in the mid-term report [1]. The MAGEOS mission can be divided into 4 phases. The Pre-Launch: All operations and facilities required onground before its ready to launch, the Orbit Insertion: CubeSat constellation is deployed and will manoeuvre to the intended orbit, the Conduct Science: CubeSat constellation will start taking measurements and occasional maintenance and the End-of-Life: CubeSat constellation will burn up into the Earth's atmosphere.

9.1.1. Phase 1: Pre-Launch

For the realization of the CubeSat mission, a variety of facilities are required. The components need to be fabricated, assembled, then tested both before and after integration. In general for the fabrication of a CubeSats, the use of commercial off-the-shelf components is maximized. This reduces the costs greatly. Even if those off-the-shelf components are not specifically qualified for the use in space [118]. This has led to the creation of catalogues full of commercial off-the-shelf CubeSat components with their performance stated. The reliability is often not provided by the manufacturer and is therefore determined by its flight heritage. This way the flight hours made without a failure can be used to estimate the reliability of a component. The reliability is rather important since CubeSats have a higher probability of failure at begin-of-life than large spacecraft [119]. The drive for cheaper space projects often compromises the success in orbit. The main cause is that the CubeSat designers are often new to the field and lack the knowledge on good design, assembly en testing [120]. It is therefore important to do hardware-in-the-loop simulations, these use real components integrated with emulated components and together with fault injection the system is tested to check if it complies with its specifications. [121].

Unfortunately, not all components are available off-the-shelf and thus need to be custom made. This is detrimental for the cost of the CubeSat, since it requires expensive tools and qualified people. Most likely only one of each component is manufactured which drives the price up even more e.g. moulds would only be used once. No matter if the component is manufactured in-house or commercially off-the-shelf available, they all need to be cleaned, checked and integrated. This is done in a cleanroom to prevent contamination, since that could corrode exposed circuits or hinder performance, especially for sensors and optical systems. The norm for communication satellites around earth is an ISO Class 6-8 cleanroom. Class 8 is 10x cleaner than average air, and the lower the class the cleaner the room. Deepspace satellites require an ISO Class 3 cleanroom, which is 100,000x cleaner than average air [122]. However, CubeSats often have lenient requirements when it comes to cleanrooms. Since they are more robust, carry less sensitive instruments and together with the fact that CubeSat mission are generally of short duration, cleanliness plays a less significant role [123]. For some testing procedures special conditions are required such as weightlessness or a vacuum. For the latter, the ESA ESTEC-test centre located in Noordwijk can be used. It has the facilities to perform thermal vacuum tests. For the weightless tests, the PH-LAB aircraft can be used, it is a flying laboratory shared between the TU Delft and NLR and is certified for zero g flights [124]. The final step on ground is preparing the CubeSat for transportation, since it needs to be transported to the launcher.

9.1.2. Phase 2: Orbit Insertion

The first task of the spacecraft when it is released by the launcher is to detumble itself and establish contact the a ground station. After the initial checks of all systems a coasting phase begins to get to the operational orbit. MAGEOS will make use of a ride-share launch and it is unlikely the other spacecraft onboard the launcher will operate at a VLEO orbit. Therefore the orbit after separation will most likely

at a higher altitude and different inclination than required. With several burns and coasting phases the operational orbit is achieved, this will take approximately half a year. Once in the correct orbit the spacecraft can fully deploy; extending the boom with the magnetometers and the solar array can be expanded.

9.1.3. Phase 3: Conduct Science

Operations

After orbit insertion, the spacecraft will start nominal operations. From this point onward, the spacecraft will collect data throughout its entire orbit, to map the magnetic and gravitational field. The collected data sent towards ground stations using its TT&C system. This data will include both scientific data, as well as telemetry data. The ground station will be equipped to receive this data, and store it in a database. During normal operations, the drag needs to be compensated roughly every 3.7 hours, to raise the orbit again, since it is continuously lowered due to drag.

Analyze Telemetry and Perform Maintenance

Under nominal operation, the telemetry will be sent to the ground station on a regular basis. The telemetry will provide mission control the possibility to monitor the well-being of subsystems. If harmful, or non-optimal conditions are observed, mission control can disable certain subsystem to prevent failure of the entire spacecraft. Maintenance can be performed by altering the executed commands by the spacecraft. Solutions must be able to be communicated to the spacecraft, and implemented onboard. Such solutions can only be in the form of changing the nominal operations of the spacecraft: orbit, subsystem's schedule for when to be operative/inoperative, power distribution, terminating one of the scientific data instruments before end of life, etc. No manned mission will ever be economically viable for maintenance, only sending commands can improve the lifetime of the mission, and the precision of the scientific data. If one of the two spacecraft fails, not the whole mission is doomed, since only the gravimetry suffers. The magnetometry can still be performed.

9.1.4. Phase 4: End-of-Life

The final phase of the mission is to implement the end-of-life plan. At the end of life, the spacecraft must burn up in the atmosphere over a lowly populated area. When the mission is to be terminated, the mission-end command will be sent to the spacecraft. The spacecraft will then send a transmission asking for a confirmation signal. The ground station will then either send a confirmation signal, or abort the mission-end command. If the mission end is received, the spacecraft will rotate to expose its solar array surface area to increase the drag and passively deorbit. This will bring the deorbit time down from 12 to 2 days. It can be controlled with thrusters if necessary, since there will be a small ΔV budget for the deorbiting.

9.2. Project Design & Development Logic

For the post-DSE phases of the project, the 'Space Project Management: Project Phasing and Planning' established by the European Cooperation for Space Standardization [125] will be used as a guide.

- **Phase 0 - Mission analysis and Identification**

In the first phase the global mission is outlined and defined, this is then converted to first level customer requirements and performance needs. Different possible system concepts are identified and research should be performed on related missions. The initial project planning should be established, so e.g. the tasks, budgets, possible partners and organisational layout/project management. This phase is executed in the beginning of the DSE in the baseline report and project plan.

- **Phase A - Feasibility**

The system concept options should have detailed technical and economical characteristics. Their cost, time, implementation, technology readiness level and production should be evaluated. Next to that are the margins for each concept established. Through which the feasibility can be deter-

mined. At this phase the project requirement documents and preliminary development plan are also prepared. In the DSE this is done in the baseline report and midterm report.

- **Phase B - Preliminary Definition**

With the feasibility known, the final concept can be selected. The design justification should be well documented. Then preliminary mission analyses together with technical specification and interfaces are assessed. The reliability, maintainability and safety margins are addressed. This phase is done mostly in the final report of the DSE.

- **Phase C - Detailed Definition**

The design selected in phase B is worked out in great detail, to even how the components are mounted to the structure and the layout of the cabling. The detailed definition is finalised between the customer and supplier, it needs to be verified that it will satisfy all the requirements and technical specifications. The interface control is defined, together with all the verification requirements after production. This phase is partially outside the scope of DSE.

- **Phase D - Qualification and Production**

The design for the production needs to be fully established. Then it can be produced and qualified. The entire system shall be tested on ground with in the appropriate facilities, it can then be checked if it meets the requirements. The operational readiness of the system and its components shall be verified. The system database, flight control procedures and ground facilities operation procedures are all validated. This entire phase is outside of the scope of DSE.

- **Phase E - Utilisation**

The launch and the in-flight testing shall be performed. The customer shall review the operations and give baselines to the technical and management goals, aiming for what the spacecraft is designed for.

- **Phase F - Disposal**

All activities between the last conducted science and end-of-life that are required before the mission is over.

For the post-DSE activities, phases C-F will have to be performed. This starts with the completion of the definition of the system, in order to derive the required detail of every subsystem for production. This phase will start after DSE, July 2022. MAGEOS is expected to launch in 2028, this leaves more than 5 years for the development, production and testing, which is more than sufficient, since most CubeSat are developed in a shorter period [126]. However, MAGEOS is estimated to take longer than an average CubeSat design, since it flies in a constellation and is rather large and complex with its boom. Further activities include deciding which components are commercial off-the-shelf bought and which need to be custom made. Furthermore, accurate models of the spacecraft need to be created, the environment needs to be analyzed carefully, since the drag will be high and the solar cycle needs to be low. Other activities include, determining the exact layout, selection of materials for custom parts, methods for production and assembly, determining test setup for all subsystems alone and integrated in the spacecraft, scheduling the purchase of all components, organising all of the managerial sides of the mission. All activities for phases C-F are shown in the phase breakdown structure, Figure 9.1. The planning and duration of all activities is further detailed in Section 9.5.

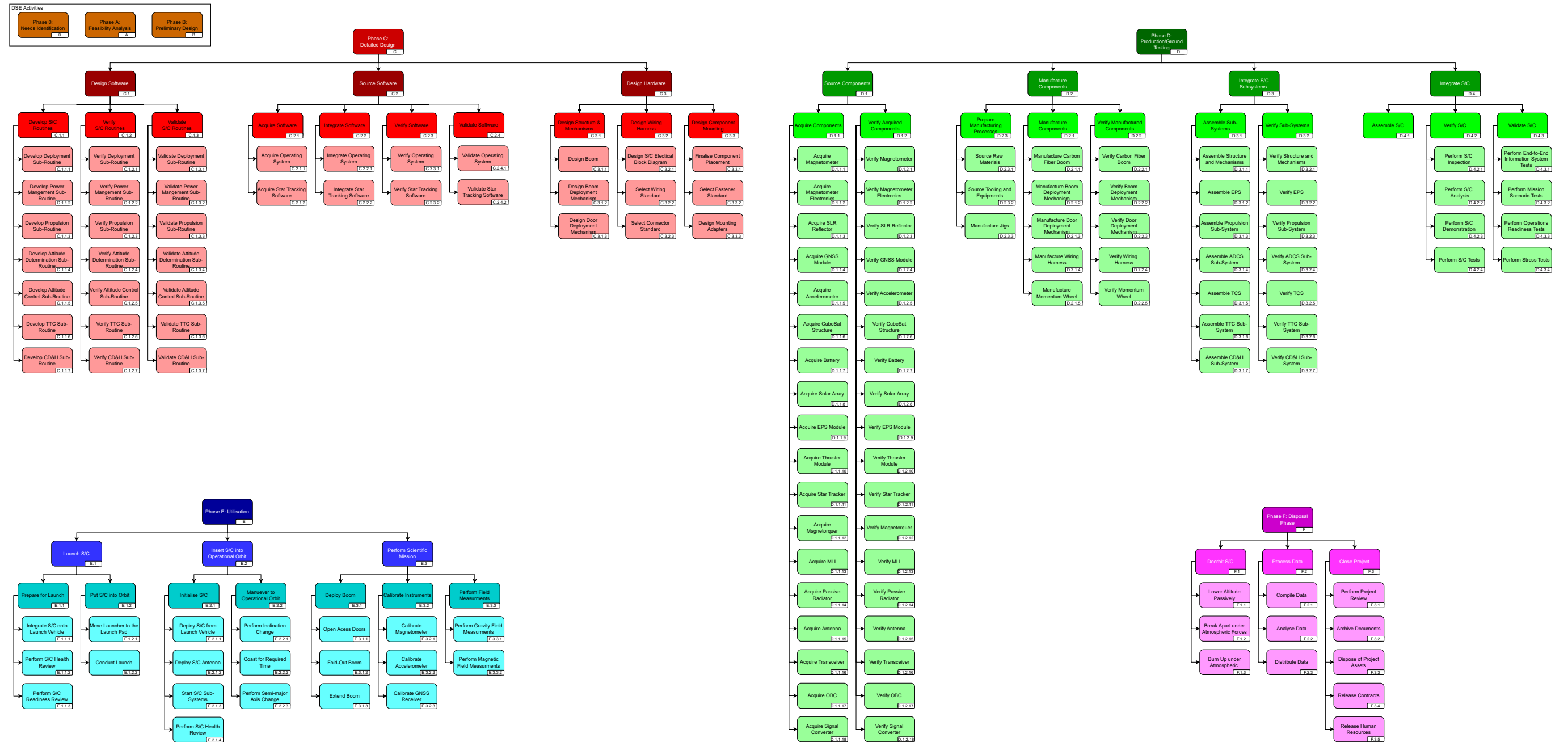


Figure 9.1: Post-DSE Phase Breakdown Structure.

9.2.1. Regulatory Licensing

Another important aspect that may not be overlooked is the regulatory licensing. All CubeSats need to obtain the required licenses before they are allowed to launch. It is often a lengthy process, in the order of 4-6 months [127]. First the regulatory constraints should be understood and the necessary information should be identified, before the system design and operations plan is finalized. One of the necessary licenses is a radio license because it is not allowed to use any frequency desired, since there is limited bandwidth available. There are 4 different licenses types available: Amateur, Commercial, Experimental and Government [128]. MAGEOS would require the Experimental license, it is used for spacecraft conducting experiments, most university CubeSats use this license. If the spacecraft also has a camera onboard, a separate licence is required for its use. This is not the case for MAGEOS.

9.2.2. Flight Certification Documentation

Before the spacecraft is allowed to launch, the mission integrator/launch provider requires a list of documentation of the mission and spacecraft. This list consists of

- **Orbital Debris Mitigation**

This document assures there is no unacceptable danger to other spacecraft in orbit, the deorbiting is done within a sensible amount of time and that the spacecraft will burn up in the atmosphere and does not pose any danger to a populated area.

- **Transmitter Survey**

The transmitter survey contains all the information about the communication system on board. It is used to assess the electromagnetic interference with the launch vehicle and to check the compliance with the radio frequency allocation.

- **Material List**

All the materials used in the spacecraft, to verify no forbidden or dangerous materials are used. Next to that is the amount of the material used on the spacecraft noted, together with its outgassing properties. Outgassing is the process of sublimation of a material in deep-space, this can effect the mission success over time if sensitive components are damaged.

- **Mass Properties**

The mass properties report discusses the mass, center of mass, moments and products of inertia of the spacecraft. The final spacecraft should stay with the tolerances, otherwise the spacecraft is not allowed on the launch vehicle. This can cause unknown risks to the launch vehicle and primary mission.

- **Battery Report**

The battery onboard a spacecraft imposes a risk on the launch vehicle since it is a fire hazard. Therefore the battery report must contain all the information about the electrical circuit protection and battery specifications.

- **Dimensional Verification**

The dimensions of the spacecraft need to be verified after assembly and testing to make sure it still complies with the launch vehicle adapter's requirements.

- **Electrical Report**

This report is used to check if the spacecraft is self contained and identification of the separation switches and remove before flight pin. The pin is the element that separates the electrical circuit from the power system, this pin is removed after integration. The separation switches have a similar purpose and cut the power source from the circuit. But these switches only get released after separation from the launch vehicle.

- **Venting Analysis**

During the launch, the pressure rapidly decreases as the atmosphere gets thinner. It is therefore required that the spacecraft does not contain trapped pockets of air, which could cause a break in the structure and endanger other spacecraft on board the launch vehicle.

- **Testing Procedures**

This document will state all testing performed together with all the anomalies encountered during the testing. These tests include; day-in-the-life test, performed to assess the spacecraft electronics and software work as planned, after this test it is not allowed to alter the flight software. Vibration and Shock testing, since the launch vehicle can shake vigorously during launch, the spacecraft needs to be able to survive the launch loads. After successful testing it is not allowed to alter the hardware or appendages/deployables. Thermal Vacuum Testing, during this test the spacecraft is subjected to a vacuum and the temperatures encountered during its mission. Next to that, a thermal cycling test can be performed to improve the mission success.

9.3. Production Plan

The manufacturing, assembly, and integration plan (production plan) is used to ensure the spacecraft is built correctly. It provides an ordered timeline of all the activities that must be carried out during the production of the spacecraft. Since most components used in MAGEOS are commercially off-the-shelf (COTS) available components, fabricating components needs a low amount of complex tools and qualified personnel. The off-the-shelf components only need to be tested upon arrival to verify that they function as desired. The scheduling of the production should incorporate plenty of margin, since the spacecraft has never been manufactured before, making it difficult to accurately predict how much time is necessary for each step. The assembly should not be rushed, since this compromises quality and mission success. Additionally, the duration of the assembly is heavily dependent how experienced the assembly team is. The MAGEOS mission will fly in a constellation of 2 spacecraft which are built simultaneously. This is beneficial since it reduces the production costs per and assembly time for each spacecraft. During the entire assembly and integration process, documentation is extremely important. Taking pictures and transcribing progress throughout the process can save the mission. This way mistakes can be traced back in time when it's still on the ground. It also ensures no knowledge is lost if, for example, people leave and join the team during its development. It also helps with the continuity of the project, since the wheel will not have to be invented again.

The testing phase of the production will consist out of two types of testing; internal and verification testing. The first is to ensure that the design works and meets the requirements. The second form of testing is to provide the correct documentation for the mission integrator/launch provider to prove the spacecraft is able to launch safely. During testing, it is important to never assume that individual subsystems, that passed their standalone testing, will function the same when integrated with other systems. Furthermore, it is helpful to thermal vacuum test individual components and subsystems before integration. This will catch issues early on in the process which saves time and reduces over-testing the system.

Since the MAGEOS mission is a first of its kind, there are greater risks associated with it, as discussed in Chapter 10. It is therefore important to thoroughly test the spacecraft, this is done according to the philosophy in Figure 9.2, based on the EIRSAT-1 mission [129]. First, the development models (DM) are created. These serve as an engineering test unit where all the in-house manufactured components are tested. Next, a FlatSat is assembled, this is a workbench with all the spacecraft components laid out flat, easily accessible, not integrated in the structure. This will serve as the engineering qualification model (EQM). This model is used to functionally test all components, after which they are assembled together to test them integrated. Next the EQM is tested if it can withstand the harsh conditions of space. This model is then not disassembled, but instead kept intact. This is done because it can support the

ground crew, functioning as a debugging tool to support the spacecrafts in orbit. This does increase the costs of the mission, since an extra spacecraft needs to be made. However, this also increases the mission success rate, which is deemed more valuable since the mission is used for technology demonstration and therefore already has a relatively high associated risk. Next, the flight model (FM) is build with the feedback gained from the EQM. The FM is not tested to the same extent as the EQM. While the EQM is tested to qualification levels, the FM is only tested to acceptance levels. If it passes all the tests it is send to space to conduct science.

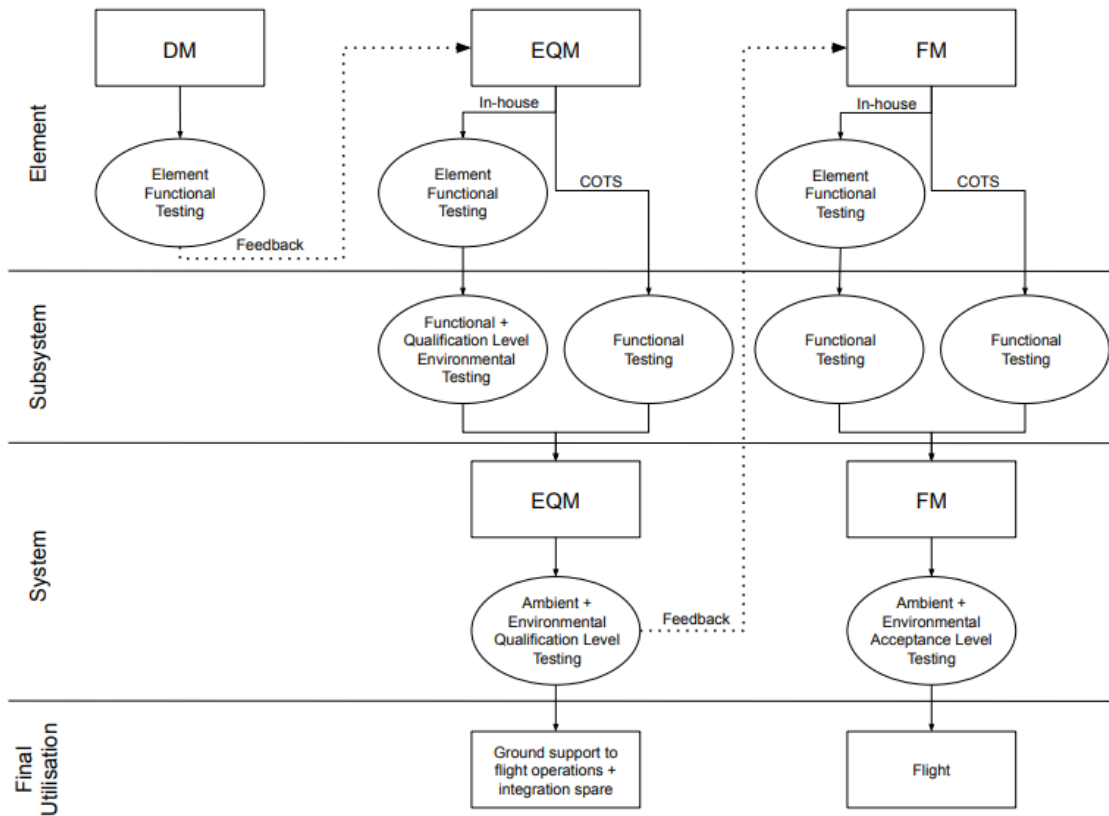


Figure 9.2: Testing procedure of the MAGEOS mission, showing all the testing performed for each component, subsystem and system. The EQM will serve as a spare system used to support the FM once in space. [129]

9.4. Cost Breakdown

In this section the cost of the MAGEOS mission is estimated. It is important to assess the feasibility of the project, since investors/companies need to be convinced before they approve the budget.

9.4.1. MAGEOS mission cost

Firstly, all the commercial off-the-shelf available components' costs have been determined. Table 9.1 shows a detailed cost breakdown of the commercial off-the-shelf available components per spacecraft. Not all manufactures share the price of their products, if this is the case, the price will be estimated based on similar products on the market. The cost breakdown of the in-house manufactured components are shown in Table 9.2. These costs exclude the labour cost, since they will be addressed later on in the cost breakdown. A single spacecraft costs only 324 [k\$], where most of the costs come from the magnetometer setup. It requires two magnetometers and two star trackers which together are responsible for 30% of the total costs. The thrusters alone are responsible for 25% of the costs, these can be drastically reduced if the orbital altitude increases.

Table 9.1: Cost breakdown of the commercial off-the-shelf available components on MAGEOS.

Component	Cost [€]	Amount	Total Cost [€]
Magnetometer	15,000	2	30,000
GNSS Module	19,000	1	19,000
Accelerometer	15,000	2	30,000
Retro-Reflector	2,250	1	2,250
CubeSat Structure	3,650	5	18,250
Batteries	4,400	1	4,400
Solar Arrays	1,900	14	26,600
EPS Module	2,900	1	2,900
Thruster Module	40,300	2	80,600
Star Tracker	35,000	2	70,000
Magnetorquer	600	3	1,800
MLI	4,000	1	4,000
Passive Radiator	2,000	2	4,000
Antenna	2,150	1	2,150
Transceiver	9,300	1	9,300
OBC	6,500	1	6,500
Converter	100	1	100
Total	164,050	41	311,850

Table 9.2: Cost breakdown (ex. labour costs) of the in-house manufactured components on MAGEOS.

Component	Cost [€]	Amount	Total Cost [€]
Carbon-Fiber Boom	500	2	1,000
Boom Deployment Mechanism	200	1	200
Door Deployment Mechanism	200	1	200
Wiring harness	1,000	1	1,000
Momentum Wheel	10,000	1	10,000
Total	11,900	6	12,400

Since the MAGEOS mission is planned to launch in 2028, the cost throughout the mission should be compared in a fair manner. Money received in the future is worth less than the same amount today. This is corrected for by the net present value (NPV), reducing value to its present worth. This is done with the discount rate in Equation 9.1, where R is the net cash flow, i is the discount rate, and t is the time of the cash flow in years. A realistic discount rate in the Netherlands is 2.5% [130].

$$NPV = \frac{R}{(1+i)^t} \quad (9.1)$$

Since the components for MAGEOS only need to be bought in the beginning of 2024, the net present value currently is 312 [k€]. The labour costs of all post-DSE are summarized in Table 9.3, these are based on all the activities defined in Figure 9.1. The labour cost per day per person are estimated to be 800 [€], which stems from the 100 [€] per hour for a junior engineer [131]. The workload is introduced since some tasks take weeks, as stated by the Gantt chart, but do not require dedicated work for each of those days. The 'Years' indicate how long it takes before the expense is made. The biggest expenses are developing the S/C sub-routines software, integrating the custom software, assembling sub-system and lastly processing the acquired data.

Table 9.3: Labour costs per the tasks defined in the phase breakdown structure (Figure 9.1), some tasks do not require labour and are left out.

Task ID	Work Days	Workload	# of People	Task Cost	Years	NPV Costs
C.1.1	130	50%	4	208,000	0.5	205,207
C.1.2	65	25%	4	52,000	1.0	50,678
C.1.3	66	25%	4	52,800	1.3	51,138
C.2.1	24	5%	1	960	0.1	957
C.2.2	44	50%	4	70,400	0.2	70,030
C.2.3	23	25%	4	18,400	0.4	18,228
C.2.4	22	25%	4	17,600	0.5	17,400
C.3.1	45	50%	2	36,000	0.1	35,886
C.3.2	45	50%	2	36,000	0.1	35,886
C.3.3	45	50%	2	36,000	0.1	35,886
D.1.1	45	5%	1	1,800	1.5	1,733
D.1.2	44	25%	2	17,600	1.7	16,872
D.2.3	45	25%	1	9,000	1.5	8,663
D.2.1	44	50%	2	35,200	1.7	33,744
D.2.2	44	25%	2	17,600	1.9	16,802
D.3.1	66	75%	2	79,200	1.8	75,764
D.3.2	45	25%	2	18,000	2.0	17,114
D.4.1	45	75%	2	54,000	2.2	51,126
D.4.2	21	25%	2	8,400	2.4	7,920
D.4.3	23	25%	2	9,200	2.5	8,657
E.3.1	22	5%	1	880	6.0	758
E.3.2	22	100%	1	17,600	6.0	15,160
E.3.3	283	25%	1	56,600	6.0	48,752
F.1	23	25%	1	4,600	7.1	3,857
F.2	110	75%	2	132,000	7.1	110,693
F.3	22	50%	2	17,600	7.5	14,638
Total				1,007,440		953,546

9.4.2. Return on Investment

The total cost breakdown of the MAGEOS mission is shown in Table 9.4. The costs during DSE are assumed to be zero, since it is part of the bachelor. After that, engineers need to be hired for the completion of the mission. The MAGEOS mission will consist of two spacecraft following each other in orbit, however, there is budgeted for three spacecraft. This is necessary in order to build the EQM described in Section 9.3, in order to increase the success rate of the mission. Almost all costs are in the development and production of the mission. The operational costs are dominated by the Amazon Web Services and the operational labour costs, which do not have a significant impact on the total costs, less than 11%. For commercial products, higher total unit production results in lower unit production costs, since the development costs can be divided over more units. Unfortunately, this does not hold for MAGEOS (and spacecraft in general) since most of the time only one or a couple are produced.

Speaking in basic economic terms, investing in a project is only done if the expected return is higher than the investment and outweighs the risk. However, this is different for a science mission like MAGEOS. The project does not have a direct measurable return. No money is earned throughout the process and the value of scientific data is hard to put a figure on. The data gathered by MAGEOS can be used to more effectively counter climate change and help scientists get a better understanding of how the planet functions. One could argue that contributing to saving the environment is worth any amount of money. The question still is, who is going to pay for it. Next to that, MAGEOS will serve as a technology demonstration mission. It will demonstrate gravimetry and magnetometry being performed

by a CubeSats at an extremely low earth orbit, while in constellation and for a significantly lower costs than similar missions. If the mission performs nominally, the advanced state-of-the-art technology can be used by other companies, that in their turn get valuable information about these technologies. These companies can develop the technology further and avoid the risks associated with such technology demonstration missions. This can lead to innovations that benefit the general public. Which is, again, hard to determine the total value of. Due to the complex nature of the problem, the assumption has been made that the scientific data is at least as much worth as the mission costs. This way it would be a reasonable investment to make. Therefore, the total cost breakdown shows the MAGEOS mission is expected to break-even in terms of net present value.

Table 9.4: Total cost breakdown of the MAGEOS mission, corrected to the net present value (NPV).

Category	Unit Cost [\$]	Amount	Total Value [\$]	Date of cashflow	NPV [\$]
Bought Components	311,850	3	935,550	1/1/2024	900,428
Manufactured Components	12,400	3	37,200	1/1/2024	35,803
Labour	1,007,440	1	1,007,440	5/9/2024 ^a	953,482
Launch Services	2,050,000	1	2,050,000	1/1/2028	1,787,477
Orbital Transfer Vehicle	384,280	1	384,280	1/1/2028	335,069
Amazon Web Services	96,251	1	96,251	1/1/2028	83,953
Total Cost	-	-	4,434,348	-	4,030,954
Scientific Value ^b	4,845,367	1	4,845,367	1/12/2029	4,030,954
Total Profit	-	-	411,019	-	0

^a Average date for labour cost, ^b Estimated value of data in order to break-ever.

9.5. Gantt Chart

The Gantt chart of the post-DSE activities of the MAGEOS mission is shown in Figure 9.3. It is planned to end in 2029, but this is dependent on how well the mission performs, and if any anomalies show up. The tasks that take most of the time are the design of the software, integration of the S/C subsystems, performing the scientific mission, and processing the data.

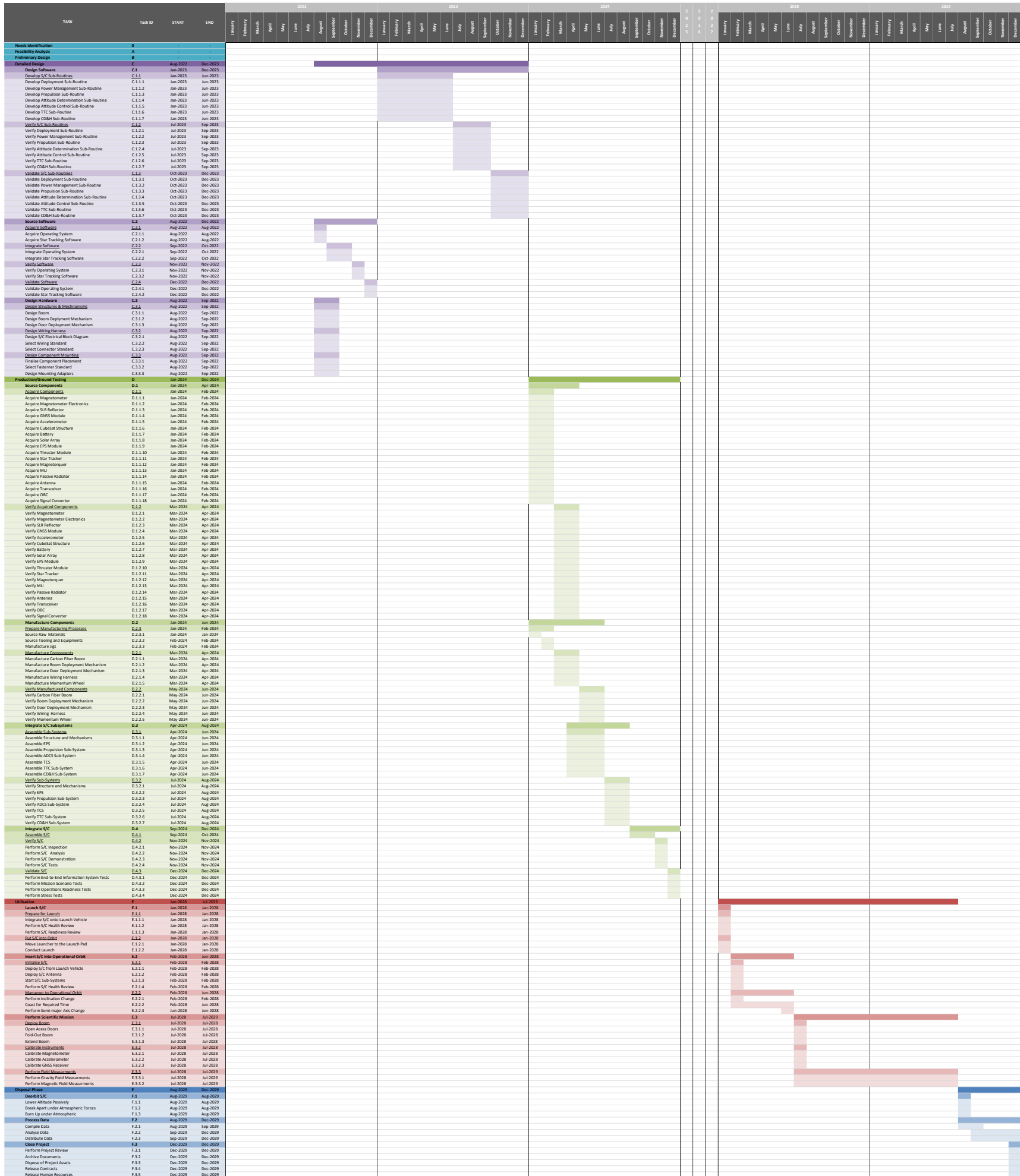


Figure 9.3: Gantt Chart of the post-DSE activities.

Chapter 10: Risk Assessment

For every developed product, failures of parts can occur. In some cases, these failures could lead to a total failure of the purpose of the product. In this chapter, the risks that could lead to damage or total failure of the MAGEOS mission will be examined. These risks could originate from technical systems, operation of these systems, and external events. To prevent mission failure, it is important to identify the risks and manage them to acceptable levels, since risks can never be fully removed. Most risks have already been identified in the mid-term report [1]. The likelihood of these events as well as their impacts will be updated and justified with the final mission design. Furthermore, new risks have been identified and will be added. For the risks with a high risk rating a mitigation plan is developed to reduce the risk's impact or likelihood. In Section 10.1, the risks will be identified, labeled, and given a likelihood and impact to the system. After this, in Section 10.2, two risk maps will be presented: one pre-, and one post-mitigation. Risk mitigation strategies will be given in Section 10.3.

10.1. Risk Identification

In this section, the identified risks for the MAGEOS mission will be mentioned and explained. The risks will be split up in 3 categories: system failures, external influences and operational failures. All risks are organized with a risk ID and a title. Their event, cause, and effect will be discussed, and their likelihood, impact, and risk rating is determined. The likelihood rating has 5 levels: very unlikely, unlikely, possible, likely, or very likely. Similarly, the impact and risk rating both also have 5 levels: very low, low, moderate, high, or very high.

The likelihood rating is justified through literature, as likelihood of subsystem failures as well as other types of failures have been found [113]. In Table 10.1, the likelihood rating is coupled to the failure rate found in literature.

Likelihood level	failure rate [113]
Very unlikely	0-10%
Unlikely	10-20%
Possible	20-50%
Likely	50-80%
Very likely	80-100%

The failure rates has been determined by making use of Figure 10.5, where the reliability has been taken for a mission duration of two years. To find the failure rate, $1 - Reliability$ is used.

The results for each subsystem is given in Table 10.2. These are the failure rates after two years mission duration. These will be used for the entire duration of the mission.

Subsystem	failure rate [113–115]
ADCS	6%
CDHS	9%
COMMS	8%
STS & DepS and P/L	6%
EPS	21%
Prop	$\approx 0\%$
TCS	4%
TT&C	24%

The failure rates has been determined by making use of Figure 10.5, where the reliability has been taken for a mission duration of 2 years. To find the failure rate, $1 - Reliability$ is used. two

10.1.1. System Failures

This subsection explains the risk associated with the failure of systems and their subsystems. Table 10.3 originates from the mid term report [1], and is updated here.

Risk ID	Risk Title	Event, Cause and Effect	Likelihood, Impact of Risk, Risk Rating
TR-SYS-01	EPS Failure	EPS failure can be caused in numerous ways, including but not limited to broken solar panels, improperly deployed solar array, power condition unit failure, power distribution unit failure and power storage failure. In case an EPS failure occurs, the spacecraft is not able to provide the spacecraft bus with enough power. Due to this, other systems and subsystems that require power can no longer be operated and used as intended.	EPS failure is likely as can be seen in Table 10.2. Depending on the extent of the damage, the mission can at best partially continue, and at worst end immediately. The impact is high, meaning the risk rating is high as well.
TR-SYS-02	AD Failure	When the attitude determination system fails, the spacecraft is unable to determine its own attitude in space. In case this event occurs, multiple subsystems can not fully operate, including: attitude control, EPS, TT&C, and the payload.	The AD is very unlikely to fail as can be seen in Table 10.2. Since commercial off the shelf components will be used with a high TRL level, it is justified to make use of the aforementioned analysis of ADCS failure. In case AD failure occurs, it has a high impact to the mission. The risk rating is low.
TR-SYS-03	AC Failure	If the spacecraft loses all attitude control, the mission will be quickly lost. The instruments can not properly gather data, the propulsion system can not counteract drag and communication is not possible. Attitude control failure can occur due to a failure of the magnetic bias momentum wheel as well as failure of the magnetorquer.	The likelihood of attitude control failure is unknown. Due to the new technology of the biased magnetic bearing momentum wheel and the newly developed magnetorquers, the chance of a failure occurring is higher compared to the failure rate of the ADCS system given in Table 10.2. The impact is very high, since a failure to control the attitude renders many subsystems useless, and also reduces mission lifetime significantly. The risk rating is very high.
TR-SYS-04	Prop Failure	Propulsion system failure can have a lot of causes, including but not limited to: feed line failures, faulty valves, and nozzle misalignment. In case this happens, the mission time will be shortened, but there will still be a possibility to perform measurements. Since the MAGEOS mission uses electric propulsion, failures are different compared to chemical propulsion.	In Table 10.2, it can be seen that the the failure rate of the propulsion system is approximately zero. This is due to there not having been any failures of the propulsion system in LEO [114]. Therefore, failure is very unlikely. The impact is moderate, as failure won't end the mission, but will significantly reduce its lifetime. The risk rating will be low.
TR-SYS-05	TT&C Failure	If the telemetry, tracking and command module fails, the spacecraft is no longer being able to make contact with the ground station, or vice versa. In case an uplink failure occurs, the spacecraft can not receive commands anymore. In case there is a downlink failure, the mission is effectively over since the payload data won't be received on earth.	The likelihood of these events taking place are possible, as can be seen in Table 10.2. The impact is very high. The risk rating is high.
TR-SYS-06	TC failure	The thermal control system prevents the spacecrafts' systems, subsystems and payload from reaching temperatures outside their operational range. Damage to TC may result in heating up or cooling down of the spacecraft beyond these ranges. Since the TC system is only passive, the likelihood of failure is reduced.	TC failure is very unlikely as can be seen in Table 10.2, and the impact is moderate. Therefore the risk rating is low.

TR-SYS-07	Payload failure	Multiple sensitive instruments are dedicated to measuring the Earth's gravitational and magnetic field. This means there are numerous common causes for payload failure. However, if a subsystem fails, only the measurements of one of the fields will be missing.	The likelihood of a payload failure is unknown, since the payload of the MAGEOS mission exists out of new equipment that contain many components. The impact is high, as it directly reduces the amount of data the spacecraft can provide, but not very high because it does not affect the other measurements made on the spacecraft. The risk rating is high.
TR-SYS-08	Telescopic mast failure (Deploy mechanism failure)	The telescopic mast motors might fail and prevent deployment of the mast. The effect is that magnetic field measurement cannot be conducted.	The likelihood of deployment failure is very unlikely as can be seen from Table 10.2. The impact is however high. The risk rating is low.
TR-SYS-09	Structures failure	Structure failure includes, failure of bolts, nuts, parts of the structure and many more. The spacecraft exists out of a modular structure. In case the structure fails due to launch loads or impacts, the spacecraft will be severely damaged and can not be used anymore.	Structure failure is according to Table 10.2 very unlikely. The impact is very high, since a structures failure for the MAGEOS mission could lead to the end of the mission. The risk rating is moderate.

10.1.2. External Events

This subsection concerns contingent external events that pose a risk to the spacecraft. Table 10.4 originates from the mid term report [1], and is updated here.

Risk ID	Risk Title	Event, Cause and Effect	Likelihood, Impact of Risk, Risk Rating
TR-EE-01	Critical Impact	Collision with other objects in orbit are highly destructive, especially for a small satellite like a Cube-Sat. Collisions can happen with other spacecraft, space debris, as well as micro asteroids.	The likelihood of a collision is, despite increasing amounts of space debris, very unlikely, as there are just a few examples of critical impacts in the history of space flight [132]. This is especially true since the spacecraft is in VLEO, and the mission will only take one year. This impact is very high, with an immediate end of the mission. This leaves the risk rate as moderate.
TR-EE-02	Solar Flare	Solar flares are largely unpredictable releases of high energy electromagnetic radiation. This radiation indirectly increases the drag on spacecraft, reducing mission lifetime, as well as disturbing radio communications such as GPS.	Small solar flares are common enough that the spacecraft will be disturbed by them multiple times, but have very low impact. High intensity solar flares, that may have significant impact on the mission lifetime and communications, are not very common. The spacecraft will be launched in a solar cycle minimum, reducing the likelihood of high intensity solar flares. Solar flares are very likely, but their impact is very low, meaning the risk rating is moderate.
TR-EE-03	Market Instability	The spacecraft design will likely require highly technical and specific components. These components may come from all over the world, meaning global events may impact their market price and availability. This can have a negative impact on the cost and time necessary for design and production	It is unfeasible to determine the likelihood that relevant markets are disrupted, due to an endless list of variables effecting them. This also means the risk rating can not be determined. The impact of this risk can, however, be high.
TR-EE-04	Change in Legal Regulations	Legal regulations changing concerning the certification of the spacecraft is a risk that may impact the development of the spacecraft. If these changes mandate killer requirements late into the design process, this will result in a large increase of costs, time, as well as re-negotiations for the requirements of the stakeholder.	The likelihood of such a change in regulation that specifically impacts this mission is very low, however the impact is high. This means the risk rating is low.

TR-EE-05	Dust Contamination	During production, and pre-launch operation, dust contamination can enter the spacecraft. Dust Contamination can degrade the performance of systems, particularly with optics, and solar panels.	It is an impossibility to account for every particle found in the spacecraft. Therefore, the likelihood of particles on the spacecraft is very likely. However, the impact these particles have is very low, especially since no optics are being used in the spacecraft. This means the risk rate is moderate.
TR-EE-06	Highly charged particles exposure	During its stay in space, the spacecraft will be exposed to highly charged particles that will collide with the spacecrafts structure, such as its solar panels. This could lead to degradation of the solar panels and could damage the spacecrafts electronics and computers on board.	The likelihood of the spacecraft being exposed to highly charged particles is very likely. The impact however is very low. Therefore, the risk rate is moderate.

10.1.3. Operational Failures

This subsection explains the risk associated with the operational failures. Table 10.5 originates from the mid term report [1], and is updated here.

Risk ID	Risk Title	Event, Cause and Effect	Likelihood, Impact of Risk, Risk Rating
TR-OF-01	Wrong Orbit Insertion	Post launch, the spacecraft may end up in an orbit other than the one designed for. This could happen due to launcher malfunction, loss of communication during periods of launch, or miscalculations concerning the aerodynamic and propulsive properties of the spacecraft. The effect this has on the orbit as a whole is large and widespread. This is because every system is designed for one specific orbit: the resolution of the instruments, the thrust to overcome decay, the solar panels and battery to stay powered through eclipse, the TT&C system for power of transmitter and bit rate.	The likelihood that an insertion into a wrong orbit takes place is unlikely, since a launcher will be used that will launch the spacecraft very close to the correct orbit. The effect this has on the mission is high and varied. The severity mostly depends on how different the orbit is to the design orbit. The risk rating is therefore moderate.
TR-OF-02	Launcher Failure	Launch failures occur, meaning any mission has a risk of failing due to a complete, or partial, failure in the launch. The result of a failed launch is the immediate termination of the mission, the spacecraft will be destroyed.	The launcher for the MAGEOS mission has been chosen to be the Falcon 9. Due to this, the likelihood of a launch failure is very unlikely [116]. However, if a launch failure occurs, the impact is very high. The risk rating is therefore moderate.
TR-OF-03	Damage due to launch	During launch, launch loads, vibrations, and acoustic vibrations can damage the spacecraft. This can lead to damage to specific components and systems.	The likelihood of damage due to the launch is possible. The impact is low, meaning the risk rating is low.
TR-OF-04	Failures in Transportation to Launch Site	During transportation of the spacecraft to the launch site, the spacecraft could be damaged, stolen, missing its launch due to arriving to late, or arrive at the wrong location.	The likelihood of these events is very low. The impact is high, meaning the risk rating is low.
TR-OF-05	Failure in EOL Plan	Requirement CON-SUS-1 mandates that the spacecraft shall be disposed by total burning in the atmosphere. There is a risk that this EOL requirement will fail if the spacecraft does not entirely burn up.	The likelihood of this risk is very low, since the Delta-V budget is analysed to make sure that the spacecraft will fully burn up during re-entry. The environmental impact will be low since the spacecraft will be made with non-toxic materials. The risk rating is overall very low.
TR-OF-06	Orbital maintenance failure	If the maintenance of the orbit is not correctly performed, the spacecraft may not be in the desired orbit, or even be in an orbit with a lower altitude than desired. This may have a negative effect on the lifetime of the mission	The likelihood is unlikely. The impact is low as the spacecraft can likely still perform its tasks in a slightly different orbit. The risk rating is therefore moderate.

TR-OF-07	Constellation failure	During the mission the constellation formation will deviate. This will cause the spacecraft to measure different values	The likelihood of constellation failure is unknown. The impact which this has is very low as the spacecraft could operate individually. However, the complexity of the calculations associated with the gravitational measurements increases, and the accuracy decreases. The risk rating is moderate.
----------	-----------------------	---	--

10.2. Risk Analysis

In Figure 10.1, a risk map before risk mitigation is shown, as presented in the mid term report [1]. The risk map is updated with the newly identified risks, as well as the lower likelihoods or impacts of certain risks by making use of the the design choices made. For some of the identified risks the likelihood is still unknown, as they are unable to be estimated accurately. These risks are shown in the 5 blocks going from green to red below the risk map. From the risk map it can be seen that only a few risks pose a threat to the mission. The very likely risks have a very low impact, while the risks that cause a higher impact on the mission have a low likelihood. The risks are placed in colored boxes. The meaning of the colours is as follows: dark red for very high risk, red for high risk, orange for moderate risk, yellow for low risk, and green for very low risk.

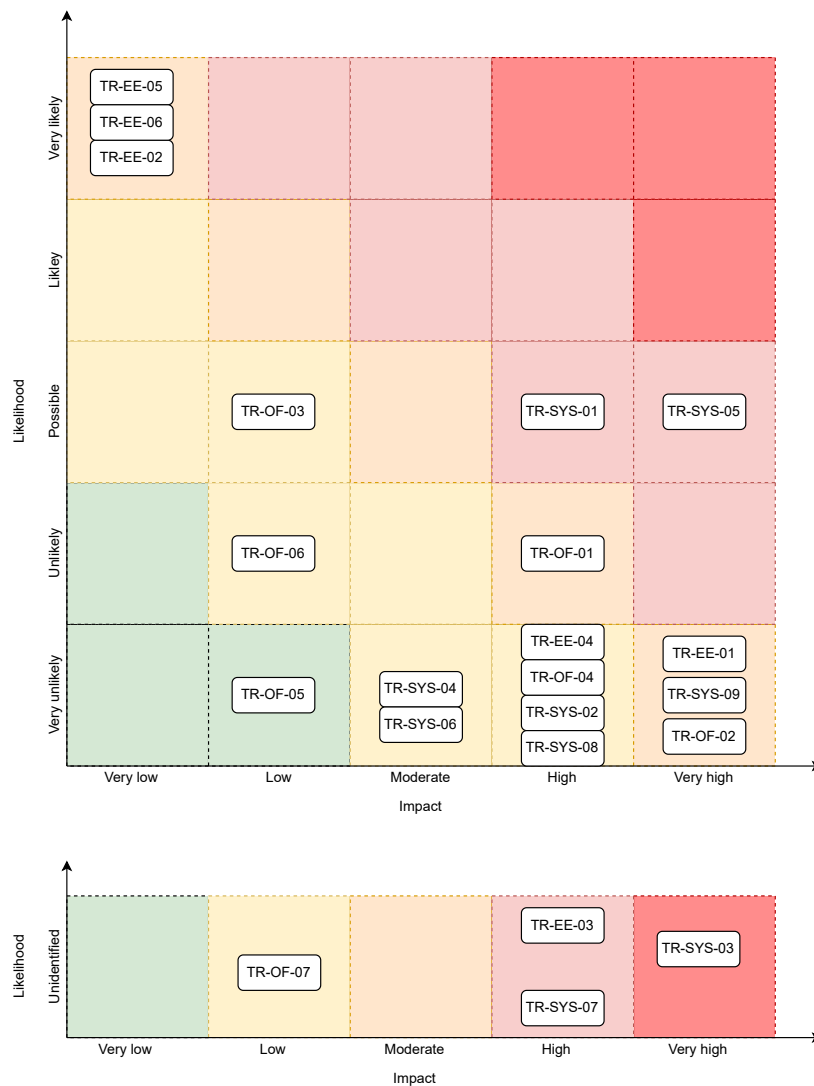


Figure 10.1: Risk map before risk mitigation strategies are applied, divided into risks with an identified likelihood, and without.

From Figure 10.1 it can be seen that only a few risks have a high risk rating. In the next section, the risks which have a higher risk rating than moderate will be discussed in the next section where risk mitigation will be applied. Other risks are considered to be acceptable since they will not cause significant harm to the mission.

10.3. Risk Mitigation

After the risk map has been created, risk mitigation and prevention strategies can be applied to risks with a risk rating higher and equal to moderate, to try decreasing the risk rating. This can be done by making use of strategies to either decrease the likelihood, or the impact to the mission. Unfortunately, some risks can not be mitigated and will therefore be accepted. In Table 10.6, the mitigation and prevention strategies for the risks with a risk rating of moderate and higher will be presented.

Risk ID	Mitigation/Prevention Strategy
TR-SYS-01	The EPS system is vital in making sure all other systems are able to operate. If there is insufficient power, yet the EPS system still divides the power the same way as designed, it may be that no systems are able to operate. A mitigation strategy to implement is that different combinations of powered subsystems are identified for different power levels. By cutting losses, the spacecraft as a whole would still be able to provide some data, instead of none. This reduces the impact of the risk to moderate, leading to a low risk rating.
TR-SYS-07	In case the payload fails, the mission could potentially not be executed anymore. However, due to the constellation design, the instruments are doubled. In case the magnetometers fail, the other spacecraft could still perform measurements. Furthermore by making use of two different magnetometers, some measurements could still be performed if one of the two fails. In case the GPS the same holds since two GPS sensor are brought on board each spacecraft for redundancy. The impact will therefore be reduced from high to low, meaning a risk rating of moderate.
TR-SYS-09	Structure failure could lead to a mission failure. However, by splitting critical systems over the entire spacecraft, the impact of certain structure failure can be reduced. The impact of a structure failure can be reduced from very high to high, leading to a risk rating of low.
TR-EE-03	Market instability can occur at any moment. The impact of such an occasion is high, since components can become more expensive or are no longer being available. This impact can be reduced by choosing back-up components. This is for now outside the scope of this report. The impact of this risk will decrease from high to moderate, leading to a risk rating of moderate.
TR-EE-05	Dust contamination will unfortunately always happen. However, the likelihood of this occurrence can be prevented by making use of clean rooms for assembly and testing, as well as making use of a clean storage box for the spacecraft during transportation. The likelihood of this event will than be decreased from very likely to likely, resulting in a low risk rating.
TR-OF-01	Insertion into a wrong orbit can have a large scope of effects on the functioning of every subsystem. A full-scale analysis should be performed as soon as possible for this new orbit, the most important new value being the altitude. If, through changes in the designed operations of the spacecraft, it can still fulfill part of its mission, these changes should be communicated to the spacecraft. Furthermore, a Delta-V margin will be added to make sure that these corrections can be performed. This reduces the risk impact from high, to moderate or even low, depending on how well the spacecraft can function in this new orbit. This will lead to a new risk rating of low.

Through the implementation of these mitigation and prevention strategies, risk impacts of 8 risks are reduced, to a more acceptable level. The position of affected risks in a post mitigation/prevention risk map is seen in Figure 10.2.

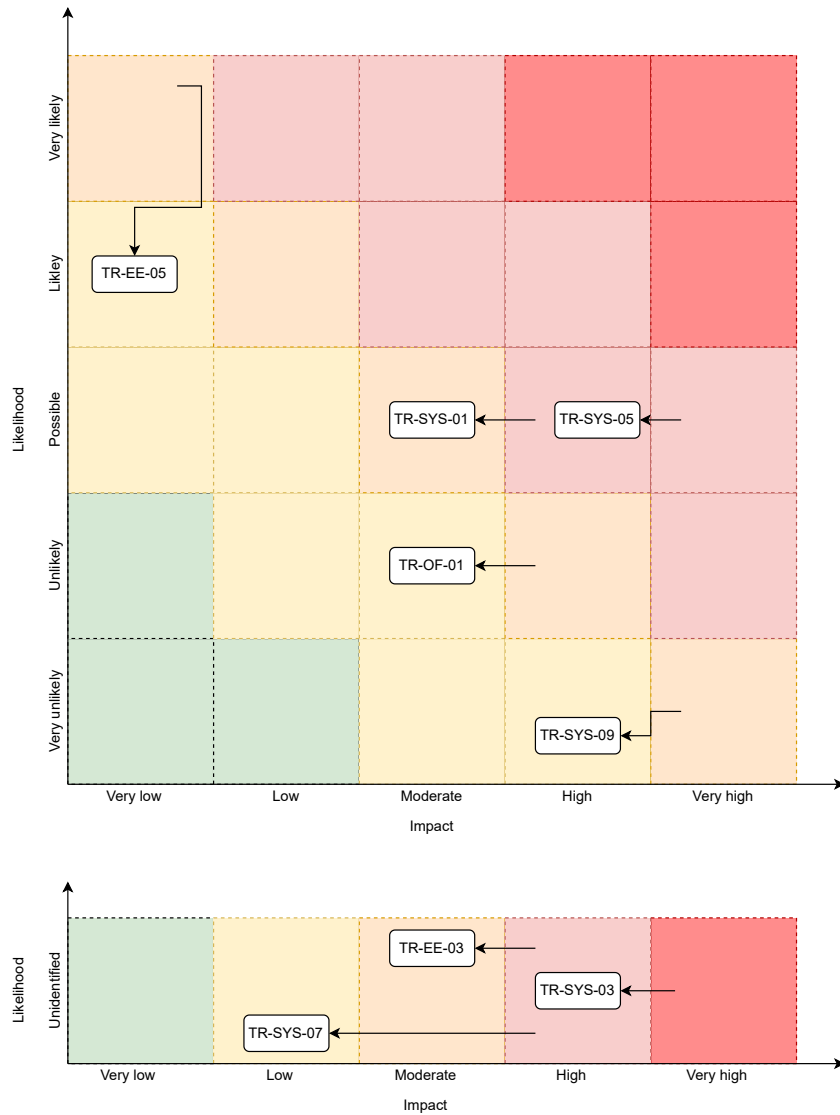


Figure 10.2: Risk map after risk mitigation strategies are applied, not including the risks that must be accepted.

The arrows show the path the risk takes, from pre-mitigation to post-mitigation. Note that the position within each box has no significance. After the mitigation and prevention strategies has been applied, some risks have, unfortunately, still a risk rating of moderate or higher and must be accepted. These risks are:

1. System failures: 1, 3, 5
2. External events: 1, 2, 3, 6
3. Operation failures: 2

It should be noted that this mission is also a demonstration mission. Therefore, the AC system will not be changed to a more reliable one, which would have decreases the impact rating of the entire ADCS system. Furthermore, the risks that will be accepted are considered to be normal for a space mission and will therefore be accepted.

10.4. Reliability

Reliability of the spacecraft and its components is an important part of risk assessment. The reliability of components will determine if mitigation measures have to be taken. In this section the overall reliability of the spacecraft mission is assessed using previous CubeSat missions. Further, a comparison is made between development strategies and its impact on the reliability. Lastly, reliability of all subsystems is assessed.

10.4.1. Impact of Development Strategies on Mission Life-time Reliability

Analysing the impact of the development strategies on the mission life-time reliability gives a good overview which mitigation strategies are required to fall in a acceptable reliability range. The improvement of mission reliability lies within the development strategy and the amount of redundancy in a spacecraft. Figure 10.3 gives an overview of the reliability over the mission life-time with the different development strategies. It also gives an indication of the redundancy impact on reliability.

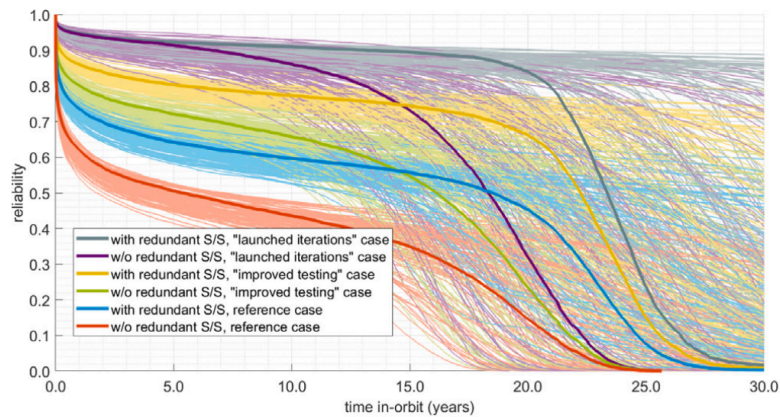


Figure 10.3: Reliability of the CubeSats as a function of time [113]

The three different development strategies include: the reference cases without any strategy, improved testing strategy, and the launched iterations strategy. The improved testing strategy is to test the spacecraft on earth before the actual launch. With feedback from the testing, multiple design improvements can be made. the launched iterations strategy uses multiple design iterations to obtain a more optimal and reliable spacecraft. For each development strategy a extra option for redundancy is included to see the impact for each case. As seen in Figure 10.3, the least reliable case is the reference case without redundancy. the reliability for this option drops down to around 0.6 at a fast rate and keeps decreasing quickly over time. The best option is the launched iterations case with redundancy. This option keeps its reliability above 0.9 for over twenty years during its mission, where after the reliability drops to below 0.2 over five years. looking at the difference in reliability for the reference case with redundancy and the improved testing without redundancy, differences improved reliability are observed at different time stamps. The improved testing without redundancy still has a better reliability in the first fifteen years. From that point, the reference case with the included redundancy gives a better reliability. This observation is also seen with the improved testing case with redundancy and the launched iterations case without redundancy.

Further investigation into the impact of redundancy is done by comparing the reliability of the launched iteration strategy cases. Figure 10.4 showcases the redundancy impact on the reliability for different mission life-time lengths. From the figure, it can be observed that the impact on the reliability is seen for the ten year instance. The impact of the redundancy is extended reliability as the redundant components can overtake functioning ones if the current component is broken. However, it is observed that this difference in reliability is almost negligible for the one and three year instances.

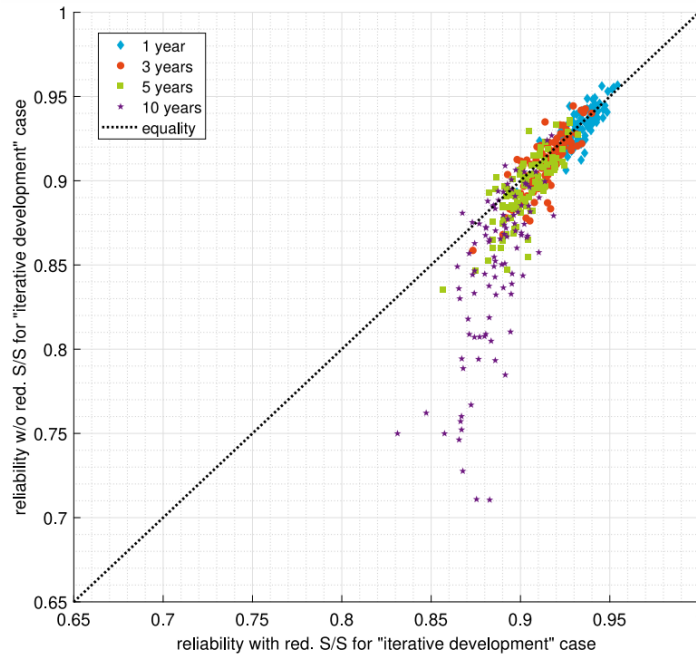


Figure 10.4: Reliability of the CubeSat with redundancy and without redundancy using iterative design process [113]

For the MAGEOS mission, which has a mission life-time of one year, launched iterations without redundancy is the best development strategy. The reason for using this strategy instead the case with redundancy is because the difference in reliability is negligible, looking at Figure 10.3 and Figure 10.4. The expected reliability for the overall mission life-time is between 0.9 - 0.95 during the mission.

10.4.2. Subsystem Reliability

The assessment of subsystem reliability is of extreme importance. If a subsystem fails, the whole mission is compromised of limited functionality is available for the rest of the mission life-time. To prevent this, mitigation strategies or inclusion of redundancy can be applied to the less reliable subsystems, as shown in Figure 10.5.

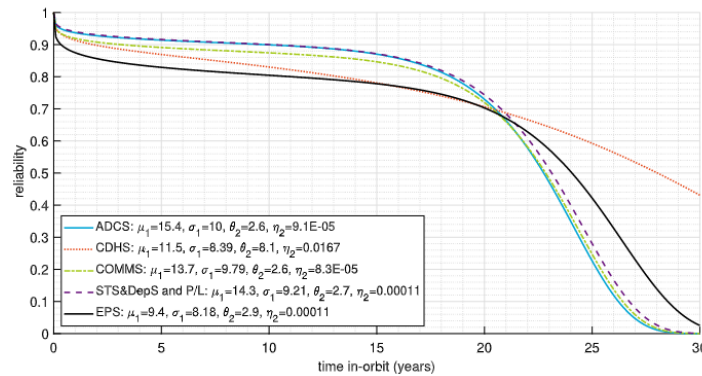


Figure 10.5: Reliability of subsystems during the mission life-time [113]

Reliability of different subsystems as a function of time is shown. At one year, the subsystem reliability of different subsystems is between 0.87 and 0.94. The subsystem with the lowest reliability is EPS, with a reliability of 0.87 after one year. The reliabilities of the subsystems post one year is not much lower, as after one year, with the reliability of most systems only dropping significantly after 20 years, far outside of the mission lifetime.

Due to the high reliability of all subsystems on MAGEOS, additional mitigation strategies or redundancy is not necessary, and will not be implemented.

Chapter 11: Market Review

The Earth observing market is a multi billion dollar market with great application variety. Establishing a picture of the customers and competitors in this market will determine how the mission will be set up. The main aspects of the competitiveness of an mission are cost, sustainability and mission performance.

11.1. Market Customers

Establishing the market customers can be done by looking at what the mission can deliver. Since MAGEOS' main outputs are gravitational and magnetic field data, the market customer who will be continuously interested is the scientific community.

With the knowledge from the gravitational field, deviations from the ideal geoid can be estimated. The geoid is the surface of an ideal global ocean in the absence of tides and currents, only shaped by gravity. This crucial reference is used for measuring ocean circulation, sea-level changes and ice dynamics, which are all affected by climate change [133]. The magnetic field data obtained by MAGEOS can be used to determine space weather [134]. The magnetic variations in space weather affect several technologies, as can be seen in Figure 11.1. Consequently, affected technological companies are market customers of MAGEOS. They can be either direct or indirect customers. In case MAGEOS delivers the data through the scientific community to these companies, the technological companies are indirect customers.

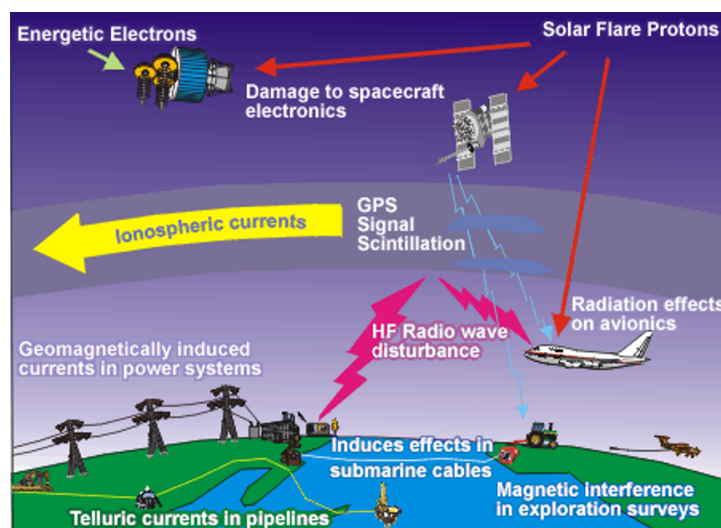


Figure 11.1: Space weather effects on technology [135].

Moreover, the space community has been identified as a customer of MAGEOS. Although the revenues received will be low/zero, MAGEOS might consider data sharing with certain space companies / institutions, to increase revenues/recognition.

The fourth and last clearly identified customer can be dedicated CubeSat companies, who want to demonstrate that the CubeSats they possess are functional. These companies might want to adapt/develop MAGEOS further. However, this requires permission from MAGEOS' team and money to be paid to MAGEOS' team.

11.2. Market Competitiveness

In spite of VLEO EO systems being a relatively young and niche sector, the number of competitors is ever-increasing due to its rapid emergence. This means that the MAGEOS mission being developed under the scope of this project is entering a market which already has some well-established players but also a considerable number of upcoming competitors. The competition for the MAGEOS mission can be broadly divided into two categories: direct competition, and indirect competition. Direct competition comprises current as well as future missions that fall under the domain of miniaturized (distributed) VLEO EO systems, whereas indirect competition comprises current and future VLEO EO missions that utilise larger systems.

11.2.1. Direct Competitors

The direct competitors of the MAGEOS mission can be defined as currently active or planned missions which fulfill the same purpose, i.e. VLEO EO, as the MAGEOS mission while falling under the same target market area. Since VLEO is a region that has only recently started to attract the attention of players in the space industry, it is currently sparsely populated. In addition to this, miniaturized EO S/C, similar to CubeSats in scale, account for an even smaller proportion of this already thin population, owing to the novelty of miniaturized systems. This means that the MAGEOS mission has a mere handful of direct competitors, with some of the key direct competitors listed in the undermentioned text.

- **Planet Labs SkySat** is a mission comprising a constellation of 21 microsattellites that are responsible for the provision of high-resolution visuals for purposes such as vegetation mapping and monitoring, land use mapping, and hydrology monitoring, among others [136]. Initially, this mission was designed by Terra Bella, but was acquired by Planet Labs later in 2017. The satellites orbit Earth at an altitude of 400 km, in a roughly polar circular orbit, with a repeat period of 4-5 days. The constellation is made up of three satellite types based on a 3U CubeSat but scaled up to the size of a minifridge: SkySat-A, SkySat-B, and SkySat-C. While SkySat-A and -B are roughly identical in configuration, with a mass and dimensions of 83 kg and 60 cm × 60 cm × 80 cm respectively [137], SkySat-C is taller and heavier with a mass of 110 kg and dimensions of 60 cm × 60 cm × 95 cm. The constellation was completed on 18 August 2020, and can capture 90-second videos at 30 frames-per-second at a time along with high definition images at a resolution of 50 cm.
- **Planet Labs Flock** is a mission comprising multiple constellations of 3 to 48 3U Dove CubeSats [138]. These constellations are responsible for capturing and transmitting high resolution imagery with a resolution of 3-5 m. The first few constellations included satellites which orbit Earth at an altitude of 640 km, but the more recent constellations are situated at an altitude of 400 km. The Dove satellites used in the Flock constellations have a mass of 5.8 kg and dimensions of 10 cm × 10 cm × 30 cm, in compliance with the 3U cubesat standard [139]. Launches for this mission are still ongoing, with the most recent 44 satellite constellation being launched on 13 January 2022.
- **NSPO-1** is a low-cost Earth observation satellite designed and build by ArkEdge Space [140]. The satellite has a size of 6U and is expected to launch in 2022. The orbit will have an altitude of 400 km and an inclination of 51.6°.
- **Lemur-2** is a constellation of satellites orbiting in Low Earth orbit, performing meteorology measurements and ship and air traffic control tracking [141]. It has been designed and developed by Spire. The total constellation size will be around 100 satellites. The first satellite has been launched in 2015.

11.2.2. Indirect Competitors

In contrast to the direct competition, the majority of the VLEO S/C population consists of missions that can be classified as indirect competitors of the MAGEOS mission as they fulfill the same purpose but utilise systems which do not fall under the same target market area. These S/C are much larger than the MAGEOS mission, which is a CubeSat. A number of these indirect competitors are from well-established players in the space industry such as government space agencies like NASA, ESA, and JAXA. The undermentioned text details some of the more prominent indirect competitors.

- **Aeolus** is a mission for measuring the Earth's wind profile, and is operated by ESA to improve weather forecast and climate models [**Aeolus**]. It was launched on the 22nd of August 2018, and had a mission lifetime of 3 years. Its orbital altitude has been 320 km and had a repeat cycle of 7 days. Its main instrument was a Doppler wind lidar, which measures wind sweeping around our planet.
- **EarthCARE** (Earth Clouds, Aerosols and Radiation Explorer) is a mission planned to be launched in March 2023 [142]. It is a joint partnership satellite between ESA, JAXA and NICT. The main goal of the mission is to cloud observation and aerosols characteristics, as well as measuring solar radiation and infrared radiation reflected from Earth's surface and atmosphere. The mission lifetime is 3 years. The spacecraft will have a launch mass of 2350 kg, a dry mass of 2037 kg and has a size of 2.5 m x 19 m. It will have a power generation of 1700 W. The spacecraft will be located in a sun-synchronous, geocentric orbit, with an altitude of 393 km, and an inclination of 97.1°.
- **Cartosat 3** is an Indian satellite used for Earth observations and weather mapping [143]. It was launched on the 27th of November 2019, and has a mission duration of 5 years. The spacecraft has a launch mass of 1625 kg and has a power generation of 2000 W. The spacecraft is located in a sun-synchronous, geocentric orbit, with an altitude of 450 km and an inclination of 97.5°.
- **Global Precipitation Measurement** is an Earth observation satellite which observes precipitation [144]. It works in a constellation for full coverage. The spacecraft is a joint collaboration between JAXA and NASA. The launch mass of the spacecraft was 3850 kg, and had a power generation of 1.95 kW. The spacecraft had an expected lifetime of three years. The orbit of the spacecraft is a geocentric, Low Earth orbit, with an altitude ranging between the 401 and 415 km. It has an inclination of 65°.
- **RISAT-2B** is an Indian Radar reconnaissance satellite [145]. The mission of the spacecraft is to monitor Earth during the day and night, for any weather conditions. It was launched on the 22nd of May 2019. The launch mass of the spacecraft was 615 kg and had a power generation of 2000 W. The spacecraft has been launched in a sun-synchronous, geocentric orbit, with an altitude of 555 km and an inclination of 37°.
- **Worldview Legion** is a constellation of Earth imaging satellites operated by Maxar [146]. The spacecraft can be used for remote monitoring, mapping, and a 3D presentation of the Earth. The spacecraft are being launched into a mix of sun-synchronous orbits and mid latitude orbits. Maxar's satellites observe the invasion of Russia into Ukraine on a daily base from the start of the invasion. Four satellites are currently in orbit.
- **Swarm** is a constellation existing out of three spacecraft which measures strength, direction, and variation of Earth's magnetic field. Furthermore, each spacecraft has accurate navigation, an on-board accelerometer, and measures the electric field of the Earth [147]. This data will lead to the possibility of modelling the geomagnetic field and its interaction

with other physical aspects of Earth’s system. The mission is led by ESA. Each spacecraft has a launch mass of 468 kg and a power generation of 608 W. The spacecraft are located in two different polar orbits, two flying side by side at an altitude of 450 km and a third at an altitude of 530 km. The SWARM constellation was launched on the 22nd of November 2013. The mission duration was four years, however it is still operational.

- **JPSS** (Joint Polar Satellite System) is a constellation of environmental satellites [148]. The satellites will provide global environmental data used in numerical weather prediction models for weather forecast and scientific data for climate monitoring. The constellation is being operated by NASA. The first satellite was launched in 2011. More spacecrafts will be launched between 2022 and 2023. The spacecrafts will be orbiting in a non-geosynchronous polar orbit.

11.2.3. SWOT analysis

The SWOT analysis for MAGEOS is shown in Figure 11.2.

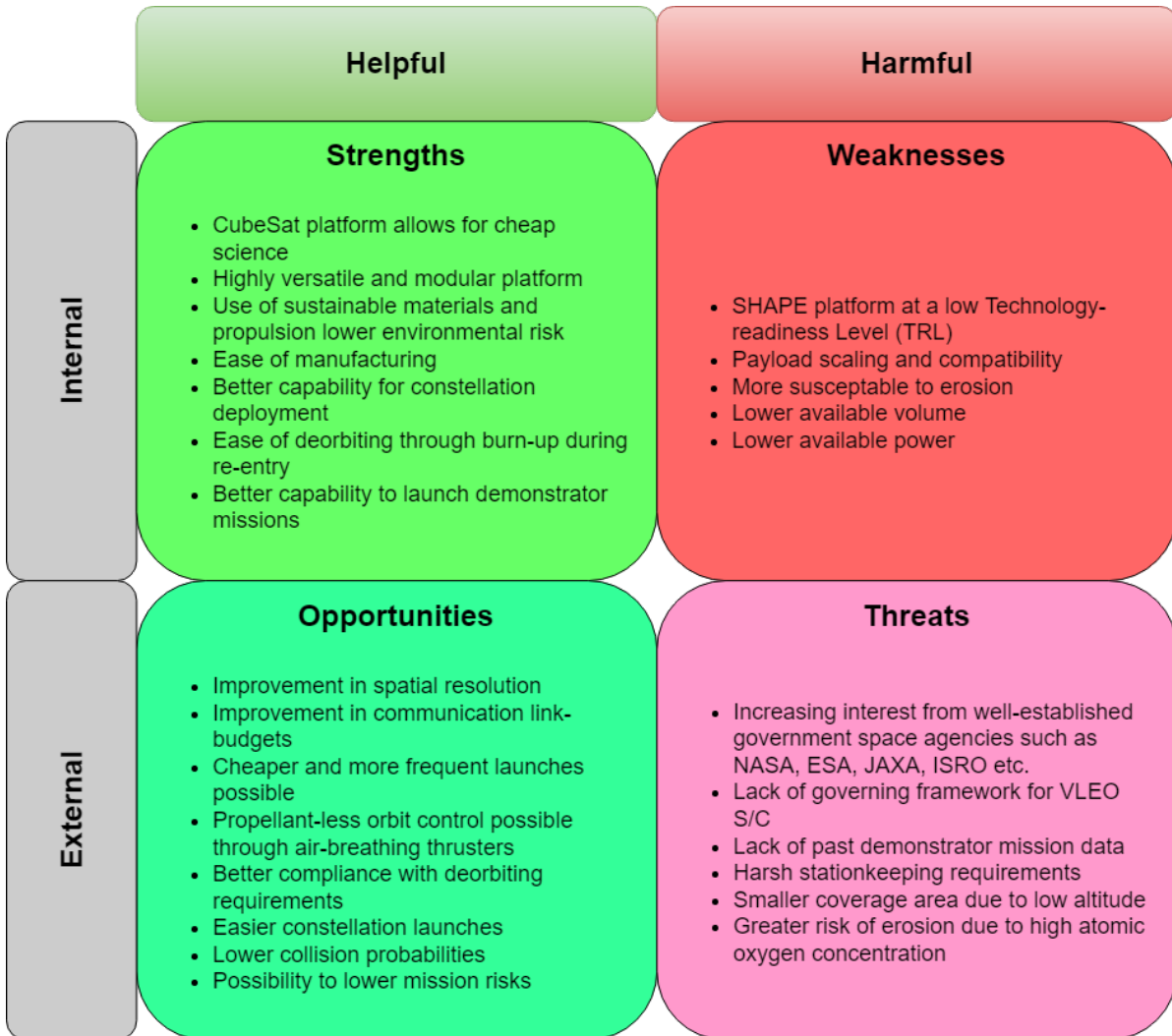


Figure 11.2: SWOT analysis for MAGEOS mission

Chapter 12: Requirements compliance

After the final design has been obtained, it should make sure that all set user requirements are met. To obtain a clear overview, a compliance matrix will be generated. In a compliance matrix, the requirements as well as their IDs are given in a table, together with a compliance columns, which indicates if a requirement is met or not. The compliance matrix is given in Section 12.1.

12.1. Requirements Compliance Matrix

In this section, the compliance matrix for the MAGEOS mission is given. This can be seen in Table 12.2. The table contains an ID, the requirements, followed with if the requirement is met or not. An explanation of the colors is given in Table 12.1.

Table 12.1: Legend for the compliance matrix of the MAGEOS mission

Color	Meaning
(K)	Key (Shortened to (K))
(D)	Driving (Shortened to (D))
(R)	Removed (Shortened to (R))
	Not met
	Met

Table 12.2: Requirements list of MAGEOS [2]

Identifier	Requirement	Compliance
CON-RES-1 (K)	The cost of the space mission shall be less than €5 million	The final cost is €4.2 million
CON-RES-2	The space mission shall be designed in 4000 man-hours	More man-hours than this were spent
CON-RES-3	The space mission shall be designed by ten people	10
CON-USR-1 (D)	The spacecraft shall orbit at a height of less than 280 [km]	<230 km
CON-USR-2	The spacecraft shall perform science for at least 1 years	Mission lifetime is 1 year
CON-USR-3	The spacecraft shall use a GPS system for orbit determination	GPS is used Section 4.3.1
CON-USR-4	The spacecraft shall comply with the CubeSat standard for safety and reliability [149]	Yes
CON-USR-5	The spacecraft shall conform to ISO clean-room standards during assembly, transportation and integration	Yes
CON-USR-6	The spacecraft volume shall be between 4U and 16U	14U
CON-LEG-1	The spacecraft shall use communications within the allocated frequency ranges	Yes
CON-LEG-2	The spacecraft transmitter shall have a power less than 2 [W]	Yes
CON-LEG-3	The spacecraft shall deorbit within 25 years of mission end [150]	Propellant depleted after 1 year mission lifetime, after which it deorbits in the order of weeks
CON-SUS-1	The spacecraft shall be disposed of by total burning in the atmosphere	Yes
CON-SUS-2	The spacecraft shall be disposed of over an area with fewer than 100 inhabitants/km ²	
CON-SUS-3	The spacecraft structure shall be composed of 50% recycled materials	Not analyzed
CON-SUS-4	The spacecraft shall be launched using a reusable first stage	Falcon 9 [®] first stage is reusable Section 7.2.1.5
TECH-EPS-GEN-1	The electrical power system shall provide 32 [W] of power during daytime at EOL	The average power during daytime is 26.5 [W]
TECH-EPS-GEN-2	The electrical power system shall provide 32 [W] of power during eclipse at EOL	The average power during elipse is 14.28 [W]
TECH-EPS-STR-1	The electrical storage system shall have an available capacity of 36 Wh at EOL	The available capacity is 15.8 [Wh]

TECH-EPS-STR-2	The electrical storage system shall be able to withstand at least 11900 charge/discharge cycles with less than 20% degradation	Due to doubling the capacity, it can endure this many cycles
TECH-EPS-STR-3	The batteries shall not be charged above 90% or depleted below 20% during operations	The battery capacity is doubled to accommodate for this
TECH-EPS-DIS-1	The power management system shall protect the spacecraft systems against electrical anomalies	The selected PMS is rated to achieve this
TECH-EPS-DIS-2	The electrical path efficiency shall be no less than 90%	The losses due to PMS and cabling are less than 10%
TECH-TTC-UP-1	The uplink data rate shall be more than 15 kbits/s	12 kbits/s
TECH-TTC-UP-2	The uplink signal to noise ratio shall be more than 6 dB	17 dB
TECH-TTC-UP-3	The spacecraft shall be able to decode received transmissions	Yes
TECH-TTC-DOWN-1	The downlink data rate shall be more than 60 kbits/s	108 kbits/s
TECH-TTC-DOWN-2	The downlink signal to noise ratio shall be more than 6 dB	11
TECH-TTC-DOWN-3	The spacecraft shall have a unique downlink identifier	Yes
TECH-TTC-DOWN-4	The spacecraft shall be able to encode data for transmission	Yes
TECH-ASTRO-ORBIT-1 (K)	The spacecraft shall be able to take measurements at a latitude of 80°	Inclination is within 80°-100° Table 7.1
TECH-ASTRO-ORBIT-2	The ground track shall only repeat after 30 days	Earth-repeat orbit of 30 [days] is chosen Section 5.7
TECH-ASTRO-ORBIT-3	The spacecraft shall be in range of a ground station during 5% of its orbit	6.1% is possible at 230 [km] altitude Section 7.3.2
TECH-ASTRO-ORBIT-4	The spacecraft shall need no more than 500 [m/s] of ΔV to reach its target orbit from its orbit after deployment	417.7 [m/s] is needed Table 7.5
TECH-ASTRO-CONF-1 (D)	The spacecraft constellation shall be comprised of two spacecraft	2 S/C separated at 2.5 [s] Section 5.8
TECH-ASTRO-CONF-2	The spacecraft constellation arrangement shall have the same ground track	Same orbital plane, separated at 2.5 [s] -> approximately same ground track Figure 5.14
TECH-ASTRO-1	The probability of collision shall be less than 0.5% during the operational mission phase	0.0%
TECH-OBC-1	The on-board computer shall be able to store 1 GB of data	2 x 2 GB
TECH-OBC-2	The on-board computer shall be able to perform the nominal mission operations autonomously	Yes
TECH-OBC-3	The on board computer shall have a command data rate of at least 0.4 kb/s	0.59 kb/s
TECH-OBC-4	The on-board computer shall have soft error correction	Software implementation
TECH-STRUC-1	The spacecraft structural integrity shall not be compromised by radical particles	
TECH-STRUC-2 (R)	The spacecraft structure shall maintain the temperature of temperature-sensitive components	
TECH-STRUC-3	No components in the spacecraft structure shall cold weld during the entire mission	Structure qualified
TECH-STRUC-4	The spacecraft structure shall provide mountability for all spacecraft systems	
TECH-STRUC-5	The spacecraft's center of mass shall be within 7 millimeters of the momentum wheel's location in all directions	<2.1 mm difference in all directions
TECH-LCH-LOADS-1	The spacecraft shall be able to endure the forces exerted during launch	Untested
TECH-LCH-LOADS-2 (D)	The spacecraft shall be able to endure the vibrations exerted during launch	Untested
TECH-LCH-1	The spacecraft shall not exceed the allocated launcher mass budget	
TECH-LCH-2	The spacecraft shall fit within the allocated volume within the launcher payload fairing	
TECH-LCH-3	The spacecraft shall be compatible with the launcher's payload deployment mechanism	S/C is compatible with Orbiter, which is compatible with 24" port of Falcon 9 Figure 7.14
TECH-ADCS-1 (K)	The ADCS system shall be derived from the SHAPE ADCS platform	
TECH-ADCS-2	The center of mass of the spacecraft shall be within 7 [cm] of the spacecraft centroid	The center of mass has a maximum deviation of 26.8 [mm]

TECH-ADCS-DET-1	The spacecraft shall be able to determine its attitude with an accuracy greater than 1°	The accuracy for the attitude is 0.0014°
TECH-ADCS-CTRL-1 (R)	The ADCS system shall provide a stable platform for the magnetometer measurements	
TECH-ADCS-CTRL-2 (R)	The ADCS system shall provide a stable platform for the gravimeter measurements	
TECH-ADCS-CTRL-3 (R)	The ADCS system shall provide a stable platform for Earth observation	
TECH-ADCS-CTRL-4 (R)	The ADCS system shall continuously counteract the disturbance torques on the spacecraft	
TECH-ADCS-CTRL-5	The ADCS system shall provide a pointing accuracy smaller than 1°	The system provides a pointing accuracy of 1°
TECH-ADCS-CTRL-6	The ADCS system shall provide an attitude stability greater than 0.1°/s	The system provides a stability of less than 0.1°
TECH-PROP-1 (R)	The propulsion system shall have a specific impulse greater than TBD seconds	
TECH-PROP-2 (R)	The propulsion system shall have a ΔV budget of TBD m/s	
TECH-PROP-3 (R)	The propulsion system shall deliver an acceleration smaller than TBD m/s ²	
TECH-PROP-4 (R)	The propulsion system shall be capable of restarting TBD times	
TECH-PROP-5	The propulsion exhaust plumes shall not obstruct the path of the S/C	The plume aperture is deemed to be sufficiently small and non-disruptive through analysis
TECH-PROP-6 (R)	The propulsion system shall have a throttle range of TBD% to 100% of nominal thrust	
TECH-PROP-7 (R)	The propellant shall not degrade within the mission duration	
TECH-PROP-8 (R)	The propulsion system shall have a minimum pulse duration of less than TBD s	
TECH-PROP-9 (D)	The propulsion system shall deliver a minimum total impulse of 2687 [N · s]	The chosen system offers a total impulse >4400 [N · s].
TECH-PROP-10 (D)	The propulsion system, including propellant, shall not occupy more than 6U of volume	The propulsion modules occupy 4U of volume as a whole
TECH-PROP-11 (D)	The propulsion system shall deliver a minimum thrust of 100 [mN]	The propulsion system delivers a minimum thrust of 780 [mN]
TECH-PROP-12	The thrust delivered by each thruster shall not be more than 1000 [mN] during operation	The thrusters are to be operated at a nominal thrust of 0.5 [N] each during the mission
TECH-PROP-13	The propulsion system shall have an equal number of thrusters placed symmetrically about the S/C's yaw axis	The propulsion system uses two symmetrically placed thruster modules.
TECH-PROP-14	The thrust delivered by each thruster shall be throttleable within ±10% of the nominal thrust	The thrusters can throttle from 0.39-1.37 [N], which exceeds the 0.45-0.55 [N] 10% limit
TECH-PROP-15 (D)	The propulsion system shall have a minimum lifetime of one year	The propulsion system has a lifetime of >12000 cold starts i.e. three times the current lifetime of one year, and the propellant does not degrade before five years
TECH-PROP-16	The propulsion shall consume a maximum of 1400 [J] of electrical energy during burns	The propulsion system consumes a maximum of 40.74 [J] of electrical energy during burns
TECH-PROP-17 (K)	The propellants used by the propulsion system shall be compliant with REACH regulations	The propulsion system utilises a non-toxic REACH compliant nitrous oxide-propene mix
TECH-INS-CAM-1 (K) (R)	The camera instrument shall have a spatial resolution of TBD m/pixel	
TECH-INS-CAM-2 (K) (R)	The camera instrument shall have a sampling speed of TBD Hz	
TECH-INS-CAM-3 (R)	The camera instrument shall take images in the visible light spectrum (380 nm to 750 nm) using three color channels	
TECH-INS-CAM-4 (R)	The camera instrument shall output TBD bits/color channel	

TECH-INS-GRAV-1 (K)	The gravitometer instrument shall take measurements with an accuracy better than 3 [cm] EWH	$\sigma = 80$ [m], significantly above 3 [cm]
TECH-INS-GRAV-2 (K)	The gravitometer measurements shall be calibratable with GRACE	Same data types are collected as in GRACE
TECH-INS-GRAV-3	The gravitometer shall have a sampling speed of 10 measurements/s	10 Hz sampling speed
TECH-INS-GRAV-4	The gravitometer shall output measurements in digital format	GNSS standard output is digital
TECH-INS-GRAV-5	The gravitometer shall output no more than 200 bits/measurement	168 bits/measurement
TECH-INS-GRAV-6 (R)	The gravitometer shall be either a downscaled gravitometer or atomic clock	Table 4.2 and GPS sensor used
TECH-INS-MAG-1 (K)	The magnetometer shall make measurements with an accuracy greater than 1 nT	Accuracy of $\sigma = 0.5$ nT achieved
TECH-INS-MAG-2 (K)	The magnetometer measurements can be calibrated with those of the SWARM spacecraft	Same data types are collected as in SWARM
TECH-INS-MAG-3 (R)	The magnetometer shall be an adapted SHAPE magnetometer or a different downscaled magnetometer	
TECH-INS-MAG-4	The magnetometer shall output measurements in digital format	Output will be vector of magnetic components
TECH-INS-MAG-5	The magnetometer shall output be less than 200 bits/measurement	196 bits/measurement
TECH-INS-MAG-6	The magnetometer shall have a sampling speed of at least 10 measurements/sec	160 Hz
TECH-INS-MAG-7	The interference of other systems on the magnetometer measurements shall be less than 0.5 nT	$\sigma = 0.5$ nT achieved
TECH-1 (D)	The probability that any mission terminating failure occurs within the mission lifetime shall be less than 0.15%	>0.15%
TECH-2	All spacecraft systems shall be able to start up remotely	
TECH-ENV-1	The spacecraft shall be able to withstand the vacuum of space	Only vacuum-proven components are used
TECH-ENV-2	The spacecraft shall be able to withstand 10 [Gy] throughout the mission lifetime [151]	Only radiation-proven components are used
TECH-ENV-3	The spacecraft shall survive within the temperature range of 73 K to 473 K throughout the mission lifetime	

12.2. Power and battery storage

Requirements TECH-EPS-GEN-1 and TECH-EPS-GEN-2 state that the power supplied by the EPS system should equal 32 [W] continuously in both daylight and eclipse. These requirements have not been fulfilled, as the EPS system provides less than this amount to the other subsystems. This is not a problem however, as this power requirement was set based on initial estimates. The EPS system does currently provide sufficient power to the other subsystems, but this power need is less than the requirement. It is therefore not an issue that this requirement was not fulfilled.

Similarly, requirement TECH-EPS-STR-1 was not fulfilled, as this battery capacity was a first estimate. The available battery capacity of 15.7, from both the main batteries and the PMS backup battery, is sufficient for the spacecraft to function, and therefore this requirement need not be fulfilled.

12.3. Pointing accuracy

According to requirement TECH-ADCS-CTRL-5, the ADCS system shall provide a pointing accuracy smaller than 1 [°].

What will be discussed in this section:

- Reason for why the pointing accuracy should be below 1 [°]

12.4. Attitude stability

Requirement TECH-ADCS-CTRL-6 stipulates that the ADCS system shall provide an attitude stability greater than 0.1 [°/s]. The stability requirement is conditionally fulfilled if the the requirement TECH-STRUC-5 is fulfilled. This requirement states that the difference in center of mass with respect to the momentum wheel's location is less than 7 mm for all directions. Obtaining this requirement constraints the design and the placement of all components. validating this requirement is done by using the simulation tool which calculates the center of mass using the geometry and component information (Seen in section 6.7.1.1). Using the verified model by using pre-calculated reference geometry with dummy components.'

Chapter 13: Conclusion & Recommendations

The MAGEOS mission, Magnetic And Gravitational Earth Observation Spacecraft, was designed to obtain magnetic and gravitational field measurements in very low Earth orbit, providing cheap and high quality science to the science community. The most important user requirements, measuring in a very low Earth orbit and obtaining a magnetic field accuracy of less than 1 [nT] has been met. The operational altitude of the MAGEOS mission will be 229.7 [km]. The maximum accuracy the spacecraft could provide for magnetic field measurements has been determined to be < 1 [nT]. The main goals of the projects has therefore be obtained. However, the gravitational field measurement accuracy was determined to be better than 3 [cm]. Unfortunately, the accuracy has been found to be 80 [m]. This leads to the conclusion that the gravitational measurements do not meet the requirements. In general, the design can be called a success, since the overall mission costs are less than 5 million euros, providing a higher magnetic field accuracy compared to current mission. At the beginning of the project, a high resolution camera has been provided to the team as possible payload for the mission. Considering the fact that the gravitational field accuracy is too high to provide meaningful data, it is recommended to remove the components for the gravitational field measurement and replace them with the camera. In that way, more meaningful data will be obtained.

Now the total mission has been discussed, the individual subsystems design and mission characteristics can be concluded and discussed. The orbit has been set on 229.7 [km]. The drag at this altitude has been found to be high. It is recommended to move this mission to a higher altitude to obtain a longer mission lifetime. The current lifetime of one year was concluded to be too short to be competitive with other missions. Furthermore, it was concluded that in case the altitude would be raised, the drag decreases which saves up more propellant. This leads to more Delta-V available for orbit insertion and therefore, the orbital transfer vehicle does no longer need to be used for orbit insertion. It is recommended not to make use of the orbital transfer vehicle, to reduce mission cost and risks of mission failure due to separation failures. The aerodynamics of the spacecraft has been determined making use of simplified equations and are therefore not very reliable. It is recommended to update the drag and lift coefficient for the spacecraft making use of the finalised design CAD model, making use of the ADBsat software. This will lead to a more accurate prediction for the drag and lift coefficient. The total system characteristics are given in Table 8.1 and Table 8.2.

The total wet mass of the each spacecraft is 18.46 [kg]. If the orbital transfer vehicle is not being used, it is recommended to add more mass for the spacecraft. This eases the drag compensation manoeuvres, extending the mission lifetime. Since, for a rideshare mission, 200 [kg] of mass is allowed to bring onboard, adding more mass to the spacecraft is not considered to be an issue. The total amount of power consumption of each spacecraft will be 17.23 [W]. In the post DSE activities, it is recommended to perform subsystem tests for each subsystem, once they have arrived at the assembly facility, to check the proper working of each subsystem. During the assembly, verification procedures should be performed to make sure that the interconnections between each subsystem works.

References

- [1] D. G. 09. *MAGEOS: Cubesat Mission for Measurements in Extreme VLEO, Midterm Technical Design Report*. Brightspace. 2022.
- [2] D. G. 09. *Cubesat Mission for Measurements in Extreme VLEO*. Brightspace. 2022.
- [3] T. Segert. *The Carbon Footprint of a Satellite*. 2021. URL: <https://www.linkedin.com/pulse/carbon-footprint-satellite-tom-segert> (visited on 06/03/2022).
- [4] *Calculate and compensate your CO2 emissions*. 2022. URL: <https://www.greentripper.org/en> (visited on 06/03/2022).
- [5] F. Kordina. *WHAT IS THE ENVIRONMENTAL IMPACT ROCKETS HAVE ON OUR AIR?* 2020. URL: <https://everydayastronaut.com/rocket-pollution/> (visited on 06/03/2022).
- [6] H. Centre. *What Earth's gravity reveals about climate change*. 2019. URL: <https://www.sciencedaily.com/releases/2019/04/190416132155.htm> (visited on 06/03/2022).
- [7] H. Schafel. *Earth's Magnetosphere: Protecting Our Planet from Harmful Space Energy*. 2022. URL: <https://climate.nasa.gov/news/3105/earths-magnetosphere-protecting-our-planet-from-harmful-space-energy/> (visited on 06/03/2022).
- [8] T. Pultarova. *Air pollution from reentering megaconstellation satellites could cause ozone hole 2.0*. 2021. URL: <https://www.space.com/starlink-satellite-reentry-ozone-depletion-atmosphere> (visited on 06/04/2022).
- [9] "The Swarm magnetometry package". In: *Small satellites for Earth observation*. Springer, 2008, pp. 143–151.
- [10] "Precision Magnetometers for Aerospace Applications: A Review". In: *Sensors* 21.16 (2021). ISSN: 1424-8220. URL: <https://www.mdpi.com/1424-8220/21/16/5568>.
- [11] D. D. R. Williams. *Magsat*. 2022. URL: <https://nssdc.gsfc.nasa.gov/nmc/spacecraft/display.action?id=1979-094A> (visited on 05/25/2022).
- [12] Not_specified. *VFM Overview*. 2022. URL: <https://earth.esa.int/eogateway/instruments/vfm/description> (visited on 05/25/2022).
- [13] *How a fluxgate works*. URL: <https://www.imperial.ac.uk/space-and-atmospheric-physics/research/areas/space-magnetometer-laboratory/space-instrumentation-research/magnetometers/fluxgate-magnetometers/how-a-fluxgate-works/>.
- [14] Sensorland. *What is a Fluxgate?* URL: <https://www.sensorland.com/HowPage071.html> (visited on 05/06/2022).
- [15] N. F. Ness et al. "Use of two magnetometers for magnetic field measurements on a spacecraft". In: *Journal of Geophysical Research (1896-1977)* 76.16 (1971), pp. 3564–3573. DOI: <https://doi.org/10.1029/JA076i016p03564>. eprint: <https://agupubs.onlinelibrary.wiley.com/doi/pdf/10.1029/JA076i016p03564>. URL: <https://agupubs.onlinelibrary.wiley.com/doi/abs/10.1029/JA076i016p03564>.
- [16] NSS. *NSS Magnetometer*. 2021. URL: <https://www.cubesatshop.com/product/nss-magnetometer/>.
- [17] D. Wallis et al. "The CASSIOPE/e-POP magnetic field instrument (MGF)". In: *Space Science Reviews* 189.1 (2015), pp. 27–39.
- [18] *6U CubeSat Bus*. URL: <https://www.isispace.nl/product/6u-cubesat-bus/> (visited on 05/30/2022).
- [19] E. S. Agency. *Swarm Data Access*. 2022. URL: https://swarm-diss.eo.esa.int/#swarm/Level1b/Entire_mission_data/MAGx_HR.
- [20] S. Teunissen. private communication. 2022.
- [21] NASA. *Spherical Harmonic Representation of the Gravity Field Potential*. URL: https://spsweb.fltops.jpl.nasa.gov/portaldataops/mpg/MPG_Docs/Source\%20Docs/gravity-SphericalHarmonics.pdf.
- [22] J. Wahr, M. Molenaar, and F. Bryan. "Time variability of the Earth's gravity field: Hydrological and oceanic effects and their possible detection using GRACE". In: *Journal of Geophysical Research: Solid Earth* 103.B12 (1998), pp. 30205–30229. DOI: <https://doi.org/10.1029/98JB02844>. eprint: <https://agupubs.onlinelibrary.wiley.com/doi/pdf/10.1029/98JB02844>. URL: <https://agupubs.onlinelibrary.wiley.com/doi/abs/10.1029/98JB02844>.
- [23] *Actions*. URL: <https://people.csail.mit.edu/sparis/sh/index.php?img=64>.
- [24] B. F. Chao and R. S. Gross. "Changes in the Earth's rotation and low-degree gravitational field induced by earthquakes". In: *Geophysical Journal of the Royal Astronomical Society* 91.3 (1987), pp. 569–596. DOI: <https://doi.org/10.1111/j.1365-246X.1987.tb01659.x>. eprint: <https://onlinelibrary.wiley.com/doi/pdf/10.1111/j.1365-246X.1987.tb01659.x>. URL: <https://onlinelibrary.wiley.com/doi/abs/10.1111/j.1365-246X.1987.tb01659.x>.
- [25] P. Ditmar and A. V. E. van der Sluijs. "A technique for modeling the Earth's gravity field on the basis of satellite accelerations". In: *Journal of Geodesy* 78 (2004), pp. 12–33.
- [26] T. L. Abt. "Determination of a gravity field model from one month of CHAMP satellite data using accelerations". PhD thesis. University of Stuttgart, 2004, pp. 1–87. URL: <https://elib.uni-stuttgart.de/bitstream/11682/3713/1/abt.pdf>.
- [27] GranStal Solutions Ltd. *GSD800 GNSS Receiver*. 2021. URL: https://gnssmart.com/wp-content/uploads/2021/07/GranStal_Solutions_GNSSINS_Brochure_Ver4.1.2021_EN-1.pdf.
- [28] "COTS based GNSS Receiver with Precise Point Positioning for CubeSats". In: *MATEC Web of Conferences*. Vol. 304. EDP Sciences. 2019, p. 07009.
- [29] *Datasheet ANT-GNCP-C25L15100 L1/L5 Active Ceramic Patch GNSS Antenna*. URL: <https://linxtechnologies.com/wp-content/uploads/ant-gncp-c25l15100-ds.pdf> (visited on 05/25/2022).
- [30] *GSD800 GNSS receiver*. URL: <https://satsearch.co/products/gnssmart-gsd800-gnss-receiver>.
- [31] *Real Time Kinematics*. 2014. URL: https://gssc.esa.int/navipedia/index.php/Real_Time_Kinematics (visited on 06/03/2022).
- [32] P. L. Aleš Bezděk. "General relativistic effects and estimation of time-varying earth gravity field". In: *Journal of Applied Geophysics* 161 (2019).
- [33] J. Benkhoff et al. "BepiColombo-Mission overview and science goals". In: *Space science reviews* 217.8 (2021), pp. 1–56.
- [34] V. Iafolla et al. "The BepiColombo ISA accelerometer: Ready for launch". In: *2016 IEEE Metrology for Aerospace (MetroAeroSpace)*. IEEE. 2016, pp. 538–544.
- [35] L. J. Tyahla. *Welcome to ILSR*. 2022. URL: <https://ilrs.gsfc.nasa.gov/> (visited on 05/23/2022).
- [36] *NERC Space Geodesy Facility: SLR Specifications*. 2019. URL: <http://sgf.rgo.ac.uk/sysspec/slr.html> (visited on 05/25/2022).
- [37] "The dielectric constant of air at radiofrequencies". In: *Physics* 7.4 (1936), pp. 133–136.
- [38] "The influence of temperature on the dielectric permittivity and complex electrical resistivity of porous media saturated with DNAPLs: a laboratory study". In: *Journal of Applied Geophysics* 172 (2020), p. 103921. DOI: 10.1016/j.jappgeo.2019.103921.
- [39] C. S. Gardner. "Effects of horizontal refractivity gradients on the accuracy of laser ranging to satellites". In: *Radio Science* 11.12 (1976), pp. 1037–1044. DOI: <https://doi.org/10.1029/RS011i012p01037>.
- [40] *What Is Refraction of Light?* 2022. URL: <https://www.ti.meanddate.com/astronomy/refraction.html> (visited on 05/30/2022).
- [41] J. W. Marini and C. W. Murray. *Correction of laser range tracking data for atmospheric refraction at elevations above 10 degrees*.

- radiation-hardened-2-terminal-temperature-transducer#document.
- [93] S. Consortium et al. "Standard commands for programmable instruments (SCPI), volume 1: Syntax and style". In: *USA, May* (1999).
- [94] *ISIS on board computer*. 2021. URL: <https://www.isispace.nl/product/on-board-computer/>.
- [95] *Industrial RS-232 To RS-485/RS-422 Converter*. URL: https://www.serialcomm.com/datasheets/CDN-485_422-PI9.pdf.
- [96] D. Ju. "Attitude Control Subsystem Design of the Stable and Highly Accurate Pointing Earth-imager". In: (2017).
- [97] I. van Hengel. 2018. URL: <https://repository.tudelft.nl/islandora/object/uuid:dc8b7355-cf46-410c-94c3-cc85570b94a7/datastream/OBJ/download>.
- [98] L. KAIROSPACE Co. *Star tracker*. 2021. URL: <https://satsresearch.co/products/kairospace-star-tracker> (visited on 06/03/2022).
- [99] *SATELLITE DRAG*. 2021. URL: <https://www.swpc.noaa.gov/impacts/satellite-drag> (visited on 05/25/2022).
- [100] *Shape Effects on Drag*. 2021. URL: <https://www.grc.nasa.gov/www/k-12/airplane/shaped.html> (visited on 05/25/2022).
- [101] E. Doombos. *Thermospheric density and wind determination from satellite dynamics*. Springer Science & Business Media, 2012.
- [102] L. H. Sentman. *Free molecule flow theory and its application to the determination of aerodynamic forces*. Tech. rep. LOCKHEED MISSILES and SPACE CO INC SUNNYVALE CA, 1961.
- [103] S. Bender. *PyNRLMSISE-00*. 2020. URL: <https://pynrlmsise00.readthedocs.io/en/latest/README.html#> (visited on 06/01/2022).
- [104] E. K. Sutton. "Normalized force coefficients for satellites with elongated shapes". In: *Journal of Spacecraft and Rockets* 46.1 (2009), pp. 112–116.
- [105] *Design Synthesis Exercise Group 09*. 2022. URL: https://github.com/adriaan740/DSE_MAGEOS.git (visited on 05/25/2022).
- [106] *ADBSat (Aerodynamic Database for Satellites)*. 2022. URL: <https://github.com/nhcrisp/ADBSat/blob/master/README.md> (visited on 06/02/2022).
- [107] *Orbiter*. URL: <https://www.launcherspace.com/orbiter>.
- [108] SpaceX. *SMALLSAT RIDESHARE PROGRAM*. URL: <https://www.spacex.com/rideshare/>.
- [109] *Database nanosats*. 2022. URL: <https://airtable.com/shrAfcwXODMMKeRgU/tblDJo0BP5w1N0JQY>.
- [110] *How do satellites deorbit? KRAKsat case study*. 2022. URL: <https://alicja.space/blog/how-satellites-deorbit-kraksat-study/>.
- [111] *Space debris: feel the burn*. 2021. URL: https://www.esa.int/Safety_Security/Clean_Space/Space_debris_feel_the_burn.
- [112] S. E. T. Corp. *FALCON USER'S GUIDE*. 2021. URL: <https://www.spacex.com/media/falcon-users-guide-2021-09.pdf>.
- [113] J. Bouwmeester, A. Menicucci, and E. Gill. "Improving CubeSat reliability: Subsystem redundancy or improved testing?" In: *Reliability Engineering & System Safety* (2022), p. 108288.
- [114] "Electric propulsion reliability: Statistical analysis of on-orbit anomalies and comparative analysis of electric versus chemical propulsion failure rates". In: *Acta Astronautica* 139 (2017), pp. 141–156.
- [115] J. Guo, L. Monas, and E. Gill. "Statistical analysis and modelling of small satellite reliability". In: *Acta Astronautica* 98 (2014), pp. 97–110.
- [116] *Falcon 9*. 2022. URL: https://en.wikipedia.org/wiki/Falcon_9#Reliability (visited on 06/03/2022).
- [117] J. H. Kuiper. *Advanced Earth Observation Systems Faculty of Aerospace Engineering with High Spatial Resolution*. 2016. URL: https://www.ruimtevaart-nvr.nl/wp-content/uploads/NLR_IAC_2016_IP_JMKuiper_last.pdf.
- [118] C. Nieto-Peroy and M. R. Emami. "CubeSat Mission: From Design to Operation". In: *Applied Sciences* 9.15 (2019). DOI: 10.3390/app9153110.
- [119] M. Langer et al. "A reliability estimation tool for reducing infant mortality in Cubesat missions". In: *2017 IEEE Aerospace Conference*. 2017, pp. 1–9. DOI: 10.1109/AERO.2017.7943598.
- [120] C. L. G. Batista et al. "Towards increasing nanosatellite subsystem robustness". In: *Acta Astronautica* 156 (2019), pp. 187–196. DOI: <https://doi.org/10.1016/j.actaastro.2018.11.011>.
- [121] C. Nieto and R. Emami. "Integrated Design and Simulation Environment for Space-qualified Onboard Computers". In: : 2018.
- [122] *Cleanrooms for Satellite & Spacecraft Construction*. 2022. URL: <https://blog.gotopac.com/2018/08/31/satellite-cleanrooms/> (visited on 06/08/2022).
- [123] *JPL CubeSat Clean Room: A Factory For Small Spacecraft*. 2022. URL: <https://www.nasa.gov/feature/jpl/jpl-cubesat-clean-room-a-factory-for-small-spacecraft> (visited on 06/08/2022).
- [124] *NLR Research Aircraft Cessna Citation II*. 2022. URL: <https://www.nlr.nl/downloads/e1123-nlr-cessna-citation-ii.pdf> (visited on 06/08/2022).
- [125] E. C. for Space Standardization. *Space Project Management: Project Phasing and Planning*. Tech. rep. ESA-ESTEC, 1996.
- [126] J. Debes et al. "Rapid Build and Space Qualification of CubeSats". In: 2011.
- [127] *CubeSat101: Basic Concepts and Processes for First-Time CubeSat Developers*. 8th ed. USA: NASA CubeSat Launch Initiative, 2017.
- [128] T. Mai. *Spectrum Guidance for NASA: Small Satellite Missions*. Tech. rep. NASA Spectrum Management Program, 2015.
- [129] S. Walsh et al. "Development of the EIRSAT-1 CubeSat through Functional Verification of the Engineering Qualification Model". In: *Aerospace* 8.9 (2021). DOI: 10.3390/aerospace8090254.
- [130] R. E. R. Department. *A realistic discount rate*. 2012. URL: https://economics.rabobank.com/contentassets/ff8d00e02a2c4926b18011079a271e94/sr1216tsm_a_realistic_discount_rate.pdf.
- [131] E. Mooij. *Project Management and Systems Engineering in the DSE*. 2022.
- [132] E. Gregersen. *Space debris*. May 2022. URL: <https://www.britannica.com/technology/space-debris>.
- [133] ESA. *Best view yet of global gravity*. 2011. URL: https://www.esa.int/Applications/Observing_the_Earth/FutureEO/GOCE/Earth_s_gravity_revealed_in_unprecedented_detail.
- [134] Canada.ca. *Learning about space weather*. 2021. URL: <https://spaceweather.gc.ca/info-gen/index-en.php>.
- [135] Canada.ca. *Space weather effects on technology*. 2021. URL: <https://spaceweather.gc.ca/tech/index-en.php>.
- [136] H. J. Kramer. *SkySat constellation of Terra Bella*. 2022. URL: <https://directory.eoportal.org/web/eoportal/satellite-missions/s/SkySat#spacecraft> (visited on 06/13/2022).
- [137] Skysat. *Mission Description*. 2022. URL: <https://earth.esa.int/eogateway/missions/skysat/description> (visited on 06/13/2022).
- [138] G. D. Krebs. *Gunter's Space Page*. 2022. URL: https://space.skyrocket.de/doc_sdat/flock-1.htm#:~:text=The%20Flock%20earth%20observing%20constellation,in%20longer%20lived%20polar%20orbits (visited on 06/13/2022).
- [139] H. J. Kramer. *Dove-1 and Dove-2 Nanosatellites*. 2022. URL: <https://directory.eoportal.org/web/eoportal/satellite-missions/d/dove> (visited on 06/13/2022).
- [140] E. Kulu. *NSPO-1*. 2022. URL: <https://www.nanosats.eu/sat/nspo-1> (visited on 06/13/2022).
- [141] G. D. Krebs. *Lemur-2*. URL: https://space.skyrocket.de/doc_sdat/lemur-2.htm (visited on 06/13/2022).
- [142] Wikipedia. *EarthCARE*. URL: <https://en.wikipedia.org/wiki/EarthCARE> (visited on 06/13/2022).
- [143] Wikipedia. *Cartosat-3*. URL: <https://en.wikipedia.org/wiki/Cartosat-3> (visited on 06/13/2022).
- [144] Wikipedia. *Global Precipitation Measurement*. URL: https://en.wikipedia.org/wiki/Global_Precipitation_Measurement (visited on 06/13/2022).

- [145] Wikipedia. *RISAT-2B*. URL: <https://en.wikipedia.org/wiki/RISAT-2B> (visited on 06/13/2022).
- [146] H. J. Kramer. *WorldView Legion Constellation of Maxar*. URL: <https://directory.eoportal.org/web/eoportal/satellite-missions/v-w-x-y-z/worldview-legion> (visited on 06/13/2022).
- [147] Wikipedia. *SWARM*. URL: [https://en.wikipedia.org/wiki/Swarm_\(spacecraft\)](https://en.wikipedia.org/wiki/Swarm_(spacecraft)) (visited on 06/13/2022).
- [148] Wikipedia. *Joint Polar Satellite System*. URL: https://en.wikipedia.org/wiki/Joint_Polar_Satellite_System (visited on 06/13/2022).
- [149] ESA. *Product and Quality Assurance Requirements for In-Orbit Demonstration CubeSat Projects*. 2013. URL: [\url{https://www.google.com/url?sa=t&rct=j&q=&esrc=s&source=web&cd=&ved=2ahUKEwi71cr116r4AhXziv0HHZnqB_kQFnoECAUQAQ&url=http%3A%2F%2Femits.sso.esa.int%2Femits-doc%2FESTEC%2FA08352_AD2_IOD_CubeSat_PQA_Reqs_Iss1_Rev1.pdf&usg=AOvVaw2JY3hXMrxJBIqpuIut_1x0}](https://www.google.com/url?sa=t&rct=j&q=&esrc=s&source=web&cd=&ved=2ahUKEwi71cr116r4AhXziv0HHZnqB_kQFnoECAUQAQ&url=http%3A%2F%2Femits.sso.esa.int%2Femits-doc%2FESTEC%2FA08352_AD2_IOD_CubeSat_PQA_Reqs_Iss1_Rev1.pdf&usg=AOvVaw2JY3hXMrxJBIqpuIut_1x0) (visited on 06/13/2022).
- [150] ESA. *Mitigating space debris generation*. URL: https://www.esa.int/Safety_Security/Space_Debris/Mitigating_space_debris_generation (visited on 06/13/2022).
- [151] NASA. *Space Radiation Effects on Electronic Components in Low-Earth Orbit*. URL: <https://llis.nasa.gov/lesson/824> (visited on 06/13/2022).